

# Fluidic Dielectrophoresis: Electrokinetic Polarization and Manipulation of Electrical Liquid Interfaces for Biological and Sensing Applications

by  
Nicholas Mavrogiannis

A dissertation submitted to Johns Hopkins University in conformity with the requirements for the degree of Doctor of Philosophy

Department of Chemical and Biomolecular Engineering  
Baltimore, MD

February 2018

© Nicholas Mavrogiannis 2018  
All Rights Reserved

# *Abstract*

---

Development of rapid, sensitive and portable detection systems are important for effective detection of diseases in developing countries, biowarfare/anti-terrorism applications, environmental monitoring, and for basic biological research. One of the most specific and popular sensing platform is the enzyme-linked immunosorbent assay (ELISA) platform, which identifies the presence of a substance, specifically an antigen, in a liquid sample. Biosensing assays, like ELISA, offer sensitivity and selectivity, however, its assay time is long due to immobilization and detection through a secondary antibody. The assay also requires periodic rinsing steps to avoid non-specific binding and to remove excess proteins. Finally, the fluorescent detection instrumentation is required, and is still too bulky and costly for widespread daily laboratory, clinical and point-of-care use. The main challenge for producing low cost, portable, and easy to operate biosensing systems is then to miniaturize the sensing platform without any sophisticated instrumentation and complicated reagent protocols.

In this work, we first explore a well-known electrokinetic phenomenon called dielectrophoresis (DEP), which traditionally has been studied in cells and particles, but here at a liquid-liquid interface, which we call fluidic dielectrophoresis (fDEP). The liquid-liquid interface with disparaging electrical properties – conductivity and permittivity – is shown to move when subjected to an alternating current (ac) electric field and the direction and magnitude is studied at varying applied frequencies and voltages.

We found that when a biomolecular reaction occurs at the liquid-liquid interface it alters the electrical properties, which is transduced by interfacial displacement; we call this novel transduction method interfacial electrokinetic transduction (IET). We began with

a model biomolecular reaction between biotin and avidin to validate our detection scheme. We then performed detection of hCG in human serum. Finally, we implemented impedance spectroscopy to non-optically monitor the position of the interface. Coupled with IET, the system non-optically monitored the position of the electrical interface in the presence of a biomolecular reaction.

Collectively, we successfully developed the first, in solution, label-free non-optical biosensor. This novel biosensor was shown to detect biomarkers down to femtomolar concentration in human serum within minutes.

*Thesis Advisor: Dr. Zachary Gagnon*

*Thesis Committee: Dr. Joelle Frechette, Dr. Jordan Green, Dr. Jamie Spangler & Dr.*

*Youseph Yazdi*

Intended to be blank

# *Acknowledgements*

---

I would first like to thank my advisor, Dr. Zachary Gagnon. We began our journey during my time as an undergraduate student. When I first began as a junior, Dr. Gagnon treated me as an equal and always valued my opinions, a quality that is not exhibited by many. He was a master at balancing both being a mentor, boss and friend to me. The opportunities he has given me, specifically allowing me to remain in his lab and pursue my PhD were unimaginable to me when I first started and still leave me unwaveringly grateful to him. I was extremely lucky to have a mentor who always challenged me to learn and grow as a theorist and experimentalist.

I also must thank others in the Gagnon Microfluidics Lab that helped me during my time as an undergraduate till a graduate whom I am lucky enough to call my colleagues and friends: Dr. Markela Ibo, Dr. Xiaotong Fu, Francesca Crivellari, Mitchell Desmond, Josh Cole, Steven Doria, Luis Rodriguez, Edwin Lavi, Kenny Ling and Robert McLarnon. They have trained me in numerous techniques and provided immeasurable intellectual support, which were critical to the development of this work, as well as my personal development as a researcher. First, I would like to give a special thanks to Mitch Desmond who joined the lab with me in 2012. Together we taught ourselves microfabrication, basics in microfluidics and electrokinetics and developed the seminal work that would be the foundation of my dissertation. I would also like to thank Dr. Xiaotong Fu and Francesca Crivellari for always being a support system when I had too much on my plate, as well as helping me with numerous projects that I could not have completed without their help and advice. Lastly, all the master's and undergraduate students: Steven, Edwin, Luis, Kenny

and Robert, who worked tremendously hard to assist in projects and see them to completion.

I would also like to thank those at JHU outside of my laboratory experience who were supportive throughout everything else. These people helped me keep my hopes up and remember my overall goal and will always be my friends and my family: Jimmy Sowers, Jordan Pryor, Ayobami Ward, Aniket Parikh, Kimberly Ellis, Angela San, Mark Sowers, Maya Hernandez, Jacky Tse and Alex Schiffhauer. First, I want to thank my group of friends we refer to as the “Cresmont Crew.” We became friends during our undergraduate studies and you all have supported me unconditionally ever since. I could not have made it through JHU without you and I am eternally grateful for you all and proud to call you my family. Next, I would like to thank my other group of friends who were also ChemBEs and helped me through countless nights completing projects and homeworks, studying for exams and also destressing from all said work. Without you, my ChemBE and JHU experience would not have been the same and I am so fortunate to call you my friends and family.

Lastly, and most importantly, I would like to thank my family for supporting me and being in my corner unwaveringly and without question. I decided to pursue a degree in chemical engineering because of my mother, who is a chemical engineer as well. You have always been a constant inspiration, and your love, drive, work ethic and compassion have made me the person I am today. I would not have even considered pursuing a PhD without the support from my father. All the sacrifices you have made for me will never be forgotten and I will never take the lessons you have taught me for granted. Finally, my sister who has always defended me, even as children, has been a constant driving force

in pursuing greater things. I have always looked up to you and tried to follow the path you have set for me.

Thank you.

# Table of Contents

---

<b>Abstract</b> .....	<b>ii</b>
<b>Acknowledgements</b> .....	<b>v</b>
<b>Table of Contents</b> .....	<b>viii</b>
<b>List of Tables</b> .....	<b>xii</b>
<b>List of Supplementary Tables</b> .....	<b>xiii</b>
<b>List of Figures</b> .....	<b>xiv</b>
<b>List of Supplementary Figures</b> .....	<b>xvii</b>
<b>1 Executive Summary</b> .....	<b>1</b>
<b>2 Introduction</b> .....	<b>4</b>
2.1 Electrokinetics for fluid manipulation .....	6
2.2 Electrokinetic Flows .....	8
2.2.1 Induced double layer .....	8
2.2.2 AC electroosmosis .....	9
2.2.3 Electrothermal (ET) flow .....	11
2.3 Classic dielectrophoresis .....	12
2.4 Biosensors – various types .....	15
2.4.1 Optical biosensors .....	16
2.4.1.1 Fluorescent biosensors .....	16
2.4.1.2 Surface Plasmon Resonance (SPR) biosensors .....	17
2.4.1.3 Chemiluminescence (CL) biosensors .....	19
2.4.1.4 Colorimetric biosensors .....	20
2.4.1.5 Paper-based biosensors .....	20
2.4.2 Electrochemical biosensors .....	21
2.4.2.1 Amperometric biosensors .....	22
2.4.2.2 Potentiometric biosensors .....	23
2.4.2.3 Impedimetric biosensors .....	23
2.4.3 Piezoelectric biosensors .....	24
2.4.4 Magnetic biosensors .....	25
2.4.5 Thermometric Biosensors .....	26
2.5 State-of-the-art: Microfluidic biosensors .....	26
2.6 Liquid-Liquid interfacial biosensors .....	27
2.7 Thesis Aims .....	28
2.8 Thesis Overview .....	29
<b>3 Overview of Methods</b> .....	<b>31</b>
3.1 Microelectrode fabrication .....	31
3.1.1 Metal deposition .....	31
3.1.2 Standard lithography procedure .....	32
3.1.3 Metal etching .....	32
3.2 Microchannel fabrication .....	33
3.2.1 Microchannel fabrication by soft lithography .....	33
3.2.2 Alignment and sealing of microchannels .....	35
3.3 Constant-pressure flow source .....	36
3.3.1 A low-cost microfluidic flow controller .....	36



3.3.2	Hydraulic circuit analysis .....	37
3.3.3	Hydraulic circuit analysis .....	39
3.3.4	Flow controller assembly and testing method .....	40
3.3.4.1	Essential components .....	40
3.3.4.2	Flow controller assembly .....	41
3.3.4.3	Sample holder assembly .....	41
3.3.4.4	Connecting the tubing .....	42
3.4	Supplementary Materials .....	42
3.4.1	Hydraulic resistance measurements .....	42
3.4.2	Flow rate capabilities, stability and response time .....	43
3.4.3	Flow switches prevent fluid back flow .....	45
3.4.4	Flow contributions from hydrostatic pressure .....	47
<b>4</b>	<b>Polarization of Liquid-Liquid Interfaces .....</b>	<b>49</b>
4.1	Introduction .....	49
4.2	Materials and Methods .....	51
4.3	Results and Discussion .....	54
4.4	Conclusion .....	60
<b>5</b>	<b>Fluidic Dielectrophoresis .....</b>	<b>62</b>
5.1	Introduction .....	62
5.2	Theoretical formulation .....	65
5.2.1	Governing equations .....	65
5.2.2	Scaling and simplifications .....	66
5.2.3	Boundary Conditions .....	68
5.2.4	Interfacial Surface Charge .....	69
5.2.5	One dimensional model .....	71
5.3	Materials and Methods .....	74
5.4	Results .....	76
5.4.1	Interfacial displacement at varying AC frequency .....	79
5.4.2	Influence of electrical properties on interfacial displacement .....	80
5.5	Discussion .....	81
5.6	Conclusion .....	87
<b>6</b>	<b>Manipulating liquid interfaces with fluidic dielectrophoresis: Active mixing at the micron-scale .....</b>	<b>89</b>
6.1	Introduction .....	89
6.2	Materials and Methods .....	91
6.2.1	Reagents and Chemicals .....	95
6.2.2	Characterizing the magnitude of mixing .....	95
6.3	Results and Discussion .....	97
6.3.1	Mixing with fluidic dielectrophoresis .....	97
6.3.2	The influence of field frequency and voltage on mixing .....	99
6.3.3	Using AC electrokinetic mixing to create finely tunable concentration gradients .....	101
6.4	Conclusion .....	103
<b>7</b>	<b>Homogeneous, label-free detection at liquid interfaces with interfacial electrokinetic transduction (IET) .....</b>	<b>105</b>
7.1	Introduction .....	105

7.2	Materials and Methods .....	109
7.2.1	Sensor measurement .....	109
7.2.2	Protein Solutions .....	110
7.2.3	The electrical interface .....	110
7.2.4	Measuring interfacial frequency response .....	112
7.2.5	Electrokinetics of an electrical interface – fluidic dielectrophoresis .....	113
7.2.6	Using interfacial crossover frequency to detect specific binding .....	115
7.3	Results and Discussion .....	117
7.3.1	The IET sensorgram .....	117
7.3.2	Avidin-Biotin Binding Influences Interfacial Conductivity .....	119
7.3.3	Selective and Specific Biosensing in a BSA Background .....	121
7.3.4	Label-Free Femtomolar Detection in BSA .....	123
7.4	Conclusion .....	125
<b>8</b>	<b>Heterogeneous, label-free detection at liquid interfaces with interfacial electrokinetic transduction (IET) .....</b>	<b>127</b>
8.1	Introduction .....	127
8.2	Materials and Methods .....	129
8.2.1	Creating the electrical interface .....	129
8.3	Results and Discussion .....	131
8.3.1	Maxwell-Wagner Polarization .....	131
8.3.2	Biotin-streptavidin binding .....	133
8.3.3	Limit of detection and varying binding sites .....	135
8.3.4	Background protein and human IgG detection .....	137
8.3.5	Product formation affects interfacial conductivity .....	138
8.4	Conclusions .....	140
<b>9</b>	<b>Non-optically monitoring interfacial position using impedance spectroscopy .....</b>	<b>142</b>
9.1	Introduction .....	142
9.2	Materials and Methods .....	145
9.2.1	Design and Fabrication of Microfluidic Device with Embedded Electrokinetic and Impedance Electrodes .....	145
9.2.2	Chemicals and Reagents .....	147
9.2.3	Impedance Measurement .....	147
9.3	Results and discussion .....	148
9.3.1	Imaging Interfacial Position During Electrokinetic Displacement .....	148
9.3.2	Characterization of Electrokinetic Interfacial Flow Using Impedance Spectroscopy .....	149
9.3.3	Determining Interface Position Using Impedance Spectroscopy .....	152
9.4	Conclusions .....	155
<b>10</b>	<b>Non-optical, label-free detection of pregnancy hormones in unadulterated human serum .....</b>	<b>157</b>
10.1	Introduction .....	157
10.2	Materials and Methods .....	159
10.2.1	IET System .....	159
10.2.2	Portable IET System .....	159
10.2.3	Chemicals and Reagents .....	160

10.3 Results .....	161
10.3.1 Measuring Interfacial Displacement .....	161
10.3.2 Monitoring avidin:biotin binding by interfacial displacement .....	161
10.3.3 Detecting immunoglobulin proteins in human serum .....	163
10.3.4 Human chorionic gonadotropin detection.....	165
10.3.5 Non-optical, label-free detection of human chorionic gonadotropin .....	166
10.3.6 Label-free detection at the push of a button .....	168
10.4 Discussion .....	170
10.5 Conclusion.....	173
10.6 Supplemental Materials .....	174
<b>11 Conclusions and future work .....</b>	<b>176</b>
11.1 Conclusions .....	176
11.2 Suggestions for future work .....	179
<b>References.....</b>	<b>182</b>
<b>Curriculum Vitae.....</b>	<b>193</b>

## *List of Tables*

---

Table 3-1. Photolithography process parameters .....	34
------------------------------------------------------	----

## *List of Supplementary Tables*

---

Supplementary Table 3-1. Detailed list of all the materials which make up the flow controller .....	48
-----------------------------------------------------------------------------------------------------	----

## *List of Figures*

---

Figure 2-1. AC Electroosmosis .....	10
Figure 2-2. Traditional Dielectrophoresis .....	15
Figure 2-3. Schematic of traditional sandwich assays .....	17
Figure 2-4. Surface plamon resonance .....	18
Figure 2-5. Liquid-Liquid interfacial biosensors .....	28
Figure 3-1. Microfluidic ‘T-channel’ device with embedded electrodes .....	35
Figure 3-2. Constant-pressure flow source .....	37
Figure 4-1. Electrical interface created between two co-flowing fluids.....	51
Figure 4-2. 3D stacks of polarized liquid interface .....	54
Figure 4-3. Illustration of frequency dependent MW polarization .....	55
Figure 4-4. Maxwell-Wagner theory of polarizable liquid interfaces .....	60
Figure 5-1. Microfluidic device with embedded electrodes .....	64
Figure 5-2. Schematic of the T-channel used to create a liquid interface .....	74
Figure 5-3. A top and side view of fDEP.....	78
Figure 5-4. Interfacial displacement measurements at different applied frequencies .....	80
Figure 5-5. Maxwell-Wagner theory of polarizable liquid interfaces for interfacial permittivity and conductivity.....	81
Figure 5-6. Demonstration of the polarization scaling .....	86
Figure 6-1. Schematic of the electrokinetic mixer .....	92
Figure 6-2. Comparison of non-actuated versus actuated electrokinetic mixing .....	94
Figure 6-3. Electrokinetic mixing analysis .....	97

Figure 6-4. Monitoring electrokinetic mixing along the z-axis .....	99
Figure 6-5. Normalized concentration is affected by applied frequency .....	100
Figure 6-6. Normalized concentration versus applied voltage .....	101
Figure 6-7. Magnified view of the microfluidic gradient chamber .....	103
Figure 7-1. Schematic of IET sensor.....	108
Figure 7-2. A top and side view of fDEP. The liquid interface enters the electrode array and displaces across the flow channel .....	111
Figure 7-3. Crossover frequency is influenced by a biomolecular reaction .....	116
Figure 7-4. Normalized displacement is affected by a biomolecular reaction .....	120
Figure 7-5. Sensorgram with a background protein concentration .....	122
Figure 7-6. Theoretical limit of detection from an IET sensorgram .....	125
Figure 8-1. Heterogeneous IET Detection .....	130
Figure 8-2. fDEP crossover frequency with nanoparticle suspension .....	132
Figure 8-3. IET Bead-Based Biosensing Assay .....	134
Figure 8-4. Streptavidin Limited Detection by Varying Particle wt% .....	136
Figure 8-5. Biotin Detection in BSA Background .....	137
Figure 8-6. Heterogeneous detection of human IgG .....	139
Figure 8-7. Influence of Binding Reaction on Electrical Properties Measured by Interface Displacement .....	140
Figure 9-1. Confocal micrograph with two embedded electrode arrays: displacement and sensing .....	146
Figure 9-2. Frequency changes direction of interfacial motion, leading to different surface coverage on the impedance sensing electrodes.....	150

Figure 9-3. Obtaining optimal excitation frequency through a frequency sweep .....	152
Figure 9-4. Liquid interface subjected to varying applied voltages is monitored by impedance spectroscopy .....	154
Figure 9-5. Monitoring COF of two different interfacial conductivity systems .....	155
Figure 10-1. Monitoring biotin-avidin biorecognition through interfacial displacement .	163
Figure 10-2. Monitoring the displacement of human serum against protein A functionalized nanoparticles .....	164
Figure 10-3. Homogeneous and heterogeneous hCG detection in human serum using IET .....	166
Figure 10-4. Heterogenous detection of five human serum samples with five different hCG concentrations using a non-optical IET sensor .....	167
Figure 10-5. Portable IET sensing platform .....	168
Figure 10-6. Heterogeneous hCG detection in human serum using a portable IET sensing platform .....	170



## *List of Supplementary Figures*

---

Supplementary Figure 3-1. Flowrate versus applied pressure with and without a capillary tube .....	43
Supplementary Figure 3-2. Comparison of constant-pressure source and syringe pump .....	44
Supplementary Figure 3-3. Customized sample switch preventing backflow and implementing stable flows .....	46
Supplementary Figure 10-1. Microparticle functionalization process .....	174
Supplementary Figure 10-2. Comparing heterogeneous detection of hCG with different anti-hCG functionalization concentrations .....	174
Supplementary Figure 10-3. Sensor response is affected by washing between trials ..	175

*For my family*

# ***1 Executive Summary***

---

Development of rapid, sensitive and portable detection systems are important for effective detection of diseases in developing countries, biowarfare/anti-terrorism applications, environmental monitoring, and for basic biological research. One of the most specific and popular sensing platforms is the enzyme-linked immunosorbent assay (ELISA) platform, which identifies the presence of a substance, specifically an antigen, in a liquid sample. Biosensing assays, like ELISA, offer sensitivity and selectivity, however, its assay time is long due to immobilization and detection through a secondary antibody. The assay also requires periodic rinsing steps to avoid non-specific binding and to remove excess proteins. Finally, fluorescent detection instrumentation is required, and is still too bulky and costly for widespread daily laboratory, clinical and point-of-care use. The main challenge for producing low cost, portable, and easy to operate biosensing systems is then to miniaturize the sensing platform without any sophisticated instrumentation and complicated reagent protocols.

In this work, we first explore a well-known electrokinetic phenomenon called dielectrophoresis (DEP), which traditionally has been studied in cells and particles, but here at a liquid-liquid interface, which we call fluidic dielectrophoresis (fDEP). The liquid interface consisting of two co-flowing fluids with disparaging electrical properties – conductivity and permittivity – is shown to move when subjected to an alternating current (AC) electric field. The direction and magnitude of displacement is dependent on varying applied frequencies and voltages. Briefly, when a low frequency AC field was applied, the

high conductive, low dielectric stream displaced into the low conductive, high dielectric stream. At high frequencies, however, the direction reversed, and the high dielectric, low conductive stream displaced into the low dielectric, high conductive stream. The applied frequency at which the direction reverses is known as the crossover frequency (COF). In the liquid-liquid system, when the COF is applied, the liquid interface does not move and looks as if no AC field is applied.

After fully investigating and formulating an electrohydrodynamic (EHD) model for interfacial displacement, we demonstrated several applications utilizing fDEP. First, the newly developed electrokinetic phenomenon was used for microfluidic mixing. The system consisted of a tri-laminar liquid interface consisting of two outer solute streams and an inner solute-free stream. When the electric field is applied, the outer streams inject into the inner stream creating vortical mixing. The magnitude of mixing is affected by applied frequency and voltage.

Next, we found that when a biomolecular reaction occurs at the liquid-liquid interface it alters the electrical properties, which is transduced by interfacial displacement; we call this novel transduction method interfacial electrokinetic transduction (IET). We begin by demonstrating the system's capabilities by performing biosensing experiments on a traditional, well-known biomolecular reaction between biotin and avidin. We quantified the reaction response, specificity and selectivity by calculating the limit of detection between biotin and avidin as well as biotin and avidin with a background of 5 mg/ml bovine serum albumin (BSA). We pushed the sensor's capabilities further by performing the same reactions in a bead-based assay, effectively increasing the limit of detection by three orders of magnitude.

Next, we integrated impedance spectroscopy to non-optically monitor the position of the liquid-liquid interface. Impedance is the effective resistance of an electrical circuit or component to an alternating current, arising from the combined effects of ohmic resistance and reactance. We modified our microfluidic device to consist of two microelectrode arrays, one of which delivers the AC electric field to polarize and displace the interface, the second, downstream from the first array, measures the effective impedance of the bulk fluid. Impedance spectroscopy was used to detect interfacial position, crossover frequency and electrical properties of the liquids.

Finally, we combined the IET biosensor with impedance spectroscopy to create a truly, label-free, non-optical biosensor. We tested the capabilities of the newly developed liquid-liquid interfacial biosensor by detecting biomarkers in unadulterated human serum. We first sought to detect immunoglobulin proteins in human serum using nanoparticles functionalized with protein A, a protein that binds to all immunoglobulin (Ig) proteins. Finally, we tested the IET sensor against a female reproductive hormone, human chorionic gonadotropin (hCG) in human serum.

Collectively, we successfully developed the first, in solution, label-free non-optical biosensor. This novel biosensor was shown to detect biomarkers down to femtomolar concentration in human serum within minutes.

## 2 *Introduction*

---

Development of rapid, sensitive and portable biosensing systems are important for the detection and prevention of disease in developing countries<sup>1</sup>, biowarfare/anti-terrorism applications<sup>2-4</sup>, environmental monitoring<sup>5,6</sup>, point-of-care diagnostic testing and for basic biological research. Currently, the most established inexpensive commercially available and widespread assays for biomolecular detection and disease testing are paper-based dipstick and lateral flow test strips<sup>7-9</sup>. These paper-based devices are often small, cheap and simple to operate<sup>10,11</sup>. The last three decades in particular have seen an emergence in these assays in diagnostic settings for detection of pregnancy<sup>12,13</sup>, HIV/AIDS<sup>14-16</sup>, glucose<sup>17-19</sup>, Influenza<sup>20-22</sup>, urinary protein<sup>23,24</sup>, cardiovascular disease<sup>25-28</sup>, respiratory infections<sup>29,30</sup> and blood chemistries. Such assays are widely available largely because they are inexpensive, lightweight, portable, are simple to operate, and a few platforms are capable of multiplexed detection for a small number of sample targets.

On the opposing end of the financial spectrum, a widely used biosensing platform capable of sensitive and multiplexed biomolecular detection is surface plasmon resonance (SPR) spectroscopy<sup>31,32</sup>. SPR – based on measuring changes in refractive index at a bioreceptor conjugated metal surface or on colloidal metal particles in suspension – was the first biosensing instrument to be commercialized, and has become a common tool for obtaining kinetic information for a wide variety of biomolecular interactions across thousands of laboratories<sup>33,34</sup>. In terms of portability, however, such systems require bulky complex free-space optics and are often cost prohibitive to the

general consumer or to a developing country.

There is a critical need for sensitive, quantitative and multiplexed detection capabilities for point-of-care diagnostics and for the detection and prevention of disease in the developing world that cannot be satisfied by either current state-of-the-art paper-based assays or cost prohibitive laboratory grade instruments such as SPR. For example, applications including the detection of cardiac and cancer biomarkers and biothreat applications require sensitive multiplexed detection of analytes in the nM and pM range and cannot currently be satisfied with current inexpensive portable platforms due to their lack of sensitivity, quantitative capabilities and often unreliable performance.

The ideal biosensing platform with the ultimate attractiveness for both portable point of care use and commercialization potential is an inexpensive system, which can go from sample loading to facile biomolecular detection in a single step without the need for external supporting equipment. These types of systems are especially needed in the developing world and rural settings where inhabitants lack access to basic technical services, human resources and trained personnel.

A major obstacle is the lack of an available system that is rapid, sensitive and specific to small concentrations of target biomolecules yet still (1) does not require the labeling of probes or optical microscopy and (2) can operate without the need for complex and bulky supporting instrumentation. The significance of this project is based on its effort to overcome this underlying limitation.

Biosensors typically integrate three basic components for successful operation: a biological sensing element which is a specific biomolecular interaction, such as an antibody that binds to a target protein, a signal transducer, which converts this targeted

binding event into a measurable signal, and a detector.

One problem with current biosensing methods is they typically require bulky and expensive supporting equipment such as fluorescent microscopy or electrical instrumentation in order to measure changes in refractive index, current, voltage or impedance signals in response to biomolecular binding. A second problem is that bioaffinity reactions typically occur at biomolecular-functionalized solid surfaces, which are prone to non-specific binding, commonly require complex surface functionalization chemistry, tedious rinsing steps, and a long assay time (tens of hours) in order for a ligand to diffuse to the solid substrate, specifically bind to the bound complimentary receptor, and trigger a detectable signal.

One platform scientists have used to perform biosensing applications is in solution liquid-liquid interfacial sensing<sup>35</sup>. In this manner, the liquid interface becomes the substrate upon which a biomolecular event occurs. This eliminates the need for surface functionalization, washing and rinsing steps, and surface fouling. One of the major limitations with these methods is that the majority rely on fluorescence or other optical methods, therefore the transducing element remains a costly and bulky machine, limiting most applications in a laboratory setting. Here, we present a novel liquid interfacial biosensor coupled with electrokinetics, in which the liquid-liquid interface becomes the substrate and transducer.

## ***2.1 Electrokinetics for fluid manipulation***

Lab-on-a-chip (LOC) technology was first invented in 1954, however it did not develop as a serious platform and focus of research until the late 1980's, early 1990's.



Since then lab-on-a-chip technology has vastly advanced performing complex, inexpensive, robust and fast detection schemes. While LOC technology is capable of many applications, one particular challenge remains; robust and precise manipulation of fluids, particles and cells along micron length scales. The ability to precisely control the movement and location of these elements within a micro-geometry is essential in LOC devices<sup>36</sup>. Basic chip functions such as fluid pumping<sup>37</sup>, sample mixing<sup>38</sup>, particle concentration<sup>39</sup>, separation<sup>40</sup>, and analyte detection all require some type of sample movement to a specific location; the development and integration of micron-scale pumps, mixers, concentrators, separators and sensors is required and essential for a fully functional miniaturized diagnostic device.

Conventional solutions to this problem have often involved scaling down peristaltic, diaphragm, and other popular macro-scale mechanical pump or micromanipulators to micro-scale dimensions. Most such devices, however, contain moving parts which can lead to clogging and cell lyses, and render them unsuitable for biological applications and often subject to unexpected device failure. Due to such drawbacks, the use of electrokinetic (EK) devices with no moving parts to transport<sup>41-44</sup>, mix fluid<sup>45-47</sup> and manipulate cells and particles<sup>48-50</sup> has attracted considerable attention.

The term 'electrokinetic' is used to describe the motion of a liquid or particle under the influence of an external electrode-driven electric field. It is a very promising phenomenon at the micro-scale as the well-developed integrated circuit (IC) fabrication techniques from the microprocessor industry have made the fabrication and assembly of microelectrodes within encapsulated micro-geometries a simple reality. This allows for the delivery of highly spatially controlled time varying alternating current (AC) or direct

current (DC) electric fields to specific regions of a device – typically within a polymer enclosed microchannel. The design, control, and implementation strategies of microelectrodes for use in LOC applications, specifically in biological microfluidic applications, however, can be non-trivial and exceedingly challenging. Investigation into the discovery, development and optimization of such strategies and their integration into LOC devices for specific sample control and manipulation tasks is the purpose of this work.

Before confronting these challenges, however, we will begin by reviewing some fundamental properties of electrokinetics and provide a basic analysis of the important field driven body forces - namely electroosmosis (EO), electrothermal (ET) flow, and Dielectrophoresis (DEP) - that can be exploited for liquid and bioparticle manipulation along micron scales.

## **2.2 Electrokinetic Flows**

Electrokinetic flow encompasses the transport of both fluids (electroosmosis)<sup>51</sup> and samples (electrophoresis)<sup>52</sup> in response to an electric field. Both motions are a result of the electric double layer formed between the solid-liquid interface where there is a net charge density. Compared to traditional pressure-driven flow, electrokinetic flow is more suited for microfluidics due to its nearly plug flow-like velocity profile and lower resistance.

### **2.2.1 Induced double layer**

AC electrokinetic flows arise from the formation of a microelectrode induced electrical double layer. Charging an electrode with an externally applied AC electric field

can attract counter ions to the surface; the counterions will act to neutralize the induced surface charge. Due to the ions' finite size, ions closest to the surface form what is known as the Stern layer and do not fully neutralize the charge. Additional counterions are attracted to the Stern layer, however, are mobile and have the freedom to diffuse. The outer region, known as the mobile diffuse layer, can screen the field from the bulk solution and neutralize the surface charge. The combination of the Stern and diffuse layers form what is called the electric double layer,  $\lambda_D$ , whose thickness is described as  $\lambda_D = \sqrt{\frac{\epsilon k T}{2 e^2 z^2 c}}$  where  $c$  is the molar density and  $z$  is the charge number.

### 2.2.2 AC electroosmosis

AC electroosmotic (ACEO) flow uses an externally applied electric field to drive a bulk fluid motion typically generated by applying an AC voltage across a pair of microelectrodes in contact with an electrolyte solution. The normal field component acts on the electrolyte ions and polarizes the electrode surface with electrolyte counterions to form a field induced double layer; the tangential component acts on this charged region, driving a net fluid flow. While DC electroosmosis is popular in biotechnological applications, its high voltage operation put serious limitations on their applications. AC electroosmosis requires much lower voltage and simpler system structure. Operating at relatively high frequencies also helps to eliminate electrolysis. These advantages can be used to develop new techniques for biomedical processes.

Ramos et. al derived the time-averaged slip velocity on the electrode as,

$$u_{ACEO} = -\frac{\epsilon_m}{4\mu} \frac{\partial}{\partial x} |\phi - V_0|^2, \quad (2.1)$$

where  $\phi$  is the potential at any given location above the electrode surface, and  $V_0$  is the potential applied to the electrode. There exists an optimum frequency where a maximum slip velocity exists. Because ion migration to the surface of each electrode requires a finite amount of time, the electrode charging dynamics will have some dependence on the applied AC signal frequency. The dependence can be estimated by simple scaling arguments. The circuit equivalent to the electrode system can be approximated as a double layer capacitor, with charge separation over a length,  $\lambda$ , in series with a bulk fluid resistor. The resulting RC charging time for this equivalent resistor-capacitor in series is simply,  $\lambda L/D$ , where  $L$  is the electrode separation and  $D$  is the ion diffusivity ( $\sim 10^{-5}$  cm<sup>2</sup>/sec).

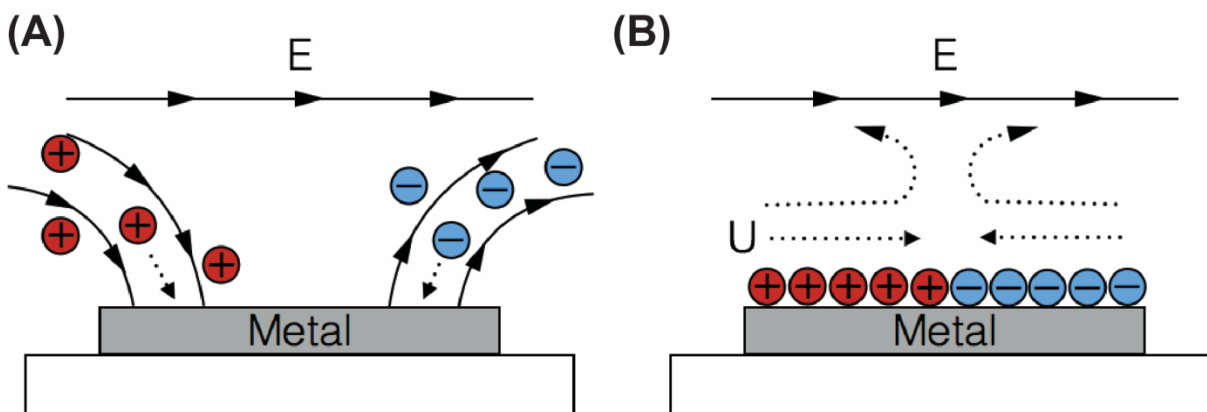


**Figure 2-1. AC Electroosmosis**

(A) The double layer is induced by an applied field. The externally applied electric field initially intersects the working surface at right angles. Ions in solution are driven along field lines, with positive ions accumulating near the left half of the working electrode and negative ions on the right half. (B) The interaction of the tangential field at the surface with the charge in the double layer gives rise to a surface velocity, and a resulting bulk flow.

Similar to a capacitor, for frequencies below  $D/\lambda L$ , the half-cycle is long enough such that counterions have enough time to saturate the double layer, effectively shielding the electric field from the bulk solution. At frequencies above  $D/\lambda L$ , the counterions do

not have enough time to migrate to the electrode surface to form a double layer. Since the time-averaged electrokinetic flow requires both double layer polarization and external field, it vanishes at these two extremes, yielding a maximum AC electrokinetic velocity at a frequency  $\sim D/\lambda L$ .

### 2.2.3 Electrothermal (ET) flow

Electrothermal (ET) fluid flow arises from the interaction of the external electric field with temperature-induced inhomogeneities in medium conductivity and permittivity due to joule heating. Unlike ACEO flow that relies on an electric field interaction with a charged double layer, the resulting temperature gradients induce a space charge accumulation and depletion under an AC field with charge density

$$p = \left( \sigma \cdot \left( \frac{\partial \varepsilon}{\partial T} \right) \right) - \frac{\varepsilon \cdot (\partial \sigma / \partial T)}{\sigma + i\omega \varepsilon} \cdot \nabla T \cdot E, \quad (2.1)$$

which can then interact with the applied field to generate a net body force on the liquid. In order for strong temperature gradients to exist, reported ET pumping has been limited to higher conductivity fluids, typically greater than 1 S/m. Electric fields produced by small microelectrodes are quite high, typically on the order of  $E = 10^5$  V/m for a potential of 10 V dropped across a 25  $\mu\text{m}$  gap, and a large power density is generated in the fluid surrounding the high field edges of the electrodes. The power generation per unit volume is,  $\sigma E^2$ , and for a medium conductivity of  $\sigma_m = 0.1$  S/m and electric field of  $10^5$  V/m the average power dissipation is estimated to be approximately 10 mW. Because of the large power generation within a small volume, temperature gradients are generated. An order-

of-magnitude estimate of this localized temperature increase can be approximated from the steady state energy balance equation as

$$\Delta T \sim \frac{\sigma V^2}{k}, \quad (2.2)$$

where  $k$  is the thermal conductivity of the electrolyte. Therefore, one expects temperature induced space charge density to scale quadratically with the applied voltage, resulting in a quartic scaling with voltage for the electric body force as

$$f_E = \rho E \sim E^2 \nabla T. \quad (2.3)$$

### **2.3 Classic dielectrophoresis**

Classical dielectrophoresis occurs when a force is exerted on a suspended particle in a non-uniform electric field. The simplest theoretical model is that of a homogenous sphere surrounded by conductive, dielectric media. The theory illustrates the DEP force,  $F_{DEP}$ , induced by a non-uniform field,  $E$ , with frequency,  $\omega$ , as

$$F_{DEP} = 2\pi r^2 \varepsilon_m \text{Re}\{f_{cm}\} \nabla |E|^2 \quad (2.4)$$

where  $r$  is the particle radius,  $\varepsilon_m$  is the real part of the permittivity of the suspending media,  $\varepsilon_p^*$  and  $\varepsilon_m^*$  are the complex permittivities of the particle and medium respectively. Each complex permittivity is described by  $\varepsilon^* = \varepsilon + \sigma/(i\omega)$ , where  $\sigma$  is the electrical conductivity,  $\omega$  is the frequency and  $i$  is the imaginary unit. For a shell-less lossy dielectric sphere,  $f_{cm} = (\varepsilon_p^* - \varepsilon_m^*)/(\varepsilon_p^* + 2\varepsilon_m^*)$ , is the frequency-dependent Clausius-Mossotti (CM) factor. Equation (2.4) illustrates that conductivity dominates polarization at low frequency, while permittivity dominates at high frequency.

$$\omega_{COF} = \frac{1}{2\pi} \sqrt{\frac{(\sigma_m - \sigma_p)(\sigma_p + 2\sigma_m)}{(\varepsilon_p - \varepsilon_m)(\varepsilon_p + 2\varepsilon_m)}} \quad (2.5)$$

The sign of the CM factor governs the resulting pDEP or nDEP particle mobility. At low AC frequency, below the inverse charge relaxation time ( $\varepsilon/\sigma$ ), material with greater conductivity conducts ionic charge to the interface at a rate faster than it is removed by the adjacent lower conductive phase. As such, charge accumulates at the interface, and low frequency interfacial polarization is driven by material differences in electrical conductivity. At high frequency, above the charge relaxation time scale, the electric field oscillates faster than charges can electromigrate to the interface. As conductive charging does not have enough time to occur over every field half-cycle, high frequency polarization is driven by differences in material dielectric constant; charge accumulates due to interfacial differences in dielectric polarization. If neither interfacial phase has both a greater electrical conductivity and dielectric constant, the high-conductivity phase dominates interfacial charging at low frequency and the adjacent high-dielectric phase drives charging at high frequency. Hence, the net sign of the induced interfacial charge reverses at a frequency high enough to relax away conductive charging to the extent that it is trumped by opposing dielectric polarization. This frequency is on the order of the inverse charge relaxation time scale, and is defined as the crossover frequency (COF), illustrated by *Equation (2.5)*. The charging mechanism, known as Maxwell-Wagner (MW) polarization, has been exploited to pump liquid (electroosmosis), and manipulate bubbles, particles, biomolecules, and cells.

For example, particles with conductivity higher and permittivity lower than that of the surrounding medium exhibit pDEP below the COF and nDEP above the COF

according to the simple model. This can be experimentally proven using a quadrupole array, as shown in **Figure 2-2**, where every other electrode is active with adjacent electrodes grounded. This configuration creates high electric field regions near the parallel electrode edges and low field regions in the center of the array, as well as blank spaces far between the electrodes. The theory can be tested by applying two separate alternating current electric frequencies, one above and below the observed COF, shown in **Figure 2-2B**. In **Figure 2-2B** we see that a particle polarized under pDEP will be attracted to high field regions, i.e. electrode edges. If the AC field frequency increases the particle eventually experiences nDEP, leaving the high field regions and migrates towards regions of low field intensity, i.e. the center. The frequency at which the direction of motion reverses is known as the crossover frequency (COF), i.e. the applied frequency when the particle experiences nDEP after pDEP.



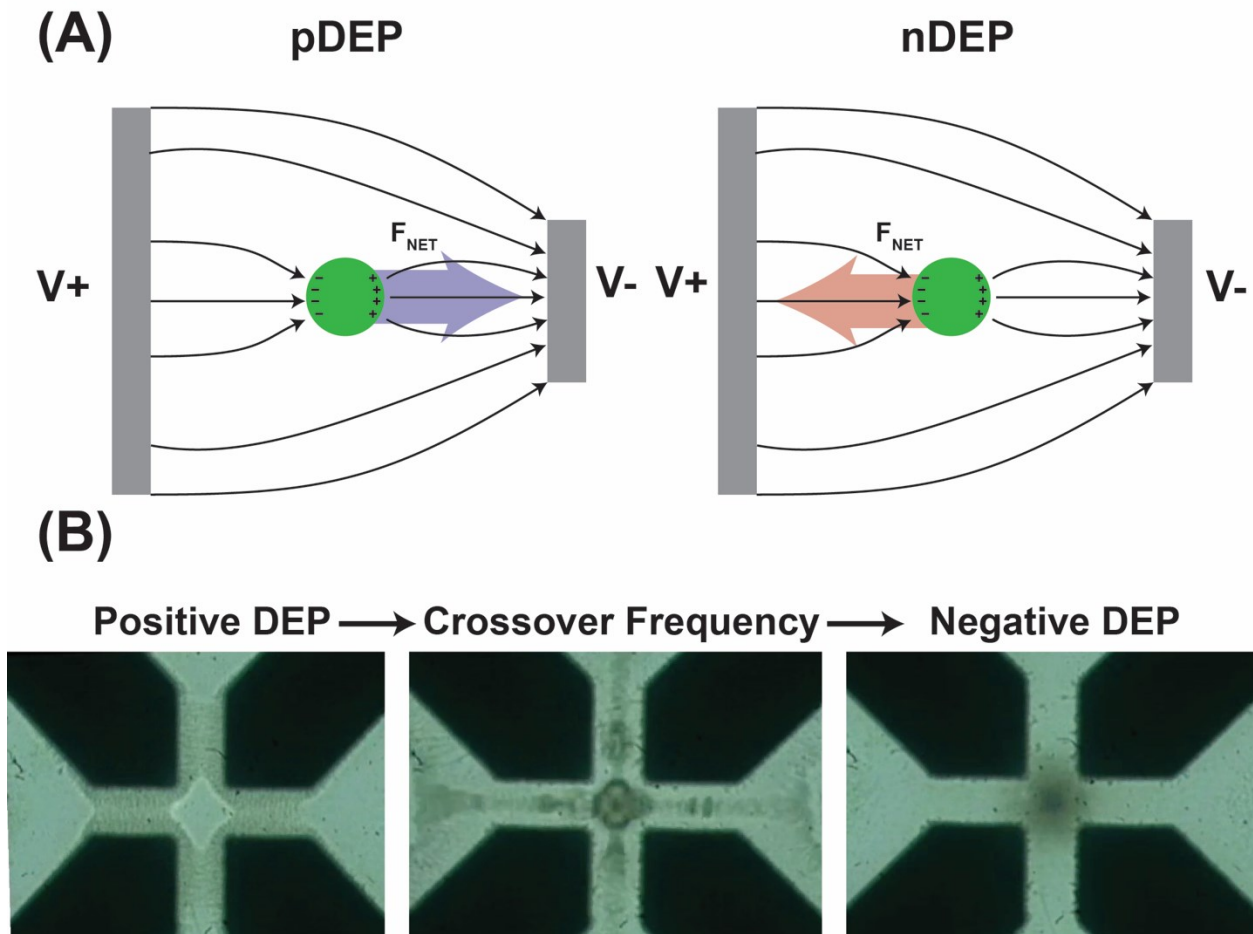


**Figure 2-2. Traditional Dielectrophoresis**

(A) In positive DEP (pDEP), the dielectrophoretic force moves the object towards the higher electric field region and in negative DEP (nDEP) towards the lower electric field regions. (B) Suspended silica particles in DI water experience positive DEP at low frequencies and crossover to negative DEP as the frequency increases.

## 2.4 Biosensors – various types

A biosensor is an analytical device used to detect an analyte-of-interest which combines a biological component with a physiochemical detector. The biological element is a biologically derived material or biomimetic component that interacts with the analyte-of-interest. The transducing, or detecting, element transforms the signal resulting from the biological interaction into another signal that can be more easily measured and quantified. Generally transducing elements work in a physiochemical way: optical,

piezoelectric, electrochemical, mass, etc. Finally, there is a reader device that displays the signal produced by the transducer, in a user-friendly way, generally on a computer screen or other projector. The optimal biosensor has both a high specificity and selectivity as well as fast response times<sup>53</sup>.

### **2.4.1 Optical biosensors**

Optical biosensors are the most commonly reported class of biosensors. Optical sensing devices contain a biorecognition sensing element coupled with an optical transducing element. Optical biosensors produce a signal which is proportional to the concentration of the analyte-of-interest. These biosensors offer many advantages including high specificity and sensitivity.

#### *2.4.1.1 Fluorescent biosensors*

Fluorescent biosensors perform detection most often through a “sandwich assay.” First, the primary antibody is immobilized onto a surface. The target-of-interest is flowed over top of the newly functionalized surface giving it ample time to bind to the primary antibodies. Next, a secondary antibody, which is labeled with fluorophores is introduced to the system and binds to the target-of-interest. Lastly, the surface is washed removing excess, unbound secondary antibodies. The surface is excited at a certain wavelength and the fluorescent intensity is proportional to the concentration of the analyte. While fluorescent biosensors are far and beyond the most widely used approaches in the field, multiple steps for antibody incubation, rinsing and washing, make the process far too time-consuming. Furthermore, these methods complicate the system rendering them to

a laboratory with trained technicians. These are significant limitations when developing an easy-to-use, portable diagnostic tool<sup>54</sup>.

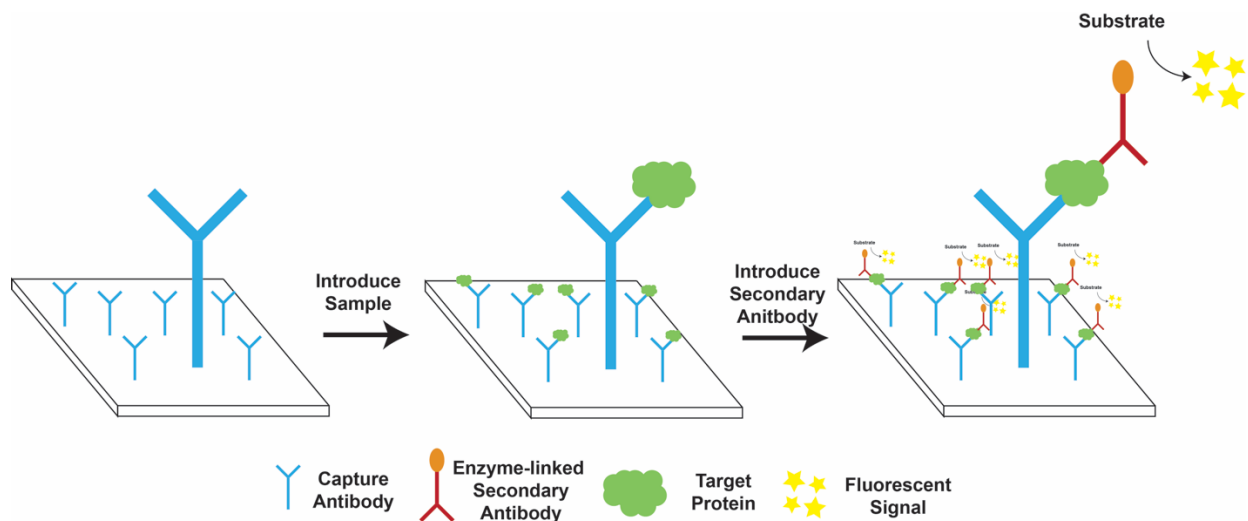


**Figure 2-3. Schematic of traditional sandwich assays**

Schematic of a traditional ELISA sandwich assay. A surface is functionalized with a capture antibody. The sample is introduced and target proteins in solution bind to the capture antibody. A secondary, enzyme-linked antibody binds to the captured target protein. A substrate is added which is converted by the enzyme to a detectable form, in this case a fluorescent signal.

#### 2.4.1.2 Surface Plasmon Resonance (SPR) biosensors

Surface plasmon resonance (SPR) biosensors are a label-free detection method which has been popularized within the last two decades<sup>55</sup>. SPR measures interactions in real-time with high sensitivity and can determine specificity, affinity and kinetic characteristics of many biointeractions including protein-protein<sup>56-58</sup>, protein-DNA<sup>59,60</sup>, enzyme-substrate or inhibitor<sup>61</sup>, receptor-drug, lipid membrane-protein<sup>62</sup>, protein-polysaccharide<sup>63</sup>, cell or virus-protein<sup>64</sup>. This optical technique measures the refractive index changes when polarized light hits a metal film where biomolecular interactions are present, shown in **Figure 2-4**. In order to detect an interaction, one molecule, the receptor, is immobilized onto the sensor surface. The sample buffer containing the target analyte-

of-interest is injected through the flow cell under continuous flow. As the analyte binds to the receptor the accumulation of product on the surface results in an increase in the refractive index; this change in refractive index is measured in real time. However, a background response is also generated if there is a difference in the refractive indices of the sample buffers. This background response must be subtracted from the sensorgram to obtain the actual binding response. The background response is recorded by injecting the sample containing the analyte-of-interest through a reference flow cell, which has no receptor bound to the sensor surface.

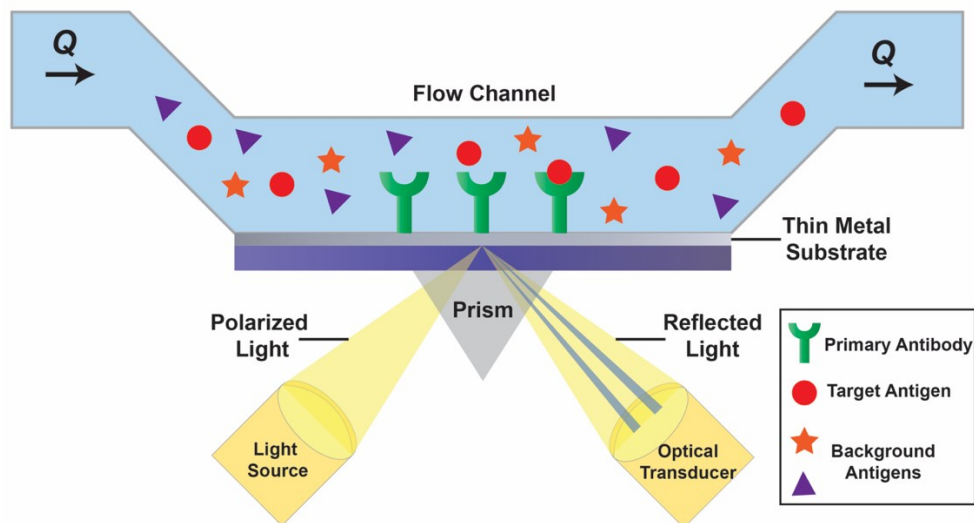


#### Figure 2-4. Surface plasmon resonance

Schematic of a surface plasmon resonance assay. A receptor is functionalized to a thin metal surface. A sample containing an unknown concentration of the target antigen is flowed across the surface allowing for a receptor-antigen complex to form. A light source focuses light to the prism. Upon specific binding, the reflected light is then detected by an array of photodiodes.

The major advantages of SPR biosensors include high sensitivity and ability to detect biomolecular interactions in real-time without labels. However, SPR biosensors require expensive and sophisticated optical instrumentation as well as trained personnel. Much like immunofluorescent assays, these methods are limited to a laboratory setting.

### 2.4.1.3 Chemiluminescence (CL) biosensors

Chemiluminescence is the generation of light resulting from released energy from a chemical reaction; minimal heat emission can occur<sup>65-67</sup>. Two chemicals react to form an excited intermediate, which breaks down releasing energy as photons of light to return back to ground state. A perfectly efficient reaction would have a chemiluminescence quantum yield,  $\Phi_{QY}$ , of one:

$$\Phi_{QY} = \Phi_E \times \Phi_F \times \Phi_R \quad (2.6)$$

The chemiexcitation quantum yield,  $\Phi_E$ , is the probability of producing an excited state in a reaction and has a value between 0 and 1, where 0 is a completely dark reaction and 1 when all products have been excited.  $\Phi_F$ , represents the fluorescent quantum yield, and is the probability of the excited state emitting a photon by fluorescence rather than decaying by other reactions. The reaction quantum yield,  $\Phi_R$ , is the fraction of molecules which go through the luminescent reaction rather than a side reaction.

Chemiluminescent detection has a very low detection limit and wide dynamic range. Assay samples contribute little to no background chemiluminescence. Because of this, compared with other optical methods, it does not require an external light source for excitation, which makes the system more affordable. Nevertheless, as it still has a labelling step, chemiluminescent detection is often too complicated. Furthermore, results can be affected by external environmental factors, such as temperature.

#### *2.4.1.4 Colorimetric biosensors*

Colorimetric biosensors have attracted a lot of attention over the last decade due to their ease-of-use and low cost. Colorimetric assays do not require expensive or sophisticated transducing elements, changes can be read out by the naked eye. Therefore colorimetric assays can be directly applied to point-of-care diagnostics<sup>68,69</sup>. The key challenge for colorimetric biosensing is transforming the detection events into color changes. Because of this, several smart materials have been developed, including gold nanoparticles, magnetic nanoparticles, cerium oxide nanoparticles, carbon nanotubes, graphene oxide, and conjugated polymers.

#### *2.4.1.5 Paper-based biosensors*

Microfluidic paper-based analytical devices ( $\mu$ PADs) are an attractive platform for point-of-care devices, due to low cost and portability<sup>70,71</sup>. This platform was first developed by the Whitesides group, where microfluidic devices consisting of paper were patterned through traditional lithographical techniques. Fluid flow was driven by capillary action without external equipment and pumps, where the sample was driven towards specific detection locations. Since then,  $\mu$ PADs have been popular in a variety of applications, such as diagnostics<sup>72</sup>, food<sup>73,74</sup> and environmental monitoring<sup>75</sup> and bioterrorism.

$\mu$ PADs, consist of paper, which is inherently hydrophilic, with hydrophobic barriers. The hydrophobic barriers confine the fluid flow within a desired location or direct the fluids through a specific path. Several patterning techniques, including photolithography<sup>76</sup>, wax printing<sup>77</sup>, screen-printing<sup>78</sup>, plasma treating<sup>79</sup>, flexography<sup>80</sup> and laser treating<sup>81</sup> have been developed to manufacture hydrophobic barriers.

Photolithographic techniques are the primary method for microfabrication in traditional PDMS devices and offer a wide variety of potential patterns. However, hydrophilic areas are exposed to chemical and solvents and photoresists and the photolithography equipment increase fabrication costs. Wax printing offers high speeds, on the order of minutes, and require only a commercially available printer and hot plate. One drawback is accounting for wax spreading during fabrication. Screen-printing offers slightly higher resolutions than wax printing but is limited by the requirements of various printing screens when patterns change. Plasma treating is optimal in labs equipped with plasma treaters and produces patterns without affecting flexibility or surface topography. However, hydrophilic areas are exposed to polymers and solvents, and cannot produce arrays of free-standing hydrophobic patterns. Finally, laser treating offers high resolution, but it increases paper stiffness, making it difficult to fold or store. All methods offer both advantages and disadvantages, but the ease-of-use, cost and portability make paper-based devices an excellent option for point-of-care diagnostics.

#### **2.4.2 Electrochemical biosensors**

Electrochemical biosensors are an important part of the biosensing field and have been used for basic and applied research for nearly half a century. Electrochemical biosensors detect a specific electrical signal upon a biomolecular event. Based on the operating transducing element, electrochemical biosensors can be divided into three subgenres, amperometric, potentiometric and impedimetric.

#### *2.4.2.1 Amperometric biosensors*

Amperometric sensors are usually used with affinity sensors. Since amperometric detection yields minimal charging current, it minimizes the background signal that would normally affect the limit of detection. Generally, sensors utilizing this system consist of three electrodes, a working, reference and counter electrode. The working electrode is usually either a noble metal or screen-printed layer covered by the biorecognition component. The reference electrode usually consisting of silver metal coated with a layer of silver chloride. The reference electrode is usually placed far from the site of the redox reaction in order to maintain a stable reference potential. One main benefit of using a three electrode system is that charge from electrolysis passes through the counter electrode, rather than the reference, which protects the reference electrode from charging its half-cell potential. Two electrode systems are preferred for disposable sensors because the reference electrode does not need long-term stability, and this lowers the cost. However, these systems are only useable when the current density is low enough so the electrode can carry a charge without adverse effects<sup>82,83</sup>.

Amperometry has popularized over the past few decades, as it offers a straightforward, easy-to-use method. In fact, many commercially available point-of-care biosensing systems are based on amperometric detection. Among them, electrochemical glucose biosensors based on amperometric sensing are regarded as one of the most successfully commercialized amperometric sensors. However, amperometric sensors generally have a poor limit of detection and lower stability, not making them optimal for more complex detection schemes.



#### *2.4.2.2 Potentiometric biosensors*

Potentiometric biosensors combine a biorecognition element (essentially an enzyme) with a transducer that senses the variation in the number of protons, and other ions<sup>84,85</sup>. The signal is measured as a potential difference between the working and reference electrode. The working principle of the potentiometric transduction relies on the potential difference between the active electrode and reference electrode which accumulates during the recognition process in an electrochemical cell when zero or negligible amount of current flow through the electrode. The electrical potential difference or electromotive force (EMF) between two electrodes is measured using a high impedance voltmeter. The working electrode is made of permselective ion-conductive membrane which is sometimes called an ion-selective electrode (ISE). The working electrode's potential must depend on the concentration of the analyte in the gas or solution phase. The reference electrode provides a defined reference potential. The measurement of potential response of a potentiometric device is governed by the Nernst equation in which the logarithm of the concentration of the substance being measured is proportional to the potential difference.

#### *2.4.2.3 Impedimetric biosensors*

Electrochemical impedance spectroscopy (EIS) is a sensitive technique for detecting biomolecular recognition events including binding proteins, lectins<sup>86,87</sup>, nucleic acids<sup>88</sup>, whole cells<sup>89-91</sup>, antibodies or antibody-related substances<sup>92</sup>. EIS techniques are both simple and sensitive, and most importantly, do not require complex labeling steps. Many applications utilizing impedimetric biosensors focus on immunosensors<sup>93,94</sup> and

aptasensors<sup>95</sup>. In impedimetric immunosensors, antibodies and antigens bind to each other and form an immunocomplex on the electrode. When the complex forms on the electrode surface, it alters the resistance which is detected through impedance. Aptasensors have been exploited to alleviate issues associated with immunosensors, specifically with respect to antibodies: high manufacturing costs, short shelf life, and instability at certain temperatures and pH. Aptamers are synthetic, single-stranded nucleic acid molecules which bind to targets based on structure recognition. In impedimetric aptasensors, impedance changes following the binding of target sequences and conformational changes<sup>96</sup>.

### **2.4.3 Piezoelectric biosensors**

Piezoelectricity is the electric charge that accumulates on certain materials due to an applied mechanical stress. This can occur from reconfiguration of atoms within the material whereby electrical charge, specifically positive and negative becomes unbalanced, leading to a net charge. Piezoelectric biosensors work by measuring the change in frequency which occurs when the analyte-of-interest binds to the receptor<sup>97,98</sup>.

The most widely applied piezoelectric biosensor is quartz crystal microbalance (QCM) <sup>99,100</sup>. It works by measuring the change in frequency of the quartz crystal which occurs due to biorecognition without labels. A QCM biosensor includes an AT-cut quartz crystal placed between two electrodes. Applying an external AC electric field causes the crystal to vibrate and the magnitude changes upon biorecognition.

Sauerbrey developed a method for correlating changes in the oscillation frequency of piezoelectric crystal with mass deposited on it. This method is valid provided the

assumption that added mass causes the thickness of the quartz crystal itself to increase. This allows the user to neglect electrode geometry, which eliminates the need for calibration. The Sauerbrey equation is defined as:

$$\Delta F = -2.3 \times 10^6 f^2 \frac{\Delta m}{A} \quad (2.7)$$

Where  $\Delta F$  is the frequency change in hertz,  $f$  is the resonant frequency of piezoelectric quartz crystal,  $\Delta m$  is the mass change, and  $A$  is the area of the electrode surface. When biorecognition occurs on the surface of the crystal, the resonance frequency changes based on the concentration of the analyte, thus quantitative analysis can be achieved.

Compared with optical biosensors, piezoelectric biosensors do not require a labelling step, which is the biggest advantage. In addition, they have high sensitivity, real-time readouts, and low cost. However, sample enclosures and sample handling systems can interfere with the mechanical motion. Nevertheless, the greatest limitation facing piezoelectric biosensor is its accuracy and repeatability, since it is extremely hard to achieve a uniform surface coating with piezoelectric materials.

#### **2.4.4 Magnetic biosensors**

Magnetic biosensing introduces magnetic beads as labelled particles. Upon biorecognition, the formation of the biocomplex is measured by detecting the appearance of the magnetic particles, which can be performed in several ways<sup>101,102</sup>. A simple method to detect magnetic particles is to optically measure the fraction of the surface that has been covered, yet it does not exploit the magnetic features of the particle. To capitalize on that, a more general way is to detect the changes in the magnetic field caused by the

presence of the magnetic particles, which is performed by using giant magnetoresistance sensor (GMRS). When magnetic particles get close to a GMRS, the resistance of the magnetoresistor will decrease because the magnetic field is influenced by the magnetic particles.

#### **2.4.5 Thermometric Biosensors**

Thermometric biosensors exploit the fundamental property of biological reactions, i.e. absorption or release of heat. Originally, wider applications utilizing thermometric biosensors were hindered due to the high cost and sophistication of microcalorimeters. However, with recent advances in immobilized enzymes in bioanalysis, researchers have developed simple, low-cost calorimeters for biosensing. Biorecognition is reflected as a change in the temperature within the reaction medium. Enzymes are immobilized in small packed bed reactors, held at constant temperature. Thermistors monitor temperature changes in the presence of a reaction at both the entrance and exit of the packed bed. Even a small change in the temperature can be detected by thermal biosensors<sup>103,104</sup>.

### **2.5 State-of-the-art: Microfluidic biosensors**

There has been a tremendous push to create easy-to-use, portable detection devices that can perform measurements in a matter of minutes with smaller sample volumes. Micro/nanofluidic-based biosensors are an attractive platform capable of sample handling and biodetection utilizing nano- to picorange sample volumes. There are several commercially available biosensing platforms including point-of-care kits such as at-home pregnancy tests for detection of human chorionic gonadotropin (hCG), a

pregnancy-indicator. The most well-known example is an at-home blood glucose meter for diabetics. The goal of microfluidic biosensors is to achieve higher specificity for detection with the eventual goal of single-molecule detection.

Microfluidics was developed in the late 1990s and has since become a popular platform for executing complex and multiple processes in an easy-to-use, portable device. Platforms such as micro total analysis systems ( $\mu$ -TAS) or lab-on-chip (LOC) allow for sample handling, separation, detection and data analysis onto one platform. The sample, which can be a buffer, blood, urine, is injected into the chip, generally using an external pump; some devices have also been designed and built with integrated micropumps. Depending on the LOC device, biorecognition occurs either through electrokinetics, impedance or fluorescence. The key challenge in microfluidic-based POC devices is detecting with high specificity and sensitivity given the smaller sample volumes. However, the ability to integrate multiple unit operations including sample amplification, separation and biorecognition and detection make LOC technology optimal for biosensing.

## ***2.6 Liquid-Liquid interfacial biosensors***

Liquid-liquid interfacial biosensors have long since been used to alleviate the issues and limitations of traditional biosensors: multiple washing and rinsing steps, surface fouling and non-specific binding. In these sensors, the liquid interface becomes the substrate upon which the biomolecular event occurs. There are two main sensing methods utilizing a liquid interface: moving and pinned interfaces, shown in **Figure 2-5**<sup>105</sup>. In moving interfacial sensors, the device relies on diffusion<sup>106</sup>. The sample containing the analyte-of-interest is flowed side-by-side against a buffer containing the receptor for the

analyte. Both the receptor and analyte diffuse and product forms at the interface. Generally, a reaction front forms as the faster diffusing molecule diffuses across the interface and more product forms. Conversely, pinned interfaces uses immiscible fluids. The system is similar to moving interfaces, whereby product forms at the liquid interface, however, there is no diffusion<sup>107,108</sup>. While these biosensing techniques eliminate many drawbacks, they still require expensive transducing elements such as optical or electrochemical transducers. Therefore, while the device itself is portable and easy-to-use, these devices are still limited to a laboratory setting.

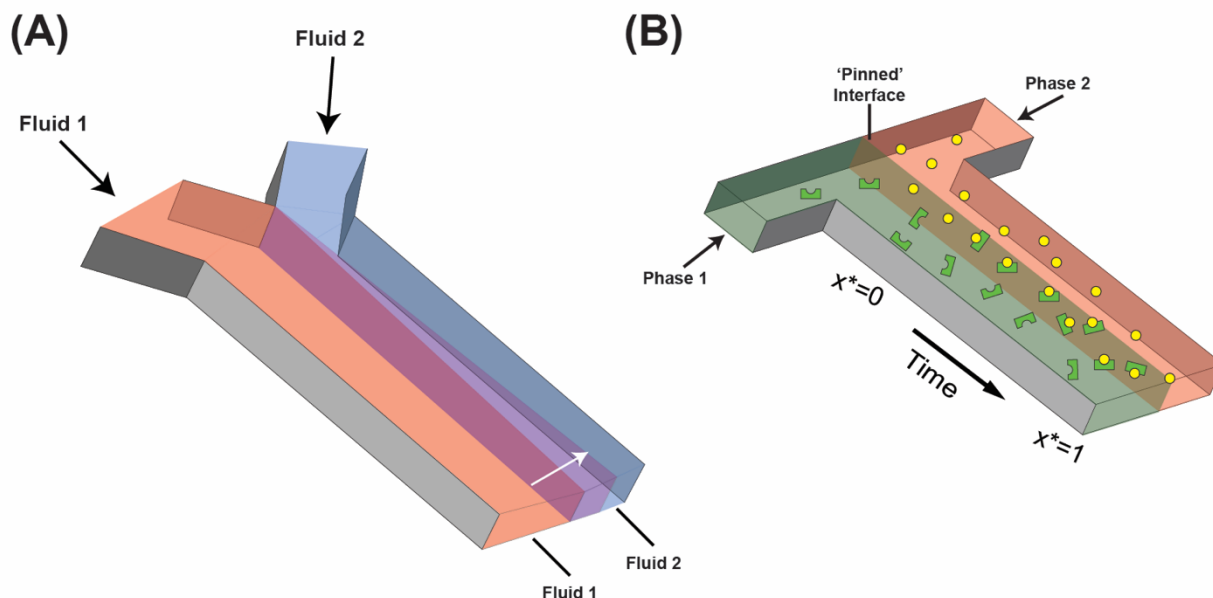


### Figure 2-5. Liquid-Liquid interfacial biosensors

(A) Moving interfaces between miscible liquids are created under laminar flow conditions between two co-flowing fluids. Due to the low Reynolds number they do not mix except by diffusion, creating a diffusive interface with predictable geometry. (B) Pinned interfaces between immiscible liquids are created by selective surface patterning of a microchannel. The two fluids do not diffusively mix, creating a stark where the reaction only takes place.

## 2.7 Thesis Aims

The overall goal of this thesis is to develop a non-optical, label-free liquid interface

biosensor. For this, the work has been divided into three specific aims outlined below:

**Aim 1: Characterize the Maxwell-Wagner polarization of a liquid-liquid interface. Specifically, understand the relationship between the electrical properties of each fluid – conductivity and permittivity – and applied frequency.**

**Aim 2: Characterize and quantify how interfacial polarization is affected when a biomolecular event occurs at a liquid interface.**

**Aim 3: Incorporate impedance spectroscopy into the developed biosensing scheme. Enabling detection of female reproductive hormones in the first non-optical, label-free liquid interface biosensor.**

## ***2.8 Thesis Overview***

In this thesis, we present the experiments taken to develop a non-optical, label-free sensor capable of fast, selective and sensitive detection.

To do this, we sought to develop a novel transducing element for a liquid-liquid substrate sensor that could be leveraged to detect biomarkers in-solution without the use of labels or optics. The biosensor combines both microfluidics and electrokinetics; a detailed overview of the fabrication techniques is described in **Chapter 3**. A new electrokinetic method for manipulating an electrical interface created by two co-flowing fluids is described in **Chapters 4 and 5**. These chapters outline how an external alternating current (AC) electric field applied to a liquid-liquid interface with disparaging

electrical properties, leads to interfacial displacement. The direction and magnitude of displacement is dependent on both applied frequency and electrical properties of the fluids, specifically conductivity and permittivity. Since this electrokinetic phenomenon is similar to traditional DEP, we have called it fluidic dielectrophoresis (fDEP). In **Chapter 6**, we describe a novel application for this electrokinetic phenomenon, electrokinetic mixing. **Chapters 7 and 8** detail how a biomolecular reaction at a liquid interface alters the electrical properties of the interface, which can be transduced by changes in interfacial displacement; we call this method of transduction, interfacial electrokinetic transduction (IET). A model reaction between avidin and biotin is detected in solution and with a bead-based assay in solution in **Chapters 7 and 8** respectively. In **Chapter 9**, a method for non-optically monitoring the position of the liquid interface by impedance spectroscopy is described. We then combine impedance spectroscopy with the IET sensor to create the first non-optical, label-free liquid interfacial sensor in **Chapter 10**. In **Chapter 10**, we demonstrate non-optical detection of human chorionic gonadotropin (hCG) in human serum. The thesis will conclude with **Chapter 11**, providing discussion and proposal for future work.



# 3 *Overview of Methods*

---

In this chapter, the experimental methods used to create microfluidic devices for crossover frequency and displacement measurement, and deliver samples are described. The fabrication techniques used for microelectrodes are standard lithography procedures. The section following the microfabrication procedures describes the soft lithography methods that were used to fabricate, align and seal polymer microchannels atop the microelectrode structures. Finally, a detailed description and construction of a customized, portable, constant-pressure flow system used to deliver samples is described.

## **3.1 *Microelectrode fabrication***

The following sections describe the standard lithography procedures modified for electrode fabrication.

### **3.1.1 Metal deposition**

The microelectrodes used in the body of this work consist of chromium and gold. First, glass coverslips (Fisher Scientific, 50x30mm - #1) are cleaned in Acetone and Isopropanol. They are then heated to 115 °C for 15 minutes on a hotplate. Metal is deposited onto the coverslips using an electron beam vacuum deposition coater system. Electron beam vapor deposition is a form of physical vapor deposition in which a target anode is bombarded with an electron beam under high vacuum. The electron beam cause

atoms from the target to sublime into the gaseous phase. These atoms then precipitate into solid form, coating the entirety of the vacuum chamber, within line of sight, with a thin layer of the target material. The microelectrodes consist of two metals, chromium and gold, whereby chromium acts as an adhesion layer. In all microelectrode arrays used in the body of this work, metal was deposited at 20 and 30 nm thickness for chromium and gold respectively. Once deposition concluded, the chromium/gold slides were baked at 115 °C for 15 minutes.

### **3.1.2 Standard lithography procedure**

Photolithography is a microprocessing technique that uses a non-transparent photomask to block and expose regions of photoresist or other photosensitive materials to ultraviolet (UV) light. In contact photolithography, the photomask is placed in direct contact with a substrate covered in photoresist. The substrate-mask is then exposed to UV light source to create a photopatterned positive or negative image with a 1:1 aspect ratio in size to the mask. The resolution in contact lithography is dependent on the processing techniques and the smallest image that can be projected onto the photoresist.

In this work, microelectrodes were fabricated using a positive photoresist, S1813 (Shipley). The areas exposed to UV light are rendered soluble in developer, thus creating a positive of the image of the photomask on the surface.

### **3.1.3 Metal etching**

Upon finishing the lithography processes, the photoresist defines the electrode design. Metal can now be removed using wet chemical etching techniques. First, the slide

is submerged in gold etchant, removing excess, unwanted gold. Next, the slide is submerged in chromium etchant. Finally, the glass coverslip is washed with acetone, to remove excess photoresist, and isopropanol to remove acetone. The coverslip with the microelectrodes is now ready to be bonded to the flow channel.

### **3.2 *Microchannel fabrication***

These sections outline the process for fabricating and sealing polymer microchannels to the electrode patterned glass slides.

#### **3.2.1 *Microchannel fabrication by soft lithography***

Soft lithography is a term used to describe the fabrication of photo patterned resist structures in flexible polymer microchannels. The processing steps are similar as those mentioned earlier for electrode fabrication. Unlike standard lithography procedures that employ the photoresist structures for use as metal deposition masks, however, soft lithography uses such structures as molds for microchannel formation.

This process utilizes a thick, viscous negative photoresist (Microchem Corp., SU-8 3050). The photoresist is spun onto a silica wafer (University Wafers) and subjected to a heating cycle to evaporate the solvent from the resist. A photomask is placed atop the SU-8 coated wafer and exposed to UV light (KLOE, UV-KUB 2) at an energy of 225 mJ/cm<sup>2</sup>. The exposed areas of SU-8 crosslink under the UV radiation and become insoluble in developer (MicroChem Corp., SU-8 Developer) and remain as raised structures, while the unexposed regions are dissolved. Depending on the spin coating

speeds, the structure heights can change; increasing the revolutions per minute (rpm) will lead to shorter structures. The relevant process parameters are highlighted in **Table 3-1**.

	<b>SU-8 3050</b>
Microchannel height ( $\mu\text{m}$ )	50
Spinning Parameters	500 rpm, 100 acc. 10 seconds
	3000 rpm, 300 acc. 30 seconds
Pre-bake	5 minutes at 65 °C
	20 minutes at 95 °C
Post-bake	1 minute at 65 °C
	5 minutes at 95 °C
Developing	8 minutes
Hard-bake	120 minutes, 200 °C

**Table 3-1. Photolithography process parameters**

An elastomeric polymer, polydimethylsiloxane (PDMS) is used as the material for microchannel fabrication. A 10:1 ratio of elastomeric base and curing agent is mixed and poured atop the SU-8 mold and baked for 30 minutes at 85 °C. During this time, the elastomeric base conforms to the SU-8 mold and cures, hardening into a flexible polymeric slab. The slab is then gently peeled of the silica wafer, releasing the mold from the hardened polymer and creating regions of space where the resist once existed. When the PDMS slab is aligned and placed on the electrode patterned glass coverslip, the polymer conforms to the glass surface and the regions of empty space become the microchannels for which fluid can be transported through.

### 3.2.2 Alignment and sealing of microchannels

The final fabrication step involves aligning the PDMS polymer slab atop the microelectrode geometry, bringing them into conformal contact and creating an irreversible bond at the PDMS-glass interface. This is done by oxygen plasma treatment to both the PDMS and microelectrode-glass coverslip. This is done by oxygen plasma treatment to both the PDMS and microelectrode-glass coverslip. Both components are placed in an oxygen plasma chamber (Jelight, Model 42A) where oxygen is delivered at 15 lpm and plasma treatment occurs for 90 seconds. The PDMS and glass coverslip are immediately aligned and sealed under an inverted microscope. This results in an irreversible bond between the PDMS and glass surface which is capable of sustaining pressures up to 20 psi. Since the resulting PDMS oxidation is highly unstable and reversible in an oxygen environment – lasting no more than 3 minutes – it is important to have perform alignment rather fast.

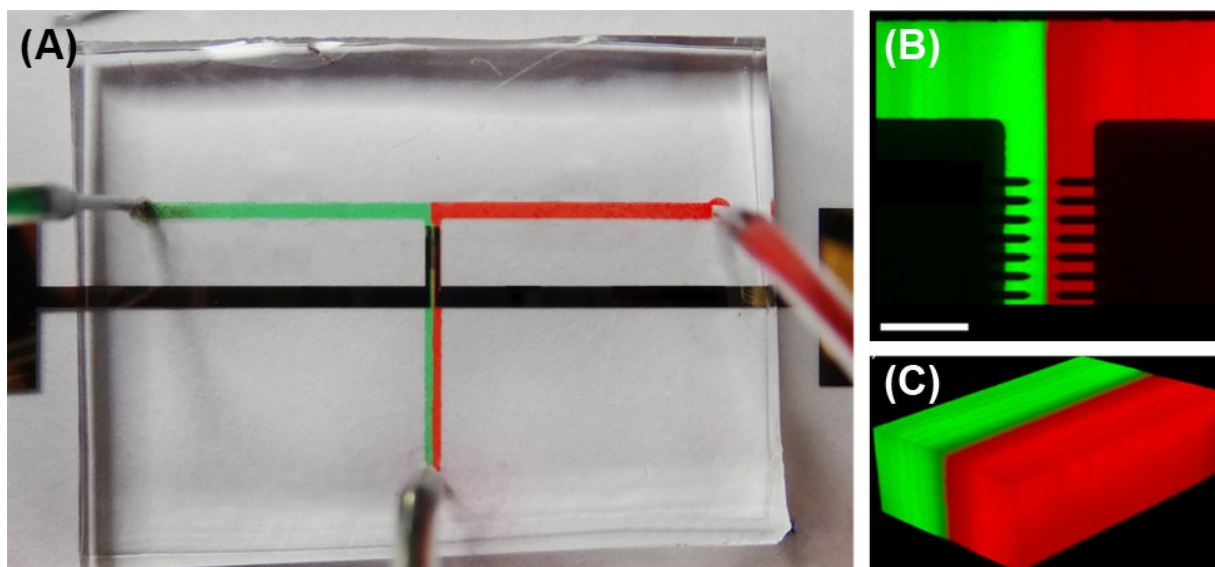


**Figure 3-1. Microfluidic ‘T-channel’ device with embedded electrodes**

(A) Microfluidic device made from PDMS, plasma bonded to a glass coverslip with metal electrodes. Feature sizes are 3x larger than experimental devices to image the buffers and interface. The liquid interface is created by an external constant-pressure flow system and consists of DI water dyed with colored food dye. (B) Confocal image of the microfluidic T-channel with embedded electrodes. (C) 3D confocal stack of sharp liquid interface created by two co-flowing streams.

### **3.3 Constant-pressure flow source**

There exist two main types of systems to deliver samples to a microfluidic device: constant pressure and constant flow. In constant flow sources, a specific flow rate is programmed, and the machine applies a force to deliver the specified flow rate. Regardless of channel geometry, the machine will deliver a constant flow source. However, these devices are prone to pulsatile flows at low flowrates, as well as device fouling from debonding. In constant pressure sources, a pressure is applied to the sample container to deliver flow. However, changes in volume can alter the flow rate with respect to applied pressure. Another drawback is depending on the geometry of the device, the flow rate can also vary with applied pressures.

#### **3.3.1 A low-cost microfluidic flow controller**

Our microfluidic flow controller drives fluid flow through microfluidic channels using a constant pressure source. Unlike commercial solutions, the entire system uses readily available plastic fittings, costs less than \$600.00 USD and requires less than one hour to assemble; the system is illustrated in **Figure 3-2**. Pressurized house air (50 psi) powers the flow controller. As shown in **Figure 3-2**, blue airline tubing exits a pressure regulator and is split into four lines using a pressure manifold. A 3-way air switch controls the direction of pressured air into each line. When activated, the airline is sent into a precision pressure regulator, which controls the output pressure and directs this into a fluid-filled cryogenic vial. The pressure increases inside the vial which drives fluid flow through the tubing and the microfluidic device. We control the flow rate by adjusting the precision pressure regulator and monitoring the air pressure on the accompanying pressure gauge.

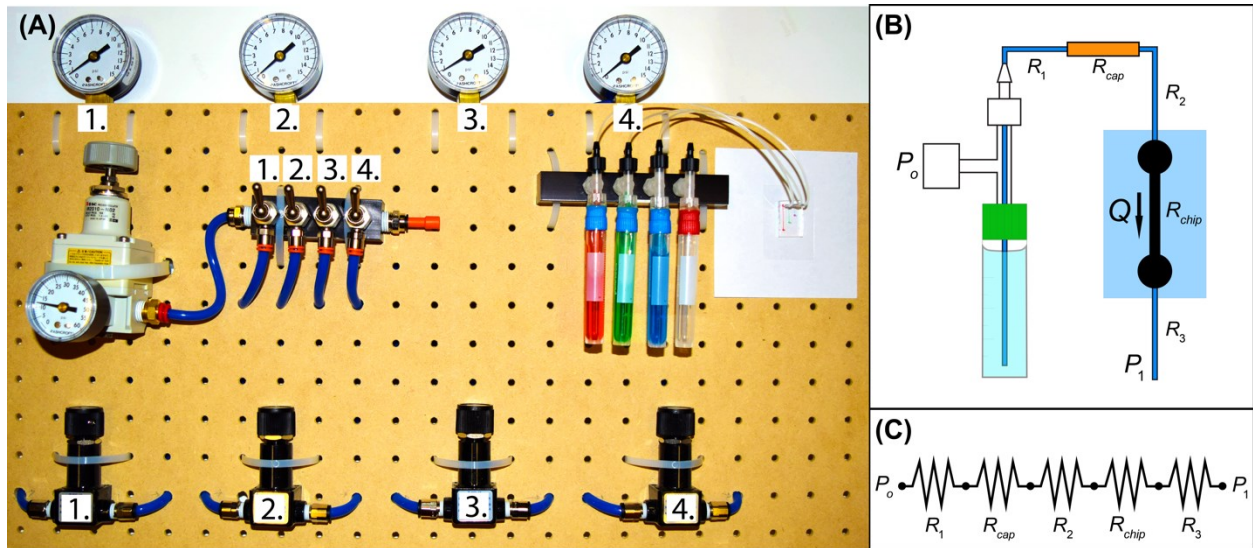


**Figure 3-2. Constant-pressure flow source**

(A) Low-cost microfluidic flow controller for controlling flows through four fluidic inlets. (B) Schematic of pressurized sample vial. A pressure ( $P_o$ ) is applied to a cryovial and fluid flows through a series of tubing resistors ( $R_1$ ), a capillary resistor ( $R_{cap}$ ),  $R_2$ , into the device ( $R_{chip}$ ) and exiting through outlet tubing ( $R_3$ ) at a flow rate  $Q$ . (C) Hydraulic circuit diagram of the fluidic system.

### 3.3.2 Hydraulic circuit analysis

Constant pressure sources can be reliably engineered to produce well-controlled flows in microfluidic systems using hydraulic circuit analysis. This method treats a network of microchannels as a circuit of fluidic resistors. For low Reynolds number flow in microchannels, there is an approximately linear relationship between pressure and flow rate, known as the Hagen-Poiseuille law. For an infinitely long cylindrical microchannel with a uniform circular cross section area,  $A$ , radius  $R$ , and aligned in the positive  $z$ -direction, the fluid velocity profile is given by:

$$u_z = -\frac{1}{4\mu} \frac{\partial P}{\partial z} (R^2 - r^2), \quad (3.1)$$

where  $u_z$  and  $\partial p/\partial z$  are the fluid viscosity and channel pressure gradient, respectively. The velocity profile can be integrated over the channel area to calculate the volumetric flow rate  $Q$ :

$$Q = -\frac{AR^2}{8\mu} \frac{\partial P}{\partial z}, \quad (3.2)$$

Assuming the channel length,  $L$ , is much larger than the radius, we can neglect entrance effects and treat each channel as an infinitely long tube. Replacing  $\frac{-dP}{dz}$  with  $\Delta P/L$ , where  $\Delta P = P_{IN} - P_{OUT}$ , is the pressure drop across the channel. *Equation (3.1)* can be written as:

$$Q = \frac{\Delta P \pi R^4}{8\mu L}, \quad (3.3)$$

which is known as the Hagen-Poiseuille law. Based on *Equation (3.3)*, an applied pressure drop produces a flow rate,  $Q$ , that is proportional to the channel's hydraulic resistance ( $R_h$ ):  $8\mu L/\pi R^4$ . The Hagen-Poiseuille law describes to a good approximation the relationship between applied pressure and flow rate. It is analogous to Ohm's law for electrical circuits, where the voltage (pressure) is proportional to the current (flow rate).

$$\Delta P = QR_h. \quad (3.4)$$

This equation provides a good estimate for steady flow through long and narrow cylindrical microchannels, however, this relation can be extended to other channel shapes by replacing  $R$  with the hydraulic radius,  $r_h = 2A/P$ , where  $A$  and  $P$  are the channel cross-sectional area and perimeter, respectively.



### 3.3.3 Hydraulic circuit analysis

We used hydraulic circuit analysis to design fluidic resistor elements that can predictably restrict the flow rate through an arbitrary microfluidic device. To generate microfluidic flow, we apply a known air pressure ( $P_o$ ) to a sealed fluid-filled vial and maintain the device outlet at 1atm ( $P_1$ ), as depicted in **Figure 3-2B**. Each flow line has five fluidic circuit components that influence the flow rate in a microfluidic device (**Figure 3-2C**). When the flow controller delivers a pressure,  $P_o$ , to the sample vial, the pressure drives fluid flow into the submerged tubing and into the microfluidic device.

One way to control fluid flow to the microfluidic chip is to insert flow elements with a large hydraulic resistance such that it dominates the pressure-flow rate behavior of the entire fluidic circuit. Illustrated in **Figure 3-2C**, fluid will flow through five hydraulic resistors — the submerged inlet tubing ( $R_1$ ), the capillary resistor ( $R_{cap}$ ), tubing at the microfluidic inlet ( $R_2$ ), the microfluidic device ( $R_{chip}$ ), and the outlet tubing ( $R_3$ ). Modifications to any of these components directly influence the overall resistance of the entire fluidic circuit and resulting pressure- flow rate relationship. To design capillary circuit elements with sufficiently large enough hydraulic resistance to regulate flow, but not too large that flow is impeded, we measure the resistance of the microfluidic device ( $R_{chip}$ ) and calculate the length of capillary tubing required such that  $R_{cap} \sim 10 \times (R_{chip} + R_1 + R_2 + R_3)$ . If the capillary tubing has a resistance significantly larger than the remaining elements in the hydraulic circuit, it will serve as a predictable bottle- neck for regulating fluid flow rate.

### **3.3.4 Flow controller assembly and testing method**

The following section describes the assembly and operation of the microfluidic flow controller.

#### *3.3.4.1 Essential components*

Construction of the flow controller takes less than one hour and requires three primary assemblies: a pressure manifold, a multi-line manifold, and a sample holder. The entire system is powered by pressurized air and uses a series of pressure regulators, pneumatic air switches, and manifolds to control gas pressure inside sealed liquid-filled cryotubes and direct flow to microfluidic channels. To regulate the air pressure, house gas (50 psi) is directed through an air filter and into a primary pressure regulator (SMC Pneumatics, IR2010-NO2), where it exits at a fixed pressure (20psi). The pressure manifold with one inlet and four outputs (McMaster-Carr, 5469K121) delivers the regulated air pressure to four separate fluid-filled cryovials. Each manifold output is fitted with a 3-way air switch (Pneumadyne, C030621) to control the gas flow to downstream precision pressure regulators with accompanying pressure gauges (McMaster-Carr, 3846K411). The precision regulators control the gas pressure delivered to each cryovial, and the corresponding pressure gauges provide an easy way to monitor regulator pressure. Each of the air lines then connect to a multi-line manifold, which holds fluid-filled cryotubes for sample holding and pressure-driven fluid delivery to the microfluidic device. To deliver flow, a precision regulator is used to increase the air pressure inside a desired cryovial, which then forces flow through the submerged tubing and out into the chip. The flow rate in each sealed vial is controlled by increasing or decreasing the vial pressure using the appropriate precision pressure regulator.

#### *3.3.4.2 Flow controller assembly*

To make this system easy to setup and operate, the pressure manifolds, air regulators, and gauges are attached to a tempered pegboard (Ace Hardware) using zip ties (McMaster-Carr). Before assembly, all threaded fittings were wrapped with two layers of Teflon tape to ensure a proper seal and prevent gas leaks. All components are fitted with push-to-connect fittings and connected with 1/4" PTFE tubing. The pressure manifold inline/outline is fitted 1/4"–1/8" National Pipe Thread (NPT) male fittings (McMaster-Carr, 5779K108), and each gas outlet threaded to 3-way switches (Pneumadyne, C030621) with 1/4-10-32 UNF male connectors (McMaster Carr, 5779K246). Each switch controls the airflow on/off to a precision pressure regulator (Airtrol, R-800-10) with 1/4-1/8 NPT male connectors. Regulator outlets are attached to pressure gauges (0–15 psi, McMaster-Carr, 3846K411) threaded into 1/8" brass T's with 1/8" NPT male fittings.

#### *3.3.4.3 Sample holder assembly*

Sealed cryovials are used as the pressure vessels for delivering fluid flow to microfluidic channels. The cryovial assembly houses the necessary components to load the fluid samples and to pressurize and direct their flow. Tubing from the outlet of each pressure gauge is connected to the back end of a multi-line manifold with 1/8" NPT connections and we connected male luer-lock fittings (7/16" hex–1/8-27 NPT, Value Plastics) to the front of the manifold. To attach a sealed vial to each of these fittings, the top of each cryovial is modified by drilling a small 3 mm diameter hole in the cap of each cryotube and attaching it to a plastic male luer fitting (7/16" hex–1/8-27 NPT, Value

Plastics) using quick setting epoxy. After allowing the epoxy to cure for 15 min, the cap is fitted with the bottom of a male luer-tee fitting.

#### *3.3.4.4 Connecting the tubing*

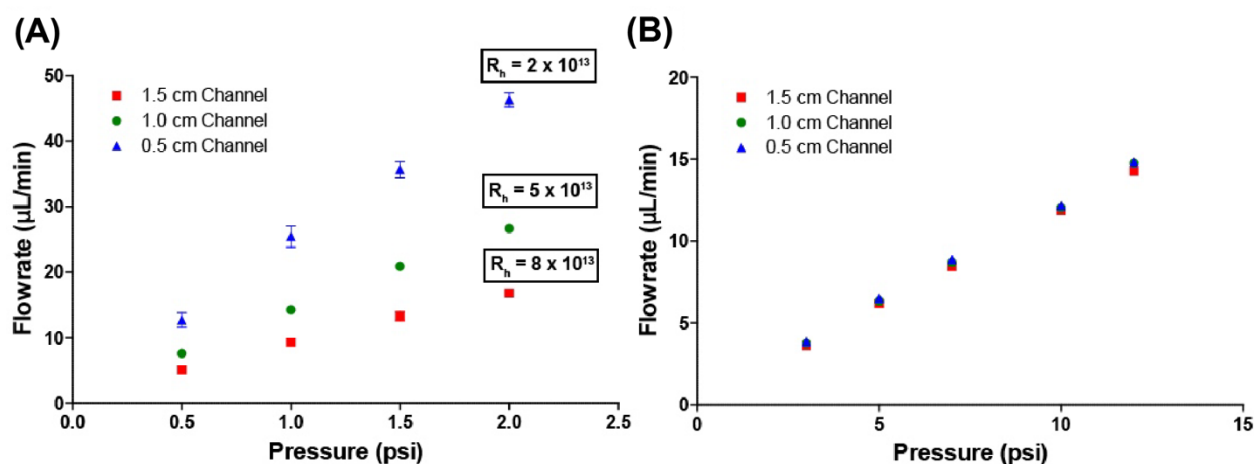
The final step in completing the sample assembly is to create an airtight connection that allows for the sample to flow from the pressurized cryotube, through submerged tubing and into the microfluidic device. To do this, a female luer lug tee fitting, having two openings and a third centered and oriented perpendicular to each opening is used. The cryovial is attached to the bottom opening of the tee fitting. At the top opening, plastic tubing (Cole-Parmer), is pushed through a fitted male lock ring (Value Plastics), leaving 4" of exposed tubing within the cryovial. Epoxy was applied to the junction of the lock ring and tubing to make an airtight seal. The other end of the tubing is connected to a specific microfluidic device inlet. When pressurized, the fluid inside the vial will be driven into the tubing and the microfluidic device.

### **3.4 Supplementary Materials**

#### **3.4.1 Hydraulic resistance measurements**

We first used the flow controller to drive fluid flow at different applied pressures through microchannels of varying length. As shown in **Figure S3-1**, the flow rate was measured through microchannels 0.5, 1 and 1.5cm in length and plotted as a function of applied pressure. All flow rate measurements were performed with microfluidic flow sensors (Elveflow, MFS 2 and MFS 3). As expected and depicted in **Figure S3-1A**, the Q-P relationship for each channel is significantly influenced by channel length and the slope of each dataset was used to determine each channel's experimental hydraulic

resistance. Using *Equation (3.3)*, we determined the length of capillary tubing required to exceed the hydraulic resistance of the longest microchannel by a factor of 10. We then repeated these experiments with this length of capillary tubing (15.5 cm) inserted upstream the inlet of each microfluidic channel. Since the capillary tube had the largest hydraulic resistance in the system, the flow rate for the system was dictated by the capillary tube, therefore, the flow rate was seen to be largely independent of the channel length (**Figure S3-1B**).



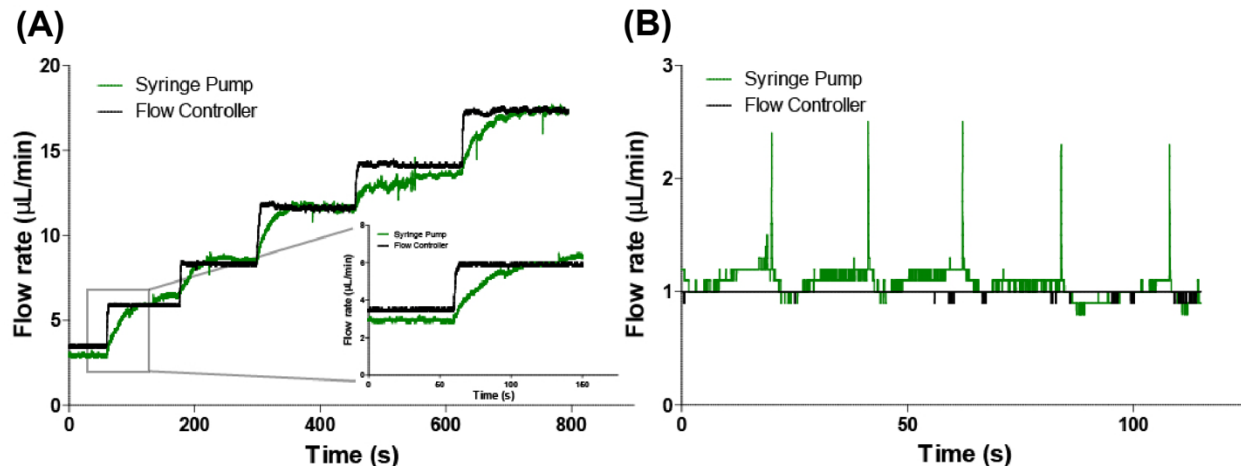
**Supplementary Figure 3-1. Flowrate versus applied pressure with and without a capillary tube**

(A) Pressure versus flow rate for three channel lengths without a capillary tube. (B) Pressure versus flow rate for three channels with an upstream capillary resistor and with a capillary tube. All three datasets collapse to single curve, with minor deviation (0.5 μL/min) at larger pressures.

### 3.4.2 Flow rate capabilities, stability and response time

To demonstrate our system is a feasible low-cost alternative to commercial syringe pumps, we performed real-time flow response comparisons between the flow controller and a commercial syringe pump. Using a passive in-line flow sensor, flow rates were measured for both the flow controller and syringe pump in response to a step change in pressure. A time-response and stability comparison between the syringe pump and flow

controller is shown in **Figure S3-2A**.



### Supplementary Figure 3-2. Comparison of constant-pressure source and syringe pump

(A) Time response comparison of the presented flow controller and a commercial syringe pump. The syringe pump requires, on average, 20 s to stabilize while the flow controller requires less than five seconds. In some instances, the syringe pump requires almost 60 s, as shown in the subplot. (B) Flow rate comparison between the flow controller and syringe pump at 1  $\mu\text{L}/\text{min}$ . The syringe pump exhibits pulsatile flow at low flow rates while the flow controller offers stable flow rates.

As illustrated, the flow controller has a significantly faster response time than the syringe pump, requiring less than 5 seconds to switch from a flow rate of 3  $\mu\text{L}/\text{min}$  to 6  $\mu\text{L}/\text{min}$ . The syringe pump, however, took upwards of 60 seconds to reach steady state. The flow rate stability is approximately the same for both the syringe pump and flow controller with an approximate 0.2  $\mu\text{L}/\text{min}$  variation. The syringe pump, however, becomes pulsatile and unstable at a low flow rate (1  $\mu\text{L}/\text{min}$ ), shown in **Figure S3-2B**. Comparing the stability of both the flow controller and syringe pump, one can see the syringe pump produced a pulsatile flow, while under the same conditions the flow controller produced a constant flow. Finally, it is important to note the operating range of the flow rates produced by the flow controller. We found the flow controller can provide reliable and steady flow rates from 0.5 to 35  $\mu\text{L}/\text{min}$  with a 15.5 cm long capillary resistor.

However, the user can alter this range by adjusting the length of the upstream capillary tubing. A longer capillary, for example, will produce a smaller flow rate, while a shorter capillary tube will allow for increased flow rate.

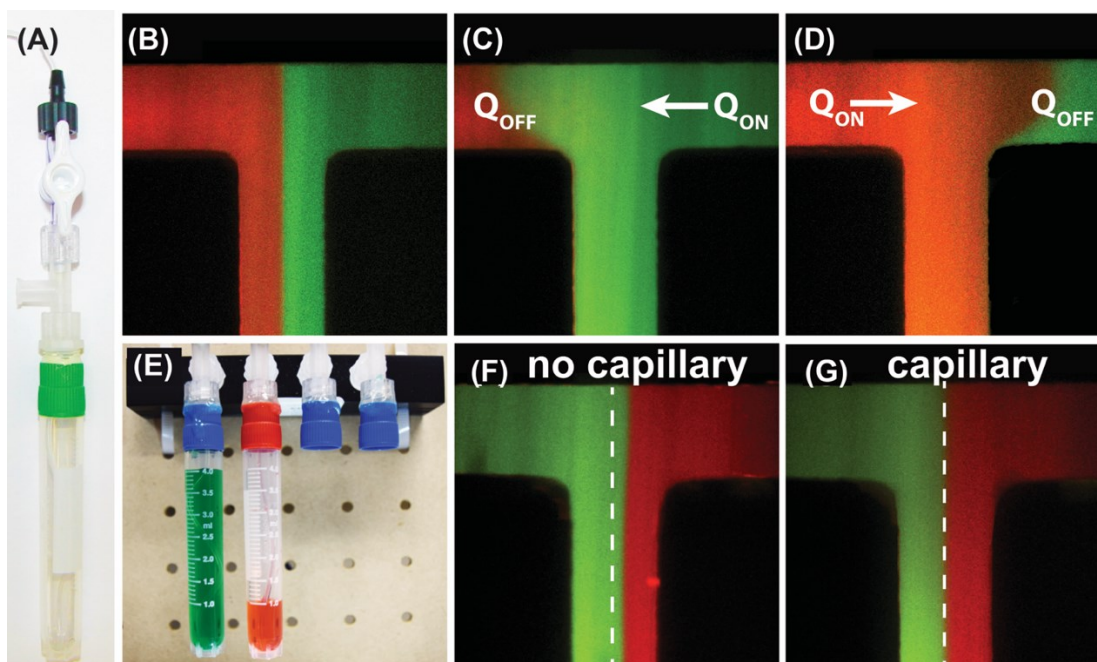
### **3.4.3 Flow switches prevent fluid back flow**

For many microfluidic applications, it is not sufficient to simply control when a single flow stream is on or off. Experiments in cell biology, for example, often require the ability to vary the fluid flow rate and switch between multiple streams. To accommodate these requirements, we also developed a simple and inexpensive switching solution to make our flow system suitable for a broader range of microfluidic applications. This is an important feature because switching flows on and off using pressurized fluid vials can be initially challenging because fluid flow follows the path of least resistance in a microfluidic network. It is important to have a method to prevent fluid backflow to sample vials: when fluid from one fluid-filled vial flows into the device and then unwantedly flows back out into a neighboring vial.

Backflow occurs when a pressure difference between two microfluidic inlets exist that is large enough to drive flow from one inlet, into the device, and out into a second inlet. Backflow is typically unwanted because it can contaminate neighboring vial samples and lead to longer setup times. To alleviate this problem, we designed a novel and inexpensive flow controller switch (**Figure S3-3A**) to prevent backflow.

To test the effectiveness of the flow controller switch, we used a microfluidic T-channel device with two inlets and one single outlet, shown in **Figure S3-3B**. Two fluid streams were driven into the device at equal pressures to produce co-laminar streams that flow side-by-side. To aid in flow visualization, one fluid stream was dyed with Alexa

Fluor 488 (green) and the adjacent stream is dyed with Alexa Fluor 594 (red). The applied pressures for both solutions were equal, producing a fluid interface centered in the main flow channel. Each fluid line was turned on or off using the appropriate flow controller switch. When the switch connected to the red solution was turned to the “off” position no backflow occurs (**Figure S3-2C**) Instead, the red solution stops in the T-channel junction. Conversely, when the red stream is turned “on” and the green stream turned “off,” the green stream stops before the junction (**Figure S3-2D**). While this is a simple application, this is an important technical ability done at a fraction of the cost of a single syringe pump.



**Supplementary Figure 3-3. Customized sample switch preventing backflow and implementing stable flows**

(A) Low-cost fluidic switch for fluid routing. When the switch is turned “off,” it prevents the sample from flowing backward from one cryotube and into another. (B) Two laminar liquids flow side-by-side at equal flow rates in a microfluidic T-channel. (C) The switch for the “red” stream is turned off and the “green” stream follows the path of least resistance. (D) The switching is reversed. (E) Two samples with different cryotube volumes are delivered to a microfluidic T-channel. (F) Without a capillary the hydraulic head of the “green” stream is greater than the “red,” resulting in the “green” stream having a faster flow rate and the interface is not centered. (G) When the capillary is introduced to the same system both flow rates become equal and the interface becomes centered. The effect of the hydraulic head is eliminated as the flow rate is bottlenecked at the high resistive capillary.



### 3.4.4 Flow contributions from hydrostatic pressure

In addition to backflow, it is important to note that gravitational forces can also influence the flow controller's fluid flow behavior. During flow experiments, we observed that when cryovial fluid volumes differed, a different pressure is required to produce equal flow rates. Because the sample volume exists over a height,  $h$ , several centimeters above the microfluidic device, a hydrostatic head pressure ( $\Delta P_g = \rho gh$ ) exists between the top of the fluid sample and the base of the microfluidic chip. While this may appear trivial to the advanced microfluidics researcher, this feature is often overlooked by beginners and so we address how to solve this problem here. To observe this gravitational influence, we used a T-channel device with a different fluid volume loaded in each cryovial, as shown in **Figure S3-3B**. Each vial was filled with a different volume of DI water, one with a volume of 4 ml dyed with Alexa Fluor 488 (green) and the other with 1 ml and dyed with Alexa Fluor 594 (red). When equal pressure was applied to both cryovials, the liquid-liquid interface is not centered in the main channel, indicating that the flowrates in each fluid inlet are not equal. This occurs because the hydrostatic pressure is greater in one cryovial, and therefore, the overall pressure driving flow is also greater. Recall *Equation (3.4)*, flow rate is dependent on both the hydrodynamic resistance and pressure. The initial pressure has two components associated with its value, the applied pressure from the flow system and gravity, leading to the following equation:

$$\frac{\Delta P}{R_h} + \frac{\rho gh}{R_h} = Q. \quad (3.5)$$

For our flow controller with a sample volume 6 cm above the chip,  $\Delta P_g = 0.1$  psi, and is large enough to impact the fluid flow rate (**Figure S3-3F**). However, if the hydraulic

circuit resistance is large relative to the chip, the gravitational contribution becomes negligible compared to the applied term ( $\Delta P/R_h = 0.1$  psi) and we observe no gravitational impact on fluid flow. This is illustrated in **Figure S3-3G**, where a capillary was inserted upstream of each microfluidic inlet to produce perfectly centered liquid-liquid interface even when the sample volume heights were significantly different.

Component on the Pegboard	Item Name	Company	Part Number	Unit Price (USD)	Parts per System	Total Price (USD)	Unit Price [System] (USD)
Pressure Gauge + Pressure Regulator Component	Sub-Miniature Precision Pressure Regulator with knob	Airtrol	R-800-10	34.08	4	136.32	136.32
	Push-to-Connect Tube Fitting for Air - Straight Adapter for 1/4" Tube OD x 1/8 NPT Male	McMaster-Carr	5779K108	3.08	16	49.28	49.28
	Medium-Pressure Brass Threaded Pipe Fitting 1/8"	McMaster-Carr	50785K75	3.73	4	14.92	14.92
	Multipurpose Gauge, Steel Case, 2" Dial, 1/8 NPT Bottom, 0 - 30 PSI	McMaster-Carr	3846K411	9.85	4	39.40	39.40
							239.92
Inlet Switching	Push-to-Connect Tube Fitting for Air - Straight Adapter for 1/4" Tube OD x 1/8 NPT Male	McMaster-Carr	5779K108	3.08	1	3.08	3.08
	Black Anodized Aluminum Manifold 4 Outlets on One Side, 1/4 Pipe Size Inlet	McMaster-Carr	5469K121	17.08	1	17.08	17.08
	Push-to-Connect Tube Fitting for Air & Water Plug, 1/4" Stem OD, Orange	McMaster-Carr	5111K504	0.97	1	0.97	0.97
	Push-to-Connect Tube Fitting for Air Straight Adapter for 1/4" Tube OD x 10-32 UNF Male	McMaster-Carr	5779K246	3.52	4	14.08	14.08
	Push-to-Connect Tube Fitting for Air - Straight Adapter for 1/4" Tube OD x 1/4 NPT Male	McMaster-Carr	5779K109	3.08	1	3.08	3.08
	Detachable Toggle 1/8" NPT Input, 3-Way Valves, 1/4" Stem OD, Orange	Pneumadyne	C030621	13.52	4	54.08	54.08
							86.29
Cryotube Manifold	Tygon <sup>®</sup> microbore tubing, 0.020" x 0.060" OD, 100 ft/roll	Cole Palmer	EW-06419-01	48.50 (roll)	1	48.50	48.50
	Multiline Block 4 Holes, 1/8 Pipe Size	McMaster-Carr	5091K52	22.96	1	22.96	22.96
	Push-to-Connect Tube Fitting for Air - Straight Adapter for 1/4" Tube OD x 1/8 NPT Male	McMaster-Carr	5779K108	3.08	4	12.32	12.32
	Female Luer Thread Style with 7/16" Hex to 1/8-27 NPT Thread, White Nylon	Value Plastics	18FTLL-1	0.3810 (100 Minimum)	4	38.10	1.53
	Female Luer Lug Style Tee, White Nylon	Value Plastics	FLLT-1	0.3250 (100 Minimum)	4	32.50	1.30
	Male Luer Integral Lock Ring to 200 Series Barb, 1/8" (3.2 mm) ID Tubing, Black Nylon	Value Plastics	MTLL230-2	0.1570 (100 Minimum)	4	15.70	0.63
	Round Bottom Self-Standing Bottoms with Writing Area	VWR	82050-220	0.27 (Case of 300)	4	80.08	1.08
							88.32
Precision Regulator	Push-to-Connect Tube Fitting for Air - Straight Adapter for 1/4" Tube OD x 1/4 NPT Male	McMaster-Carr	5779K109	3.08	2	6.16	6.16
	Multipurpose Gauge Plastic Case, 2" Dial, 1/4 NPT	McMaster-Carr	4089K62	12.07	1	12.07	12.07
	SMC IR2010-NO2 regulator, precision modular, IR PRECISION REGULATOR	SMC Pneumatics	IR2010-NO2	75.80	1	75.80	75.80
							94.03
Pegboard	3/16"x2"x4" Pegboard	Ace Hardware	-	11.99	1	11.99	11.99
							11.99
Tubing	1/4 OD x .170 ID Polyurethane Tubing (100')	Pneumadyne	PU-250PB-4	38.50	1	38.50	38.50
							38.50
						726.97	511.05

### Supplementary Table 3-1. Detailed list of all the materials which make up the flow controller

The table is broken up into sections for the different components that make up the flow system: precision regulator, switching manifold, pressure regulators and gauges, sample manifold, pegboard and connection tubing. The company, respective part numbers and unit price for each component is listed. The total price corresponds to the cost of ordering each part, in some cases there is a minimum requirement. The final unit price for the system, \$511.05, corresponds to the price for all the require components.

# 4 *Polarization of Liquid-Liquid Interfaces*

---

## **4.1 Introduction**

When an electric field is applied across the interface between two materials with disparaging electrical conductivity ( $\sigma$ ) and dielectric constant ( $\epsilon$ ), such as an insulating particle suspended in conductive electrolyte, surface charge will accumulate, and the interface will polarize. The action of the electric field on the induced charge gives rise to electrical forces and form the basis for many types of electrokinetic phenomena including particle dielectrophoresis<sup>109</sup> and liquid electro-osmosis<sup>110,111</sup>. When an alternating current (AC) electric field is applied across the interface the magnitude and sign of the induced charge is frequency ( $\omega$ ) dependent. At low AC frequency, below the inverse charge relaxation time ( $\epsilon/\sigma$ ), material with greater conductivity conducts ionic charge to the interface at a rate faster than it is removed by the adjacent lower conductive phase<sup>109</sup>. As such, charge accumulates at the interface, and low frequency interfacial polarization is driven by material differences in electrical conductivity. At high frequency, above the charge relaxation timescale, the electric field oscillates faster than charges can electro-migrate to the interface. As conductive charging does not have enough time to occur over every field half-cycle, high frequency polarization is driven by differences in material dielectric constant; charge accumulates due to interfacial differences in dielectric polarization. If neither interfacial phase has both a greater electrical conductivity and dielectric constant, the high conductivity phase dominates interfacial charging at low frequency and the adjacent high dielectric phase drives charging at high frequency.

Hence, the net sign of the induced interfacial charge reverses at a frequency high enough to relax away conductive charging to the extent that it is trumped by opposing dielectric polarization. This frequency is on the order of the inverse charge relaxation timescale and is defined as the crossover frequency (COF). The charging mechanism, known as Maxwell-Wagner (MW) polarization<sup>109</sup>, has been exploited to pump liquid (electro-osmosis)<sup>112,113</sup>, and manipulate bubbles<sup>114</sup>, particles<sup>115</sup>, biomolecules<sup>116,117</sup> and cells<sup>118</sup> (dielectrophoresis). Research and application in this area, however, has been primarily limited to interfaces formed between two or more immiscible surface-liquid, particle-liquid, or gas-liquid phases.

While there has been work done with direct current (DC) electric fields at liquid/liquid interfaces<sup>119,120</sup>, the influence of AC electric fields applied perpendicular to a liquid/liquid electrical interface remains unexplored. Here, AC polarization at an electrical interface formed between two miscible aqueous liquids is reported. In this chapter, we demonstrate that an aqueous electrical interface exposed to a perpendicular AC electric field undergoes frequency dependent polarization and liquid displacement well described by MW polarization mechanics. The electrical interface is created using a microfluidic “T-channel” with embedded metal electrodes, as shown in **Figure 4-1A**. Due to the laminar flow profile and slow diffusion timescale associated with low Reynolds number flow, two liquids of differing electrical properties can flow side-by-side in a microchannel and create a sharp electrical discontinuity at their contacting interface, as seen in the 3D confocal image of the main flow channel (**Figure 4-1B**). The electrical conductivity and dielectric constant of each liquid phase is readily adjusted with the addition of soluble salts and zwitterions<sup>121</sup>, and measured with a handheld conductivity meter and LCR impedance

analyzer, respectively. A function generator (Rigol, DG4102) is wired to the embedded electrodes and used to deliver an AC electric field across the liquid/liquid interface. As shown in **Figure 4-1A**, the electrical interface is readily observed and imaged by labeling each fluid stream with soluble red and green fluorescent dye. The resulting fluorescent interfacial cross-section (**Figure 4-1B**) is captured using a confocal microscope (Nikon/Prairie Technologies) equipped with an Andor iXon 897 camera, two 50 mW solid-state lasers for excitation at 488 nm and 561 nm.

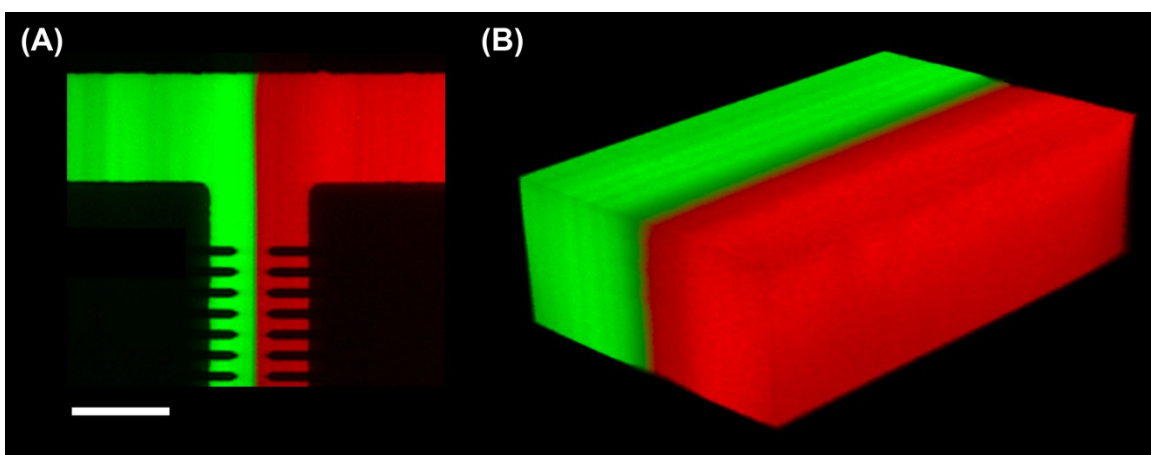


**Figure 4-1. Electrical interface created between two co-flowing fluids**

(A) Microfluidic T-channel with embedded electrodes. Two fluid streams with different electrical properties — each imaged with a fluorescent dye — flow side by side to create an electrical interface. Electrodes embedded in the channel deliver an AC electric field across the interface. Scale bar, 100  $\mu\text{m}$ . (B) The observed cross section of the electrical interface in the main flow channel when no electric field is applied.

## **4.2 Materials and Methods**

An electric field is applied across the liquid interface and fluid from one stream is observed to displace into the adjacent stream, seen in the 3D confocal image captured at  $\omega = 4$  MHz in **Figure 4-2A**. The direction of this displacement is frequency dependent. Shown in **Figure 4-2B** – a solid black line indicates the original interfacial position – the high conductivity stream (green) displaces across the interface into the neighboring high

dielectric stream (red) at an AC frequency of 4 MHz. The frequency is increased to 25 MHz and the displacement direction reverses (**Figure 4-2D**); the high dielectric liquid displaces into the adjacent high conductivity stream. Hence, there exists a fluid displacement crossover frequency (COF) that bridges these two events where no fluid displacement is observed (**Figure 4-2C**). For the experiment illustrated, a COF occurs at 7.6 MHz; the interface appears visually identical to that seen in **Figure 4-1B** when no electric field is applied. We shall proceed by describing the microfluidic setup and detailed liquid interfacial crossover frequency experiments, followed by a quantitative model predicting interfacial crossover frequency at the polarized microfluidic generated liquid/liquid interface.

The use of microfluidic flow is well suited for generating an electrical interface between two adjacent fluid streams. The microfluidic device utilized in this study, as shown in **Figure 4-1**, is fabricated using standard soft lithography and microfabrication techniques<sup>122,123</sup>. Briefly, microchannel electrodes are fabricated using wet chemical etching. Glass cover slips (Fisher Scientific, 50x30mm - #1) are coated with 2 nm of titanium and 50 nm of gold using electron beam evaporation. The cover slips are then patterned with photoresist (Shipley 1813) and the exposed metal film is etched away with titanium and gold chemical etchant creating an array of patterned metal electrodes. The microchannel is fabricated in PDMS (Momentive, RTV 615A). A 1:10 mixture of PDMS elastomer and curing agent is poured atop a lithographically fabricated SU-8 (Microchem Corp., SU-8 3050) polymer mold, cured and gently peeled off. Fluid ports are punched into the PDMS using a 0.75mm biopsy punch (Ted Pella, Inc.). The microchannel and coverslip are exposed to oxygen plasma (Jelight, Model 42A) and immediately aligned

and sealed under an inverted microscope<sup>123</sup>. As shown in **Figure 4-1**, the device consists of a main flow channel 100  $\mu\text{m}$  wide and 65  $\mu\text{m}$  high. The embedded electrodes are axially separated by 20  $\mu\text{m}$  and symmetrically bridge the channel width. Here, electrodes with sharp points are utilized in order to maximize the electric field strength across the liquid interface, as the sharp point serves to focus the electric field to the tip of the electrode.

Each fluid stream is introduced into the device via pressure driven flow from an externally pressurized cryogenic vial. Shown in **Figure 4-2A**, the left-most (green) high conductivity stream consists of diluted 10X phosphate buffered saline (PBS) labeled with 10 ng/mL of Alexa Fluor 488 (Invitrogen). The right-most (red) high dielectric stream consists of 2M 6-aminohexanoic acid (Sigma-Aldrich) (AHA) labeled with 10 ng/mL of Alexa Fluor 594 (Invitrogen). AHA is a water-soluble zwitterion used for increasing the dielectric constant of aqueous solution. Prior to fluorescent labeling, the AHA solution is vigorously shaken for 5 minutes in 5 g/mL Dowex MR-3 (Sigma-Aldrich) ion exchange resin to remove trace salts and reduce solution conductivity<sup>121</sup>. A cross-sectional view of the resulting fluid interface is imaged using dual excitation confocal microscopy (**Figure 4-1B**).

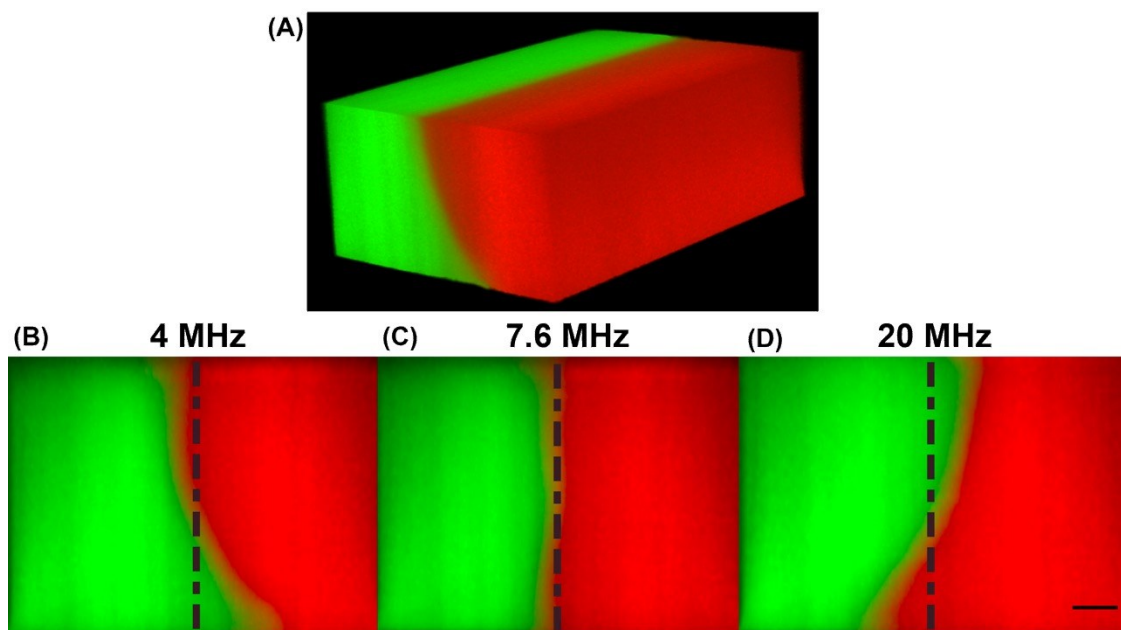


**Figure 4-2. 3D stacks of polarized liquid interface**

(A) 3D confocal image of the displaced electrical interface at  $10 V_{pp}$ , 4 MHz. (B) Confocal cross section of the interface at  $\omega = 4$  MHz, conductive fluid displaces across the interface. (C) Observed COF at  $\omega = 7.6$  MHz: the interface appears sharp and visually identical to when no electric field is applied (D)  $\omega = 25$  MHz: the high-dielectric (red) fluid displaces into the high- conductivity fluid. Black lines indicate the original interfacial position before the electric field is applied. Scale bar,  $10 \mu\text{m}$ .

### 4.3 Results and Discussion

To create the electrical interface two fluid streams, each with a different set of electrical properties, are pressure injected into the microfluidic device at a steady flow rate of  $10 \mu\text{L}/\text{min}$ . An AC potential of 10 volts peak-to-peak ( $V_{pp}$ ) is dropped across the electrodes, and the frequency is slowly varied while continuously monitoring the fluid interface. At 4 MHz the high conductive liquid phase ( $\sigma_1 = 10 \text{ mS}/\text{cm}$ ,  $\epsilon_1 = 80$ ) is observed to displace into the low conductivity fluid (**Figure 4-2A, B**). The frequency is slowly increased and the high conductive fluid continues to displace across the interface into the adjacent stream. At a frequency of 7.6 MHz, however, liquid displacement rapidly ceases (**Figure 4-2C**), and the interface is visually identical to that as seen in **Figure 4-1B** when



no AC voltage is applied. The frequency is increased above 7.6 MHz and the displacement direction reverses; the high permittivity stream ( $\sigma_2 = 19 \mu\text{S/cm}$ ,  $\epsilon_2 = 110$ ) displaces into the adjacent high conductive stream (**Figure 4-3D**). Hence, a liquid interfacial COF is observed at 7.6 MHz. Below the COF, the high conductive stream displaces into the high dielectric stream. Above this, the high permittivity stream displaces into the high conductive stream.

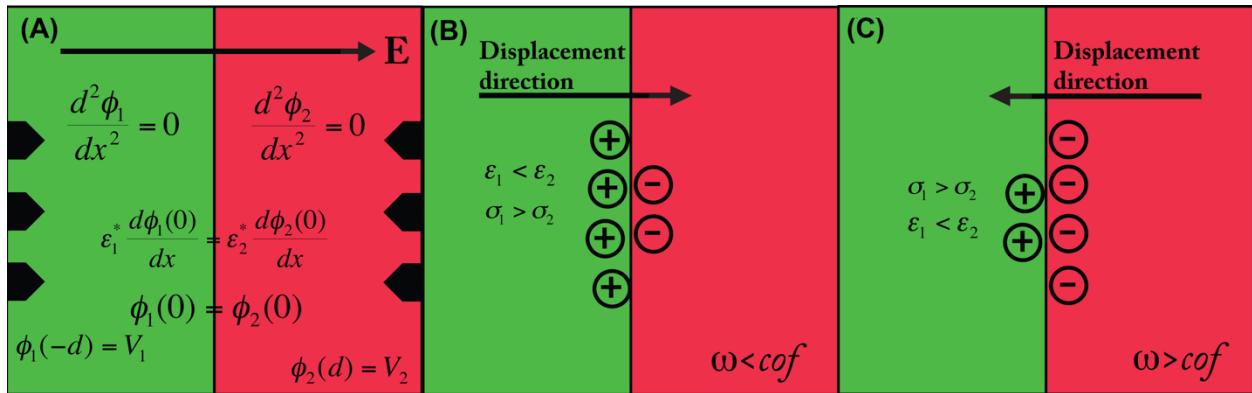


**Figure 4-3. Illustration of frequency dependent MW polarization**

(A) The interfacial crossover frequency is modeled with a 1D Laplace equation subject to MW boundary conditions at the liquid/liquid interface. (B) Interfacial polarization is driven by differences in fluid conductivity below the COF; more charge accumulates on the left side of the interface and resulting displacement of high conductivity fluid (green). (C) At high frequency above the COF when conductive charging does not have time to occur, the high dielectric liquid (red) polarizes to a greater extent and the displacement direction reverses.

Cross-sectional views of the polarized interface taken by confocal microscopy illustrate how the observed field-induced liquid displacement satisfies conservation of mass. As the field-inducing electrodes exist solely on the bottom channel wall, symmetry is broken, and field-induced fluid displacement is largely driven by the interfacial Maxwell stress at the bottom channel surface where the electric field is largest. At low AC frequency (4 MHz), below the liquid COF, the high conductivity stream (green) displaces across the channel into the high dielectric stream. To accommodate for this volume

exchange, the high dielectric fluid (red) near the top channel wall displaces in the opposite direction (**Figure 4-2A, B**). Here, a solid black line indicates the original interfacial position when no field is applied. The interfacial COF is observed at 7.6 MHz (**Figure 4-2C**), and the interface appears virtually identical in nature to when no electric field is applied (**Figure 4-2B**); no fluid displacement across the channel height is observed. Above the crossover frequency, the direction of liquid displacement reverses. At high frequency (25 MHz) the high dielectric stream (red) displaces to into the high conductivity stream. Again, mass conservation is satisfied, as high conductivity fluid at the top wall displaces to the right (**Figure 4-2D**). Hence, the interface appears to “tilt” left or right, depending upon the AC frequency applied.

It is important to note that when a series of control experiments are conducted, where each stream had identical electrical properties, no fluid motion is observed over the entire range of applied frequency or voltage (200 kHz – 25 MHz, 1 – 10 V<sub>pp</sub>). Second, no liquid COF is observed when one single stream has both a larger conductivity and dielectric constant; the high conductive/dielectric stream displaces in a single direction for all frequencies applied. Fluid systems having only differences in one electrical property – either conductivity or permittivity – produced only fluid displacement in a single direction; no COF was observed. Finally, liquid displacement is extremely sensitive to differences liquid conductivity and dielectric constant between adjacent streams. A 0.05% difference in either parameter between each stream is all that is required to optically observe fluid motion with the confocal microscopy system used in this work.

Interfacial COF measurements were repeated over a large range of electrical conductivities of the high conductivity fluid stream (0.0029 – 0.61 mS/cm), while keeping

all other electrical properties constant. An increase in COF is observed as the conductivity of the high conductivity phase is increased, shown by the data set plotted in **Figure 4-4**. At low frequency, below the inverse charge relaxation time, the high conductive stream conducts ionic charge to the interface at a rate faster than can be removed by the adjacent low conductive liquid. As such, the high conductive fluid dominates the polarization of the interface (**Figure 4-3B**). At high frequency, when ionic charging does not have enough time to occur, the high dielectric liquid governs the interfacial charging (**Figure 4-3C**). Therefore, the net sign of the induced interfacial charge between the two liquids reverses depending upon the AC frequency applied, since neither liquid has both greater conductivity and dielectric constant. As charge reversal can occur, there exists an intermediate frequency where conductive charging is equally balanced by dielectric charging, and the interface has a zero net charge. The observed increase in COF with increasing differences in electrical conductivity is consistent with this argument. Physically, as the difference in electrical conductivity between each fluid stream increases, the total amount of induced interfacial ionic charge increases, and a larger field frequency is required to relax the charge away. Hence, a larger crossover frequency is observed as the relative difference in electrical conductivity,  $[\sigma_1 - \sigma_2]$ , is increased. The interfacial liquid COF is quantitatively modeled and predicted below.

As the embedded electrodes are on the bottom channel surface, fluid displacement is largely driven by polarization dynamics in the local vicinity of the electrodes where the electric field ( $E$ ) is largest, as seen in **Figure 4-2B** and **Figure 4-2D**. A charge neutrality condition at the liquid interface at the bottom channel surface will produce an observed COF across the entire electrical interface, as seen in **Figure 4-2C**. The liquid interfacial

COF is formulated for values of the electric field very near the substrate surface where it is assumed symmetric in the y-direction (normal to the channel surface) (**Figure 4-2**). Assuming each fluid is electro-neutral, the electric potential in each phase very near the channel surface is well described by the one-dimensional Laplace equation in  $x$ ,  $\frac{d^2 \Phi_i}{dx^2}$ , where  $\Phi_i$  is the applied potential in the  $i^{\text{th}}$  liquid stream, 1 (green) and 2 (red), and  $x$  points in the direction normal to the electric interface (**Figure 4-2, 3A**). We apply the usual MW boundary conditions at the electrical interface between the two liquid streams. First, as illustrated in **Figure 4-3A**, we require the electric potential across the electrical interface ( $x=0$ ) be continuous,  $\Phi_1(0) = \Phi_2(0)$ . Second, accounting for both ohmic current (conductive polarization) and displacement current (dielectric polarization) across the interface, we require continuity in displacement current:

$$\varepsilon_1^* \frac{d^2 \Phi_1}{dx^2} - \varepsilon_2^* \frac{d^2 \Phi_2}{dx^2} = 0, \quad (4.1)$$

where  $\varepsilon_i^* = \varepsilon_i - \frac{i\sigma_i}{\omega}$  is the complex permittivity in each liquid phase. Hence, the fluid interface is subject to a net charge accumulation due to a discontinuous jump in conductivity and dielectric constant in order to satisfy the conservation of both ionic and dielectric charge. Using the above conditions, combined with boundary conditions for the applied potential,  $\Phi_1(-d) = V_1$  and  $\Phi_2(d) = V_2$ , where  $V_1$  and  $V_2$  are the applied potential at each electrode ( $x = \pm d$ ), the Laplace equation in both liquid domains is solved. The interfacial COF occurs at an AC frequency where conductive charging completely balances dielectric polarization, and the net charge across the interface is zero. This condition occurs when the normal electric field ( $E_n = \frac{d\Phi_i}{dx}$ ) is continuous across the

liquid/liquid interface,  $\frac{d\Phi_1}{dx} - \frac{d\Phi_2}{dx} = f = 0$ . Based on the two-domain solution to the 1D Laplace equation, this liquid interfacial COF occurs when

$$f(\omega) = \frac{\varepsilon_1^* - \varepsilon_2^*}{\varepsilon_1^* + \varepsilon_2^*} = 0. \quad (4.2)$$

It is important to note that  $f(\omega)$  is a complex function, and has both real (in-phase with the applied field) and imaginary (out of phase) parts. In this chapter, we apply the electric field as a single sinusoid, so there is no phase gradient, and charging is driven by the in-phase component (real part) of the electric field<sup>109</sup>. Hence, the predicted crossover frequency ( $\omega_{COF}$ ) where induced interfacial charge vanishes is determined by  $Re[f(\omega)]$ , or in functional form

$$\omega_{COF} = \frac{1}{2\pi} \left[ \frac{(\sigma_1 - \sigma_2)(\sigma_1 + \sigma_2)}{(\varepsilon_2 - \varepsilon_1)(\varepsilon_1 + \varepsilon_2)} \right]^{1/2}. \quad (4.3)$$

The predicted crossover,  $Re[f(\omega)] = 0$ , is plotted in **Figure 4-4** as a function of the electrical conductivity difference between stream 1 and 2,  $[\sigma_1 - \sigma_2]$ , holding all other electrical properties constant.

As shown in **Figure 4-4**, the experimental liquid COF data agree well with the theoretical model. These results strongly suggest that frequency dependent displacement at a polarized aqueous liquid interface is driven by the interaction between the electric field and field induced interfacial charge induced through MW polarization. This interaction produces a net Maxwell stress at the electrical interface, and displaces fluid into the adjacent stream. The direction of this displacement is dependent on the sign of the induced charge; displacement reverses above the COF where the interface

undergoes conductive relaxation and charging becomes dictated by differences in dielectric constant at the interface.

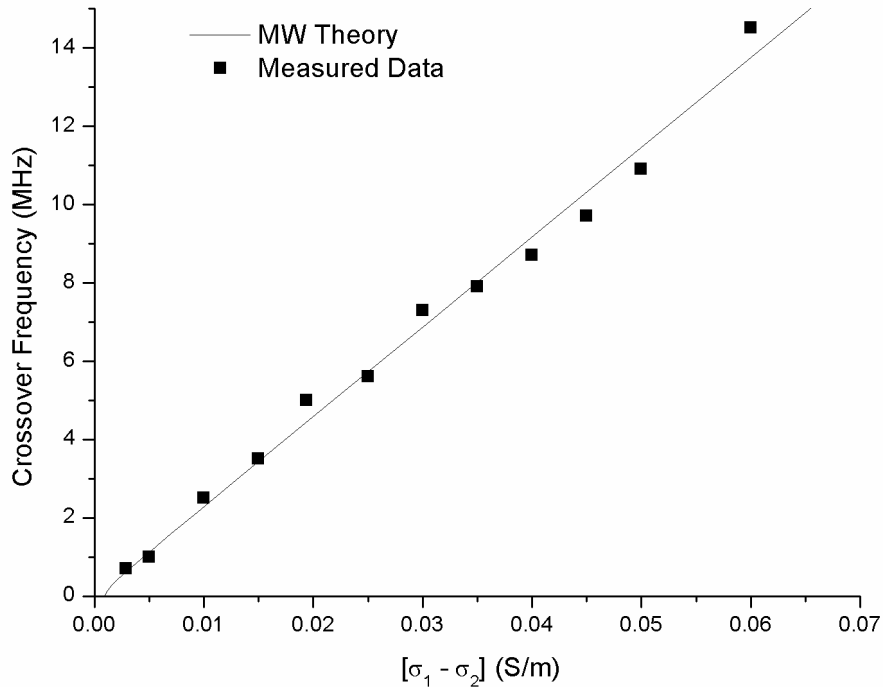


**Figure 4-4. Maxwell-Wagner theory of polarizable liquid interfaces**

Comparison between experimental (symbols) and analytical (line) interfacial COF as a function of the difference in electrical conductivity between each fluid stream,  $[\sigma_1 - \sigma_2]$ . Error bars are of the order of the size of symbols.

#### 4.4 Conclusion

We demonstrate that a microfluidic-generated electrical interface formed between two liquids of disparaging electrical properties undergoes interfacial polarization and frequency dependent liquid displacement when exposed to a perpendicular AC electric field. The crossover frequency where no displacement is observed is well described by the Maxwell-Wagner polarization model, and has been experimentally shown to increase when the conductivity difference between the two liquid streams is increased. A liquid stream with greater electrical conductivity and lower permittivity than the adjacent stream

is observed to displace across the interface into the lower conductivity phase at frequencies below the interfacial crossover frequency. At high frequencies, above this value, the direction of fluid displacement reverses; the high permittivity fluid displaces into the adjacent low permittivity stream. The interfacial crossover frequency, dependent on the differences between fluid electrical properties between each stream, is observed at an intermediate frequency where no liquid motion is observed and the interface appears identical to when no electric field is applied. These results are similar in nature to the classic crossover frequency behavior observed in dielectrophoresis (DEP), where polarized particles migrate towards high (positive DEP) or low electric field regions (negative DEP) depending upon the AC frequency applied<sup>109</sup>. Understanding and exploiting the physics of AC polarization at liquid electrical interfaces could give rise to new ways of precisely manipulating, electrically characterizing and performing fluid biosensing at the nano and picoliter scale, much the same way that DEP is currently utilized to concentrate particles and cells<sup>123</sup>, and crossover frequency measurements are exploited in biosensing applications<sup>115,124</sup>. Additionally, this work offers a new method to more precisely study interfacial polarization, as unlike the solid/liquid interface, the electrical properties in each liquid stream can be readily and independently controlled.

All data presented in this chapter was published in *Physical Review Letters*, (2012) DOI: <https://doi.org/10.1103/PhysRevLett.109.187602> and is reproduced with permission from the American Physical Society in support of a doctoral thesis.

# 5 *Fluidic Dielectrophoresis*

---

## **5.1 Introduction**

Development of techniques that can transport and manipulate liquid at nanoliter length scales is an important area of microfluidic research<sup>37</sup>. Small scale liquid routing<sup>125</sup>, mixing<sup>126</sup> and pumping<sup>127,128</sup>, in particular, are essential components in many lab-on-a-chip microfluidic applications including immunoassays<sup>129</sup>, capillary electrophoresis<sup>130</sup>, droplet-based flow assays<sup>131</sup>, cellular analysis<sup>132</sup> and automated sample processing<sup>133</sup>.

While many different liquid transport strategies have been developed, a popular method for microfluidic liquid actuation involves the use of electrokinetic phenomena<sup>134</sup>. Electrokinetics is a field of study within electrohydrodynamics (EHD) that describes the coupling between interfacial charge and electric fields to produce electrical body forces that drive fluid motion<sup>135</sup>, suspending particles<sup>136</sup>, cells<sup>137</sup> and droplets<sup>138</sup>. Owing to the ease at which metal electrodes can be fabricated and integrated into microfluidic channels<sup>123</sup>, direct current (DC) and alternating current (AC) electric fields have been widely utilized to manipulate particle and fluid contents of microfluidic systems. In terms of the electrokinetic phenomena, the major electrical forces acting on particles in an electrolyte solution are electrophoresis (EP) and dielectrophoresis (DEP). Electrophoresis arises from the coupling of the electric field with the fixed surface charge on the particle surface, while DEP occurs when the electric field induces surface charge at the particle/liquid interface and only results in a net particle motion when the electrical field is non-uniform. For liquids, EHD motion is known to occur where spatial gradients in



the electric properties are present. Electrical gradients are a common occurrence in lab-on-a-chip applications. Examples include isoelectric focusing<sup>139</sup>, amplified field sample stacking<sup>140</sup>, thermally induced gradients<sup>141</sup>, and mixing of co-flowing laminar streams<sup>142</sup>. Different types of electrokinetic flow resulting from these processes include electrothermal<sup>143</sup>, dc electroosmosis<sup>144</sup>, and AC electroosmotic flow<sup>111,145</sup>. Due to the prevalence of electrical gradients in microfluidic systems, work has been done to understand the physics, fluid dynamics, and stability of liquid interfaces during exposure to electric fields.

In terms of microfluidics, the lack of inertial influence on microscale fluid flow permits miscible fluids to flow side-by-side without convectively mixing. Hence, microfluidic systems offer the unique ability to produce interfaces between miscible liquids. These liquid interfaces are a natural consequence of laminar flow, where the mixing between streams occurs only through diffusion. Previous work has utilized microfluidic laminar flow to produce miscible liquid interfaces for use in protein fractionation<sup>146-148</sup>, immunoassay analysis<sup>149</sup>, membraneless microfluidic fuel cells<sup>150</sup>, measuring diffusion coefficients<sup>151</sup> and for continuous particle filtration<sup>152</sup>.

In this chapter, we explore the interactions of AC electric fields with electrical liquid interfaces formed between two miscible aqueous liquids. Shown in **Figure 5-1A**, the experiment consists of two co-flowing liquids that differ in electrical conductivity ( $\sigma$ ) and permittivity ( $\epsilon$ ). These two streams are forced to flow with a constant pressure source using a microfluidic T-channel with integrated electrodes, and a sharp electrical interface is formed between them, as shown in the confocal image of the flow cell in **Figure 5-1B**. When an AC field is delivered across the two co-flowing streams the electrical liquid

interface polarizes, which produces an electrical stress, and forces the fluid interface to displace in a direction dependent on the applied AC frequency (**Figure 5-1C**). Previously, we demonstrated the ability to electrically polarize and direct the deflection of these two co-flowing microfluidic liquid streams using AC electric fields<sup>153</sup>. In this chapter, we develop a more complete frequency dependent Maxwell-Wagner polarization model of the electrical liquid interface, and quantify the field-induced interfacial displacement. We discuss the differences between high and low frequency polarization behavior in terms of the fluid electrical conductivity and permittivity, and demonstrate the ability to controllably deflect co-flowing electrolytes using AC electric fields, which we define here as fluidic dielectrophoresis (fDEP).

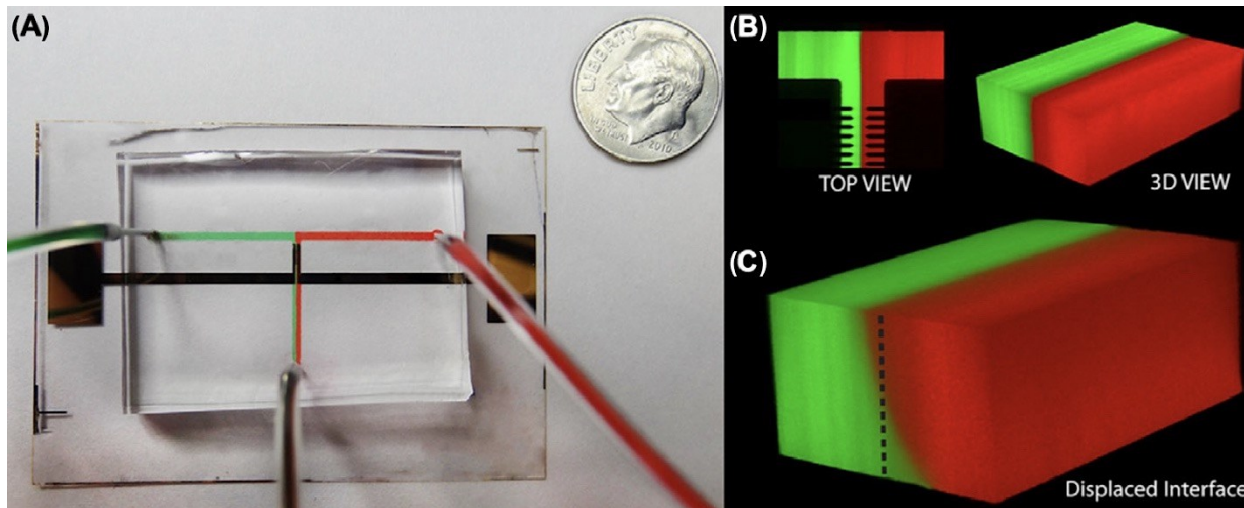


**Figure 5-1. Microfluidic device with embedded electrodes**

(A) A microfluidic T-channel with integrated electrodes. Two streams with different electrical properties flow side-by-side to create an electrical interface. The left-most stream (green) has a greater conductivity. The right stream (red) has a greater permittivity. (B) Top view of a L/L interface between an array of microelectrodes created using a microfluidic “T-channel.” 3D View. Confocal microscopy reveals a sharp ( $<2 \mu\text{m}$ ) boundary between two coflowing red and green fluorescently labeled streams. (C) The L/L interface polarizes and electrokinetically displaces when exposed to an AC electric field.

The first part of this chapter is an analysis of the polarization process occurring at

the liquid interface. The charge conservation equations are scaled and utilized to derive the relevant electrokinetic boundary conditions for our fluid system, and equations that describe the frequency dependent surface charge density and fluidic DEP force are formulated. Liquid deflection experiments are then presented.

## 5.2 Theoretical formulation

### 5.2.1 Governing equations

First, we develop a theoretical formulation to analyze fDEP at electrical liquid interfaces. We start with the general charge conservation equations for a dilute, two-species electrolyte solution:

$$\frac{\partial C_1}{\partial t} + u \cdot \nabla C_1 = \mu_1 \nabla \cdot (z_1 F C_1 \nabla \Phi) + D_1 \nabla^2 C_1, \quad (5.1)$$

$$\frac{\partial C_2}{\partial t} + u \cdot \nabla C_2 = \mu_2 \nabla \cdot (z_2 F C_2 \nabla \Phi) + D_2 \nabla^2 C_2, \quad (5.2)$$

where  $C_i$ 's are the molar concentration of each electrolyte ion species,  $\mu_i$ 's are the coefficients of ion mobility,  $F$  is the Faraday constant,  $D_i$ 's are the diffusive coefficients,  $z_i$ 's are ion valence numbers, and  $\Phi$  is the electric potential. For this problem, it is useful to redefine the system of molar concentrations ( $C_1, C_2$ ) in terms of charge density ( $\rho_E$ ) and electrical conductivity ( $\sigma$ ),

$$\rho_E = \sum_{i=1}^2 z_i F C_i, \quad (5.3)$$

$$\sigma = \sum_i \mu_i z_i^2 F^2 C_i \quad (5.4)$$

We assume the electrolyte is 1:1 symmetric (such as KCl) and the electrolyte properties

are symmetric such that  $\mu_1 = \mu_2 = \mu, D_1 = D_2 = D$  and  $z_1 = -z_2 = 1$ . Subtracting *Equations (5.1)* from *(5.2)*, and utilizing *Equations (5.3)* and *(5.4)*, we can rewrite the conservation equations in terms of  $\rho_E$  and  $\sigma$ , as

$$\frac{\partial \rho_E}{\partial t} + u \cdot \nabla \rho_E = \nabla \cdot (\sigma \nabla \Phi) + D \nabla^2 \rho_E. \quad (5.5)$$

### 5.2.2 Scaling and simplifications

We introduce the following characteristic scales for the nondimensionalization of the charge conservation equation:

$$[u] \sim U_{EV}, \quad [L] \sim L, \quad [t] \sim \varepsilon \sigma, \quad [\rho_E] \sim \varepsilon E_0 / L, \quad [\Phi] \sim E_0 L, \quad [\sigma] \sim \mu z F \rho_E \sim \mu z F \varepsilon E_0.$$

Here,  $U_{EV}$  is the electroviscous velocity scale,  $L$  is the half-width of the electrode separation and  $E_0$  is the magnitude of the applied electric field. The timescale,  $[t] \sim \varepsilon / \sigma$  represents the charge relaxation time of the media. With the Debye length,  $\lambda = \sqrt{\varepsilon D / \sigma}$ , our conservation equation in dimensionless form becomes

$$\frac{\partial \rho_E}{\partial t} + Re_e u \cdot \nabla \rho_E = \nabla \cdot (\sigma \nabla \Phi) + \left(\frac{\lambda}{L}\right)^2 D \nabla^2 \rho_E, \quad (5.6)$$

where

$$Re_e \equiv \frac{\varepsilon D}{\sigma L^2} \sim 10^{-10}, \quad (5.7)$$

is the electric Reynolds number, which is used to denote the ratio of convective current to conduction current. Since this number is much less than unity, we can neglect the electroconvection term, and the electrical equations are decoupled from the fluid momentum equations. The dimensionless number is defined as

$$\tau \equiv \frac{\varepsilon D}{\sigma L^2} = \left(\frac{\lambda}{L}\right)^2 \sim 10^{-6}, \quad (5.8)$$

which is the ratio of the charge relaxation timescale ( $\varepsilon/\sigma$ ) to the diffusive timescale ( $L^2/D$ ). The Debye length is the order of several nanometers, which is much smaller than the length scale of the system, and, charge relaxation, or electric drift, occurs over a much faster timescale than diffusion. *Equation (5.6)* can be simplified; the transient term and the divergence term are the dominant charge transport terms for this system, and the charge conservation equation reduces to

$$\frac{\partial \rho_E}{\partial t} - \nabla \cdot (\sigma \nabla \Phi) = 0, \quad (5.9)$$

At the micrometer length scale,  $L$ , Gauss' Law ( $\nabla \cdot (\varepsilon E) = \rho_E$ ) suggests that electrolytes are electrically neutral. The relative difference in ion number densities can be approximated by the ratio

$$\beta = \frac{n_+ - n_-}{n_o} = \frac{\nabla \cdot (\varepsilon E)}{en_o} \sim \frac{\varepsilon E_o}{en_o L} \quad (5.10)$$

where  $n_+$  and  $n_-$  are the number densities of positive and negative ions, and  $n_o$  is the unperturbed ion number density ( $n_o = n_+ + n_-$ ). For typical systems, values of  $E_o \sim 10^5$   $\text{Vm}^{-1}$ ,  $n_o \sim 10^{23} \text{m}^{-3}$ , and  $L \sim 100 \mu\text{m}$ ,  $\beta \sim 4 \cdot 10^{-5}$  and the bulk liquid can be considered quasi-electroneutral and the solution of the electric field ( $E = -\nabla \Phi$ ) can be obtained from Laplace's equation,

$$\nabla^2 \Phi = 0. \quad (5.11)$$

### 5.2.3 Boundary Conditions

The bulk electrolyte solution is quasi-electroneutral, however, free and bound charges are induced at the interface between the two liquids and charge conservation principles must be imposed at this boundary. First, we require that the electric potential be continuous across the liquid interface,

$$\Phi_1 - \Phi_2 = 0. \quad (5.12)$$

Interfacial charge accumulation is due to non-uniform distribution and time-dependent accumulation of free charge and perturbed bound charge at the liquid interface. To satisfy charge conservation we apply *Equation (5.9)* between the two electrolyte liquids. Free and bound charges exist only at the interfacial surface, and thus the volume charge density  $\rho_E$  is replaced with a surface charge density,  $\sigma_f$  and *Equation (5.9)* becomes

$$J_2 - J_1 + \frac{\partial \sigma_f}{\partial t} = 0, \quad (5.13)$$

where  $J_1$  and  $J_2$  are the ohmic currents,  $J = \sigma \nabla \Phi$ , for each fluid phase 1 and 2. The bound electric surface charge represents field-driven induced displacement of free unpaired surface charge due to dielectric polarization. The displacement current due to this free surface charge is defined by

$$\varepsilon_1 E_1 - \varepsilon_2 E_2 = \sigma_f. \quad (5.14)$$

In a harmonic field with  $\partial/\partial t = j\omega$ , combining *Equations (5.13)* and *(5.14)* we arrive at the following charge conservation equation at the electrical liquid interface:

$$\left[ \varepsilon_1 - \frac{i\sigma_1}{\omega} \right] E_1 = \left[ \varepsilon_2 - \frac{i\sigma_2}{\omega} \right] E_2, \quad (5.15)$$

where  $\varepsilon_i - j\sigma_i/\omega = \varepsilon_i^*$  is the complex permittivity,  $\varepsilon_i^*$ , of the electrolyte and  $i$  is the imaginary number,  $i = \sqrt{-1}$ .

As we can see from *Equation (5.15)*, at low frequency ( $\omega \rightarrow 0$ ), polarization is driven by electrical conductivity. However, as electrical conduction involves the macroscopic movement of charge carriers (typically ions), there is a finite velocity at which ions can be conducted across the material. Therefore, at high frequency ( $\omega \rightarrow \infty$ ) when ion conduction does not have time to occur, the polarization of the material is driven by electrical permittivity. Hence, the complex permittivity models the polarizable material as the electric equivalent to a resistor in parallel with a capacitor in order to capture both the low frequency conductive and high frequency dielectric charging mechanisms occurring within each liquid domain. In comparing this theory with experimental data, it is also very important to note that  $\omega = 2\pi f$ , the angular frequency of the AC electric field, where  $f$  is the ordinary frequency given in Hz, is the usual unit used by a function generator to produce sinusoidal electric fields.

#### **5.2.4 Interfacial Surface Charge**

Using the developed electrokinetic boundary conditions, we will now derive a general expression describing how induced interfacial surface charge is related to the frequency and magnitude of the applied electric field, and the liquid electrical properties. The total surface charge,  $\sigma_t$ , at the liquid interface is comprised of free (conduction) surface charge,  $\sigma_f$ , and bound (polarization) surface charge,  $\sigma_p$ , driven by dielectric polarization, such that  $\sigma_t = \sigma_f + \sigma_p$ . The free surface charge is determined by applying

Gauss' Law (*Equation (5.14)*) across the interface. The bound polarization surface charge is related to the divergence in the polarization vector,  $P$ , defined as

$$\sigma_p = -\nabla \cdot P = -(P_1 - P_2). \quad (5.16)$$

Polarization in a linear homogenous isotropic dielectric depends linearly on the electric field as

$$P = \varepsilon_0 \chi E, \quad (5.17)$$

where  $\chi$  is the electric susceptibility of the material in terms of its relative ( $\varepsilon_r$ ) dielectric constant,  $\chi = (\varepsilon_r - 1)$ . Combining *Equations (5.14)* and *(5.16)*, the total induced interfacial surface charge becomes

$$\sigma_t = \varepsilon_0 (E_1 - E_2). \quad (5.18)$$

This expression is useful for evaluating surface charge density at interfaces undergoing Maxwell-Wagner polarization. It is useful to note that induced surface charge at a polarizable interface exists only when the electric field is discontinuous across the interface. This is consistent with the charge conservation boundary condition defined in *Equation (5.15)*. The electric potential is continuous across the interface, but interfacial polarization results in the slope of the potential (electric field) to become discontinuous at the interface. Physically, surface charge is induced as a consequence of the normal component of the electric field being discontinuous, and a net interfacial surface charge density accumulates such that the current density remains continuous across the interface.



### 5.2.5 One dimensional model

In this section we develop an analytical expression for the interfacial surface charge density and the Maxwell pressure (electric force per unit area) at the liquid interface. The physical system consists of two co-flowing liquid streams, confined to numbered domains 1 and 2, and each with a different set of electrical conductivity ( $\sigma_1$  and  $\sigma_2$ ) and dielectric constant ( $\varepsilon_1$  and  $\varepsilon_2$ ), as shown in **Figure 5-2A**. As the two streams do not convectively mix, a sharp electrical mismatch is created at the contacting interface. The interface is subjected to an external field upon entering the electrode array at  $z = 0$ , and concludes when the fluid exits the array at  $z = L_e$ . We begin first by calculating the electric field distribution at the microchannel cross-section in the x-y plane (**Figure 5-2B**), and derive an expression describing the frequency dependent surface charge density at the interface. Since the electric field decays exponentially, the greatest magnitude of interfacial electric stress will occur at the channel surface,  $y=0$ . While it is possible to analytically calculate the two-dimensional electric field distribution using a conformal map, we will reserve this approach for future work in developing a more complete EHD model. Here, we calculate the electric field distribution at the channel surface ( $y=0$ ) and use this result to determine the induced surface charge at the interface.

Employing exponential time dependence  $e^{i\omega t}$  for the electric field, the instantaneous applied field at time  $t$  and location  $x$  on the channel surface is given by

$$E(x, y) = \text{Re}[E(x, y = 0)e^{i\omega t}],$$

where  $i^2 = -1$  and  $\text{Re}[\dots]$  is the real part of the complex electric field phasor  $E = E\cos\omega t + jE\sin\omega t$ . As we have shown in *Equation (5.10)*, at the microscale the electrolyte

can be regarded as quasi-electroneutral and the electric potential satisfies Laplace's equation, given by *Equation (5.11)*. In one-dimension, neglecting variations in the potential over the y-direction, we have to solve  $\frac{d^2 \Phi_i}{dx^2} = 0$  for each fluid stream.

We integrate this expression twice, employ the boundary conditions given in *Equations (5.12)* and *(5.15)*, and specify the potential at the electrodes as  $\Phi(-L) = V_1$  and  $\Phi(L) = V_2$ . The following field solutions result for each fluid domain, 1 and 2:

$$\frac{d^2 \Phi_1}{dx^2} = \frac{\varepsilon_2^*}{\varepsilon_2^* + \varepsilon_1^*} E_o, \quad (5.19)$$

and

$$\frac{d^2 \Phi_2}{dx^2} = \frac{\varepsilon_1^*}{\varepsilon_2^* + \varepsilon_1^*} E_o, \quad (5.20)$$

where  $E_o$  is the applied electric field magnitude,  $[V_2 - V_1]/2L$ . The total surface charge at the liquid interface can now be calculated using *Equation (5.18)*,

$$\sigma_t = \varepsilon_o \left( \frac{d\Phi_1}{dx} - \frac{d\Phi_2}{dx} \right) = \varepsilon_o \left( \frac{\varepsilon_2^* - \varepsilon_1^*}{\varepsilon_2^* + \varepsilon_1^*} \right) E_o. \quad (5.21)$$

Taking the time-average over the period of the monochromatic field ( $t = 2\pi/\omega$ ), the time-averaged surface charge density at the liquid interface is given by

$$\langle \sigma_t \rangle = \frac{1}{2} \text{Re} \left( \frac{\varepsilon_2^* - \varepsilon_1^*}{\varepsilon_2^* + \varepsilon_1^*} \right) \varepsilon_o E_o. \quad (5.22)$$

And the time averaged force per unit area at the interface at  $y = 0$  is

$$\langle F \rangle_{fDEP} = \langle \sigma_t E \rangle = \frac{1}{2} \text{Re} \left( \frac{\varepsilon_2^* - \varepsilon_1^*}{\varepsilon_2^* + \varepsilon_1^*} \right) \varepsilon_o E_o^2. \quad (5.23)$$

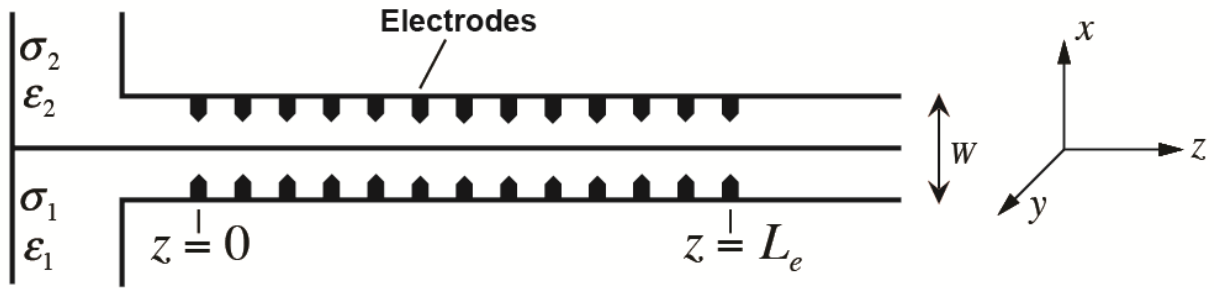
Here, we can observe that the induced surface, and therefore the induced electric interfacial force, is zero when

$$K_I(\omega) = Re \left( \frac{\varepsilon_2^* - \varepsilon_1^*}{\varepsilon_2^* + \varepsilon_1^*} \right) = 0, \quad (5.24)$$

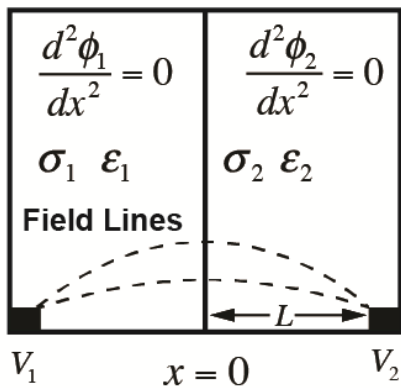
where  $K_I(\omega)$  represents the polarizability of the liquid interface. This expression is frequency dependent. There exists a critical frequency where the induced surface charge at the interface is zero, and the liquid experiences no electrical force. In terms of dielectrophoresis, this frequency is often referred to as the crossover frequency ( $\omega_{COF}$ ), and in terms of fluidic dielectrophoresis, the fDEP crossover can be expressed as:

$$\omega_{COF} = \frac{1}{2\pi} \left[ \frac{(\sigma_1 - \sigma_2)(\sigma_1 + \sigma_2)}{(\varepsilon_2 - \varepsilon_1)(\varepsilon_2 + \varepsilon_1)} \right]^{1/2}. \quad (5.25)$$

### (A) Top View



### (B) Side View



### (C) Displacement $\{-1, 1\}$

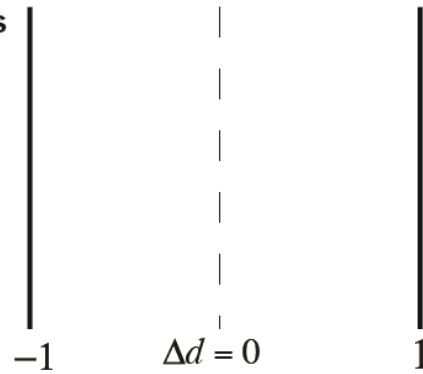


### Figure 5-2. Schematic of the T-channel used to create a liquid interface

(A) A top view of the device. Two liquid streams flow into the T-channel. They are exposed to an electric field at the electrode array ( $z = 0$ ). The field is removed when the interface exits the array at  $z = L_e$ . (B) Side view of the liquid interface. Electrodes on the channel surface produce an electric field, which polarizes the interface. The fluid is assumed electroneutral and the potential is solved at the channel surface using Laplace's equation. (C) The interfacial displacement is quantified over the channel width, which is normalized to the domain  $\{-1, 1\}$ .

## 5.3 Materials and Methods

In this section, we describe the methods used to fabricate our microfluidic devices, the electrolyte chemistry, and the confocal microscopy imaging utilized to observe electrical liquid interfaces.

Each fluid stream was introduced into the device via pressure driven flow from an

externally pressurized cryogenic vial. The resulting flow field is illustrated in **Figure 5-1A** using a microfluidic T-channel with a wider (300  $\mu\text{m}$ ) flow channel. Fluorescent dye was added to each fluid phase in order to image the electric interface under confocal microscopy (**Figure 5-1B, C**). The left-most (green) high conductivity stream consisted of PBS labeled with 10 ng/mL of Alexa Fluor 488 (Invitrogen). The right-most high dielectric stream consisted of 0.8 M 6-aminohexanoic acid (AHA) (Sigma-Aldrich) labeled with 10 ng/mL of Alexa Fluor 594 (Invitrogen). AHA is a water-soluble zwitterion used for increasing the dielectric constant of aqueous solution. The electrical conductivity and dielectric constant of each respective fluid was adjusted by dilution with DI water and used to control the relative electrical differences at the liquid interface.

In terms of experiments, PBS was diluted to three different electrical conductivities: 0.012, 0.037 and 0.060 S/m. Each sample was then driven adjacent to a low dielectric AHA solution with a conductivity of 0.002 S/m. This produced three systems with different interfacial conductivities: 0.01, 0.035 and 0.058 S/m, respectively. In order to control the fluid dielectric constant, the AHA stream was diluted with DI water, while keeping the electrical properties of the adjacent PBS stream constant. The dielectric constant for 0.8M AHA was found in previous work to be 110. AHA was diluted with DI water in order to controllably vary this initial dielectric constant. For example, 750 L of DI water was added to 250 L of AHA. This dilution yielded a dielectric constant of 87.5, leading to permittivity difference across the interface of 7.5. Two other dilutions were created, a 1:1 and 1:3 parts of DI to AHA yielding solution dielectric constants of 95 and 102.5, and permittivity differences of 15 and 22.5, respectively. The software package (Nikon Elements) was utilized to collect confocal images of the resulting electrical interface. Using this software,

the high dielectric fluid was imaged as either a red channel for better clarity in **Figure 5-1**, or a blue channel in all other figures in this chapter. Prior to fluorescent labeling, the AHA solution was vigorously shaken for 5 min in 10 g/mL Dowex MR-3 (Sigma-Aldrich) ion exchange resin to remove trace salts and reduce solution conductivity.

To create the electrical interface two fluid streams, each with a different electrical conductivity and dielectric constant, were pressure injected into the microfluidic device at a steady controlled flow rate of 10  $\mu\text{L}/\text{min}$ . An AC potential was dropped across the electrodes using a function generator (Rigol, DG4102), and cross-sectional view of the fluid interface was imaged with dual excitation confocal microscopy (**Figure 5-1B**). The electric field frequency was varied at 10 kHz increments for a given applied voltage while observing the interfacial response via confocal microscopy. Micrographs of the 2D flow field were then used to quantify the interfacial displacement for a given frequency and applied voltage.

## **5.4 Results**

When an electric field is applied across the liquid interface, free and bound charge polarize at the electrical mismatch created between the two fluids, and create a region of diffuse charge. Similar to particle-based DEP, the electric field exerts a force on this induced interfacial charge, and the interface is observed to displace from its initial “flat” position when no field is applied to a “displaced” configuration when the field is present (**Figure 5-1C**). The direction and magnitude of this interfacial displacement ( $\Delta d$ ) is proportional to the magnitude of the induced surface charge (*Equation (5.25)*), which is dependent on the electric field strength, the field frequency, and the *relative* difference in

the electrical conductivity ( $\Delta\sigma$ ) and dielectric constant ( $\Delta\varepsilon$ ) across the fluid interface. Experiments were performed to observe and quantify  $\Delta d$  for a given set of liquid electrical properties, and applied electric field strength and frequency.

The motion of the fluid interface was first imaged at varying applied electric field frequencies from both a top view, and in 2D over a channel cross section at the end of the electrode array (**Figure 5-3**). Shown from a top view, the fluid interface enters the electrode array and displaces across the microchannel. The direction of this displacement is frequency dependent. At an applied frequency of 1 MHz the high conductive fluid phase (green) is observed to displace across the flow channel into the low conductive (blue) stream (**Figure 5-3A**). For this set of liquids ( $\Delta\sigma = 0.1$  S/m and  $\Delta\varepsilon = 32$ ) the crossover frequency was found to be 9.2 MHz where no displacement is observed over the entire length of the electrode array (**Figure 5-3B**). Finally, at high frequency (20 MHz) the displacement direction reverses and the high dielectric fluid deflects into the low dielectric stream (**Figure 5-3C**).

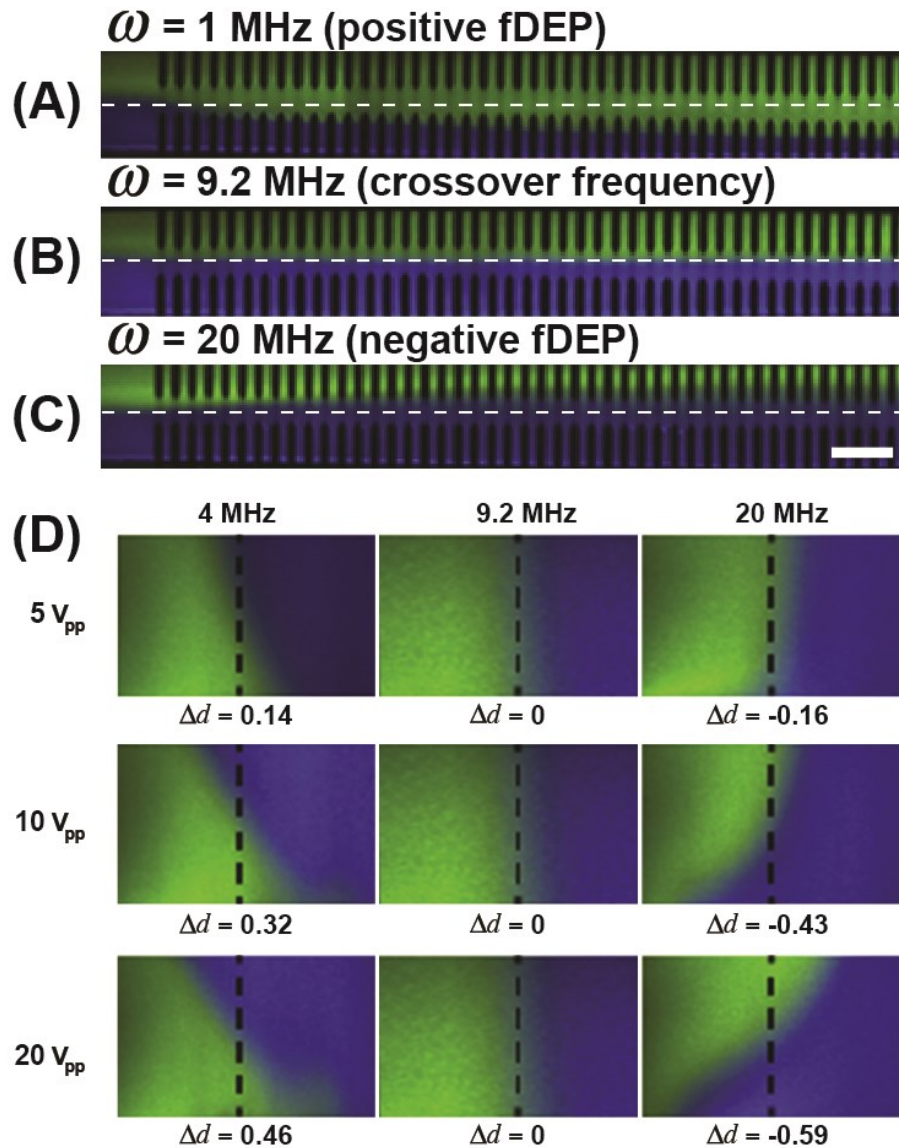


**Figure 5-3. A top and side view of fDEP**

The liquid interface enters the electrode array and displaces across the flow channel. The direction of this displacement is frequency dependent. These observations are presented from both a top and a side view. (A) At a frequency of 1 MHz the high conductive stream (green) displaces into the low conductive stream (blue). (B) The interfacial crossover frequency is observed at 9.2 MHz. No interfacial deflection is observed. (C) Above the cross-over frequency the high permittivity stream displaces into the low permittivity stream. (D) Sample displacement images taken from the experiment, shown for electric field frequencies of 4, 9.2 and 20 MHz, corresponding to the first, second, and third column. Images obtained at applied voltages of 5, 10 and 20 volts peak-to-peak are shown in the first, second, and third row. Below the interfacial crossover frequency the high conductive stream (green) displaces across the interface. Displacement is not observed at the cross-over frequency (9.2 MHz). At high frequency (20 MHz) the direction reverses, and the high dielectric stream displaces across the interface. For both low and high frequencies, the magnitude of the displacement increases with applied voltage.



#### 5.4.1 Interfacial displacement at varying AC frequency

Based on the observations shown in **Figure 5-3**, the displacement of the interface was measured at the end of the microelectrode array for varying values of the applied field frequency and voltage. As depicted in **Figure 5-2C**, the net motion of the interface was quantified over a normalized displacement domain  $\{-1,1\}$  in the direction perpendicular to the flow field, where  $\Delta d = 1$  corresponds to a net displacement across the entire channel half-width,  $L$ . Experiments were first performed to observe the frequency dependence of the liquid displacement across the  $x$ - $y$  microchannel cross section for different applied voltages. For a system with  $\Delta\sigma = 0.1$  S/m and  $\Delta\varepsilon = 32$ , the 2D flow profile over a microchannel cross section for different applied voltages and frequency was imaged using confocal microscopy, as shown in **Figure 5-3D**. Each column of 2D profile images corresponds to a different applied AC field frequency. When a frequency of 4 MHz was applied, the high conductive stream (green) was observed to deflect into the low conductive phase, and the magnitude of the displacement increased with the applied electric field strength. As we increase the frequency we observe different displacement behavior. In the center column, the frequency was increased to the interfacial crossover frequency ( $\Delta\omega = 9.2$  MHz) and no displacement was observed. It is important to note that this observation was valid for all voltages applied. We also show in the left column the interfacial displacement that occurs at  $\Delta\omega = 20$  MHz. At this frequency, the high dielectric stream (blue) deflects in the opposite direction and into the low dielectric phase. The main points to be taken concerning **Figure 5-3D** are that there is an applied crossover frequency where no displacement occurs. Above this crossover frequency the high dielectric fluid deflects into the low dielectric phase, and below this

value, the high conductive phase displaces. Shown in each row, the magnitude of these displacements increases with the applied electric fields strength. At 4 MHz the normalized displacement,  $\Delta d$ , was measured to be 0.14, 0.32 and 0.46 at 5, 10 and 20 volts peak-to-peak, respectively. At the crossover  $\Delta d = 0$  for all applied voltages. At high frequency (20 MHz)  $\Delta d$  was -0.16, -0.43 and -0.59 at 5, 10 and 20 volts, respectively.

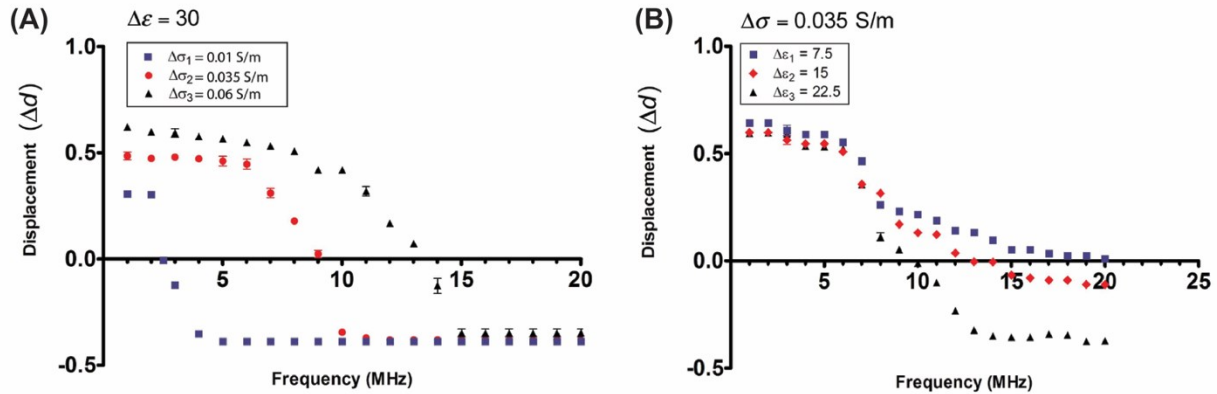


**Figure 5-4. Interfacial displacement measurements at different applied frequencies**  
**(A)** The electrical permittivity mismatch was held constant at 30. The displacement was measured over frequency for three different values of conductivity mismatch: 0.01, 0.035 and 0.06 S/m. Conductivity influences the interfacial displacement at low frequency. The displacement data at high frequency is independent of the liquid conductivity mismatch.  
**(B)** Electrical conductivity was held constant across the interface and displacement was measured for three different permittivity mismatches: 7.5, 15 and 22.5. Permittivity influences the interfacial displacement at high frequency. The displacement is independent of the permittivity at low frequency.

#### 5.4.2 Influence of electrical properties on interfacial displacement

We next quantified interfacial displacement as a function of electric field frequency. In **Figure 5-4A** we plot the experimental displacement versus applied frequency for different values of electrical conductivity mismatches ( $\Delta \sigma = 0.058, 0.035$  and  $0.01$  S/m), while keeping a constant permittivity mismatch ( $\Delta \epsilon = 30$ ) across the interface. First, we see that below the crossover frequency, the net displacement at low frequency increases with  $\Delta \sigma$ , while the high frequency measurements are independent of electrical

conductivity mismatches across the liquid interface. Second, we observe that the crossover frequency increases linearly with  $\Delta\sigma$ , as shown in **Figure 5-5B**.

The influence of liquid permittivity mismatches,  $\Delta\varepsilon$ , on displacement was also measured. In **Figure 5-4B** we plot the interface displacement as a function of frequency for permittivity differences,  $\Delta\varepsilon = 7.5, 15$  and  $22.5$ , while keeping the conductivity mismatch constant ( $\Delta\sigma = 0.035$  S/m). As we increase  $\Delta\varepsilon$  we see that the interfacial permittivity differences do not influence the displacement at low frequency, but significantly influence the high frequency measurements. Finally, the interfacial crossover frequency decreases with increasing  $\Delta\varepsilon$ , as shown in **Figure 5-5C**.

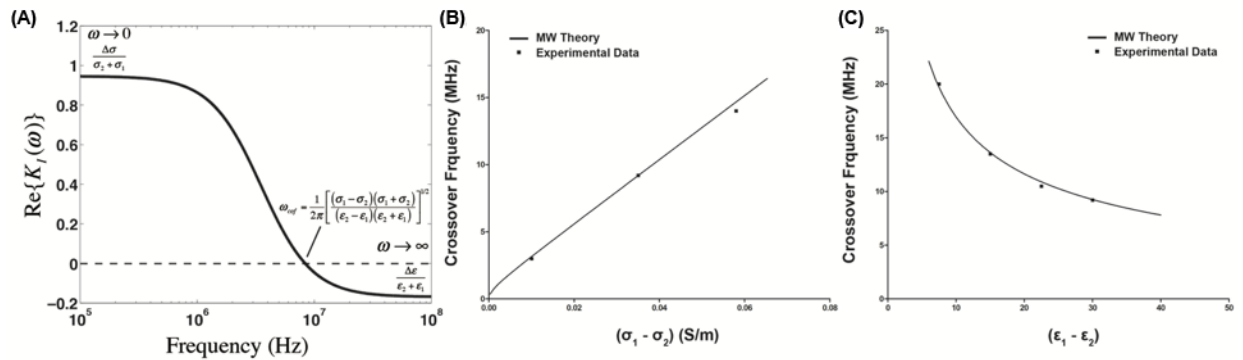


**Figure 5-5. Maxwell-Wagner theory of polarizable liquid interfaces for interfacial permittivity and conductivity**

(A) A plot of the real part of the interfacial polarization factor as a function of electric field frequency. The low frequency limit is dictated by the liquid electric conductivity differences. The cross-over frequency is frequency at which the polarization factor equals zero, and is given by *Equation (5.26)*, as shown. The high frequency limit is dependent on the differences in electrical permittivity. (B) The cross-over frequency increases linearly with differences in electrical conductivity and shows good agreement with *Equation (5.26)*. (C) The cross-over frequency decreases with increasing permittivity mismatch. The polarization theory and measured data points show good agreement.

## 5.5 Discussion

In our theoretical model, we have given our results of the induced surface charge and the polarization factor in terms of the electrical properties of the two co-flowing fluids

and the frequency of the applied field. This approach has been adopted to facilitate direct comparisons with the interfacial displacement experiments, and to develop an understanding of the liquid polarization mechanics so that a more complete EHD transport model can be developed. In this section, we turn to discuss the observed frequency and electrical characteristics of the liquid interface, particularly in terms of dielectrophoresis. The term dielectrophoresis was originally used by Herbert Pohl to describe the field-induced electrical force on a polarizable particle<sup>154</sup>. The purpose of this chapter is to demonstrate how field-induced interfacial forces also apply to aqueous electrical interfaces. The DEP force on a particle results from the formation of induced interfacial surface charge at the particle-liquid interface, which produces an induced dipole moment across the particle diameter. The interaction with this moment and an external non-uniform electric field produces a net electrical body force on the particle and drives its motion in a suspending solution<sup>155,156</sup>. The magnitude and direction of the particle DEP force is dependent on electric field frequency, and is commonly described using the well-known Clausius-Mossotti (CM) factor. This factor describes the frequency dependent polarizability of the particle interface, and for a homogenous isotropic sphere the time averaged DEP force can be shown to be:

$$K(\omega) = \frac{\varepsilon_p^* - \varepsilon_L^*}{\varepsilon_p^* + 2\varepsilon_L^*}, \quad (5.26)$$

where  $K(\omega)$  is the CM factor for a sphere, and  $\varepsilon_p^*$  and  $\varepsilon_L^*$  are the complex permittivity of the particle and electrolyte liquid, respectively. In this chapter, we can observe a similar physical effect on a liquid interface, where the observed fluid motion is proportional to the real part of the interfacial polarizability factor,  $\text{Re}[K_I(\omega)]$ , which is a complex function of

frequency, conductivity and permittivity. The real part of this factor (*Equation (5.26)*) can be expressed as:

$$K_I(\omega) = \text{Re} \left[ \frac{\varepsilon_2^* - \varepsilon_1^*}{\varepsilon_2^* + \varepsilon_1^*} \right] = \frac{(\varepsilon_2 - \varepsilon_1)\tau^2\omega^2}{(\varepsilon_2 + \varepsilon_1)(\tau^2\omega^2 + 1)} + \frac{(\sigma_2 - \sigma_1)}{(\sigma_2 + \sigma_1)(\tau^2\omega^2 + 1)}, \quad (5.27)$$

where the parameter  $\tau = (\varepsilon_2 + \varepsilon_1)/(\sigma_2 + \sigma_1)$  is the characteristic Maxwell-Wagner relaxation time associated with the induction of charge at the interface between the two liquids.

We now demonstrate that the frequency and electrical dependent displacement at a single polarizable aqueous liquid interface is directly proportional to this polarization factor for all field frequencies observed in this chapter (1 – 20 MHz). Unlike conventional dielectrophoresis where particle motion is driven by an induced particle dipole moment, for an electrical interface the electric force and the observed liquid motion results from the electric field interacting with induced surface charge at a single liquid interface. Similar to particle DEP, the sign and magnitude of this interfacial charge can be adequately captured by the surface charge polarization factor (*Equation (5.26)*). In **Figure 5-5A** we plot the real part of  $K_I(\omega)$  as a function of electric field frequency, and highlight the low and high frequency asymptote terms, and the crossover frequency. From this figure, three frequency domains become apparent. At low frequency, below the crossover, the material with greater electrical conductivity will conduct charge to the interface at a rate faster than can be removed by the adjacent lower conductivity phase. As such, low frequency interfacial polarization will be driven by material differences in electrical conductivity and be independent of dielectric constant differences. At high frequency, above the charge relaxation timescale, the electric field oscillates faster than charges can electro-migrate

to the interface. Since conductive charging does not have enough time to occur over every field half-cycle, the interfacial polarization will be driven by differences in dielectric constant. If neither material has both a greater electrical conductivity and dielectric constant, the net sign of the induced charge that results from interfacial polarization will reverse at a crossover frequency high enough to disperse conductive charging. Hence, similar to particle DEP, the surface charge density and the resulting interfacial electrical force, has a low and high frequency asymptotic value. This can be seen by taking the appropriate limits of *Equation (5.27)*: the low frequency limiting value of  $K_I(\omega)$ , ( $\omega \rightarrow 0$ ), is dependent solely on differences in the electrical conductivity between the two co-flowing fluids  $[\Delta\sigma/(\sigma_2 + \sigma_1)]$ , while the high frequency asymptote ( $\omega \rightarrow \infty$ ) depends on differences in permittivity,  $[\Delta\varepsilon/(\varepsilon_2 + \varepsilon_1)]$ . These predicted asymptotes, and their dependence on the relative differences in conductivity and dielectric constant at low and high frequency, respectively, are consistent with the experimental displacement data shown in **Figure 5-4A, B**. Here, we observed that  $\Delta d$  is independent of  $\Delta\varepsilon$  at low frequency ( $< 5$  MHz) and independent of conductivity differences  $\Delta\sigma$  at high frequency ( $> 15$  MHz). Moreover, increases in  $\Delta\sigma$  only influenced the interfacial displacement at low frequency ( $\omega \rightarrow 0$ ), while increases in  $\Delta\varepsilon$  increased displacement at only at high frequency.

The frequency dependence on surface charge reversal at the interface is also consistent with the predicted polarizability factor. In **Figure 5-5B** we plot the experimentally measured crossover frequency for each displacement curve as a function of conductivity difference  $\Delta\sigma$ , and compare these experimental measurements to that predicted by the crossover frequency expression in *Equation (5.27)*. We see that the

crossover frequency increases linearly with  $\Delta\sigma$ , and is well predicted by the polarization theory. Similarly, we plot the crossover as a function of dielectric constant difference  $\Delta\varepsilon$  as shown in **Figure 5-5C** and compare this to predicted values. Again, the measured crossover frequency evolution with varying differences in dielectric constant agrees well with theoretical prediction given by *Equation (5.27)*.

Based on the above analysis, we now examine the scaling behavior of the displacement data given in **Figure 5-4A, B**, using our interfacial polarization model. In **Figure 5-4** we plot our displacement datasets as a function of frequency for various values of interfacial  $\Delta\sigma$  and  $\Delta\varepsilon$ . The curves in **Figure 5-5A** and **Figure 5-5B, C** show the general trend that for larger  $\Delta\sigma$  and  $\Delta\varepsilon$ , the maximum displacement of the interface increases at high and low frequency, while the crossover frequency is linearly and inversely proportional to  $\Delta\sigma$  and  $\Delta\varepsilon$ , respectively. Since the electric force is proportional to the magnitude and sign of the induced surface charge, the resulting fluid interfacial displacement should also scale with *Equation (5.27)*. In **Figure 5-6**, we scale  $\Delta d$  by the real part of the polarization factor  $\text{Re}[K_I(\omega)]$  given by *Equation (5.29)*, and  $\omega$  by the crossover frequency  $\omega_{COF}$  (*Equation (5.27)*). Under this scaling, we find the evolution of  $\Delta d$  nicely collapses to a single curve for a wide range of electrical parameters,  $\Delta\sigma$  and  $\Delta\varepsilon$ . Note, the high ( $\omega \rightarrow \infty$ ) and low ( $\omega \rightarrow 0$ ) frequency asymptotes nearly exactly overlap, and each curve has a dimensionless asymptote at a normalized crossover frequency,  $\omega/\omega_{COF} \sim 1$ . The collapsed data scales as  $1/K_I(\omega)$ , which is plotted atop the data as a dotted line. The collapse of the displacement data demonstrates the dependence of the polarization factor on the interfacial fDEP displacement for all frequencies and liquid

electrical values used in this chapter and validates the Maxwell Wagner polarization process as the dominant charging mechanism over the measured frequency range.

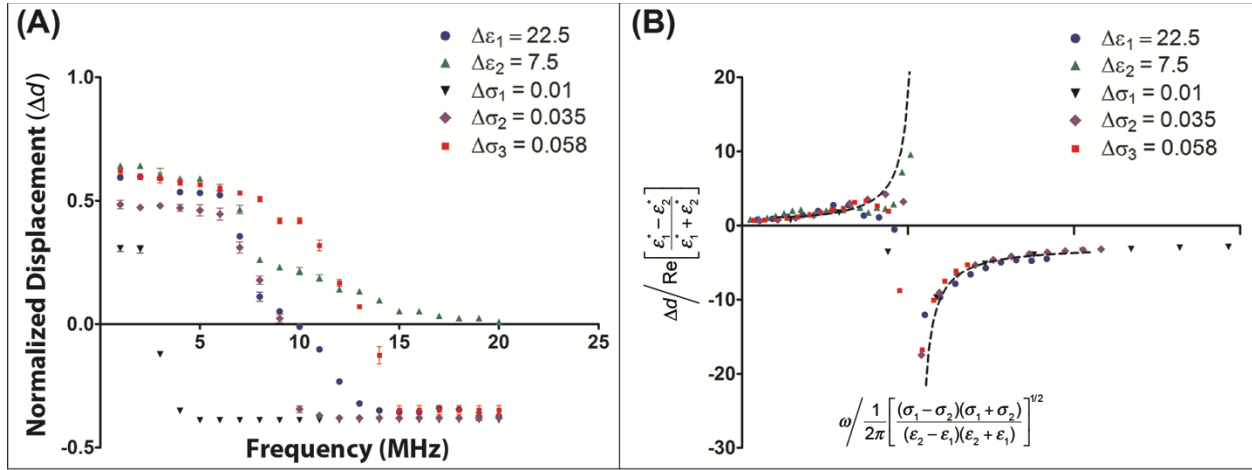


**Figure 5-6. Demonstration of the polarization scaling**

Interfacial displacement is proportional to the real part of the polarization factor,  $\text{Re}[K(\omega)]$ . **(A)** We plot interfacial displacement data for different values of permittivity and conductivity mismatches. **(B)** The displacement is scaled by the polarization factor, and the frequency is scaled by the predicted cross-over frequency. The dataset collapses almost identically to a single curve that is proportional to  $1/\text{Re}[K(\omega)]$  as highlighted with the dark dotted line. The collapse of the curve validates the Maxwell–Wagner polarization process as the dominant charging dynamics over the measured frequency range.

In terms of measuring interfacial fDEP velocity, one interesting aspect of this system is the relationship between axial distance down the microchannel and the time to which the interface has been exposed to an electric field. As the charge relaxation timescale of the liquid interface is much smaller than the viscous timescale, the fluid interface charges instantaneously relative to the time to which the fluid can respond the induced stress and displace. Hence, one can observe and quantify the evolution of the transverse field-induced fluid velocity profile in time by imaging the displacement of the interface axially down the microchannel. In **Figure 5-3** we show the evolution of the liquid interface down the electrode array at low, crossover, and high frequency. Note that the interface remains fixed in position across the entire electrode array at the crossover



frequency (9.2 MHz). At low frequency, the liquid interface enters the array, polarizes and the high conductive stream begins to deflect across the channel into the low conductive phase. As the fluid interface flows down the channel it is exposed to the field for greater times, and  $\Delta d$  continues to increase. This process continues until the interface exits the array. At this point the liquid displacement is observed to cease and due to the lack of inertial influence on the velocity field the interface remains in a displaced state. We also observe this at high frequencies, however, the deflection direction reverses, and the high dielectric stream displaces across the interface into the low dielectric phase. This process continues as the interface moves axially down the electrode array, and again ceases upon exiting the electric field.

## **5.6 Conclusion**

While traditional dielectrophoresis has been exploited to manipulate bubbles, particles, biomolecules and cells, research, and application in these areas have been primarily limited to particle-based and droplet systems. In this chapter, we have presented how to utilize Maxwell–Wagner polarization to initiate fDEP at electrically polarizable aqueous liquid–liquid interfaces. In fDEP, an AC electric field is applied across a liquid electrical interface created between two co-flowing fluid streams with disparaging electrical properties. We observe a frequency-dependent interfacial displacement that is dependent on the relative differences in the electrical conductivity and dielectric constant between the two co-flowing fluid streams. The displacement is dependent on the electric field strength and can be driven by peak-to-peak potentials as low as 2 volts. At low frequency, interfacial displacement is independent of liquid permittivity, while at high

frequency it is independent of liquid electrical conductivity. At intermediate frequencies, we observe a fDEP cross-over frequency where the displacement tends toward zero, and reverses direction. The cross-over frequency is independent of applied voltage. Our polarization model accurately predicts the liquid cross-over frequency, the dependence of interfacial displacement on electrical conductivity and dielectric constant, and collapses the measured displacement data to a single curve for all frequencies applied. The model presented in this chapter can be utilized to calculate the total induced surface charge density and electrical force at an electrical interface. Future work will involve more detailed 2D and 3D EHD models to examine the fluid velocity profile and how it relates to the electrical properties of each fluid phase.

# **6** *Manipulating liquid interfaces with fluidic dielectrophoresis: Active mixing at the micron-scale*

---

## **6.1 Introduction**

One challenge in designing miniaturized LOC processes is reagent mixing. Common laboratory tasks such as protein immunoassays<sup>157,158</sup>, DNA hybridization<sup>159,160</sup>, and cell culture<sup>161</sup> all require well-controlled mixing. Mixing at low Reynolds number<sup>162</sup>, however, can be challenging since inertial contributions to fluid motion are small and macromolecules such as protein and DNA often have low diffusion coefficients. Additionally, microfluidic mixing is often binary in nature. A fluid, for example, with an initial solute concentration is often combined and mixed together with another fluid to create a new, but fixed, solute concentration that is different from the original solution. The ability to dynamically control solute concentration during this process is challenging, and microfluidic processes often require significant off-chip sample preparation and multiple mixing steps on-chip to create mixed solutions at desired on-chip concentrations.

Microfluidic mixing can be accomplished either passively with secondary flow fields or actively using externally applied fluid forces. Because the Reynolds number is often well below one, these passive methods create mixing by stretching the interface between two liquid streams to decrease the distance over which diffusion occurs. Passive mixing approaches focus on increasing mixing fluid contact area or contact time to promote enhanced diffusion between flows. One popular passive mixing method

uses microfluidic lamination, where multiple streams are forced to split and then later gather as a multitude of smaller streams in order to increase the contact area between the flows<sup>163</sup>. While lamination can provide fast mixing times and shorter mixing lengths<sup>164</sup>, it typically requires complex fabrication methods and a complicated network of microchannels. Other passive mixers rely on the use of patterned surface chemistry<sup>165</sup>, 3D serpentine structures<sup>166,167</sup> and baffles or obstacles to create secondary flows for mixing<sup>168-172</sup>. While effective, passive methods create dispersed samples, and the final on-chip solute concentration is diluted as it spreads out longitudinally into neighboring buffer during the mixing process. Additionally, while passive mixing devices can typically mix within 55–300 ms, many devices result in lower mixing efficiency, and therefore require a longer mixing to achieve optimal mixing.

An alternative to passive mixing is active mixing, where fluid streams are combined with the use of an external driving force<sup>173,174</sup>. Common active methods include mixing by peristaltic pumps<sup>175</sup>, magnetic particles<sup>176-178</sup> or surface acoustic waves<sup>179,180</sup>. Because active mixing can often produce flow fields with larger fluid velocities than passive methods, active mixing methods generally have shorter on-chip mixing dimensions and mixing times. One way to actively drive fluid mixing is to use electrokinetics. In this approach, an electrical field is introduced into a microchannel. The field interacts with regions of non-neutral space charge to drive fluid motion. These electrokinetic flows can then be harnessed to drive the mixing of two or more fluidic streams.

While many microfluidic mixing methods exist, they are all based on the principle of binary dilution, where two or more flow volumes are combined to produce a larger volume at a fixed diluted concentration. While both active and passive mixing techniques have been effective in combating the lack of inertial influence at low Reynolds number, it is currently very difficult to control on-chip concentration in real-time during mixing. In this chapter, we present a novel electrokinetic mixing approach for dynamically tuning and controlling the on-chip solute concentration of fluid flows. Mixing is accomplished using an externally applied alternating current (AC) electric field dropped across a microchannel with three co-flowing liquid streams. Two outer streams contain a solute to be mixed with the central stream, while the inner central stream flows downstream to a chemical gradient generator. The laminar flow field is electrokinetically driven across the microchannel by the electric field and the magnitude of fluid motion can be controlled by varying the frequency and electric field strength. We show that on-chip solute concentration in the central flow stream can be dynamically controlled and demonstrate usefulness of this method by controlling the concentration in a downstream microfluidic gradient generator.

## ***6.2 Materials and Methods***

Electrokinetic mixing experiments were performed using a two-stage microfluidic device (**Figure 6-1**). An upstream stage was used to electrokinetically mix multiple laminar streams into a single stream at a desired concentration. This mixed stream was then continuously fed into a downstream stage where it was used to create a stable microfluidic gradient. The overall two-stage design offered a means to assess fluidic

mixing by our electrokinetic approach, and to demonstrate dynamic on-chip concentration control.

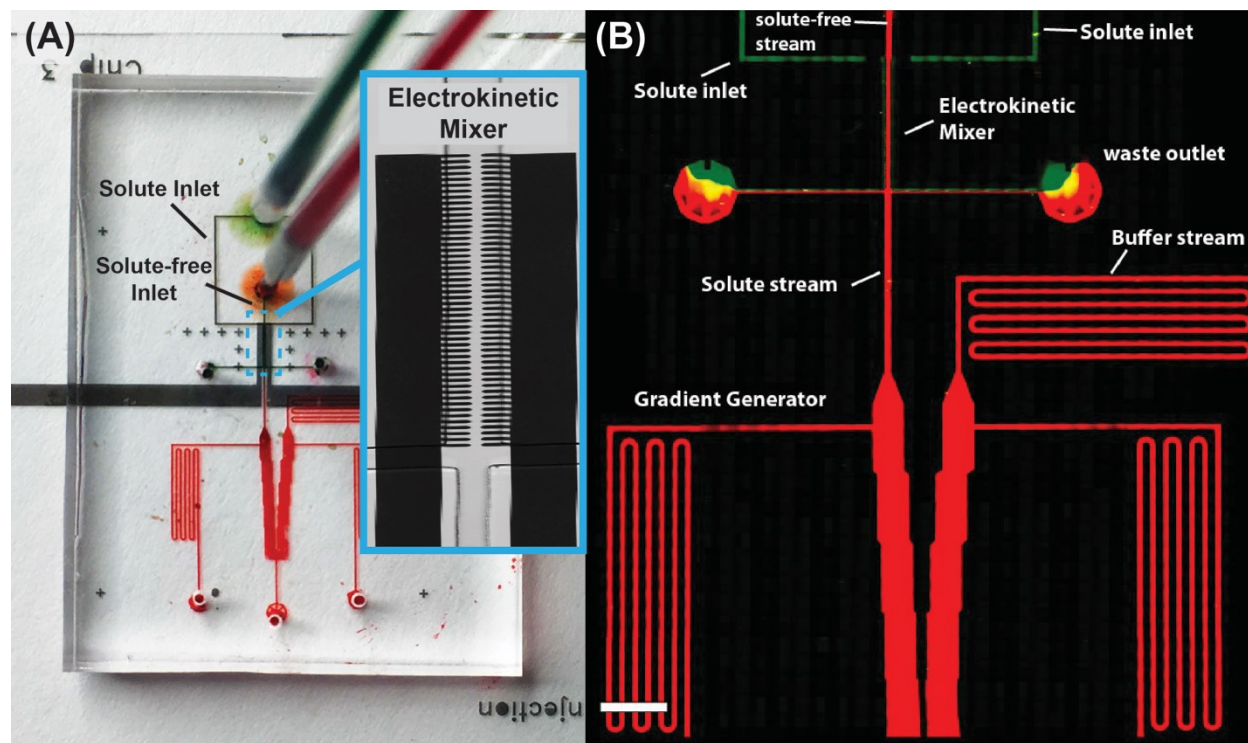


**Figure 6-1. Schematic of the electrokinetic mixer**

(A) Microfluidic device with embedded electrodes. The solute and solute-free streams are delivered to the top and bottom inlets respectively. The electrokinetic mixer, boxed in blue, is shown in a magnified brightfield image; (B) Montage of the dual-stage microfluidic device. The upstream stage consists of an electrokinetic mixer which is fed continuously downstream to a gradient generator. An electric field is used to inject two solute streams into a central solute-free stream. This stream then stream then serves as an input to the downstream gradient generator. Scale bar, 100  $\mu\text{m}$ .

The upstream electrokinetic mixing was performed using a combination of laminar and field-induced electrokinetic flow. An array of point electrodes drive fluid into motion by electrokinetic flow using fluidic dielectrophoresis (fDEP). In fDEP, laminar liquid interfaces are polarized and driven into motion by an externally applied AC electric field<sup>153,181</sup>. To produce fDEP mixing, three different fluid streams were introduced into a main flow channel using an external constant pressure source and

made to flow side-by-side in a main flow channel. The electrical properties of the two outer streams were adjusted such that they had a higher conductivity and lower dielectric constant than the inner fluid stream. Therefore, two electrical liquid interfaces were produced that could then be polarized and driven into motion with an electric field. The fluidic channel network was designed such that the two outer streams were driven into waste outlets, while the central stream remained in the device and was sent continuously downstream to a gradient chamber. Therefore, only a “clean” central fluid is sent downstream, while the two outer, high conductive green streams are forced to flow to outlet waste streams. In this chapter, we demonstrate that fDEP can be used to mix the contents of the two outer fluids with the central fluid. When an AC electric field is applied across the three streams, the two fluid interfaces polarize and deflect, and forcibly inject their contents into the center stream (**Figure 6-2**). This injection rate can be exploited to control the concentration in a downstream microfluidic system.

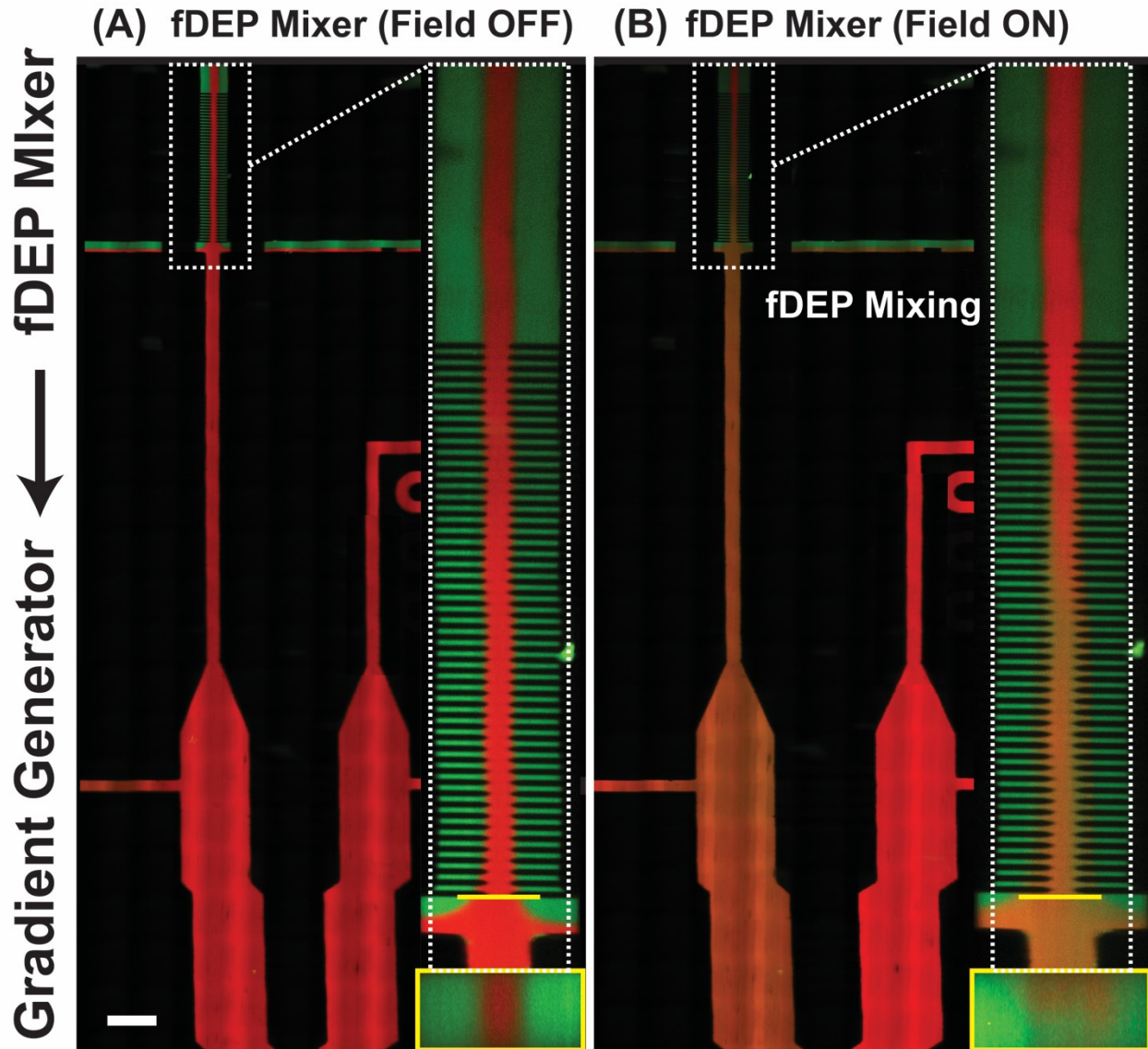


**Figure 6-2. Comparison of non-actuated versus actuated electrokinetic mixing**

(A) Left: The microfluidic device consists of two stages: an upstream mixing stage with embedded electrodes and a downstream gradient chamber. The microchannel network is designed such that when no alternating current (AC) field is applied, only the low conductive central red stream flows to the gradient chamber. Right: A magnified micrograph of the mixing section. A yellow line depicts the spatial location where a 3D cross-sectional image was capture, shown under the zoomed in image; (B) When an AC electric field was applied, mixing occurred and influenced the solute concentration supplied to the gradient chamber. The mixing sections shows that while the red stream enters the mixing zone and exits with a slight orange hue due to mixing with the two outer streams. Scale bar, 200  $\mu\text{m}$ .



### 6.2.1 Reagents and Chemicals

Fluid motion by fDEP requires a polarizable liquid interface. In this chapter, liquid interfaces were composed of three fluids with different electrical conductivity ( $\sigma$ ) and dielectric constant ( $\epsilon$ ). When forced to flow side-by-side at low Reynolds number these three fluids formed two interfaces, each with a large electrical mismatch. Each stream was injected at a constant flow rate (10  $\mu$ L/min) into the device using a low-cost flow controller equipped with an externally pressurized fluid-filled cryogenic vial<sup>182</sup>. We labelled each fluid with a different Alexa Fluor fluorescent dye to accurately image the interface position using confocal microscopy. The electrical interface was formed by flowing two outer (green) diluted phosphate buffered saline streams ( $\sigma_1=1.60$  mS/cm;  $\epsilon_1=78$ ) with 10 ng/mL of Alexa Fluor 488 (Invitrogen, Carlsbad, CA, USA). The center (red) high dielectric stream ( $\sigma_2=19$   $\mu$ S/cm;  $\epsilon_2=110$ ) was comprised of 0.8 M 6-aminohexanoic acid (AHA) (Sigma-Aldrich) labeled with 10 ng/mL of Alexa Fluor 594 (Invitrogen). AHA is a water-soluble zwitterion used for increasing the dielectric constant of aqueous solution. Prior to fluorescent labeling, the AHA solution was polished with 1 g/mL Dowex MR-3 (Sigma-Aldrich) ion exchange resin to remove trace salts and reduce solution conductivity.

### 6.2.2 Characterizing the magnitude of mixing

To analyze the degree of mixing and the voltage dependence, measurements were taken over a 100  $\times$  100 square  $\mu$ m section directly above the electrode array. Interfacial motion was captured using a confocal microscope (Nikon/Prairie Technologies) equipped with an Andor iXon 897 camera, two 50 mW solid-state lasers

for excitation at 488 nm and 561 nm, respectively, and a triggered Piezo Z stage for capturing 3-dimensional micrographs of the microchannel cross-section. When fDEP was used to drive fluid motion, the resulting mixing was calculated by capturing a fluorescent intensity profile over the microchannel cross section depicted in **Figure 6-3**. Using these confocal images, the intensity profile in the central fluidic stream was analyzed approximately 30  $\mu\text{m}$  above the channel surface across the entire channel width. Each intensity profile was normalized to the fluorescent background ( $\sim 126$  intensity units) when no AC electric field was applied (**Figure 6-3A**). Mixing was then quantified by averaging the fluorescent intensity of the Alexa Fluor 488 across the channel width, normalizing this value with the background intensity profile and then dividing by the theoretical max intensity.

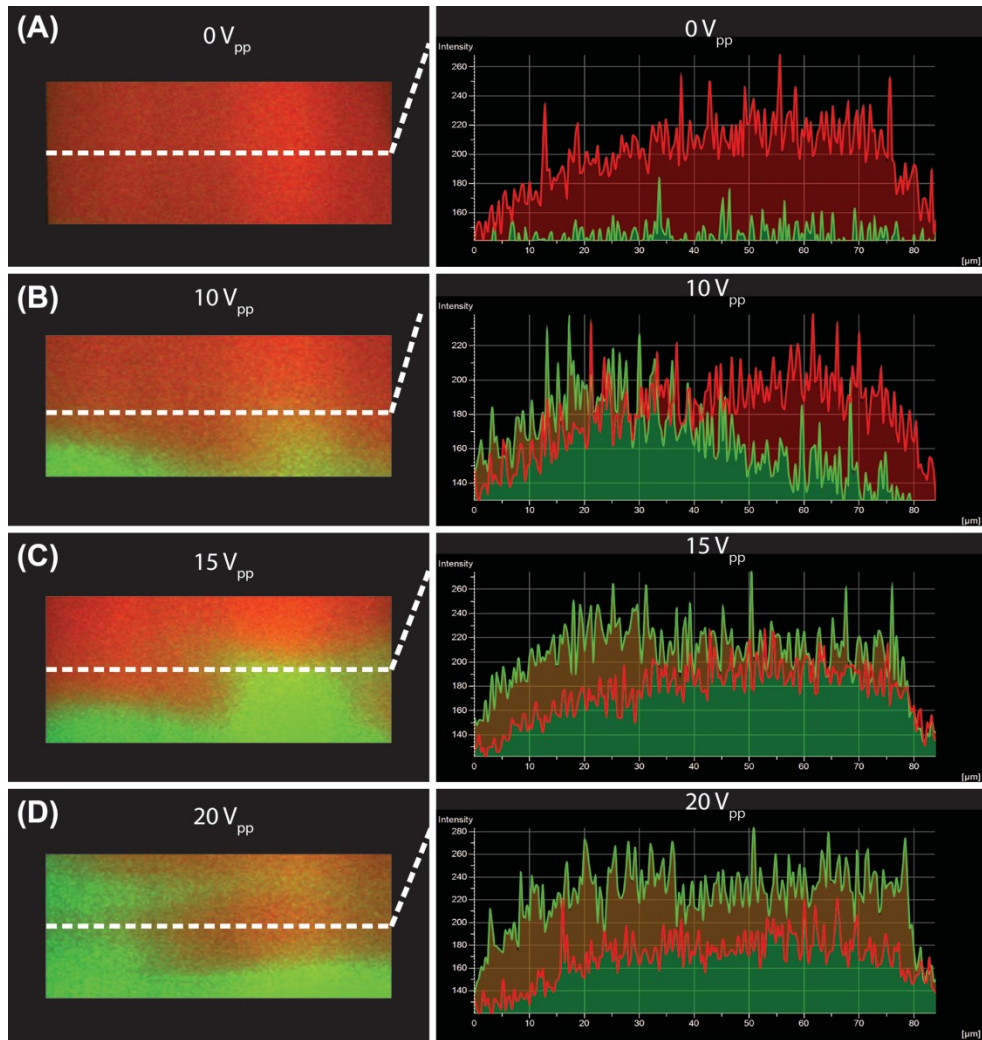


**Figure 6-3. Electrokinetic mixing analysis**

3D cross-sectional image of the device at the entrance of the gradient chamber. Fluorescent profiles (A) 0 V<sub>pp</sub>; (B) 10 V<sub>pp</sub>; (C) 15 V<sub>pp</sub> and (D) 20 V<sub>pp</sub> is applied across the tri-laminar flow streams. The fluorescent measurements were taken in center of the microchannel cross-section and indicated by the dotted white line.

## 6.3 Results and Discussion

### 6.3.1 Mixing with fluidic dielectrophoresis

We first sought to investigate the ability to mix multiple fluidic streams using fDEP. We observed rapid mixing between three co-flowing fluid streams when an AC voltage was applied across the microchannel. Mixing was observed to occur when the

high conductive (green) stream forcibly displaced into the low conductive (red) stream. In order to better investigate the mechanism by which mixing occurs, confocal images of the channel cross-section were taken for three different voltages — 10, 15 and 20  $V_{pp}$ . The degree of mixing between the red and green streams was quantified using fluorescent intensity profiles captured over the microchannel cross-section (**Figure 6-3**). Shown in **Figure 6-3**, mixing occurs when the central green stream is forcibly displaced into the low conductive red stream. When the applied voltage was sufficiently large the rate of injection is so great that an electrokinetic vortical flow formed down the axis of the mixing electrode array, as shown in **Figure 6-4**. Therefore, fDEP served to electrokinetically inject fluid from the outer two flow streams and to satisfy conservation of mass, fluid volume from the central stream was dispelled outward to the two outer streams. Therefore, the electrokinetic mixer offers a means to mix with less dilution since newly injected flow of the outer fluid is accompanied by an equal outward flow of the inner fluid.

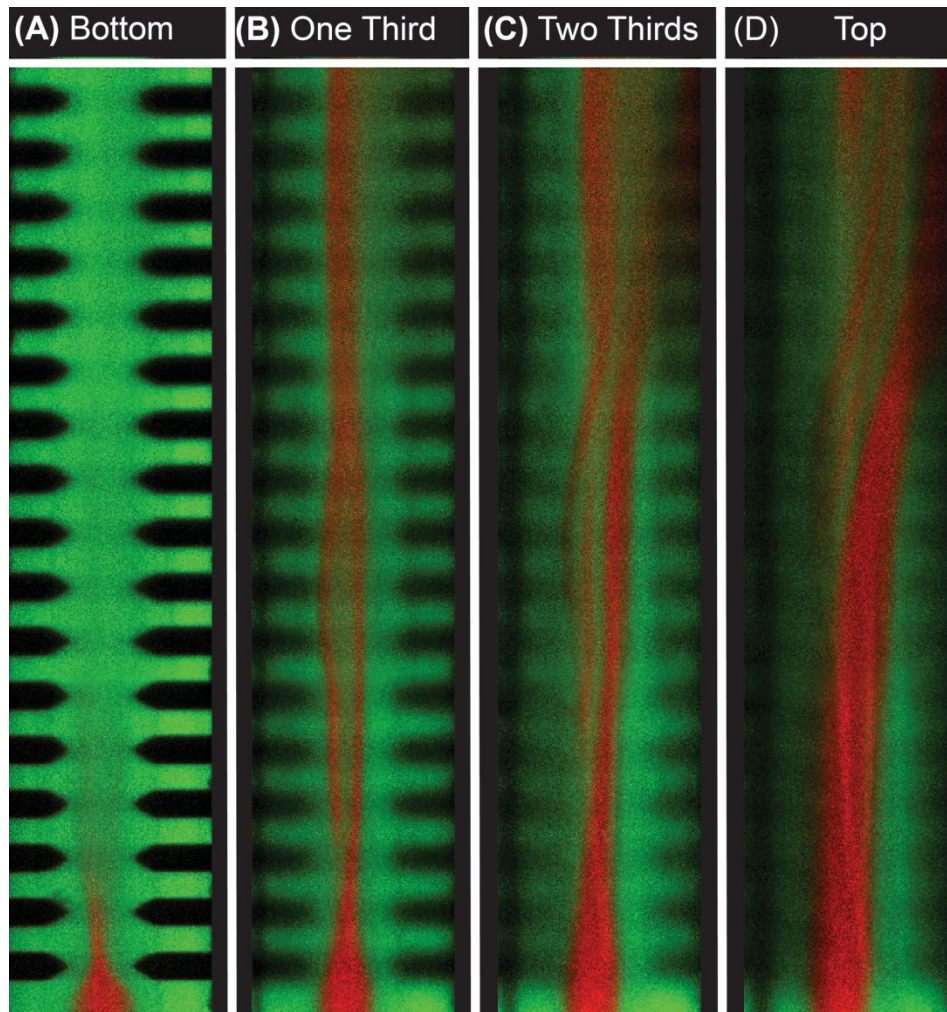


**Figure 6-4. Monitoring electrokinetic mixing along the z-axis**

A confocal montage captures fluid motion down the axial length of the mixing channel captured at different positions along the channel height. **(A)** Bottom surface of the microfluidic device. Upon entering the array with an applied voltage of 20 MHz at 1 MHz, the outer green streams inject into the center occupying the entire bottom of the channel; **(B)** 1/3 from the bottom of the device; **(C)** 2/3 from the bottom of the device; **(D)** Top of the microchannel device. Scale bar, 50  $\mu\text{m}$ .

### 6.3.2 The influence of field frequency and voltage on mixing

There are several important properties of the AC electric field that will influence fluid mixing. The field frequency will affect the direction of interfacial displacement. A low frequency field, for example, will force high conductive fluid from the two outer streams to displace into the central low conductive stream. Alternatively, if a high

frequency electric field is applied across the fluid interfaces the center high dielectric stream displaces into the two adjacent low dielectric streams. In this case, no mixing was observed. Thus, for this system where we sought to inject solute from the two outer flows, the frequency regime significant for the experiments was at low frequency (<5 MHz). The influence of AC frequency on mixing is shown in **Figure 6-5**.

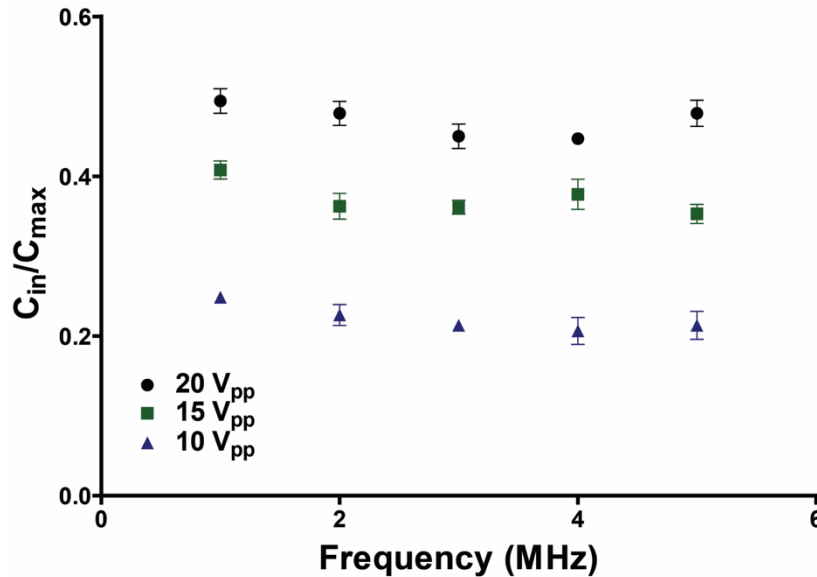


**Figure 6-5. Normalized concentration is affected by applied frequency**  
 Quantification of the degree of concentration perturbation ( $C_{in}/C_{max}$ ) versus frequency. The concentration is normalized based on the theoretical max concentration.

For the frequency ranges from 1 to 5 MHz the average normalized concentration of the high conductive stream is not significantly influenced by the AC field frequency. The observed solute concentration entering the gradient chamber ( $C_{in}$ ) was normalized by the theoretical maximum concentration. However, it was apparent that the applied voltage impacted the mixing concentration. Therefore, we next investigated the effects of applied voltage on mixing. To do this, three different AC voltages — 10, 15 and 20  $V_{pp}$  — were applied across the fluid interfaces at a constant field frequency of 5 MHz. While we could have selected any frequency between our 1–5 MHz experimental range

based on the data in **Figure 6-5**, we based our concentration data on the largest experimental frequency simply because higher frequency electric fields are known to be less likely to produce Faradaic reactions and Joule heating in conductive buffers. Shown in **Figure 6-6**, we observed a linear correlation between the applied voltage and degree of mixing. In particular, as the applied voltage increases, the degree of mixing also increases.

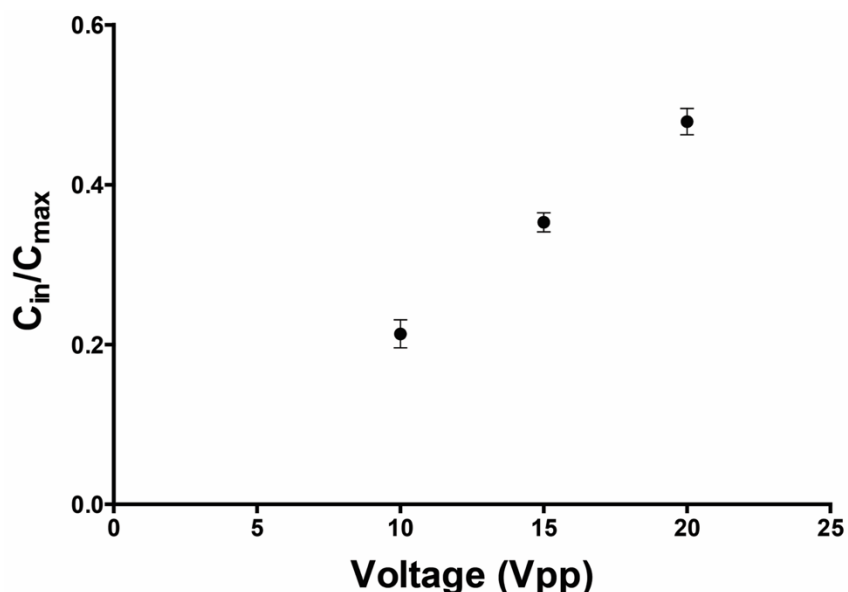


**Figure 6-6. Normalized concentration versus applied voltage**

Plot of  $C_{in}/C_{max}$  versus applied voltage. The concentration of solute increases linearly increasing applied voltage.

### 6.3.3 Using AC electrokinetic mixing to create finely tunable concentration gradients

Finally, with the ability to induce mixing and control the solute concentration within the central stream, we investigated the ability to integrate the upstream electrokinetic mixer with a downstream concentration gradient generator. Shown in **Figure 6-2A**, when no AC electric field is applied, no fluid injection occurs and the

flow central fluid stream, which is fed into the downstream chamber consists entirely of the low conductive fluid (red stream). However, when an AC electric field was applied upstream, fluidic mixing occurred and altered the downstream fluidic concentration. **Figure 6-7** shows the gradient chamber when an upstream AC electric field of 5 MHz, 20 V<sub>pp</sub> was applied. A series of consecutive micrograph images were captured at different time intervals to illustrate the rate at which the gradient is generated when upstream mixing is initiated. After the electric field was activated, a concentration gradient is formed within the gradient channels, where one chamber consists entirely of the low conductive (red) buffer and the adjacent stream consists of a mixture of the high conductive (green) and low conductive (red) buffers. When differing voltages are applied, the time for gradient generation, as well as the gradient steepness differ due to differing magnitudes of mixing and different rates of fluid injection. With lower applied voltages, less mixing occurs which produces a lower concentration gradient. Larger applied voltages result in a greater rate of fluidic injection and produce a steeper gradient.



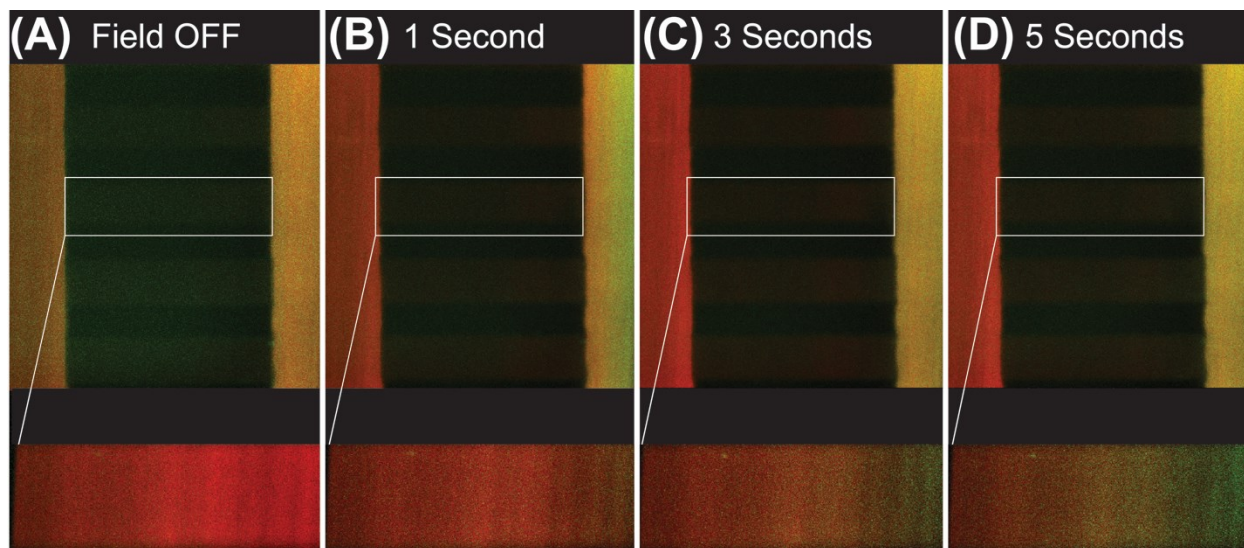


**Figure 6-7. Magnified view of the microfluidic gradient chamber**

Images were captured at varying time points after the electric field was applied over a period of 5 s. When a 5 MHz, 20 V<sub>pp</sub> AC electric field is applied upstream it modifies the concentration of mixed solution that enters the gradient (A) When the electric field is off, the connecting gradient side channel lacks any fluid from the tri-laminar outer streams. However, when the field is switched on a chemical gradient forms across the connecting channel, which increases with over a time period of 5 s; (B) 1 s; (C) 3 s and (D) 5 s. Scale bar, 40 μm.

## 6.4 Conclusion

In this chapter, we presented a novel method for electrokinetic mixing in a microfluidic device using fluidic dielectrophoresis. Using an AC electric field, the two laminar liquid interfaces between three co-flowing fluids were actively mixed through the use of interfacial electrokinetic stresses. When an electric field was applied across these interfaces, they polarized and forcibly injected the contents of the two outer streams into the center stream. The degree of mixing was monitored by labeling each fluid stream and measuring the fluorescent intensity profiles over the microfluidic channel cross-section. Mixing was shown to be influenced by both the frequency and voltage of the applied AC electric field. As the voltage increased, the magnitude of mixing increased. It was shown that there exists a linear relationship between the

degree of mixing and applied voltage. Finally, we coupled this upstream mixing device with a downstream passive gradient chamber to demonstrate the usefulness of this proposed method. Upstream, an AC electric field was used to induce mixing. This led to a change in solute concentration that was sent downstream to the gradient chamber. By controlling the degree of mixing, we can alter the steepness of the concentration gradient. Future work will focus on applying this novel electrokinetic mixing component in order to create tunable on-chip concentrations.

# *7 Homogeneous, label-free detection at liquid interfaces with interfacial electrokinetic transduction (IET)*

---

## **7.1 Introduction**

Biosensors combine targeted biological recognition with physicochemical transduction to detect specific biomolecules within a biological sample. They are used in a wide range of analytical applications, including diagnosis and treatment of infectious diseases, biowarfare detection<sup>3,183</sup>, environmental monitoring<sup>184,185</sup>, drug discovery<sup>32,186</sup>, cell biology<sup>187,188</sup>, cancer research<sup>189</sup> and point-of-care diagnostic testing<sup>190,191</sup>. Here, we address a key challenge to developing label-free homogenous biosensors for sensitive biomolecular detection and kinetic analysis using microfluidic biosensing systems that normally require fluorescently labeled biomolecules and optical quantification.

Combining biosensors with microfluidic transducers can fulfill an increasing demand for fast, inexpensive sensors capable of molecular detection and analysis. Microfluidic biosensors provide several advantages over traditional laboratory-based detection methods, including faster analysis time, reduced sample and reagent consumption, and potential automation with sample processing units using on-chip microfluidic valves<sup>192</sup>, pumps, mixers<sup>193</sup> and detectors. In microfluidics, liquid transport usually occurs at low Reynolds number where the fluid flow is laminar; fluid streams flow side-by-side and mixing is driven only by diffusion<sup>106,151,194</sup>.

Microfluidic liquid interfaces have been used as homogenous biosensing substrates for quantitative molecular detection and kinetic analysis in solution phase. The interface is created using laminar flow, where two streams combine at a fluidic junction and flow side-by-side down a main channel. One stream has a target probe and the second stream contains the biological sample of interest<sup>35,106</sup>. Biorecognition occurs in solution phase as the target and sample streams diffusively mix at their contacting liquid interface where target and sample molecules specifically bind to one another. This approach offers an inexpensive, yet extremely powerful method for biosensing and biomolecular kinetic analysis, and has been used to quantify fast kinetic processes, extract kinetic rate constants, perform sensitive on-chip immunoassays and detect DNA hybridization reactions in solution.

To create a complete biosensor, the microfluidic interface is coupled with a transducing element to convert recognition events into a detectable measurement signal. Depending on the nature of the transduced biosensor signal, detection can be performed optically<sup>195</sup>, electrically<sup>196,197</sup> or mechanically<sup>198</sup>. Biosensing at microfluidic liquid interfaces, however, is currently only performed using optical methods such as fluorescent microscopy, fluorescence energy transfer (FRET)<sup>199</sup>, fluorescence correlation spectroscopy<sup>200</sup>, confocal fluorescent microscopy<sup>201</sup>, and fluorescence lifetime imaging microscopy (FLIM)<sup>202</sup>. While effective, they require fluorescently labeled probe molecules and optical components, which can significantly increase the cost and size of the microfluidic platform.

In this chapter, we describe a label-free homogeneous electrokinetic biosensor for detecting and quantifying bioaffinity interactions in solution. Our approach combines

continuous microfluidic flow with alternating current (AC) electrokinetics. Electrokinetics integrates well with microfluidics and is a useful tool for a variety of on-chip fluidic applications including cell manipulation<sup>115,123</sup>, liquid mixing<sup>203</sup>, particle trapping<sup>115,123</sup> and fluidic routing<sup>204</sup>. In our electrokinetic approach, depicted in **Figure 7-1**, bioaffinity binding occurs at a microfluidic liquid interface. We create the interface using a microfluidic T-channel device with two fluid inlets and a single fluidic outlet; two fluids combine at the channel junction and create an interface as they flow side-by-side down the main channel to the outlet (**Figure 7-1A**). An array of microelectrodes is fabricated in the main flow channel and used to deliver a polarizing electric field across the fluid interface. To be polarizable, and capable of being manipulated with the applied electric field, we engineer an electrical mismatch into the interface. In this way, the interface is an electrical interface (EI), comprised of two co-flowing fluid streams with different electrical conductivity ( $\sigma$ ) and permittivity ( $\epsilon$ ). Using the EI as a substrate for biomolecular reaction, two solutions – one containing a target protein and the other containing an analyte probe – are pumped into separate T-channel inlets at a constant flow rate, inter-diffuse across the EI and specifically bind at the liquid interface (**Figure 7-1B**). During this process, an AC electrical field is applied across the EI. Due to the large electrical mismatch, the interface polarizes and electrokinetically displaces across the main flow channel, perpendicular to the main flow direction (**Figure 7-1C**)<sup>153</sup>. The magnitude and direction of this displacement is proportional to the electrical mismatch at the EI. Here, we demonstrate that specific biomolecular interactions influence this mismatch, and allow for biomolecular interactions to be detected and quantified without fluorescent labels by measuring the interfacial displacement under an external electric field during binding (**Figure 7-1C**).

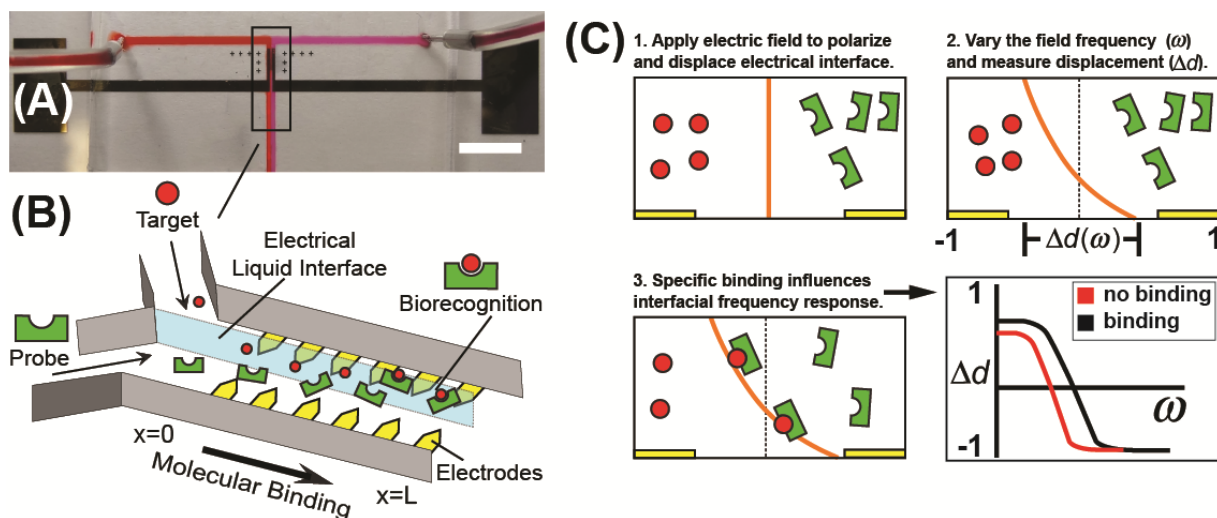


**Figure 7-1. Schematic of IET sensor**

**(A)** Microfluidic T-channel device with integrated electrodes used to create an electrical liquid interface for the IET sensor. Scale bar, 5.0 mm; **(B)** Schematic illustration of target-probe binding along the liquid interface; **(C)** Principles of IET sensor operation – 1. Specific binding occurs at the electrical interface; 2. An electric field polarizes and displaces the interface a distance  $\Delta d$ , which is a function of the field frequency; 3. Binding influences the polarizability of the interface and is detected by measuring interface frequency response at different values of field frequency.

Our label-free biosensing method uses the liquid interface as a homogenous substrate for specific binding, and its motion in an AC electric field as the transducer for biomolecular recognition. We therefore propose a new class of biosensors based on interfacial electrokinetic transduction (IET): specific binding changes the electrical properties at the EI, which is electrokinetically transduced and detected by measuring perturbations in field-induced fluid displacement.

In this chapter, we demonstrate how to use IET to monitor avidin-biotin binding kinetics in real-time without labels. Moreover, the IET biosensor is specific and sensitive, and able to detect as low as 250 femtomolar avidin concentrations against a 5 mg/mL background of bovine serum albumin (BSA). Through this study, we establish a methodology for rapid label-free IET biosensing at electrical liquid interfaces, demonstrate

sensor performance and sensitivity for the detection of biomolecules, and measure avidin-biotin binding kinetics with millisecond time resolution. This new electrokinetic sensor can provide a low-cost, rapid, and portable biosensing system for label-free real-time kinetic analysis and on-site biomolecular diagnostics in free solution.

## **7.2 Materials and Methods**

### **7.2.1 Sensor measurement**

The electrical interface was created using the microfluidic “T-channel.” Two fluid streams were introduced into the device via pressure driven flow using an externally pressurized cryogenic vial. Shown in **Figure 7-2A**, the left-most (red) high conductivity stream consists of a 0.5 M phosphate buffered saline, pH 7.4, (PBS) solution with 10 ng/mL of Alexa Fluor 594 (Invitrogen). The right-most (purple) high dielectric stream consists of 0.8M 6-aminohexanoic acid (AHA) (Sigma-Aldrich) labeled with 10 ng/mL of Alexa Fluor 647 (Invitrogen). AHA is a water-soluble zwitterion used for increasing the dielectric constant of aqueous solution. Prior to fluorescent labeling, the AHA solution is spun down in a centrifuge for 15 minutes in 1 g/mL Dowex MR-3 (Sigma-Aldrich) ion exchange resin to remove trace salts and reduce solution conductivity<sup>181</sup>. A cross-sectional view of the resulting fluid interface was imaged using dual excitation confocal microscopy (**Figure 7-2B**).

To create the electrical interface two fluid streams, each with a different set of electrical properties, are pressure injected into the microfluidic device. An AC potential of 10 volts peak-to-peak ( $V_{pp}$ ) at a frequency of 1 MHz was dropped across the electrodes,

and slowly is increased to 20 MHz while continuously monitoring the displaced position of the fluid interface.

### 7.2.2 Protein Solutions

Biotin, avidin, bovine serum albumin, and mouse anti-bovine serum albumin were purchased from Sigma-Aldrich, USA, and used as received. A 16  $\mu$ M biotin solution was made by diluting a 4 mM stock with AHA and labeled with 10 ng/ml Alexa Fluor 594, and pH adjusted to 7.4. The avidin solution was made by adding powdered avidin to PBS labeled with 10 ng/ml Alexa Fluor 647. The conductivity of the PBS solution was adjusted to 0.25 mS/cm using DI water. All subsequent solution avidin concentrations were made by serial dilutions with a stock dilute PBS. The final avidin concentration was calculated using a UV spectrometer (Thermo Scientific, Genesys 10S).

### 7.2.3 The electrical interface

IET biosensors are bioaffinity sensitized electrical liquid interfaces that electrokinetically displace in response to biomolecular binding. They require both microfluidic and electrokinetic components. The electrical interface is created using a PDMS microfluidic T-channel. An AC electric field is generated using an array of co-planar gold microelectrodes lithographically patterned onto the surface of a glass slide. The PDMS-electrode assembly is aligned under an optical microscope and plasma bonded to create a complete electro-fluidic device (**Figure 7-1A**). The EI is composed of two co-flowing electrolyte streams. Both streams – stream 1 (left) and 2 (right) – have finite electrical conductivity and permittivity, but one has a greater electrical conductivity and



the other a greater electrical permittivity such that  $\sigma_1 > \sigma_2$  and  $\epsilon_2 > \epsilon_1$ . Because the streams do not mix except by diffusion, a sharp electrical mismatch is created at their co-flowing interface, which can be polarized (e.g. charged) and displaced across the microchannel using a perpendicular AC electric field.

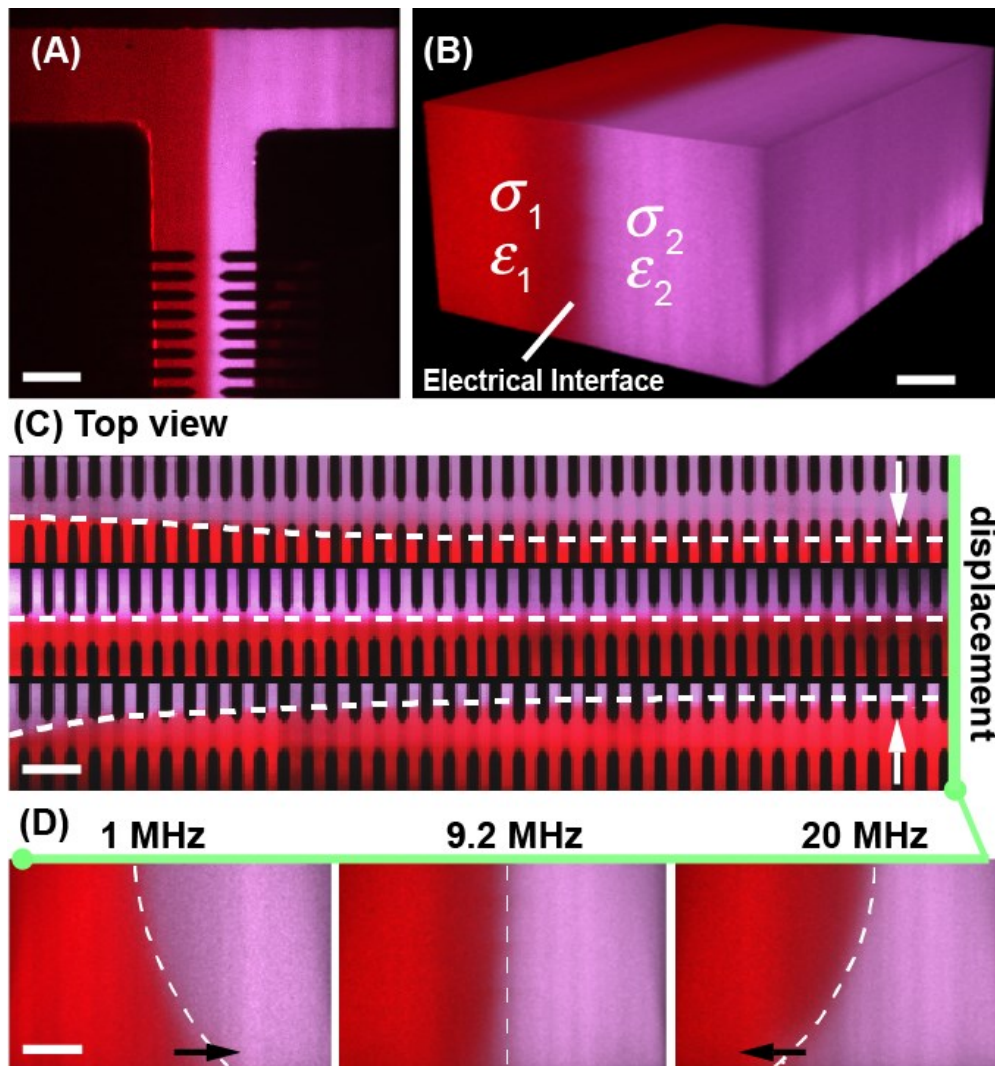


**Figure 7-2. A top and side view of fDEP. The liquid interface enters the electrode array and displaces across the flow channel**

(A) Confocal micrograph of two fluorescently labeled fluids flowing side-by-side to create a liquid interface. Scale bar, 50  $\mu\text{m}$ ; (B) 3D confocal image stack of the electrical interface formed between two fluids with different electrical conductivity and dielectric constant. Scale bar, 20  $\mu\text{m}$ ; (C) The interface enters the electrode array and displaces across the flow channel. The direction of this displacement is dependent on the frequency of the applied electric field. Scale bar, 50  $\mu\text{m}$ ; (D) Confocal micrograph illustrates a side-view of the interface at different electric field frequencies. Scale bar, 20  $\mu\text{m}$

#### 7.2.4 Measuring interfacial frequency response

To quantify displacement, the interface position is imaged using confocal microscopy; each stream is labeled with a different fluorescent marker – Alexa Fluor 594 (red) or 647 (purple) – and imaged, yielding top-down 2D (**Figure 7-2A, C**) and 3D (**Figure 7-2B, D**) micrographs of the interface and its position within the microchannel. When a perpendicular AC electric field is applied, the interface displaces across the channel in a direction and magnitude dependent on the field frequency ( $\omega$ ). This displacement response can be confocal imaged and quantified from a top-down and side view. **Figure 7-2C** shows a top-view of the EI displacement over the length of the electrode array for three different applied frequencies:  $\omega = 1$  MHz, 9.2 MHz, and 20 MHz. At a frequency of 1 MHz (**Figure 7-2C – bottom**), the interface enters the array and continuously displaces across the main flow channel into the high permittivity flow stream. At high frequency (20 MHz), the displacement direction reverses (**Figure 7-2C – top**). At an intermediate crossover frequency (COF) of 9.2 MHz, the interface does not displace in the electric field and remains stationary over the entire length of the array (**Figure 7-2C – center**).

The force driving interface motion is a surface force that exists over the separation length scale between the electrodes in the array. Because this length scale (20  $\mu\text{m}$ ) is smaller than the microchannel height (100  $\mu\text{m}$ ), field-driven displacement is localized to the bottom of the microchannel. Fluid near the top of the channel is driven in the opposite direction to satisfy conservation of mass, and the interface appears to tilt to the left or right depending on the applied field frequency. **Figure 7-2D** shows the side-view of the displaced tilted interface for each applied field frequency.

In this chapter, we propose to use the frequency response of the interface as a biosensing transducer for detecting biomolecules at a microfluidic liquid interface. To accomplish this, we measure the net displacement of the EI as a function of applied electric field frequency at the bottom surface of the microchannel. **Figure 7-3B** shows the complete frequency response of the interface calculated from the micrograph experiment presented in **Figure 7-2**. The displacement ( $\Delta d$ ) has been rendered non-dimensional over the microchannel width, and varies from -1 to 1. At the COF, the interface does not displace:  $\Delta d = 0$ . Above and below the COF the displacement is finite and varies in both direction and magnitude with the applied frequency.

### **7.2.5 Electrokinetics of an electrical interface – fluidic dielectrophoresis**

The motion of an electrical liquid interface in an externally applied AC electric field is known as fluidic dielectrophoresis (fDEP). Despite being discovered over six decades ago for particle suspensions, dielectrophoresis has only recently been applied to aqueous liquid interfaces. Here, we theoretically define the electrical and frequency dependence on the interface displacement, and apply this to our IET biosensor measurements.

For an EI subjected to a time varying monochromatic AC electric field, the magnitude and direction of the interfacial displacement is directly proportional to the interface polarization factor:  $K(\omega)$ . This factor describes the magnitude and sign of the field-induced ionic and dielectric charge that is induced at the EI in response to the electric field. Because the field oscillates monochromatically in time, the sign and magnitude of charge at the interface is dynamic, and reverses in phase with the electric field. This process takes a finite time, and depending on the field frequency, not all of the induced

charge will be able to dynamically stay in phase. To account for this phase lag,  $K(\omega)$  is a complex function with both real and imaginary parts, dependent on field frequency, and liquid conductivity and permittivity differences across the EI. Displacement is driven by the real part of this expression (i.e. interface charging that is in-phase with the applied field). The out of phase (imaginary) part produces a net interfacial electric stress with a zero time-average and does not contribute to interfacial motion. Therefore, we use the real part of the polarization factor in this chapter.

For an electrical interface composed of two co-flowing aqueous electrolytes with different electrical conductivity and permittivity, the real part of the interfacial polarization factor is:

$$Re[K(\omega)] = \frac{(\varepsilon_2 - \varepsilon_1)\tau^2\omega^2}{(\varepsilon_2 + \varepsilon_1)(\tau^2\omega^2 + 1)} + \frac{(\sigma_2 - \sigma_1)\tau^2\omega^2}{(\sigma_2 + \sigma_1)(\tau^2\omega^2 + 1)}, \quad (7.1)$$

where  $\tau = (\varepsilon_2 + \varepsilon_1 / \sigma_2 + \sigma_1)$  is the characteristic charge relaxation timescale at the interface between the two liquids.

Illustrated in *Equation (7.1)*, fDEP provides a unique method for quantifying the electrical properties of an EI because displacement direction and magnitude are both dependent on the relative electrical property mismatch between the interface's two co-flowing fluid streams. In **Figure 7-3A**, we plot *Equation (7.1)* as a function of electric field frequency, and highlight the influence of electrical conductivity and permittivity mismatches at high, intermediate, and low AC field frequencies. At low frequency below the COF, polarization is driven by differences in electrical conductivity between the two co-flowing fluids ( $\sigma_1 - \sigma_2$ ), which we define here as interfacial conductivity ( $\Delta\sigma$ ). Above the COF at high frequency, displacement is governed solely by interfacial permittivity ( $\Delta\varepsilon$ ).

The COF ( $\omega_{COF}$ ) occurs where the net polarization and displacement of the interface is zero (**Figure 7-3B**). It is sensitive to both interfacial conductivity and permittivity, shown here by setting the polarization factor equal to zero ( $Re[K(\omega)] = 0$ ), and solving for frequency:

$$\omega_{COF} = \frac{1}{2\pi} \left[ \frac{(\sigma_1 - \sigma_2)(\sigma_1 + \sigma_2)}{(\varepsilon_2 - \varepsilon_1)(\varepsilon_2 + \varepsilon_1)} \right]^{1/2}. \quad (7.2)$$

Depicted in **Figure 7-3A**, interface displacement at low and high frequency is influenced only by interfacial conductivity and permittivity, respectively, and the COF is a function of both properties.

The transducing element of our IET biosensor is based on the interface COF. First, because the interface COF is influenced by both EI conductivity and permittivity, it is a single frequency measurement capable of monitoring both of these properties simultaneously at a liquid interface. Second, because the COF occurs when interfacial displacement is zero, it is a simple measurement to observe, and can be made at any axial position along the length of the electrode array.

### 7.2.6 Using interfacial crossover frequency to detect specific binding

To detect specific binding at a liquid interface, the EI is sensitized with target probe molecules and forced to flow adjacent to a sample stream containing an analyte. With developed and continuous flow down the T-channel, the fluid at each axial position within the main channel has a different average residence time, and the binding process will be at different time points of diffusive-reactive transport. To monitor binding dynamically during this process, the COF at the EI is quantified at discrete axial positions down the

length of the main flow channel. Changes in EI electrical properties during binding influence the COF. Because specific binding progresses forward in time as fluid flows down the length of the array, biomolecular binding can be electrokinetically quantified in time by measuring the COF at varying positions in axial space down the channel length.

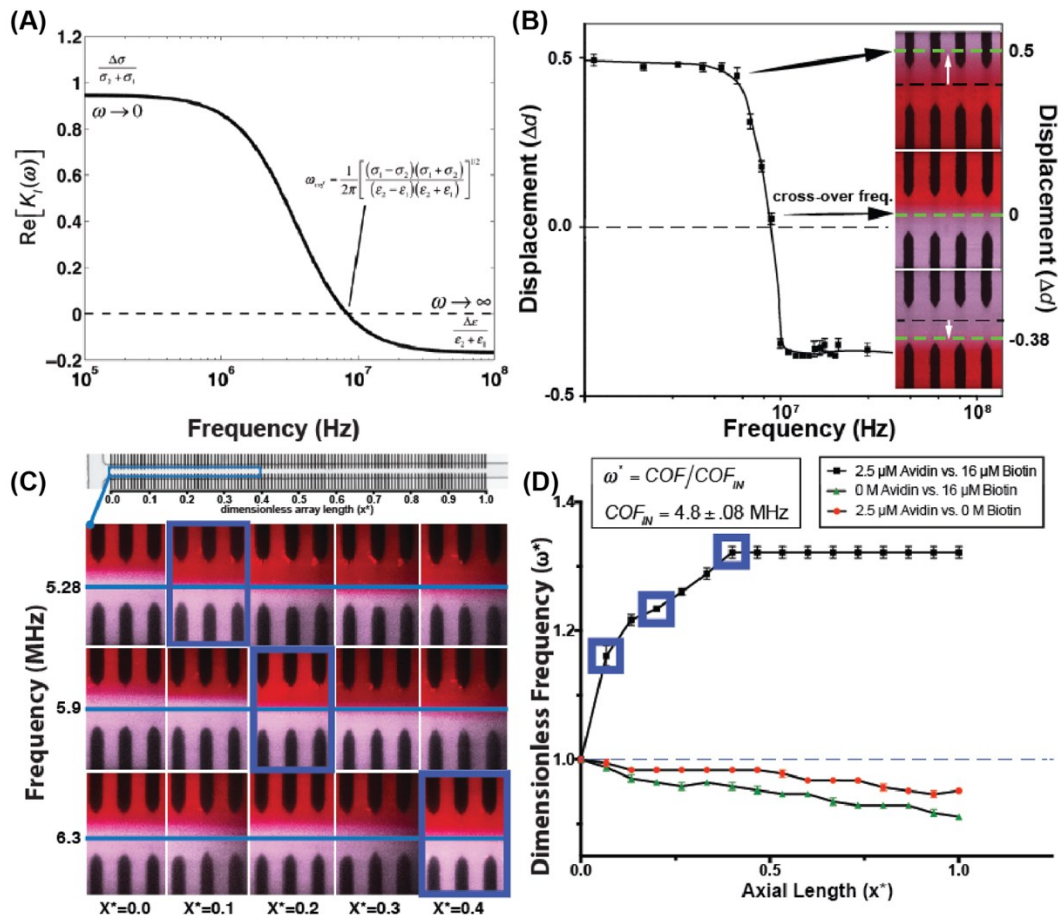


**Figure 7-3. Crossover frequency is influenced by a biomolecular reaction**

(A) Liquid interface polarization (*Equation (7.1)*) plotted as a function of field frequency. Low frequency polarization is driven by differences in electrical conductivity, while the interfacial dielectric constant governs the polarization of the interface at high frequency. A cross over frequency (*Equation (7.2)*) is dependent on both interfacial conductivity and dielectric constant. The crossover frequency increases during biomolecular binding. (B) Dimensionless interface displacement measured at different electric field frequencies. An optical micrograph highlights interface position at low (1 MHz), intermediate (9.2 MHz) and high (20 MHz) field frequencies; (C) Optical micrographs of the electrical interface captured at different positions and electric field frequencies along the length of the electrode array. The interface crossover for each axial position is highlighted in blue and plotted in the adjacent figure; (D) IET sensorgram showing the influence of binding on interface crossover frequency plotted against two biosensor negative controls.

## 7.3 Results and Discussion

### 7.3.1 The IET sensorgram

Our IET biosensor signal was the COF of the liquid interface. We performed this measurement at discrete positions over the entire axial length of the microelectrode array to detect biomolecular binding dynamically in time. We used biotin-avidin as the model system for studying the biosensor response. Avidin binds up to four molecules of biotin with high specificity and affinity, and is a useful binding model for characterizing biosensing systems. To more clearly compare sensor performance against different concentrations of avidin, both experimental variables – the COF and the array position – were rendered dimensionless. Shown in **Figure 7-3C**, the electrode array was rendered dimensionless by its total length (2.0 mm); COF measurements were quantified along a dimensionless axial variable  $x^*$ , spanning the domain  $\{0,1\}$ . To maintain consistent reaction residence times within the electrode array, the fluid flow rate was fixed at 5.0  $\mu\text{L}/\text{min}$ . We performed all biosensing experiments using buffers with constant conductivity and permittivity. Because these properties were constant, the COF at  $x^*=0$  was fixed:  $\text{COF}_{\text{IN}} = 4.8 \text{ MHz} \pm 1\%$ . To track the evolution of the COF over the axial position of the array, the COF was rendered dimensionless ( $\omega^*$ ) by  $\text{COF}_{\text{IN}}$  such that  $\omega^* = 1$  at  $x^*=0$ .

To determine if specific avidin-biotin binding influences the COF of the interface, a COF sensorgram was captured using 2.5  $\mu\text{M}$  avidin flowing adjacent to 16  $\mu\text{M}$  biotin. We used two negative controls for this experiment – one COF sensorgram was taken without biotin, and a second without avidin. Finally, we measured the COF sensorgram along the EI within the electrode array with both avidin and biotin. **Figure 7-3D** shows the  $\omega^*$  vs.  $x^*$  sensorgram from each experiment. In the absence of binding, the interfacial COF

decreases by ~8% over the microchannel length. During avidin-biotin binding, however, the interface COF increases by over 30%, reaching an equilibrium value of  $\omega^* = 1.3$  at a distance  $x^* = 0.4$  down the array.

The polarized interface behaves as a biosensor transducer; specific binding influences the interfacial electrical properties, which are transduced electrokinetically as a change in COF for a given position down the electrode array. The COF changes dynamically, transducing biomolecular binding events over axial length as they proceed forward in time. This concept is reflected in the sensorgram data (**Figure 7-3D**), where the COF appears as a binding curve, increasing over the array length and plateauing as the reaction saturates at the EI. The transduction properties of the EI can be observed optically, as depicted in the confocal micrographs shown in **Figure 7-3C**. As the field frequency is increased, the axial position where no interface displacement occurs shifts. The COF at  $x^*=0.1$ , for example, is 5.28 MHz; no displacement is observed at this point in the array. This frequency is above  $\text{COF}_N$  (4.8 MHz) at  $x^*=0$  and below the COF for any position where  $x^*>0.1$ , so the interface deflects in opposing directions surrounding this inflection point. As the applied frequency is increased, the position of the inflection point shifts, corresponding to a new position-dependent COF. These COF inflections are highlighted with blue boxes in **Figure 7-3C**. They represent COF measurements for three axial positions within the electrode array, and correspond to the sensorgram data points emphasized with square boxes in **Figure 7-3D**.



### 7.3.2 Avidin-Biotin Binding Influences Interfacial Conductivity

The response of the IET sensor is based on the influence of bioaffinity binding on the interfacial electrical properties at the EI. Because the COF is sensitive to both interfacial conductivity and permittivity, COF measurements are not enough to determine the exact electrical influence that biomolecular binding has on the interface. To determine how binding influences the electrical properties across the interface, we measured the net displacement during binding over varying AC field frequency at the saturation position  $x^* = 0.4$  down the electrode array. **Figure 7-4A** shows interfacial displacement spectrum as a function of field frequency for three different avidin concentrations: 0 nM, 25 nM, and 2.5  $\mu$ M. The electrical mismatch of each of the fluids containing both avidin and biotin were held constant for each experiment. As shown above in **Figure 7-3A**, low frequency displacement is dependent solely on the interfacial conductivity and high frequency displacement depends only on interfacial permittivity. From the spectra presented in **Figure 7-4A**, avidin-biotin binding influences the low frequency displacement measurements – displacement increases with avidin concentration. At high frequency, however, interfacial displacement remains constant and is not influenced by interfacial binding. **Figure 7-4B** shows a series of confocal micrographs depicting this observation. At 1 MHz the displacement increases as avidin concentration increases (**Figure 7-4B – left**), and high frequency (20 MHz) displacement remains unaffected with binding (**Figure 7-4B – right**).

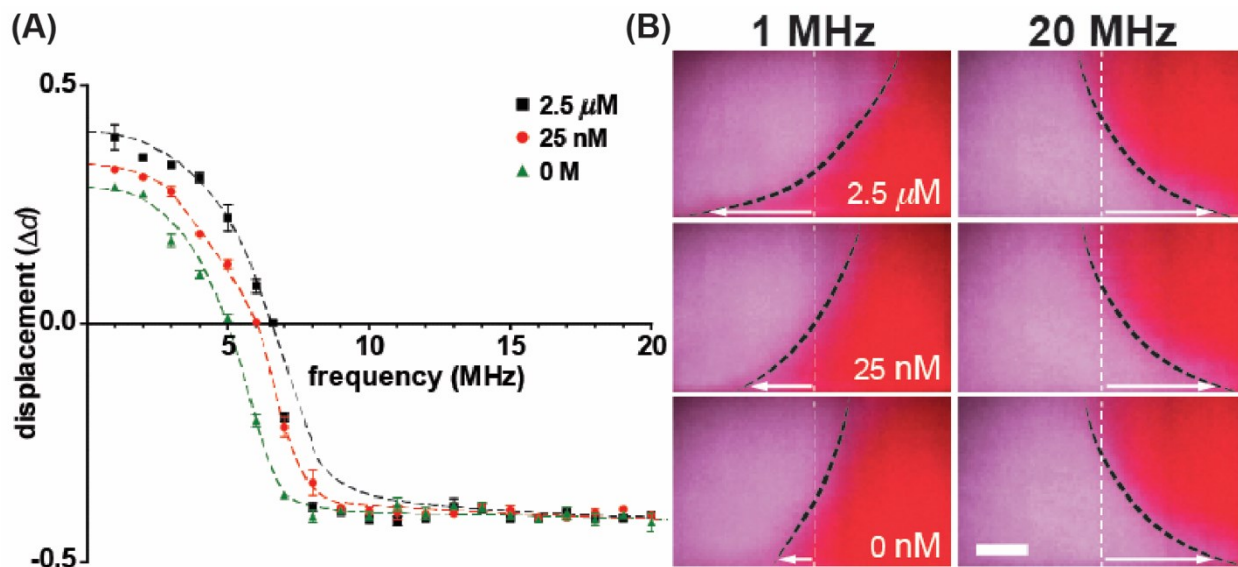


**Figure 7-4. Normalized displacement is affected by a biomolecular reaction**  
**(A)** Interface displacement measured over increasing concentrations of avidin: 0 M, 25 nM, and 2.5  $\mu\text{M}$ . **(B)** Confocal micrographs illustrate interface position at low (1 MHz) and high (20 MHz) for increasing avidin concentrations. Scale bar, 20  $\mu\text{m}$ .

The displacement measurements demonstrate that the biomolecular binding of avidin-biotin increases the interfacial conductivity ( $\Delta d$  increases at low frequency with binding), but not alter the interfacial permittivity ( $\Delta d$  remains unaffected at high frequency) (**Figure 7-4**). While fDEP can give insight as to how the interface is being influenced electrically, it cannot currently provide any mechanistic information about why this increase is occurring. The increase in interfacial conductivity may be due to counterion release during binding. One possibility is that a diffuse layer of spatially confined counterions surrounds the charged proteins in solution. During binding, ions are released, which could potentially increase the electrical conductivity in the vicinity of the interface, and produce an increase in COF. Another possibility could be due to a change in electrophoretic mobility due to the negative charge of the bound biotin molecule, which would make the complex a more effective charge carrier at the interface. Currently,

however, the precise physical mechanism for the interfacial conductivity increase remains unknown.

### 7.3.3 Selective and Specific Biosensing in a BSA Background

Surface-based heterogeneous biosensors can suffer from non-specific adsorption of background proteins, which can reduce sensor sensitivity. The IET sensor utilizes a liquid interface as a biorecognition substrate, and therefore is much less prone to suffer from biofouling or non-specific adsorption of proteins to the sensor surface. However, background interference from non-specific proteins is a major concern when working with real-world clinically relevant samples. To investigate sensor performance in the presence of an abundant background protein, we challenged the sensor with 5 mg/mL of bovine serum albumin (BSA). In order to be able to compare our findings with the avidin-biotin experiments performed without a background (**Figure 7-3D**), the inlet COF and microchannel flow rate were held to less than a 1% deviation from their previous experimental values. Shown in **Figure 7-5**, the COF increases about 25% over the length of the array when taken with 2.5  $\mu$ M avidin flowing adjacent to 16  $\mu$ M biotin in the presence of a serum background. To investigate the ability to design specific bioaffinity response into the EI, we removed avidin from the sample stream and replaced it with a 100 nM concentration of anti-BSA. Shown in **Figure 7-5**, the sensor responds to the presence of BSA instead of avidin. Two control experiments were performed to ensure these measurements were specific – removal of anti-BSA and avidin from the sample stream does not produce an increase in the COF along the length of the array.

There are several important features to note regarding the sensor performance depicted in **Figure 7-5**. First, as shown, when compared to the sensorgram without BSA, the selectivity of the sensor towards avidin in the presence of serum decreases by ~30%. This decrease could be due to several factors. There is a possibility that non-specific charge-charge interactions between BSA and the surrounding biomolecules in solution could be influencing the interfacial conductivity and total concentration of avidin available for binding. However, as shown in the BSA sensorgram in **Figure 7-5**, the addition of background avidin to the BSA solution during binding with anti-BSA does not affect the magnitude of the sensorgram. This suggests that non-specific interactions between BSA and avidin are minimal.

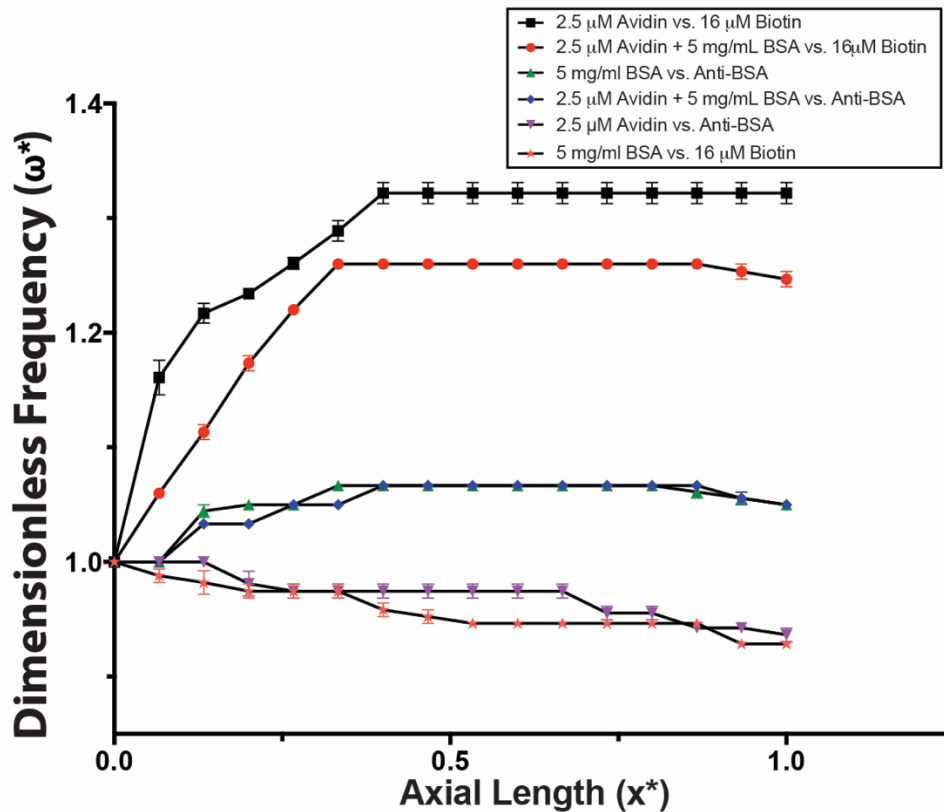


**Figure 7-5. Sensorgram with a background protein concentration**  
 IET sensorgram illustrating selective sensor response to both BSA/Anti-BSA and avidin/biotin binding.

Because the sensor COF is driven by a combination of both target-receptor binding and interfacial smoothing by ionic diffusion, we speculate that the addition of BSA hinders the rate of avidin diffusion towards and across the interface, which slows the rate of the binding and leads to a lower sensor COF. Finally, it is worth noting that the reaction between BSA and anti-BSA does not produce the same change in COF when compared to the avidin and biotin reaction. We hypothesize this difference is due to the difference in binding kinetics between these two reactions. In comparing the  $K_d$  of each reaction,  $10^{-15}$  and  $10^{-4}$ , for the Avidin – Biotin and BSA – Anti-BSA reaction, respectively, the reaction between BSA and anti-BSA occurs at a slower rate than that of avidin and biotin. Since the reaction time is slower, binding requires a longer distance down the axial length of the microchannel. Because the diffusion of ions across the electrical interface is constantly occurring and decreasing the interfacial conductivity, the reaction requiring a greater length scale must compete with an ever-decreasing interfacial conductivity, which ultimately leads to a smaller magnitude in the change of COF. Future work will focus on developing a better understanding of these physicochemical mechanisms that link species reaction and diffusional rates with interfacial conductivity in order to better optimize sensor response.

#### **7.3.4 Label-Free Femtomolar Detection in BSA**

We next performed a series of experiments to determine the IET sensor's limit of detection (LOD) and how the IE performs as a transducer against an abundant background protein (5 mg/mL BSA). The IET biosensor response was measured as a function of avidin concentration, ranging from 50 fM to 2.5  $\mu$ M, both with and without BSA.

**Figure 7-6** shows a series of sensorgrams for avidin-biotin binding at the EI (**Figure 7-6A**) and with a BSA background (**Figure 7-6B**). The net IET sensor response increases with avidin concentration, and eventually levels to a constant value some distance down the electrode array. The eventual leveling of the IET signal at a given position down the array length can be attributed to the saturation of the interface with bound avidin-biotin complex; avidin is depleted from the local EI and the sensor response saturates.

The magnitude of each saturated sensorgram response at a fixed distance down the electrode array ( $x^* = 0.5$ ) was isolated and plotted as a function of avidin concentration. The resulting calibration curve is shown in **Figure 7-6C** for an EI without BSA and in **Figure 7-6D** for the interface subjected to a serum background. For each analytical curve, the sensor exhibits a linear response with increasing concentrations of avidin up to 500 fM, as shown in the subplots of each figure (**Figure 7-6C, D**). Beyond this linear concentration range, the sensor deviates and begins to level off, eventually saturating at an avidin concentration at approximately 1  $\mu$ M. The concentration LOD was calculated using the 3-sigma method ( $S/N = 3$ ) for each binding curve. Without background BSA, the sensor LOD was 209 fM, while the addition of BSA decreased sensor sensitivity with a corresponding LOD of 626 fM.

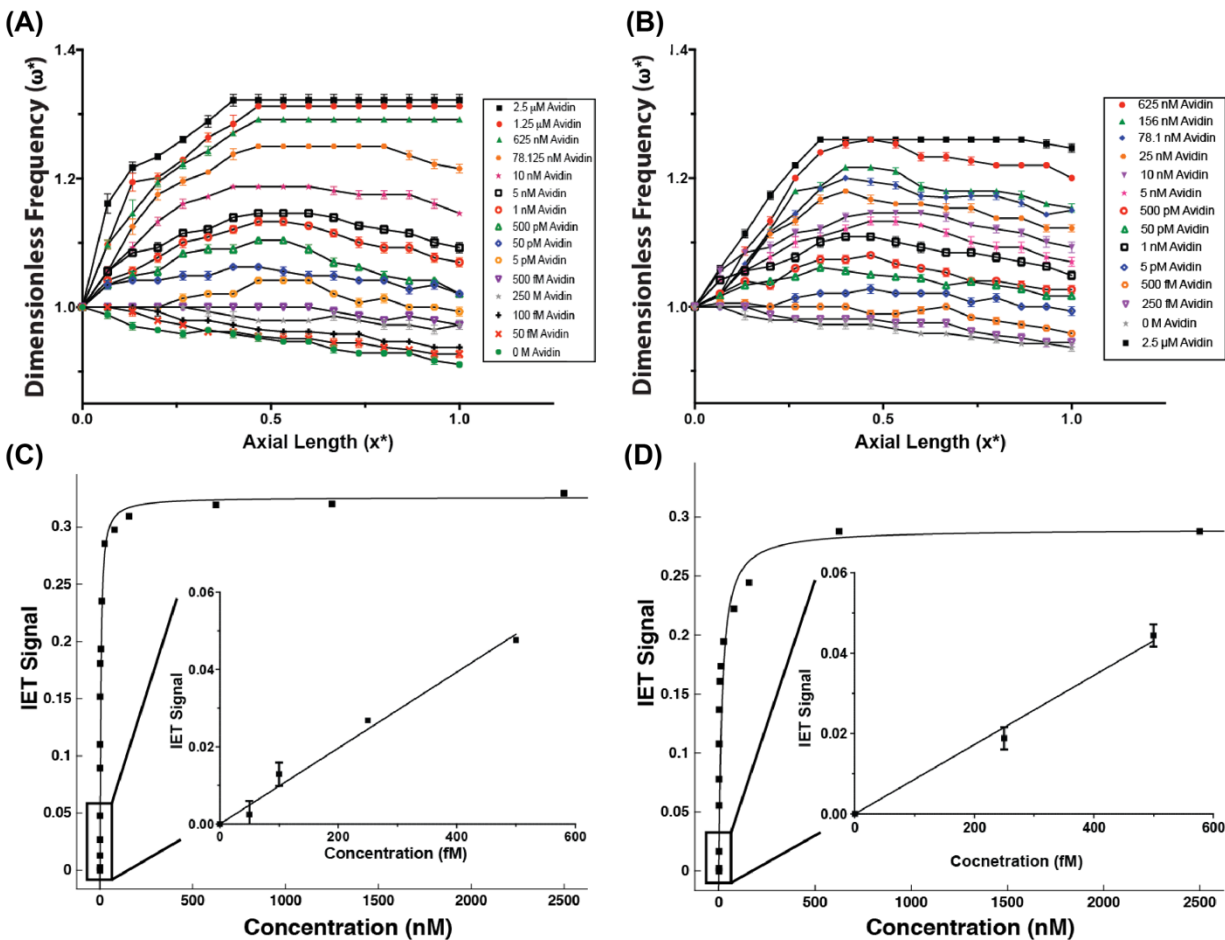


**Figure 7-6. Theoretical limit of detection from an IET sensorgram**

(A) IET sensorgram of increasing concentrations of avidin; (B) Sensorgram illustrating sensor response against a background of serum albumin; (C) Sensor binding curve showing IET limit of detection without a BSA background; and (D) with a BSA background.

## 7.4 Conclusion

In this chapter, we presented a sensitive and selective label-free electrokinetic biosensor for detecting biomolecules at electrically polarizable liquid interfaces. Biomolecular binding occurs at the diffuse electrical interface formed between two co-flowing microfluidic laminar streams with different electrical properties. The biosensor approach is based on measuring the electrical field-induced displacement frequency response of this interface, which is sensitively influenced by specific biomolecular binding.

In this manner, the biosensor design utilizes this interface as substrate for biomolecular binding, and its motion in an electric field as a signal transducer. We have shown that binding increases the electrical conductivity at the interface, which is transduced as a change in interfacial frequency response, and forms the basis for our presented interfacial electrokinetic transduction (IET) method. The system developed can detect low femtomolar avidin concentrations against a 5 mg/mL background of serum albumin, and can be reconfigured to detect other proteins. The IET sensor has the potential be extended to other biomolecular systems for the detection of disease biomarkers in serum and urine. Furthermore, because binding occurs dynamically in time over the length of the microchannel interface, it should be possible to use this IET approach to study the binding kinetics of a variety of specific ligand-receptor pairs. Finally, while fluorescent microscopy was used in this chapter to measure interface position, future work will focus on developing inexpensive methods for measuring interface displacement electrically, extending our IET approach to more complex samples such as whole blood and urine, reducing interfacial diffusion of the electric interface, and developing reactive transport models to study binding kinetics at the liquid interface.



# 8 *Heterogeneous, label-free detection at liquid interfaces with interfacial electrokinetic transduction (IET)*

---

## **8.1 Introduction**

Bead-based biosensors use nanoparticles with surface-immobilized receptors as a biosensing substrate for the detection of a wide variety of biomolecular targets including proteins<sup>205</sup>, DNA, and bacteria<sup>206,207</sup>. In comparison to traditional microarray technology, the high nanoparticle surface-to-volume ratio can lead to increased detection sensitivity and reduced assay time. Bead-based methods, for example, have been shown to increase the limit of detection (LOD) in SPR sensing<sup>208</sup>, fluorimetric assays<sup>209</sup>, and electrochemical amperic detection<sup>210</sup>, and have been used in a broad range of colorimetric<sup>207</sup>, enzymatic<sup>211</sup>, mechanical<sup>212</sup>, and electrochemical assays<sup>213</sup>.

Nanoparticle-based biosensing is often accomplished using a heterogeneous support, where particles are adsorbed onto a solid surface<sup>214</sup> or a sol-gel matrix<sup>215</sup>, functionalized, and flushed with a fluid or gas containing the relevant target analyte. Because colloids must be assembled and functionalized, these surface-based methods typically require multiple rinsing/drying steps<sup>216,217</sup>, and can suffer from functional group crowding<sup>218</sup> and surface fouling<sup>219</sup>.

To reduce detection time and assay complexity, and to improve portability, biosensors can be integrated with microfluidics. With microfluidics, biomolecular binding can be poised to occur in solution phase at the fluid interface formed between two co-

flowing laminar liquid streams. This sensing strategy is robust and has been successfully applied to detecting DNA hybridization<sup>220</sup> and for protein immunoassays<sup>221</sup>. Matthews et al., for example, reported a novel homogenous biosensor that used a laminar aqueous interface as a biorecognition substrate. Binding was initiated by driving two different fluids – one containing a target analyte and a second with complimentary receptor molecules – to flow side-by-side along a main microfluidic flow channel. Biomolecular binding occurred at the fluid interface as target and receptor molecules diffused between the two fluids. Using fluorescent microscopy, binding kinetics were quantified by measuring fluorescent intensity produced from bound product at varying distances down the microchannel length<sup>222</sup>.

Aqueous liquid interfaces are easy to create using “T-channel” or “Y-channel” microfluidic geometries<sup>112,182</sup>. When driven to flow side-by-side at low Reynolds number, the two fluids produce a quasi-stable liquid interface where mass transport is driven strictly through diffusion<sup>223</sup>. Biosensing by diffusion and binding at the fluid interface has several advantages over traditional binding on a solid substrate. First, because biomolecular binding occurs in solution phase, diffusion-limited binding occurs over much shorter timescales when compared to a surface. Second, the interface is continually replenished and renewed with molecular target and biorecognition receptors at any given position in the microchannel, and is therefore not subject to surface fouling and non-specific adsorption.

In this chapter, we extend the usefulness of IET<sup>224</sup> to that of nanoparticle bead-based biosensing assays, and show that biomolecular binding on nanoscale particles influences the deflection of a microfluidic liquid interface. Specifically, our strategy uses

a suspension of surface functionalized nanoparticles as a microfluidic substrate for biomolecular recognition. The particles are functionalized with either streptavidin or Protein A molecules, which serve as specific binding receptors for biotin or human IgG, respectively, in solution. We demonstrate that specific binding on the nanoparticles produces a change in interfacial electrical conductivity, which can be detected by IET. This colloid-based biosensing strategy does not use labels, amplified signaling, or methods for concentrating the analyte samples and is capable of detecting biotin concentrations as low as 500 aM and physiologically relevant human IgG at concentrations down to 1.25 mg/mL.

## **8.2 Materials and Methods**

### **8.2.1 Creating the electrical interface**

To create a biosensing system at the liquid interface, we integrated a biomolecular recognition event between the two fluids, where the PBS stream contained a suspension of functionalized nanoparticles and the adjacent phase containing either the target analyte or a negative control (**Figure 8-1**). We used both biotin and human IgG, and streptavidin and Protein A-functionalized nanoparticles as biomolecular systems to test our particle-based method. Because of the strong binding affinity, biotin (Sigma-Aldrich) and 100 nm streptavidin-coated silica nanospheres ( $\zeta = -34.6$  mV) (Corpuscular Inc.) were first used as a model bioreaction and 100 nm carboxylated silica nanospheres ( $\zeta = -34.3$  mV) (Corpuscular Inc.) were used as a non-reactive negative control. A 4 mM biotin stock solution was made in 0.8M AHA and subsequently diluted to experimental concentrations ranging between 500 aM and 16 M. The PBS stream contained the nanoparticle

substrate: streptavidin-coated particles were triple washed and re-suspended in PBS solution and particle suspensions were maintained at 0.0375 wt% for all experiments unless specified otherwise. Human immunoglobulin G (IgG) (Sigma-Aldrich) and 350 nm protein-A- coated silica nanospheres (Corpuscular Inc.) served as a more physiologically relevant reaction scheme. Human IgG was dissolved in deionized water and diluted to experimental concentrations (1.25, 3, 6 and 12mg/mL). The receptor/binding solutions were driven side-by-side using a constant pressure source and the resulting fluid interface was imaged using confocal microscopy by labelling the AHA “red” with 10ng/mL Alexa Fluor 594 and the adjacent PBS stream (containing either streptavidin, Protein A, or carboxylated nanoparticles) “green” with 10 ng/mL Alexa Fluor 488.

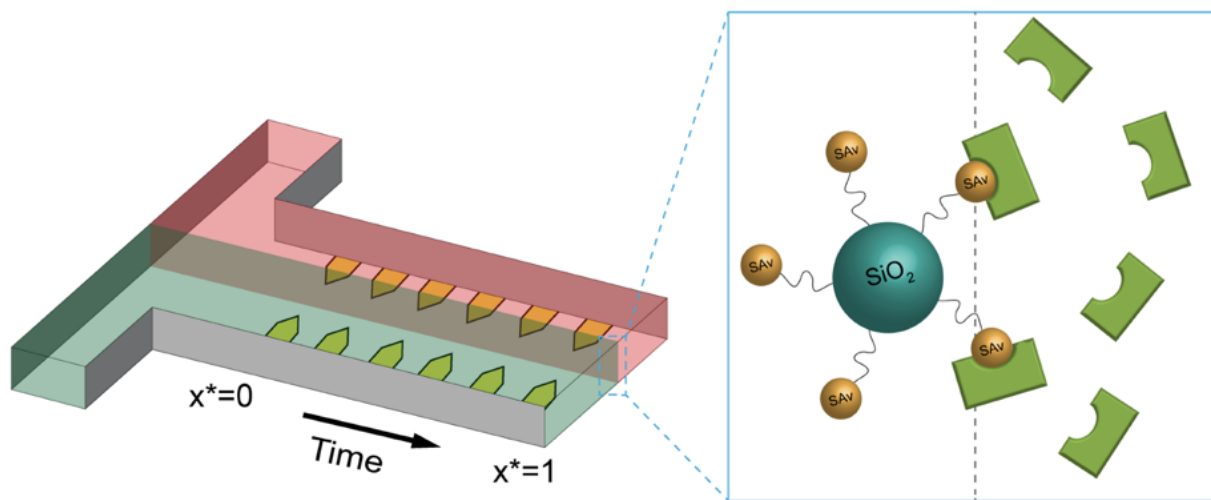


### Figure 8-1. Heterogeneous IET Detection

Schematic of the microfluidic T-channel device. Silica particles are functionalized with streptavidin and suspended in buffer. Streptavidin-biotin biorecognition occurs at the electrical interface created by the two coflowing liquids.

## 8.3 Results and Discussion

### 8.3.1 Maxwell-Wagner Polarization

In order to determine if our existing MW theory is appropriate to apply to a dilute colloidal suspension we first performed fDEP experiments to determine the interfacial COF as a function of electrolyte conductivity with a dilute colloidal suspension of 100 nm carboxylated silica particles in PBS buffer. To obtain an accurate COF reading at the interface before diffusive mixing occurred, we measured the COF near the entrance of the microfluidic T-junction ( $x^* = 0.2$ ) where the interface was sharp and the COF was uninfluenced by diffusive mixing. The resulting COF data is plotted against our theoretical model (*Equation (7.1)*) in **Figure 8-2C** for varying concentrations of colloid weight percent. The data show good agreement with the MW theory for both the pure liquid–liquid and liquid- colloid experiments. From **Figure 8-2C**, we therefore assume that the colloidal suspensions used in this chapter are dilute enough to be mathematically and electrically approximated as a pure fluid, and that the presence of particles does not require additional modifications to our existing polarization model to accurately predict the fDEP response of the fluid interface.

We next measured the net displacement of the interface at different electric field frequencies and interfacial electrical conductivities in order to determine how differences in electrical conductivity across the liquid interface influence the COF and magnitude of the interfacial deflection. To accomplish this, we adjusted the conductivity of the colloidal suspension while keeping the weight percent and adjacent stream conductivity constant. In **Figure 8-2D**, we plot the experimental displacement for three different interfacial conductivities ( $\sigma = 0.101, 0.268$  and  $0.418$  mS/cm). Each COF (labeled A–C) are

highlighted in **Figure 8-2C**. The data demonstrates that the magnitude of the interfacial displacement increases with interfacial conductivity at low field frequencies below the COF. However, the high frequency displacement remains unaffected since frequency regime is only influenced by dielectric differences between the two fluids<sup>181</sup>.

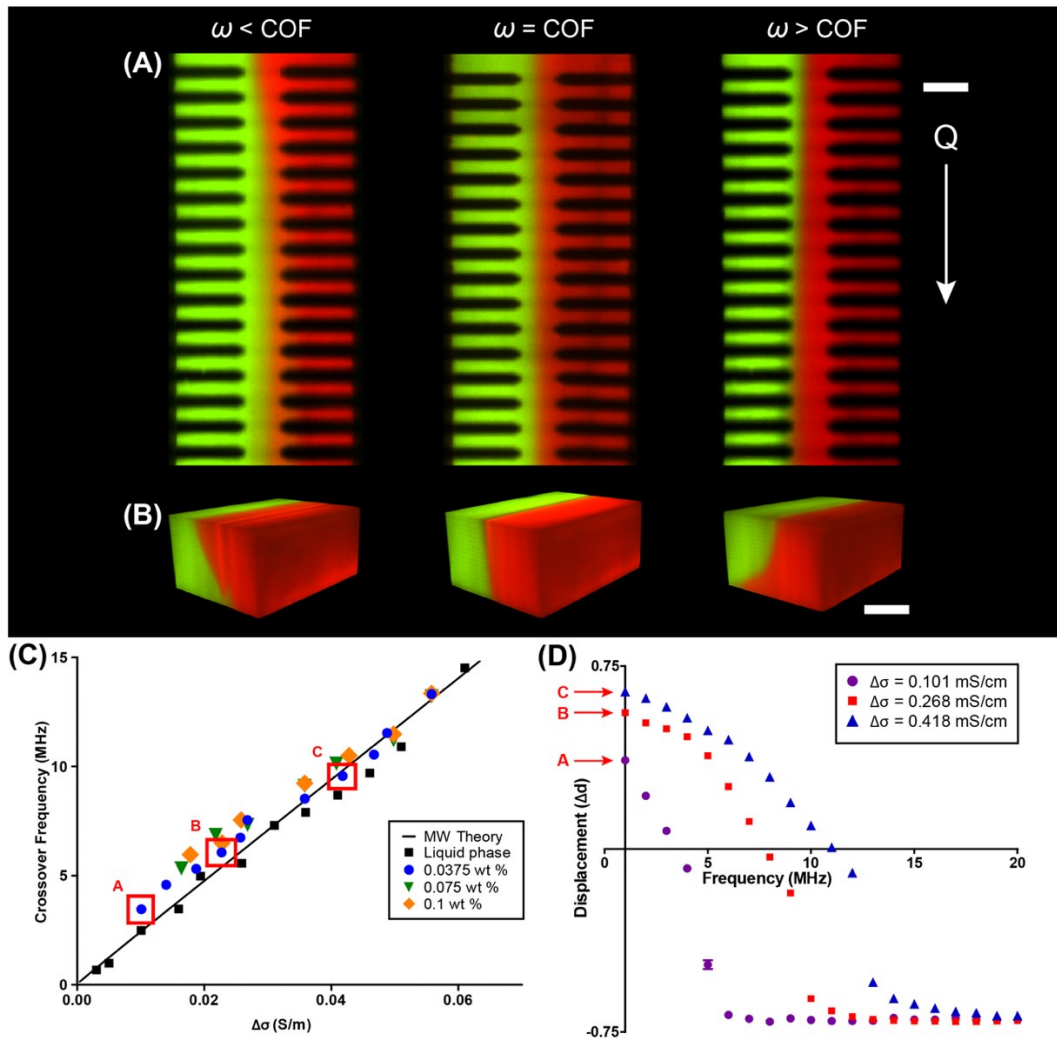


**Figure 8-2. fDEP crossover frequency with nanoparticle suspension**

(A) Top-down confocal images of the microfluidic channel, showing interfacial displacement for frequencies below the crossover, at the crossover, above the crossover. Scale bar, 25  $\mu\text{m}$ . (B) 3D confocal images showing the tilt of the electrical interface for frequencies below the crossover (left), at the crossover (center), and above the crossover (right). Scale bar, 50  $\mu\text{m}$ . (C) Crossover frequency plotted as a function of conductivity difference. The MW Theory line is plotted as *Equation (7.2)* for fixed values of  $\epsilon_1 = 78.2$  and  $\epsilon_2 = 110$ . Lettered boxes are selected from the 0.0375 wt% data. (D) Displacement of the electrical interface as a function of applied frequency. Each complete dataset's COF is highlighted in a lettered box in (C).

### 8.3.2 Biotin-streptavidin binding

With the frequency response of a non-reacting interface known, we next sought to determine if specific biomolecular binding on nanoparticles influences this behavior. To detect specific binding at the electrical interface, we flowed one stream with a target probe against an adjacent stream of analyte. We investigated a well-known model reaction: biotin and streptavidin. The biomolecular reaction between biotin and streptavidin are strongly associated with a very small dissociation constant,  $K_d \sim 10^{-15} \text{ M}^{225}$ , and therefore the reaction is rapid, nonreversible and serves as a good model system to experimentally validate our biosensing strategy. We used streptavidin conjugated nanoparticles as a substrate for binding. With a small diffusional coefficient ( $10^{-8} \text{ cm}^2/\text{s}$ )<sup>226</sup>, the particles provided a well-defined region of active binding sites at the liquid–liquid interface for biotin, a smaller, quickly-diffusing molecule, to rapidly diffuse towards the nanocolloidal interface and bind. First, biotin in an excess concentration (16  $\mu\text{M}$ ) was co-flowed against a 0.0375wt% suspension of streptavidin-silica nanoparticles. We applied an AC electric field across the interface and measured the COF at the inlet, which we denoted here as  $\text{COF}_{\text{in}}$ . Next, we performed subsequent COF measurements at varying positions down the electrode array and normalized the resulting response by  $\text{COF}_{\text{in}}$ . Shown in **Figure 8-3**, the biotin-streptavidin system produced an increase in the interfacial COF with axial position. The COF continued to increase down the axial length of the channel before reaching a plateau and declining, which we believe is indicative of a combination of binding saturation in the vicinity of the nanocolloidal-functionalized interface and diffusional smoothing between the two fluid streams.

We next performed a series of control experiments to validate our COF

measurements. First, we performed the same COF experiments without biotin and observed that the COF does not increase, but rather it decreased over the axial channel length (**Figure 8-3C**). We attribute this decrease to diffusional blending across the interface, where ion diffusion gradually reduces the sharp differences in electrical properties and reduces the interfacial COF. As a second non-reactive negative control, we replaced the 100 nm streptavidin-coated silica nanospheres with carboxylated silica beads of the same size and wt%, and tested the interface response against the same excess concentration of biotin (16  $\mu\text{M}$ ). The surface carboxyl groups (COOH) are meant to emulate the nanocolloidal interface, while providing a non-reactive surface to observe any false positive signal from non-specific adsorption. Similar to the first negative control experiment, the COF again decreased (**Figure 8-3A**).

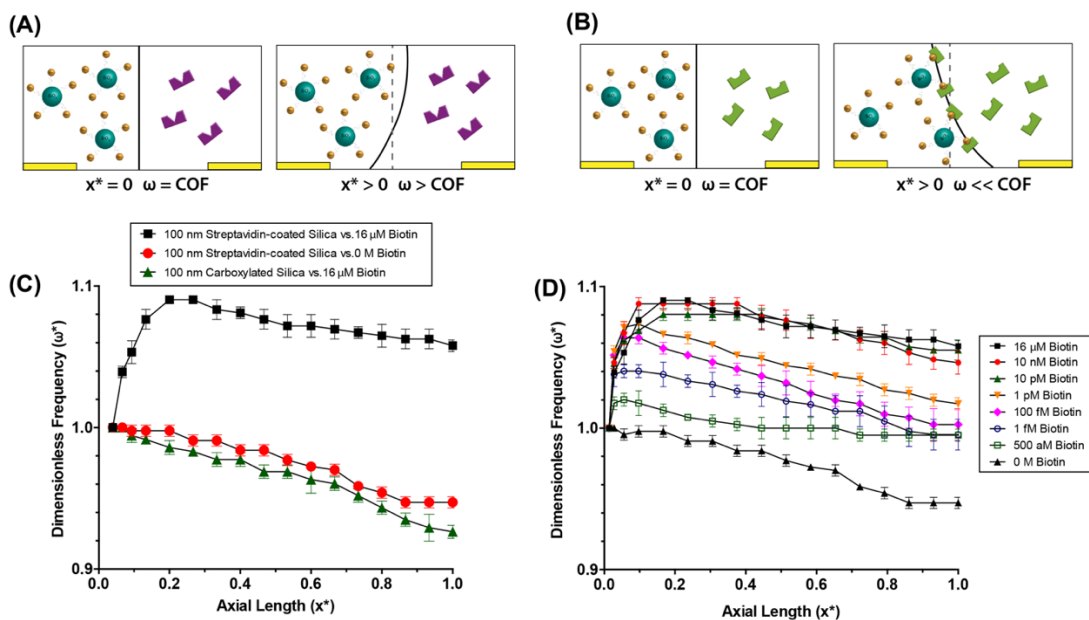


**Figure 8-3. IET Bead-Based Biosensing Assay**

(A) A schematic illustration of the case where no reaction is present. Down the the length of the channel, the crossover decreases. (B) In the case of a biomolecular reaction, the crossover increases as the reaction propagates down the channel. (C) Detection sensorgram showing positive detection in the presence of a reaction, with decreasing control signals. (D) Limit of detection sensorgram showing the lowest biotin concentration detected with the colloid-assisted platform.



### 8.3.3 Limit of detection and varying binding sites

We then repeated these biosensing experiments with different biotin concentrations varying several order-of-magnitude ranging between 16  $\mu\text{M}$  and 500 aM (**Figure 8-3D**). The biosensor response, as determined by the interface COF, increased with increasing concentrations of biotin (**Figure 8-3**). Since the wt% for each experiment was fixed at 0.0375%, the number of available binding sites remained the same for each experiment. As is expected with a substrate-based sensor response, the interface was observed to saturate for the given particle wt% at a biotin concentration of 10 pM. Above this concentration the COF signal was not influenced by further increases in the biotin concentration. Using the 3-sigma method, we determined the experimental LOD for biotin to be 500 aM. Given the dimensions of the microfluidic device (100  $\mu\text{m}$  main channel width  $\times$  35  $\mu\text{m}$  channel height) and a total internal volume of 60 nL, this concentration translates to approximately 36 molecules of biotin in the device at any given time.

In a related experiment, we varied the weight percent of the nanoparticles from 0.005–0.0375wt% in order to determine if the COF is influenced by the number of available binding sites at the liquid interface. Depicted in **Figure 8-4**, the COF response decreases with decreasing nanoparticle wt%. For this experiment, we also decreased the interfacial conductivity from 0.35 mS/cm to 0.24 mS/cm. It is interesting to note that this reduction increased the contribution of the reaction relative to the baseline conductivity difference, and thus led to an increase the magnitude of the COF signal response. This increase can be observed by comparing the sensorgram data for 16 M biotin in **Figure 8-3**, where the maximum signal response is 1.09, to the case in **Figure 8-4**, where the maximum response increased to 1.19. These sensorgrams were compared against two

different controls using carboxylated silica particles at both the low (0.005) and high (0.375) wt% concentrations. Shown in **Figure 8-4**, the COF is not influenced by the presence of varying concentration of non-reactive nanoparticles, and only increases when binding sites are available for biotin.

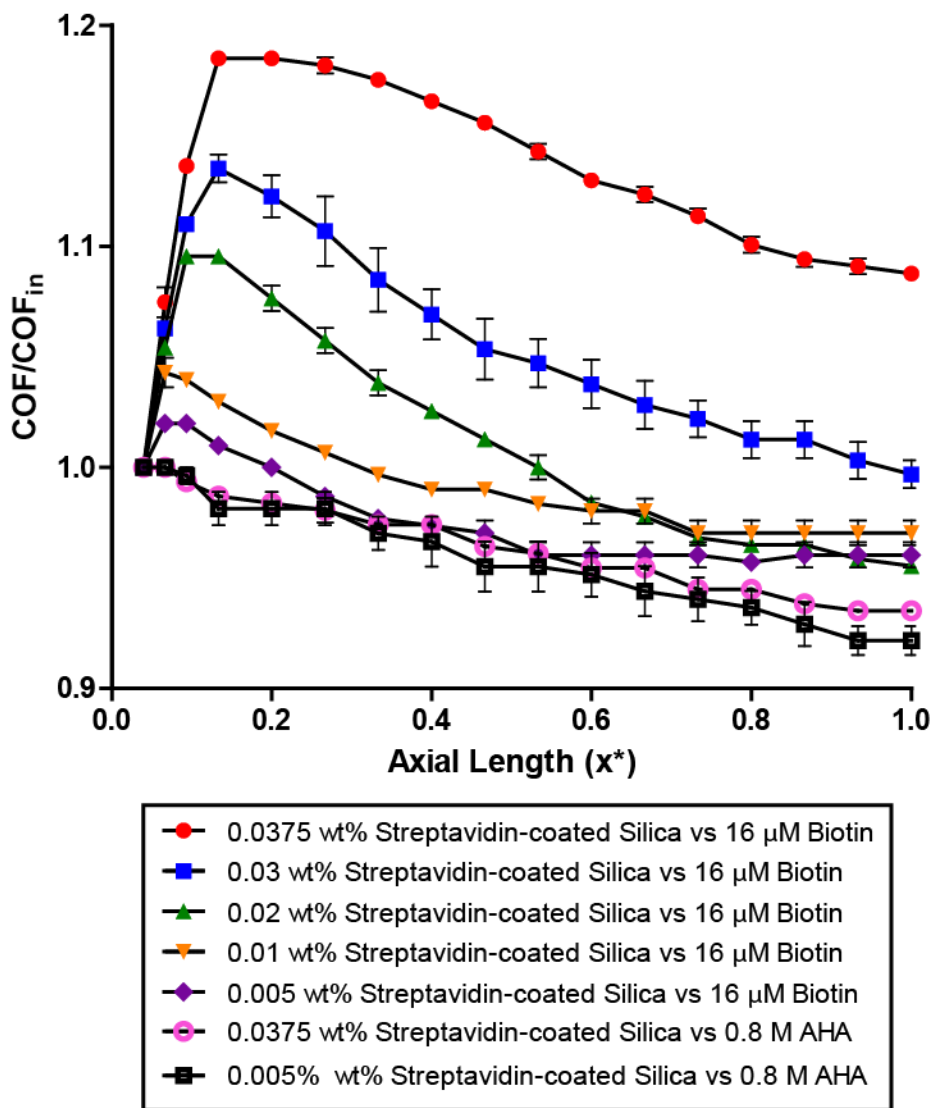


**Figure 8-4. Streptavidin Limited Detection by Varying Particle wt%**

Sensorgram illustrating the decrease in signal with decreasing weight percent of streptavidin-coated particles.

### 8.3.4 Background protein and human IgG detection

We next performed a series of experiments to test the robustness and specificity of the biosensor. First, we introduced a background of 5 mg/mL bovine serum albumin (BSA) to the biotin stream. Shown in **Figure 8-5**, we observed that the presence of BSA reduced the COF signal, but it is still capable of detecting biotin. In moving toward detection of physiologically relevant targets, we then determined if we could detect the presence of human IgG in solution using a suspension of 350 nm silica nanoparticles coated with protein A. The affinity of protein A binding to human IgG is reported to be on the order of  $K_d \sim 10^{-10}$  M<sup>227</sup>, five orders of magnitude weaker than biotin-streptavidin. In **Figure 8-6**, we were able to detect human IgG at concentrations as low as 1.25 mg/mL, which is comparable to relevant concentrations used in modern ELISA assays<sup>228</sup>.

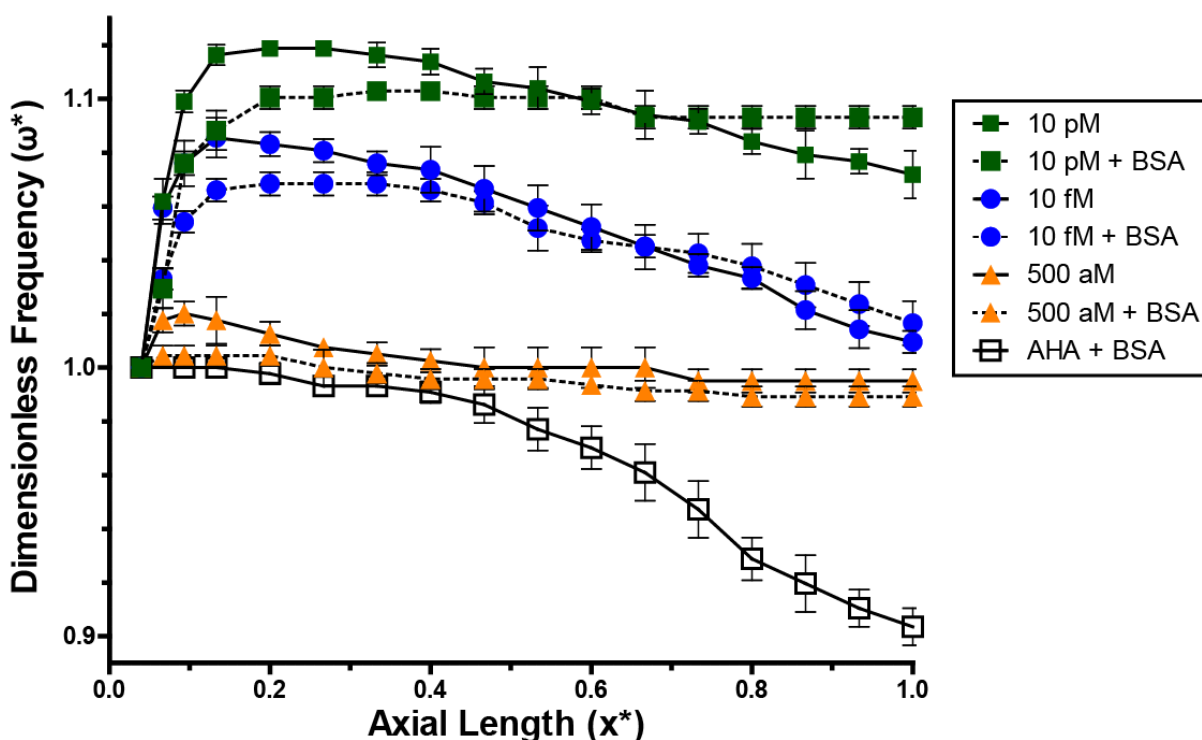


**Figure 8-5. Biotin Detection in BSA Background**

Sensorgram illustrating the ability of the fDEP biosensor to detect biotin-streptavidin binding in a background of 5 mg/mL BSA.

### 8.3.5 Product formation affects interfacial conductivity

Finally, we sought to use our polarization model to determine the electrical mechanism for why biomolecular binding increases the interface COF. In **Chapter 7**, we demonstrated that biomolecular binding in solution without nanoparticles produces a local increase in electrical conductivity difference across the liquid interface. This was demonstrated by measuring the magnitude of the interfacial deflection for different analyte concentrations during binding. This method is possible because the displacement of the interface is solely dependent on differences in electrical conductivity and permittivity below and above the COF, respectively. Therefore, by measuring the interfacial motion at both low and high frequency we can determine how the electrical conductivity and the permittivity across the interface are influenced by the reaction. For reactions without nanoparticles, we showed that increased analyte concentration only produced a measurable change in the interfacial displacement at low field frequency (e.g. only influences electrical conductivity) and fDEP motion at high frequency above the COF was not influenced by binding.

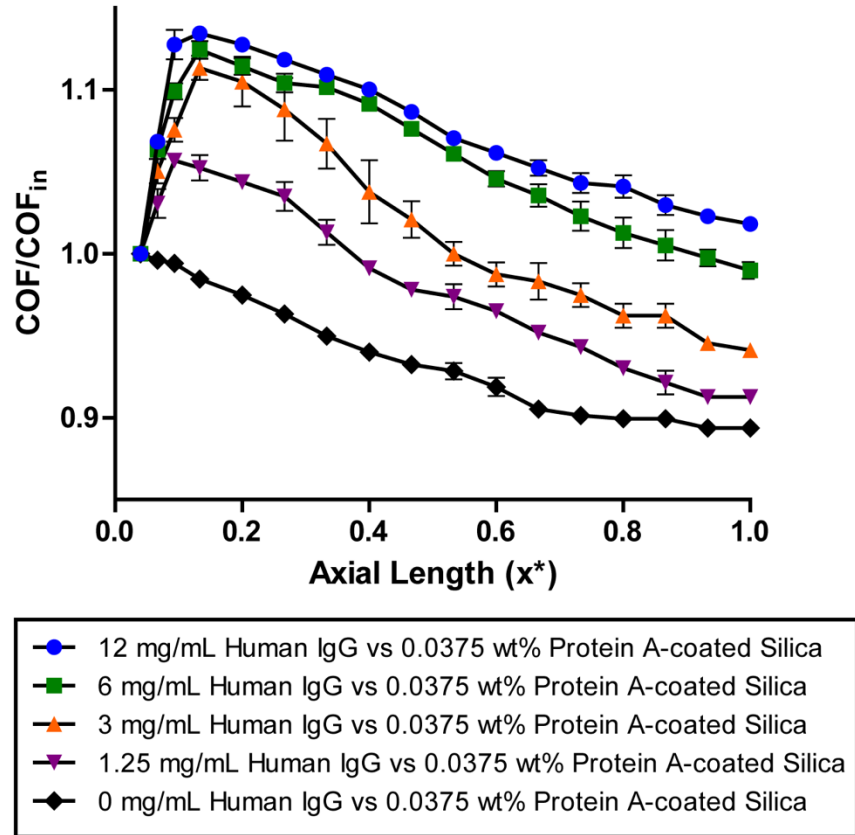


**Figure 8-6. Heterogeneous detection of human IgG**

Detection of Human IgG-Protein A Binding. Detection sensorgram showing positive detection of human IgG with 350 nm silica nanoparticles coated with protein A.

To determine what interfacial electrical properties were influenced by binding on nanoparticles, we measured the magnitude of interfacial deflection at varying voltages (1–20 V<sub>pp</sub>) and frequencies both below (500 kHz) and above (40 MHz) the COF for systems with and without a nanoparticle-based biomolecular reaction. In the presence of a biotin-streptavidin reaction, low frequency displacement was influenced by binding and no difference was observed at high frequency (**Figure 8-7**). Based on these experiments and our MW polarization model, biotin binding on streptavidin nanoparticles increases the local electrical conductivity difference across the liquid interface which produces an increase in the interfacial COF. It is worth noting that our fDEP method is unable to

determine the mechanism for this conductivity increase. We speculate that the negatively charged nanoparticles shed ions in their diffuse cloud during binding, which could account for the local increase in electrical conductivity. Future work will focus in understanding the physical mechanism surrounding this observed conductivity increase.

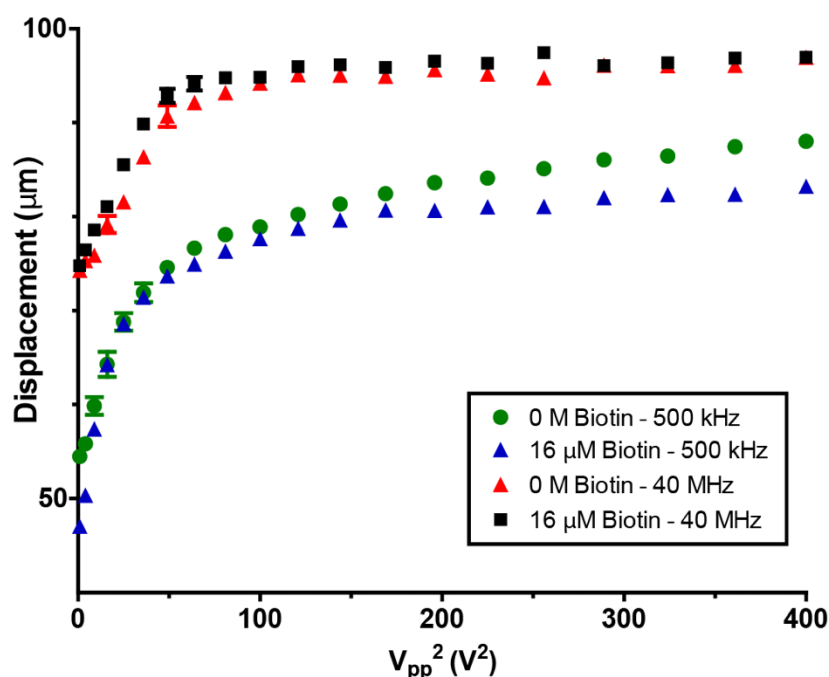


**Figure 8-7. Influence of Binding Reaction on Electrical Properties Measured by Interface Displacement**

Displacement of the electrical interface versus applied voltage squared for both the low and high frequency case, in the case of a biomolecular reaction and a negative control. The divergence of the low frequency data suggests that the presence of a reaction alters the local conductivity at the electrical interface.

## 8.4 Conclusions

We have presented results that demonstrate the ability to perform label-free detection of biotin and human IgG on nanoparticles in solution using fluidic dielectrophoresis. Using our method, we quantified the degree to which a microfluidic liquid interface deflected in an external AC electric field and showed that binding on particles in solution influences the electrical conductivity in the liquid phase at the

interface. This electrical difference produced a measurable increase in the interfacial crossover frequency. Using this approach, we were able to detect biotin-streptavidin binding at low 500 aM concentration and human IgG at concentrations of 1.25 mg/mL. We experimentally demonstrated that these biomolecular reactions produce a local increase in the electrical conductivity difference at the fluid interface. The interface only produced an increase in crossover frequency when specific binding sites were available, and exhibited a saturation response when all binding sites were depleted from the fluid interface and the crossover frequency decreased when the number of available binding sites were decreased. When compared to the previous work conducted in solution, the addition of functionalized nanoparticles increased the detection sensitivity for biotin by two orders of magnitude. Future work will involve developing this biosensing strategy for testing analytes in physiologically relevant samples. Nanoparticles can very easily be functionalized with the relevant receptors to detect malaria, various cancers, and for other diagnostic exams that require femtomolar detection capabilities. Given the nature of the microfluidic flow device, our fDEP biosensor can also be used to dynamically monitor reaction propagation and reaction kinetics since we can obtain a complete reaction sensorgram by taking COF measurements at different points down the channel length.

# 9 *Non-optically monitoring interfacial position using impedance spectroscopy*

---

## 9.1 *Introduction*

Microfluidics offers an attractive platform for performing miniaturized chemical and biomolecular analysis. Particularly useful is the ability to embed multiple laboratory steps, including preparation and chemical detection, into a microfluidic chip for automated sample processing and analysis. An important engineering design challenge in microfluidics is to develop new *in situ* analytical tools that monitor these operations within the confines of the microchannel network. Fluorescent-microscopy, for example, has been used to perform noninvasive quantification of liquid properties and flow velocity in microchannels<sup>229</sup>. Other techniques such as *in situ* Raman spectroscopy<sup>230</sup>, imaging FTIR<sup>231</sup> and cyclic voltammetry<sup>232</sup> have been used to capture microscale chemical images of microfluidic channel surfaces and fluidic flow patterns. Another strategy relies on employing electrochemical impedance spectroscopy (EIS) to monitor electrical changes on microfluidic surfaces<sup>233</sup> and cells<sup>234</sup> in contact with an electrolyte. Because EIS can be performed with micro-electrodes integrated on-chip, it has potential to be a powerful tool for rapid non-optical monitoring of microfluidic processes.

EIS is used for monitoring complex surface processes in microfluidic space without the use of fluorescent labels and fixatives. By detecting variations in impedance as a function of field frequency, EIS, for example, can be used to non-optically detect proteins<sup>235,236</sup> and DNA<sup>237,238</sup> through monitoring protein binding and DNA hybridization



on electrode surfaces, where these interactions influence current flow and the corresponding impedance spectrum<sup>239,240</sup>. EIS can also be used to quantify cell growth<sup>241,242</sup>. Cells, for example can be grown on the surface of patterned EIS micro-electrodes<sup>57</sup>. The electrode impedance has been shown to be influenced by the cell type and cell state<sup>243-245</sup>.

Because EIS can be easily integrated into microfluidic flow channels, its utility could be extended to non-optically monitoring fluidic behavior for monitoring on-chip mixing<sup>246</sup> and routing operations<sup>247</sup> where multiple fluid streams are routed, mixed, and pumped across a network of microchannels. In this chapter, we demonstrate how to use EIS for non-optically monitoring fluid motion produced by an electrokinetic flow. One feature of low Reynolds number (Re) flows is that multiple liquid streams can flow side-by-side without convectively mixing. The result is that well-controlled microfluidic laminar interfaces can be created between both miscible and immiscible liquids. Interfacial flows are ubiquitous in low Re systems and play important roles in microfluidic applications in rheology<sup>248</sup>, chemical detection<sup>249</sup>, molecular mass sensors<sup>250</sup>, immunoassays<sup>106</sup>, DNA hybridization<sup>251</sup>, and kinetic analysis<sup>220,252</sup>.

Previously, we described a new electrokinetic method for manipulating these liquid interfaces. The technique was demonstrated using two fluids with different electrical properties driven side-by-side in a microfluidic channel. When an alternating current (AC) electric field was applied perpendicular to the direction of flow, the laminar interface polarized and the fluid electrohydrodynamically displaced across the flow channel<sup>153</sup>. The motion of the fluid interface was shown to be an effective electrokinetic method for assessing fluid electrical conductivity and dielectric constant<sup>181</sup>, and for detecting

biomolecular binding<sup>253,254</sup>. In order to perform these fluidic measurements, however, the liquid interface required constant optical monitoring with confocal microscopy. While, effective, a non-optical approach could offer a smaller, less costly and potentially automated means to perform interfacial measurements.

In this chapter, we present a non-optical EIS technique for dynamically tracking the position of a miscible microfluidic liquid interface under electrokinetic flow. Our method utilizes two different electrode arrays: an upstream parallel point electrode array to polarize and induce electrokinetic flow at a liquid interface and a downstream series of interdigitated electrodes to dynamically measure the EIS on the microchannel surface. We show that the magnitude of the impedance ( $|Z|$ ) is sensitive to the position of the liquid interface and can be used to track interfacial motion in response to electrokinetically-induced fluid flow. We propose that variations of this system may be useful for non-optically monitoring the dynamics of microfluidic interfaces in electrokinetics, rheology, biomolecular detection, and microfluidic mixing applications.

We begin by describing electrokinetic flow and interfacial displacement (Section 9.2.1). We then describe the experimental strategy for producing these flows (Section 9.2.2-9.2.3) and the experimental setup used to dynamically measure impedance (Section 9.2.4). Finally, Section 9.3 presents impedance results obtained for a range of electric field frequencies and interfacial positions.

## **9.2 Materials and Methods**

### **9.2.1 Design and Fabrication of Microfluidic Device with Embedded Electrokinetic and Impedance Electrodes**

The assembled device consisted of a main flow channel 150  $\mu\text{m}$  in width and 65  $\mu\text{m}$  in height with an upstream displacement (parallel-point) and a downstream impedance (45°-interdigitated) electrode array (**Figure 9-1**). To perform an experiment, the fluid interface was subjected to an electric field using the parallel-point electrode array and forced to displace by fDEP at different field frequencies (**Figure 9-1B-D**). As fluid exited the first displacement array, the interfacial stress ceased. Because the inertial influence on the flow is minimal ( $\text{Re} < 1$ ), the fluid interface remained fixed in a displaced position immediately after exiting the fDEP array. We then determined the deflection position by measuring the magnitude of the impedance using a second array of interdigitated electrodes.

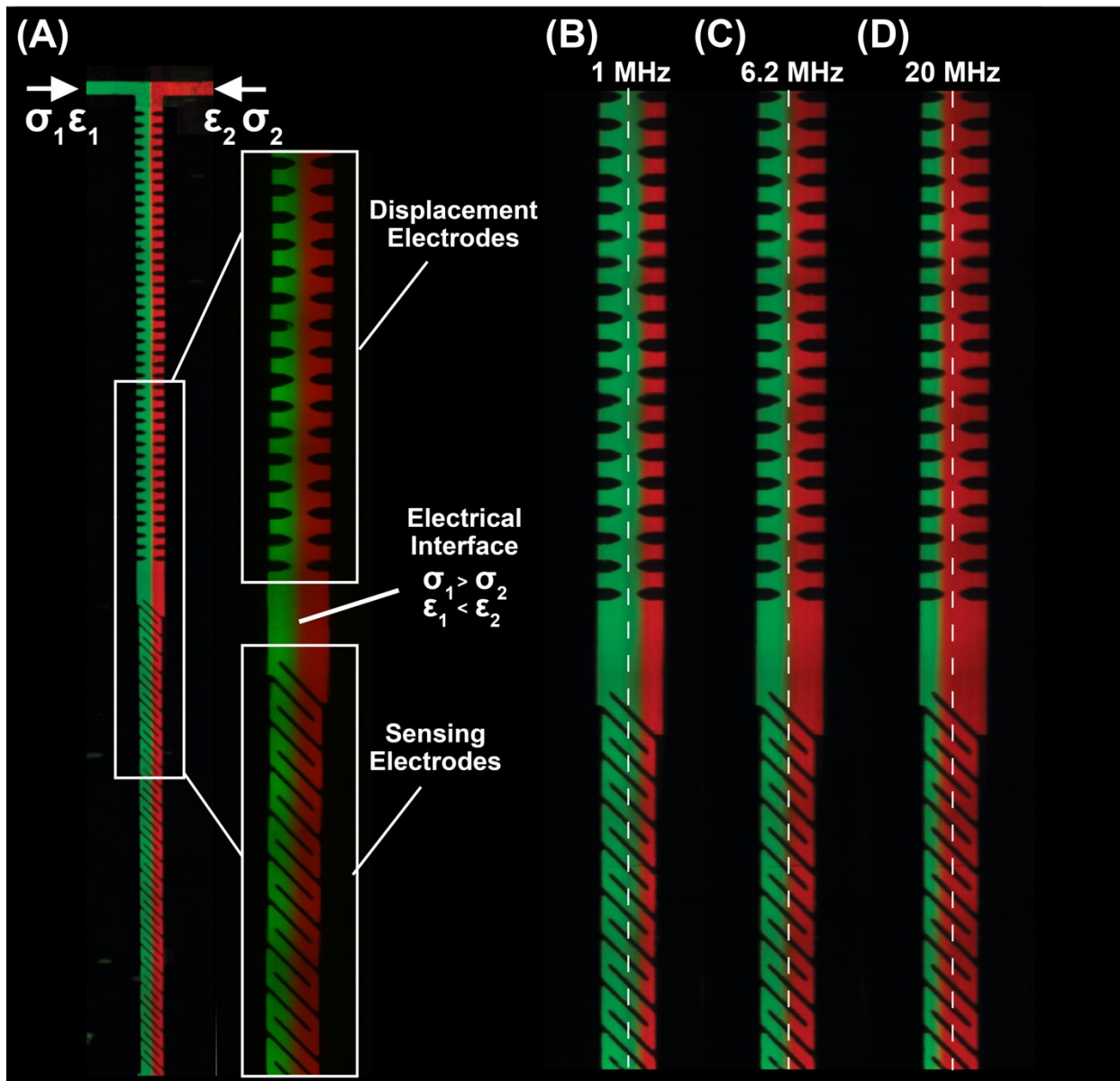


**Figure 9-1. Confocal micrograph with two embedded electrode arrays: displacement and sensing**

(A) Two co-flowing fluids with varying electrical properties in are driven into a microfluidic t-channel device. Each inlet channel (75  $\mu\text{m}$  in width) merges with a main 150  $\mu\text{m}$  wide main channel to create a sharp liquid interface. One stream has a larger conductivity (green), while the adjacent stream (red) has a large permittivity. The main channel has two embedded electrode arrays – displacement electrodes actuate the liquid electrical interface and sensing electrodes measures the local impedance. (B) A 1 MHz AC electric field is applied to displacement electrodes, displacing the high conductive stream (green) into the low conductive stream (red) A dotted white line shows the original interface position when no electric field is applied. (C) At a COF of 6.2 MHz the interface does not deflect in the field. (D) At 20 MHz the high dielectric stream (red) displaces into the low dielectric stream (green).

### 9.2.2 Chemicals and Reagents

The liquid interface was composed of two fluids, each with a different electrical conductivity ( $\sigma$ ) and dielectric constant ( $\epsilon$ ). When forced to flow side-by-side at low Reynolds number these two fluids formed an interface with a large electrical mismatch between them. Each stream was injected at a constant flow rate (10  $\mu\text{L}/\text{min}$ ) into the device using a low-cost flow controller equipped with an externally pressurized fluid-filled cryogenic vial<sup>255</sup>. We labelled each fluid with a different Alexa Fluor fluorescent dye to accurately image the interface position using confocal microscopy. Shown in **Figure 9-1**, the electrical interface was formed by flowing a left-most (green) 1x PBS solution ( $\sigma_1 = 0.29 \text{ mS}/\text{cm}$ ;  $\epsilon_1 = 78$ ) with 10 ng/mL of Alexa Fluor 488 (Invitrogen). The right-most (red) high dielectric stream ( $\sigma_2 = 19 \text{ }\mu\text{S}/\text{cm}$ ;  $\epsilon_2 = 110$ ) was comprised of 0.8M 6-aminohexanoic acid (AHA) (Sigma-Aldrich) labeled with 10 ng/mL of Alexa Fluor 594 (Invitrogen). AHA is a water-soluble zwitterion used for increasing the dielectric constant of aqueous solution. Prior to fluorescent labeling, the AHA solution was polished with 1 g/mL Dowex MR-3 (Sigma-Aldrich) ion exchange resin to remove trace salts and reduce solution conductivity. The COF of this electrolyte system was measured using previously published methods and found to be 6.2 MHz.

### 9.2.3 Impedance Measurement

We utilized the upstream parallel-point array to drive fDEP flow across the channel and a second downstream 45°-interdigitated array as an impedance sensor. The parallel-point electrodes were axially separated by 20  $\mu\text{m}$  and symmetrically bridged the width of the microchannel. We used electrodes with sharp points to focus the electric field to the

tip of the electrodes and to provide increased contact with the PDMS and glass substrate along the main flow channel walls. A function generator (DG4102, Rigol) was connected to the fDEP electrodes and delivered an AC electric field to displace the interface across the channel. The downstream impedance electrodes were interdigitated and positioned at a 45° angle relative to the flow direction to maximize the sensitivity of the array to changes in interfacial position. An impedance spectrometer (ISX-5, Sciospec) was connected to the impedance electrode array and used to measure the magnitude of the impedance as a function of interface position. For all impedance measurements, a sine-modulated AC potential of 50 mV was applied to the electrode array and the magnitude and phase angle of impedance were measured over an excitation frequency range between 100 kHz to 10 MHz.

### ***9.3 Results and discussion***

#### **9.3.1 Imaging Interfacial Position During Electrokinetic Displacement**

**Figure 9-1B-D** depicts a top-view of the interfacial motion of the interface over the length of the fDEP electrode array when a 10-volt peak-to-peak ( $V_{pp}$ ) potential was applied across the displacement electrodes at three different field frequencies (1 MHz, 6.2 MHz, and 20 MHz). When the electric field frequency was 1 MHz, the conductive PBS (green) stream displaced across the interface (**Figure 9-1B**). When the COF (6.2 MHz) was applied, both conductive and dielectric forces were equal, and the interface remained fixed as it passed through the electrode array (**Figure 9-1C**). Finally, at a frequency above the COF (20 MHz) the deflection reversed direction and the high dielectric stream (red) displaced across the microchannel (**Figure 9-1D**).

### 9.3.2 Characterization of Electrokinetic Interfacial Flow Using Impedance Spectroscopy

Because the interfacial-driven motion of the fluid ceases upon exiting the displacement electrode array, the interface's displaced position can be accurately determined using the downstream impedance electrode array (**Figure 9-2**). The top-view micrographs shown in **Figure 9-2A-C** illustrate that when the interface was subjected to either a low or a high frequency electric field, a greater degree of either high conductive-low dielectric PBS or low conductive-high dielectric AHA covered the sensing electrodes at low and high field frequency, respectively. To observe the 3D structure of the interfacial flow field, 2D confocal micrographs were captured above the impedance electrode array for three different electric field frequencies: 1, 6.2 and 20 MHz (**Figure 9-2**). Since the displacement electrodes are thin co-planar films (~50 nm) and confined to the microchannel surface, the electrical stress responsible for driving flow was localized near the surface of the microchannel. In order to satisfy mass conservation, this local electrokinetic flow was countered by a pressure driven back flow at the top of the channel which produced a "tilted" interface, as shown in the 2D confocal micrographs in **Figure 9-2**. Because the impedance electrode array is also confined to the microchannel surface, the impedance measurements were only sensitive to the electrical properties of the fluid domain very near the surface where the electric field was capable of penetrating into the liquid domain. Therefore, differences in interfacial position produced by fDEP will create changes in both the local conductivity and dielectric constant of the fluid near the impedance sensor.

**(A) 1 MHz**      **(B) 6.2 MHz**      **(C) 20 MHz**

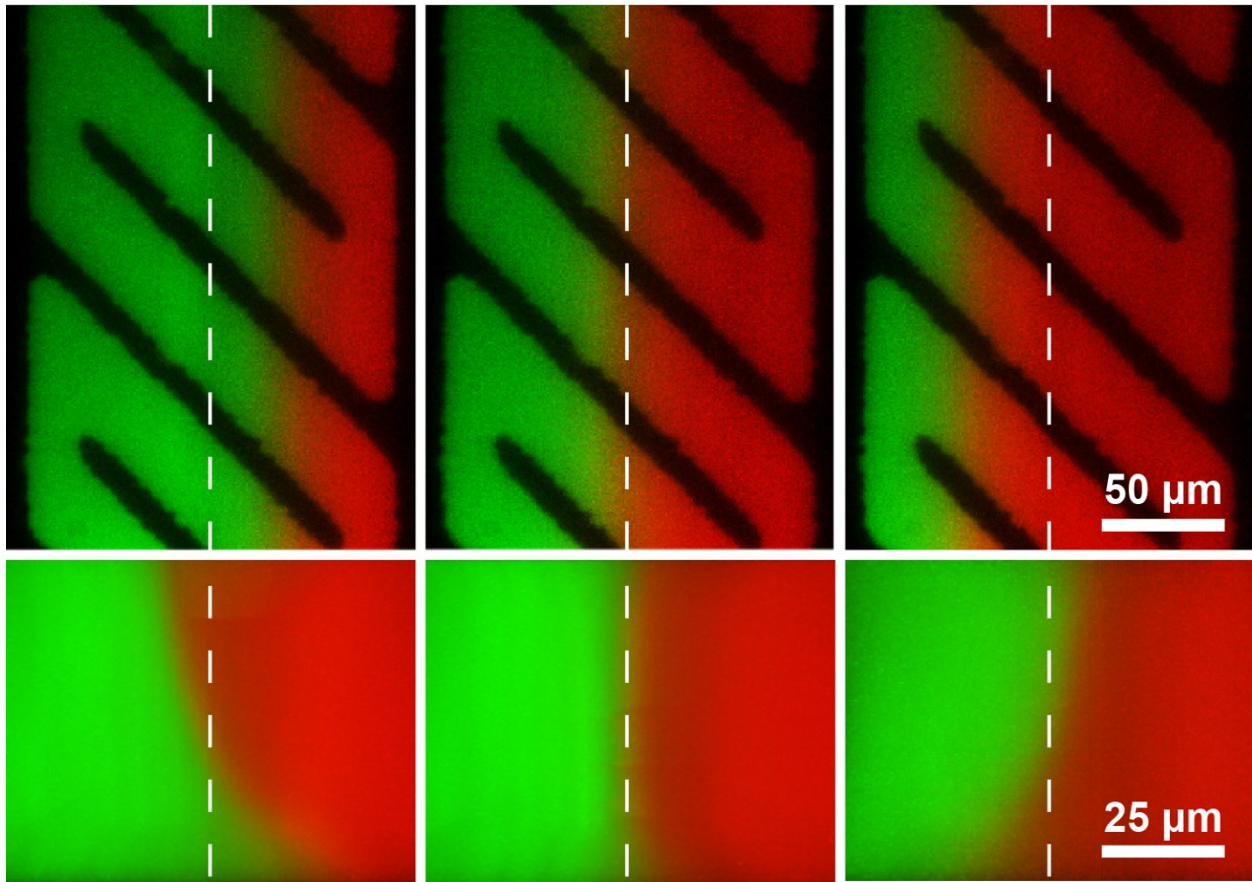


**Figure 9-2. Frequency changes direction of interfacial motion, leading to different surface coverage on the impedance sensing electrodes**

A magnified 3D confocal z-stack is depicted below each top-down micrograph. For each image pair, a dotted white line highlights the interface position when no field is applied. **(A)** At a field frequency of 1 MHz the high conductive stream (green) is driven across the channel surface. The corresponding 3D confocal stack shows that an increase in conductive green fluid covering the surface of the sensing electrodes. **(B)** The COF, 6.2 MHz, is applied and the liquid interface remains fixed. **(C)** The direction of displacement reverses at 20 MHz and the high dielectric stream displaces into the low dielectric stream. The 3D image shows the direction reversed, leading to a decrease in conductive stream covering the impedance electrodes.

In order to determine the optimum impedance conditions for measuring interfacial position, we first determined how upstream fDEP displacement influences downstream impedance over a range of impedance excitation frequencies. An electrical interface was created by co-flowing solutions of PBS and AHA, and then deflected at frequencies below



(1 MHz) and above (20 MHz) the COF, and when no field was applied (e.g. the position at the COF). For each interface position, we performed an impedance frequency sweep from 100 kHz to 5 MHz to determine the magnitude of impedance for different interfacial positions (**Figure 9-3**). Below the interfacial COF at 1 MHz, the fDEP electrodes polarized and forced the high conductive (green) stream to cover a larger area on the impedance electrode array. Conversely, when we applied a high frequency above the COF, the high dielectric stream displaced across the interface and the impedance sensor was exposed to fluid with lower electrical conductivity. The impedance data was consistent with the electrical changes that the interface position produces in the vicinity of the impedance electrodes. When high conductive-low dielectric PBS covered a greater portion of the impedance electrode array, the impedance decreased, while the opposite was seen when the low conductive-high dielectric AHA stream displaced across the impedance electrode array. When an impedance frequency sweep was performed when the COF was applied and when the field was off, the magnitude of the impedance was identical. When the COF is applied, conductive charging balances out dielectric polarization, and the net charge is zero across the interface. Since the net charge across the interface is zero, the interface does not displace and at the COF the interface remains in the same position as when the field is off. Therefore, the magnitude of impedance is the same for both cases. Shown in **Figure 9-3**, the interface deflection produced the greatest change in the magnitude of the impedance ( $|Z|$ ) at an impedance frequency of ~500 kHz. Based on these experiments, we measured  $|Z|$  at a frequency of 500 kHz for all subsequent experiments in this chapter.

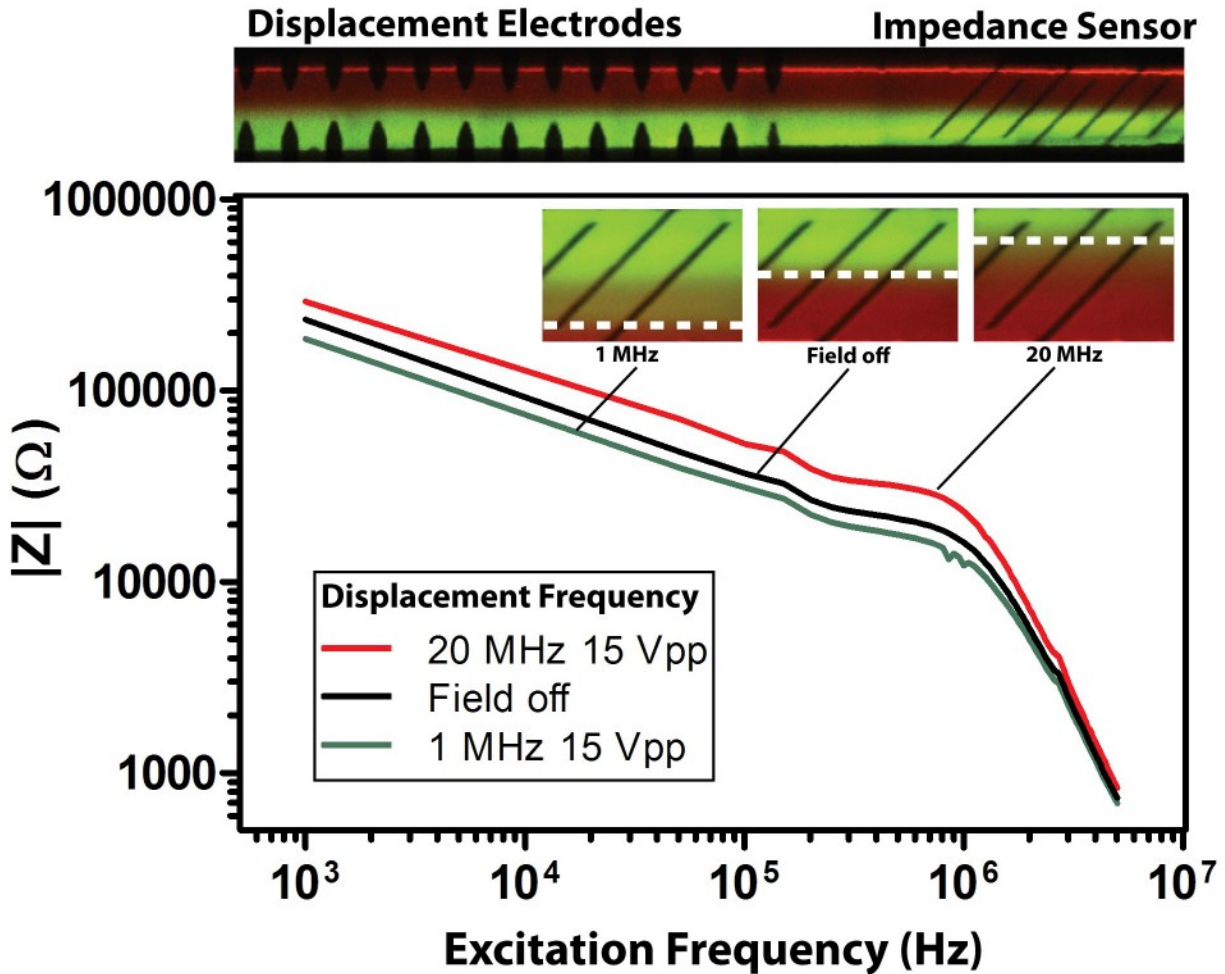


**Figure 9-3. Obtaining optimal excitation frequency through a frequency sweep**

The magnitude of the impedance  $|Z|$  versus applied excitation frequency for different fDEP interface positions. Three frequency sweeps were performed in order to determine the optimal frequency for the impedance spectrometer. When 1 MHz is applied to the displacement electrodes, the high conductive-low dielectric (green) stream covers more impedance sensor electrode area and the impedance magnitude decreases. When a 20 MHz electric field is applied the high dielectric-low conductive (red) stream occupies a larger sensing electrode area and the impedance increases. The magnitude of impedance remains the same when the field is off, and the COF is applied.

### 9.3.3 Determining Interface Position Using Impedance Spectroscopy

With the impedance excitation frequency fixed at 500 kHz, we next measured  $|Z|$  as a function interface position for three different applied voltages (5 V<sub>pp</sub>, 10 V<sub>pp</sub> and 15 V<sub>pp</sub>) delivered across the interface using the upstream displacement electrode array. For each

applied voltage the fDEP frequency was continuously swept from 1 - 20 MHz, and then back to 1 MHz while simultaneously measuring  $|Z|$  at the downstream impedance array. Shown in **Figure 9-4**, when the interface is centered at the COF,  $|Z|$  was found to be 32.5 k $\Omega$  for all three voltages applied. However, when an fDEP frequency below the COF was applied, the high conductive PBS stream covered a larger portion of the impedance sensor surface and the impedance decreased from 25 k $\Omega$  to 15 k $\Omega$  at an applied voltage of 5 V<sub>pp</sub>. When the fDEP frequency increased above the COF, the high dielectric fluid covered a greater portion of the sensor surface and  $|Z|$  increased to 45 k $\Omega$ . The impedance was also influenced when the electrical interface was subjected to larger displacement voltages. This increase was particularly noticeable at high frequencies (> COF) where more low conductive, high dielectric AHA buffer covered a greater area of the impedance sensor. In order to visualize the interface, we captured 3D confocal micrographs of the interface when a 20 MHz AC electric field was applied at voltages of 5, 10 and 15 V<sub>pp</sub>. Shown in the micrographs in **Figure 9-4**, the AHA stream (red) covers a greater electrode area with increasing applied voltage. While there is a large change in impedance with increasing voltage at high frequencies, the three  $|Z|$  datasets are not as strongly influenced at low frequencies (< COF). This is because changes in the position of the high conductivity buffer on the impedance electrodes do not influence the impedance to the same magnitude as the AHA buffer. Lastly, when the interface COF was applied to the interface, the interface did not displace in the electric field, and therefore the impedance did not change with applied voltage.

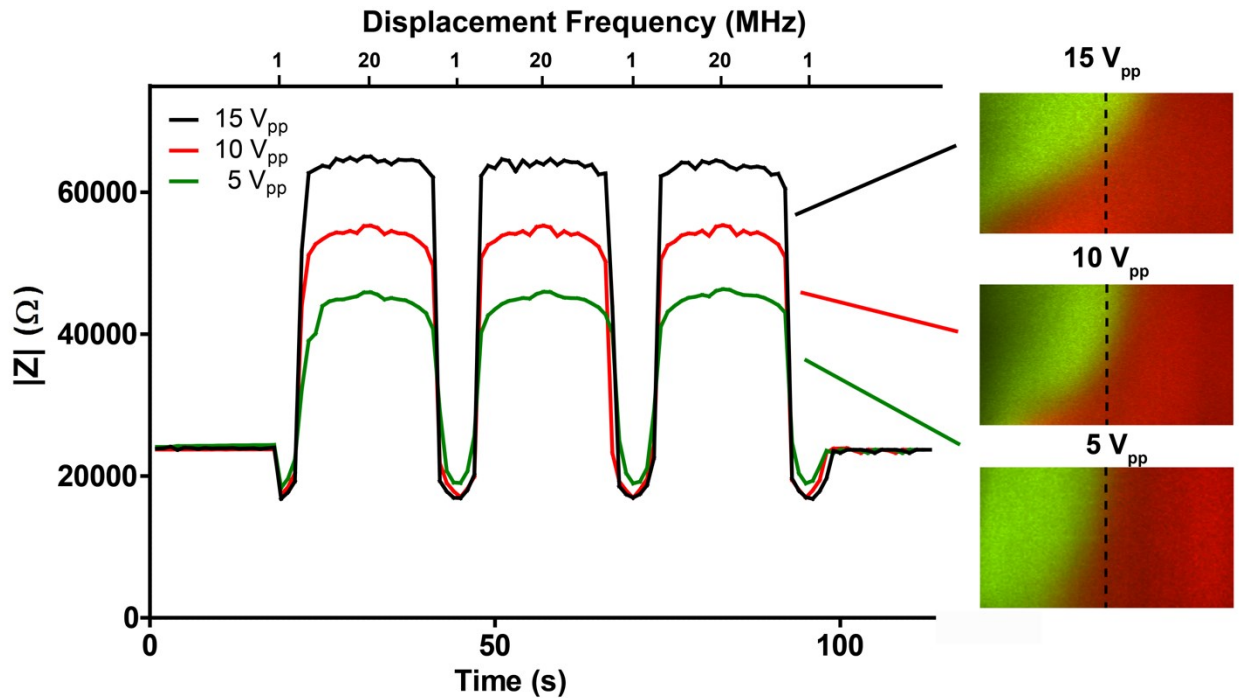


**Figure 9-4. Liquid interface subjected to varying applied voltages is monitored by impedance spectroscopy**

Magnitude of the impedance for different fDEP frequencies at an impedance excitation frequency of 500 kHz. The interface was displaced at 5, 10 and 15 V<sub>pp</sub>. As voltage increased, the displacement magnitude increased. This is illustrated in the 3D confocal images taken at a fDEP frequency of 20 MHz. As depicted, as the voltage increased the low conductive (red) stream covered a greater electrode surface area. This is quantitatively shown – the magnitude of impedance increases with increasing voltage.

Next, we determined if it was possible to distinguish the COF between two fluid interfaces with different electrical conductivity mismatches. In **Figure 9-5**, we show impedance results for two different interfacial conductivities – one where  $\Delta\sigma = \sigma_2 - \sigma_1 = 0.27$  and a second interface where  $\Delta\sigma = 0.61$  mS/cm. Shown in **Figure 9-5**, we observed a difference in measured impedance for the two different interfaces, where the impedance measurements for a given interface position increased with interfacial conductivity. For an alternative way to analyze these results, we normalized the impedance of each dataset by the initial impedance value when no electric field was applied using a time-averaged baseline impedance reading that was taken prior to applying an electric field at the

displacement electrodes. Shown in **Figure 9-5B**, we see that both fluidic systems begin and end at the same dimensionless impedance,  $|Z|^*$ , but their COF's are different and increase with interfacial conductivity, as is consistent with previous fDEP experiments.

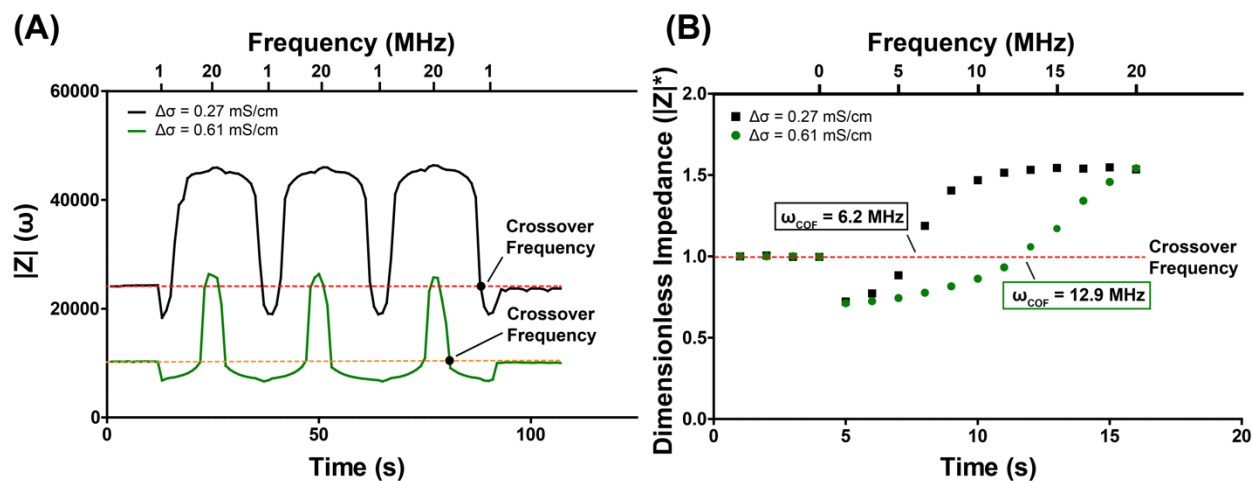


**Figure 9-5. Monitoring COF of two different interfacial conductivity systems**

Impedance taken at an excitation frequency of 500 kHz versus applied fDEP frequency for two different interfacial conductivity differences. **(A)** The magnitude of impedance for varying applied frequencies, 1 – 20 MHz. The interface with a lesser interfacial conductivity has a larger measured impedance. **(B)** The magnitude of impedance for both systems is rendered dimensionless to compare the two datasets. The impedance measurement is able to non-optically determine that the COF increases with increasing interfacial conductivity.

## 9.4 Conclusions

In this chapter, we presented a novel method for detecting an electrokinetically displaced liquid interface using impedance spectroscopy. Using an AC electric field, we forced a laminar fluid interface to deflect across a microchannel using fDEP and then measured the position of the deflected interface using a downstream impedance electrode array. The interface was composed of two co-flowing fluids - one stream had a greater electrical conductivity and the other had a greater dielectric constant. When the interface was exposed to a low frequency AC electric field, high conductive fluid stream

displaced across the channel and covered a larger surface area of the impedance sensor, which reduced the magnitude of the impedance. As the frequency was increased to the COF, the interfacial position moved to its original position which reduced the amount of conductive fluid over the impedance array. At higher electric field frequencies above this COF, the interfacial deflection reversed direction and the high dielectric, low conductive stream covered a larger surface of the impedance sensor and produced an increase in impedance. This method was able to electrically detect interfacial displacement and measure the interface COF non-optically at a resolution consistent with experiments performed with confocal microscopy. We believe this method provides a new sensing technique for non-optically imaging microfluidic flow fields. Future work will focus on the limit of detection of displacement through an equivalent circuit model, using the impedance sensor with fDEP to non-optically determine the dielectric constant of aqueous liquids and to detect biomolecular binding at the liquid interface.

# **10** *Non-optical, label-free detection of pregnancy hormones in unadulterated human serum*

---

## **10.1 Introduction**

Previously, we presented a novel, label-free homogenous electrokinetic biosensor. The approach combines continuous microfluidic flows with an applied AC electric field. In our previous reports, a liquid interface was created in a microfluidic T-channel whereby one co-flowing liquid contained a protein-of-interest and the adjacent stream contained the receptor. Parallel point electrodes were embedded in the main flow channel, applying an AC electric field, polarizing the liquid interface. To be polarizable, and electrokinetically manipulated by an external AC electric field, we engineered an electrical mismatch into the interface. The liquid interface becomes an electrical interface where the two streams differ in electrical conductivity and permittivity. Due to the stark electrical mismatch of the two fluids, when an AC electric field is applied to the interface, the fluid is shown to displace perpendicular to the flow direction. It was shown that the direction of displacement was frequency dependent. At low frequencies, <10 MHz, the more conductive stream displaced into the adjacent, low conductive stream. At high frequencies, >10 MHz, the high dielectric, low conductive stream displaced into the adjacent low dielectric, high conductive stream. There exists a critical frequency in which the direction of displacement reverses, known as the crossover frequency (COF).

In previous chapters, we showed that biomolecular recognition at the EI altered the electrical response of the interface. Biomolecular binding was monitored down the

axial length of the channel by measuring the COF of the EI. Product formation at the interface caused the COF of the system to increase. Furthermore, the COF increased down the axial length of the channel due to an increase in electrical conductivity from product formation. Here, we demonstrate a new method for quantitatively monitoring product formation in a liquid-interface biosensor by interfacial electrokinetic transduction (IET). While monitoring the COF corresponds to biorecognition, in physiologically relevant samples where the conductivity of the solutions is large, the system requires a high frequency function generator, altering the cost-effectiveness of the system. Recall **Figure 7-4** which illustrated how displacement versus a range of applied frequencies (1 – 20 MHz) was affected by the presence of a biomolecular reaction. Here we see two regimes that are affected by the presence of avidin:biotin complex formation: COF and at low frequencies, displacement. In this chapter, we utilize the totality of the displacement curve in our IET system by now monitoring displacement at low applied frequencies <10 MHz.

In this chapter, we demonstrate how to use IET to monitor three reaction schemes through interfacial displacement. All three schemes are done in solution phase without labels. We begin by monitoring the biomolecular reaction between biotin and avidin. Second, we detect immunoglobulin proteins in human serum using nanoparticles functionalized with protein A. Finally, we detect a female pregnancy hormone, human chorionic gonadotropin (hCG), at physiologically relevant concentrations in solution. All detection methods are monitored by measuring the interfacial displacement down the axial length of the channel and are done in less than 10 minutes. By implementing impedance spectroscopy, we non-optically detected label-free analytes-of-interest in serum. This detection method offers a low-cost, easy-to-use, portable and quick method



for detecting proteins in serum.

## **10.2 Materials and Methods**

### **10.2.1 IET System**

The microfluidic device used consists of a T-channel flow layer with embedded electrodes. The electrodes consist of two separate arrays: displacement and sensing. A function generator (Rigol, DG4102) is attached to the displacement electrodes delivering an AC electric field, polarizing the EI leading to interfacial displacement. Downstream from the displacement electrodes are sensing electrodes, an impedance spectrometer (Sciospec, ISX-5) monitors the local impedance, thereby monitoring the interfacial position. Samples are delivered by a commercially available constant pressure source (Elveflow, OB1) with multiplexing capabilities (Elveflow, MUX Cross Chip) allowing us to deliver multiple samples in series.

### **10.2.2 Portable IET System**

A second system was developed with increased portability as well as cost effectiveness. The microfluidic device and function generator used are consistent with that described in Section 10.2.1. However, a new, hand-held impedance spectrometer (Sciospec, ISX-3 Mini) replaced the lab-scale impedance spectrometer. Lastly, in a means to increase ease-of-use and portability, as well as decrease cost, the constant pressure source was replaced with a vacuum pump (Cole Parmer, EW-79600-04). The vacuum pump is connected to a waste cryovial, which has an outlet tube connected to

the outlet port of the microfluidic device. When the vacuum pump is actuated, it pulls the fluids from the inlet ports creating a stark, interface between two co-flowing fluids.

### 10.2.3 Chemicals and Reagents

The liquid interface was composed of two fluids, each with a different electrical conductivity ( $\sigma$ ) and dielectric constant ( $\epsilon$ ). When forced to flow side-by-side at low Reynolds number these two fluids formed an interface with a large electrical mismatch between them. In section 10.3.2, biotin and avidin (Sigma-Aldrich) were dissolved in aminohexanoic acid (AHA) (Sigma-Aldrich) and PBS respectively. In section 10.3.3, protein-A functionalized nanoparticles (Corpuscular Inc.) were used to detect immunoglobulin proteins in human serum (ZenBio Inc.). The serum is labeled with Alexa Fluor 594 (Red), allowing us to image the microfluidic interface. Finally, in section 10.4.4-6, male-pooled, human serum (ZenBio Inc.) was doped with human chorionic gonadotropin (hCG) (ABCam) at varying concentrations from 10 – 100,000 mIU/ml at increasing orders of magnitude. The adjacent stream was AHA doped with the antibody for hCG, anti-hCG (ABCam) and labelled with Alexa Flour 595 (Red) in order to image the microfluidic interface. Two systems were used to detect hCG in human serum: homogeneous and heterogeneous sensing. With homogeneous sensing, anti-hCG was first dissolved into DI water and then into AHA at the desired concentrations. The heterogenous sensing scheme utilized carboxylated microparticles (Bangs Labs) which were then functionalized with anti-hCG; the protocol is described in **Figure S10-1**.

## **10.3 Results**

### **10.3.1 Measuring Interfacial Displacement**

The EI is created by engineering a stark electrical mismatch between the two co-flowing streams. To quantify interfacial displacement, the interface is monitored by confocal microscopy; each stream is labeled with different fluorescent markers – Alexa Fluor 488 (Green) and Alexa Fluor 594 (Red). Because the two streams do not diffusively mix, a well-defined interface is formed and remains down the axial length of the channel; the interface is polarized by an external AC electric field. Both solutions have a finite electrical conductivity and permittivity such that one has a higher conductivity and the adjacent stream has a higher dielectric constant:  $\sigma_1 > \sigma_2$ ,  $\varepsilon_2 > \varepsilon_1$ . The two streams are delivered by a constant-pressure flow system and an AC electric field of 1 MHz is applied to the interface. Interfacial displacement is monitored at specific points down the axial length of the channel.

Through imaging software, 2D micrographs are taken at different points down the axial length of the channel at varying applied AC electric fields. Displacement is characterized such that when the green stream displaces into the red, this is positive displacement. Each displacement measurement is normalized by the initial position of the liquid interface, i.e. when there is no applied AC electric field. The normalized data are plotted against the axial length of the channel for all subsequent reaction schemes.

### **10.3.2 Monitoring avidin:biotin binding by interfacial displacement**

First, we looked at a previously monitored biomolecular reaction between avidin and biotin. Shown in **Figure 10-1**, are the displacement results for two IET systems: Biotin

vs. Avidin and Biotin vs. PBS. The magnitude of displacement for both the reaction between biotin and avidin, and the negative control biotin and PBS, are plotted in **Figure 10-1A**. The conductivity of both streams was manipulated to yield the same inlet interfacial conductivity for all experiments. By doing this, any variations at low frequency AC fields due to baseline interfacial conductivity differences are eliminated. The magnitude of displacement when the reaction is present is  $\sim 8\mu\text{m}$  greater throughout the length of the channel when compared to the negative control.

Next, we investigated the response due to an increase in voltage. Increasing the applied voltage leads to an increase in the dielectrophoretic force that causes interfacial displacement. Varying the applied voltage allows the user to potentially increase response more drastically when a reaction is present or not. Shown in **Figure 10-1B**, solutions of avidin and biotin were flowed down the channel, and the displacement was measured at 1 MHz for three voltages: 5, 10 and 15 V<sub>pp</sub>. While there was a substantial increase in the magnitude of displacement from 5 to 10 V<sub>pp</sub>, there was not a large difference between 10 and 15 V<sub>pp</sub>.

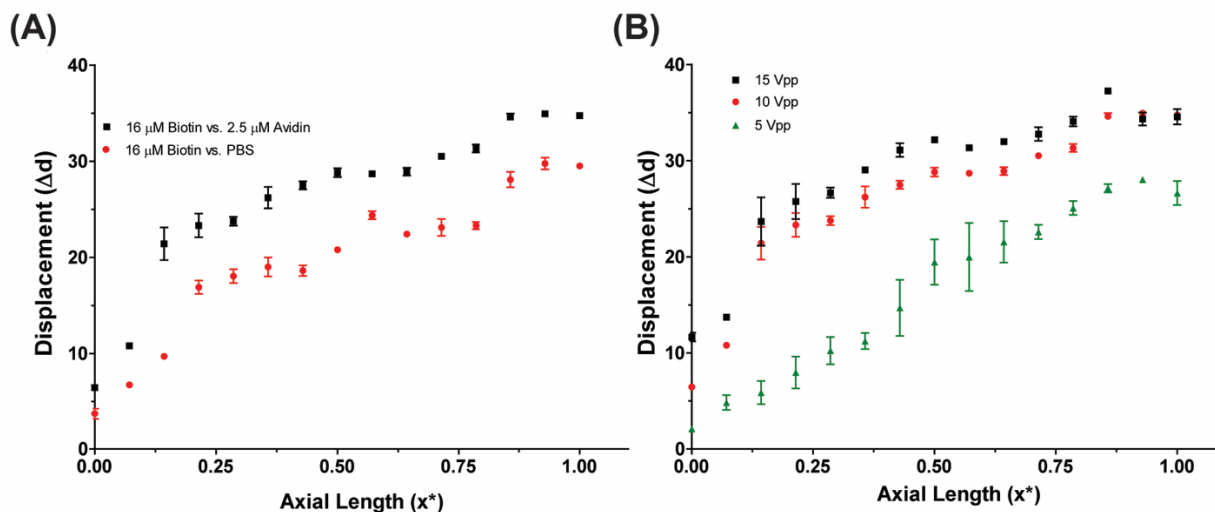


### **Figure 10-1. Monitoring biotin-avidin biorecognition through interfacial displacement**

Measured displacement down the axial length of the microfluidic channel in the presence of a biomolecule reaction: avidin-biotin. **(A)** Displacement is monitored for two systems: avidin vs. biotin and PBS vs. avidin. Specific binding influences the magnitude of displacement, when a reaction is present displacement increases. **(B)** Displacement measurements for avidin vs. biotin for 3 different applied voltages: 5, 10 and 15 V<sub>pp</sub>. Increasing the applied voltage increases the magnitude of displacement. However, eventually due to wall effects the interface cannot displace more, evident with 10 and 15 V<sub>pp</sub>.

#### **10.3.3 Detecting immunoglobulin proteins in human serum**

Next, we sought to detect protein in a physiologically relevant sample. In **Chapter 8**, we showed by introducing functionalized nanoparticles conjugated with the receptor for the analyte-of-interest decreased the limit of detection by 3 orders of magnitude. Since nanoparticles have a larger surface coverage and diffuse slower than free, in solution receptors, they are optimal for detection in our IET sensor. We obtained Protein-A functionalized nanoparticles (NP-PA) for detection; Protein-A is a surface protein that binds to all Ig-proteins, however, it has the highest affinity for IgG proteins. We engineered a new system in which human serum was flowed side-by-side to an AHA solution containing NP-PA. Serum has a wide range of conductivity values from ~10 – 20 mS/cm. Since AHA has a very low conductivity, ~50  $\mu$ S/cm, we adjusted the conductivity value by adding NaCl to the AHA/NP-PA solution. Addition of salts can decrease the dielectric constant, however the decrease is minimal. Manipulating the conductivity of AHA decreases the interfacial conductivity.

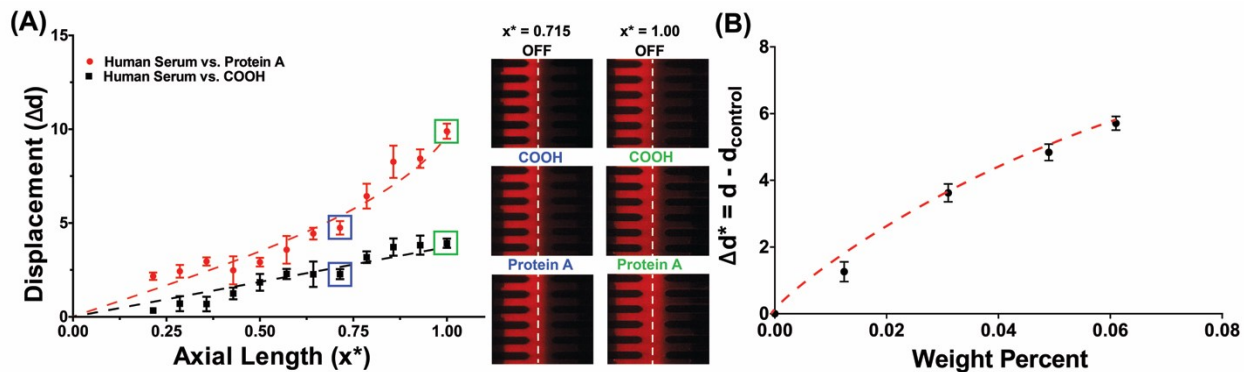


**Figure 10-2. Monitoring the displacement of human serum against protein A functionalized nanoparticles**

(A) A negative control of carboxylated nanoparticles is labeled by a black line. When protein A functionalized nanoparticles are introduced, free Ig proteins in serum bind to the nanoparticles which lead to an increase in displacement; labeled in red. 2D micrographs at two points down the axial length illustrate the magnitude of displacement when the field is off, with carboxylated nanoparticles and protein A nanoparticles. (B) To further validate binding, the normalized displacement for varying protein A weight percentages is plotted. Displacement increases with increasing nanoparticle weight percent as there are more free binding sites.

Serum conductivity was measured and the complimentary AHA solution was adjusted. Each interfacial conductivity was set to 0.1 mS/cm for each serum-AHA system. A 0.0610 weight percent of protein A was used for Ig detection. Shown in **Figure 10-2A**, the magnitude of displacement for NP-PA versus human serum was plotted. A negative control of carboxylated silica nanoparticles of the same weight percent was run against the same serum sample. When the negative control is compared to when NP-PA is present, the magnitude of displacement is substantially lower. A very interesting trend is shown in **Figure 10-2**, between NP-PA and the negative control.

To fully confirm that the introduction of protein-a was contributing to a displacement response, we next varied the weight percent of protein a and monitored the response. Shown in **Figure 10-2B**, the normalized displacement is plotted against the weight percent of protein A in solution from 0 to 0.0610. The displacement was normalized to the

magnitude of displacement without the presence of NP-PA. Since the response was proportional to the weight percent of nanoparticles, we believe this shows label-free Ig-protein in serum at a liquid interface.

#### **10.3.4 Human chorionic gonadotropin detection**

To fully test the validity of the novel biosensor, we next sought to detect a common female pregnancy hormone, hCG, in serum. Human chorionic gonadotropin is a hormone produced by the placenta upon implantation. There are two main reasons for a clinician to test for hCG levels in a patient: the first is for pregnancy detection, second, in the case of a non-pregnant patient, is as a precursor for cancer. In the case of pregnant patients, during the course of pregnancy the concentration of hCG drastically increases during the first 12-16 weeks and then begins to decline. Because of this, we modeled our experiments around the range of hCG levels a clinician would detect during the course of the pregnancy: 10 – 100,000 mIU/mL. First, a pool of male serum was obtained and doped with varying concentrations of hCG. The conductivity of the serum was measured, and the adjacent stream, AHA, was doped such that the conductivity difference between the two remained at 0.002 mS/m. The adjacent stream, AHA, was doped with the receptor for hCG, anti-hCG; both in solution and functionalized microparticles.

The two streams were introduced into the microfluidic device and a 1 MHz AC electric field was applied at the interface. Since the serum had a higher conductivity, it displaced into the adjacent stream. The magnitude of displacement was monitored for varying concentrations hCG down the axial length of the channel, shown in **Figure 10-3**. As the concentration of hCG in serum increased, the magnitude of displacement increased. At lower concentrations, we see that the magnitude of displacement rises to a

certain point down the axial length of the channel, and then begins to increase as diffusion is occurring faster than product formation.

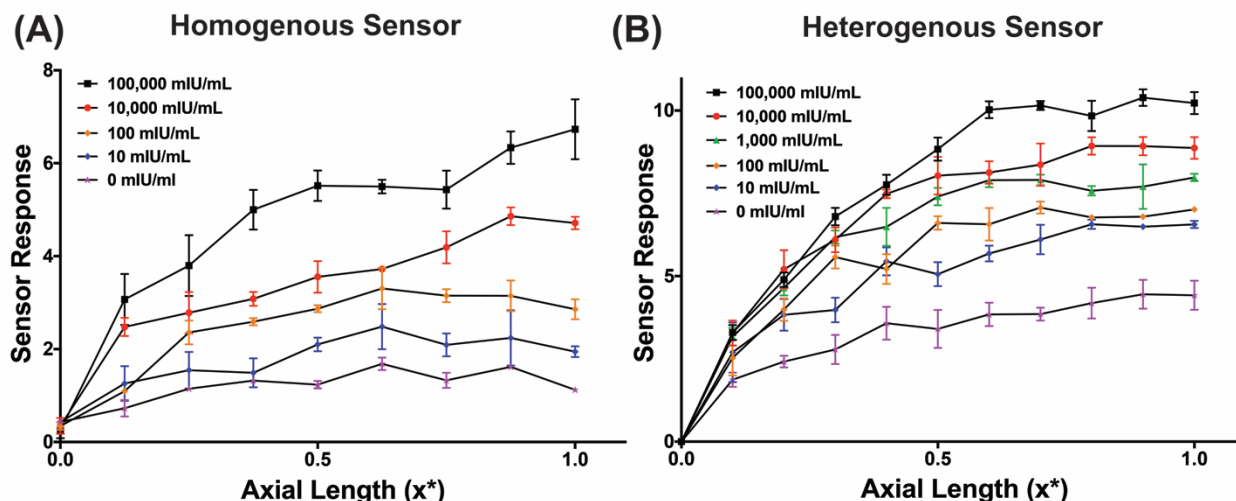


**Figure 10-3. Homogeneous and heterogeneous hCG detection in human serum using IET**

Human chorionic gonadotropin (hCG) is detected in serum using anti-hCG. (A) A homogeneous sensing platform is used where anti-hCG is in solution. Five different concentrations of hCG are detected: 0, 10, 100, 10,000 and 100,000 mIU/ml. As the concentration of hCG increases, the sensor response increases. (B) A heterogeneous sensing scheme is shown using anti-hCG functionalized microparticles. The sensor response increases compared to the homogeneous scheme, and the sensor's variation decreases.

### 10.3.5 Non-optical, label-free detection of human chorionic gonadotropin

Next, in order to create a truly non-optical biosensor, impedance spectroscopy was implemented into the device. In **Chapter 9**, we monitored the interfacial position with a secondary electrode array monitoring the bulk impedance. At low frequencies, the higher conductivity buffer displaced into the low conductivity stream, thereby decreasing the bulk impedance on the sensing electrodes. As the frequency ramped up from 1 to 20 MHz, the interface changed direction of displacement until the higher dielectric stream was covering more of the sensing electrodes, raising the impedance value; at frequencies above the crossover frequency. Here, we implemented the same electrode geometry and



monitored the interfacial displacement downstream at varying concentrations of hCG. We delivered samples with an elveflow multiplexing system, allowing for each sample to be delivered after one another in real time. Shown in **Figure 10-4**, we see that with increasing concentrations of hCG in serum, the impedance values decrease as the more conductive stream, serum, covers a larger surface area of the sensing electrodes. A negative control – silica microparticles run against serum with hCG – was performed and the impedance was monitored. The impedance remains constant with the addition of hCG-free serum. Because impedance spectroscopy is a highly sensitive method, this allows for detection of even the most minute displacements.

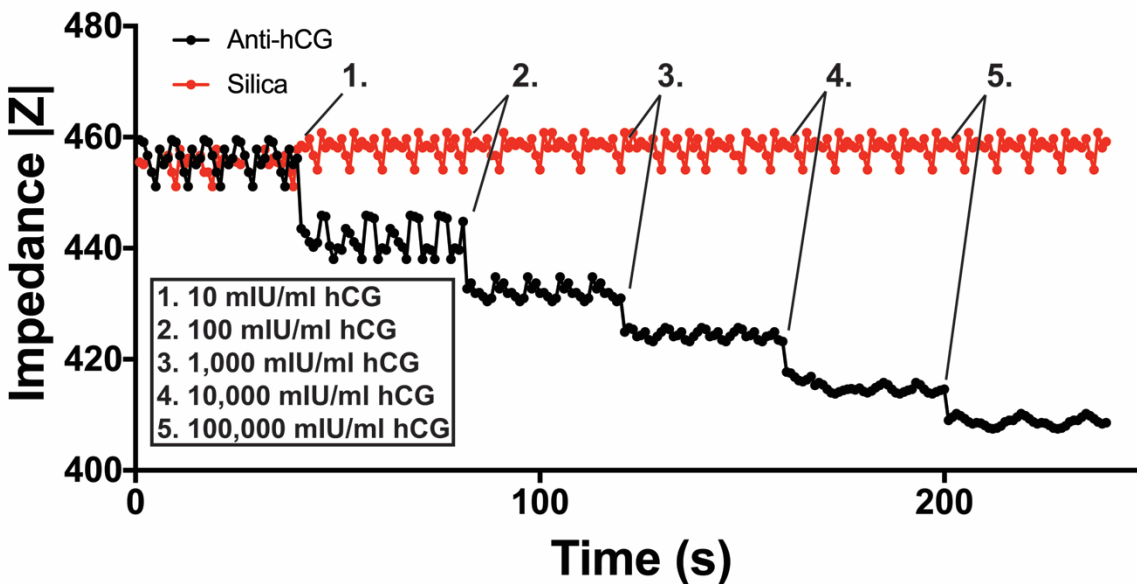


**Figure 10-4. Heterogenous detection of five human serum samples with five different hCG concentrations using a non-optical IET sensor**

Non-optical detection of hCG in human serum. A constant 1 MHz AC electric field is applied for the total duration. A negative control of silica particles is shown in red. At each number, a new concentration of hCG doped serum is introduced into the sensor. An impedance spectrometer monitors the local impedance. When larger concentrations of hCG are introduced, the magnitude of displacement increases, leading to a decrease in impedance. The control remains the same as no specific reaction occurs.

### 10.3.6 Label-free detection at the push of a button

The current biosensing system is still limited to a lab workbench. Samples are delivered by a constant pressure source, and the impedance analyzer, while light and easy to maneuver, is still large and difficult to carry. We solved these problems by implementing two changes to the system: a portable impedance analyzer and a new method of sample delivery (**Figure 10-5**). The impedance analyzer used was an ISX-3 Mini, an easy-to-use instrument that fits in the palm of one's hand. Sample delivery was performed by implementing a vacuum pump at the outlet of the device. A droplet of serum was placed over one inlet port, and AHA containing anti-hCG was placed on the other inlet port. The vacuum pump was turned on and the vacuum force was regulated with a vacuum regulator.

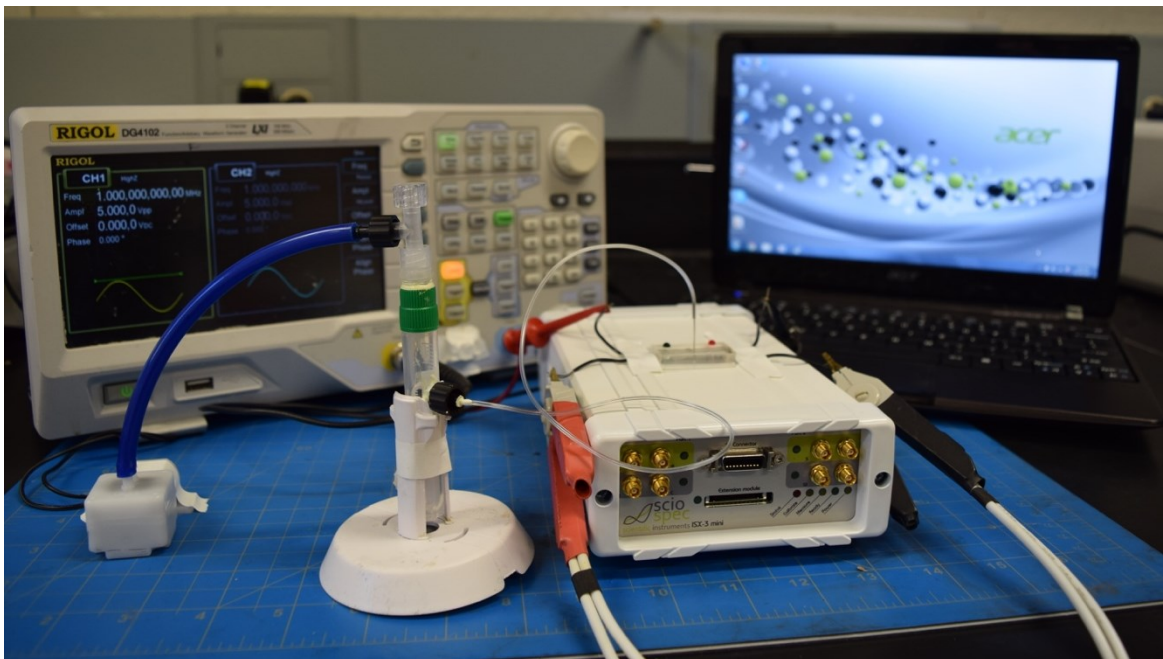


**Figure 10-5. Portable IET sensing platform**

Experimental setup for a portable IET system. A function generator applies the AC electric field at the displacement electrodes. A vacuum pump is connected to a cryovial which is connected to the outlet port of the microfluidic device. The sample and buffer containing

anti-hCG is pipetted onto the inlet ports of the microfluidic device. Under the microfluidic device sits a handheld impedance spectrometer which monitors the interfacial position through impedance. A laptop plots the response for the user to read.

We tested the effectiveness of this system by performing a reaction when hCG was present and when it was not present, negative control. We applied a vacuum that yielded a flowrate of 5  $\mu\text{L}/\text{min}$  which was similar to the previous experiments. Upon starting the vacuum pump, a 1 MHz AC electric field was applied at the displacement electrodes while monitoring the bulk impedance at the sensing electrodes. We performed two experiments to determine the presence of hCG in the sample: detection in serum and a negative control. The negative control was placed on the inlet port, the vacuum pump was initiated and the impedance was measured, shown in **Figure 10-6**. Plotted on the same graph is the impedance data when a serum sample, containing hCG, was run against AHA containing anti-hCG. When the sample was tested, the measured impedance was lower than the negative control, because the reaction between hCG in the sample and anti-hCG increased the interfacial conductivity. Therefore, serum covered a larger area of the sensing electrode when hCG was present compared to the negative control, lowering the impedance.

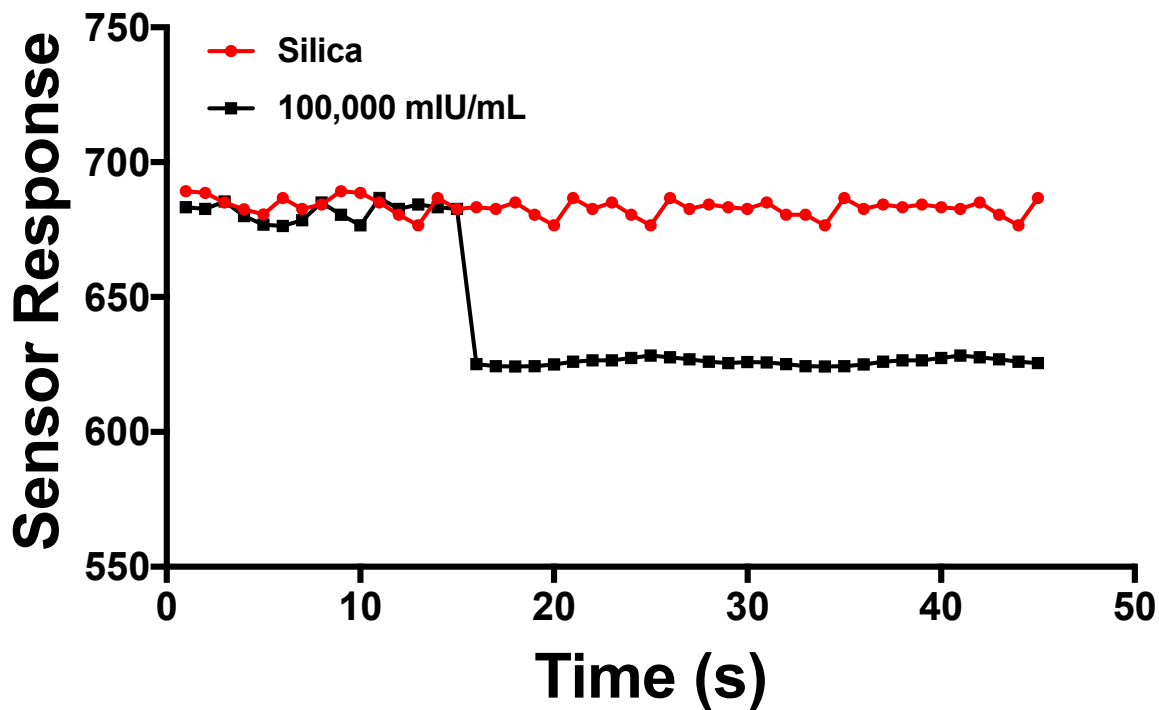


**Figure 10-6. Heterogeneous hCG detection in human serum using a portable IET sensing platform**

hCG detection using the portable system. A negative control of silica nanoparticles was used and the response does not change. When serum with 100,000 mIU/ml of hCG is introduced and run against anti-hCG microparticles, the interface displaces and the sensor response, impedance, decreases. Detection is performed in under a minute.

### 10.4 Discussion

Biomolecular reactions at the electrical interface created by two co-flowing liquids alters the electrical properties of the interface. Specifically, it was previously shown that product formation between biotin and avidin led to an increase in, not only the COF of the system, but displacement at the low frequency regime. Unfortunately, when working with physiologically relevant samples the COF is far higher than affordable and portable function generators can achieve. Because of this, we monitored the magnitude of displacement when a low frequency electric field was applied at the interface of two liquids, each containing a component of a reaction.

We first monitored a well-known biomolecular reaction between biotin and avidin. First, we saw that when the reaction is present, the magnitude of displacement increases as the reaction propagates down the axial length of the channel. However, we observed that when altering the applied voltage, there is a plateau that is reached. We believe that this is due to wall effects of the system. The microfluidic device is 100  $\mu\text{m}$  wide, therefore, the interface can only displace a certain difference before the wall of the device applies a counter force, limiting displacement. From **Figure 10-2B**, we assume the relative maximum displacement is achieved at 10  $V_{pp}$ , therefore, the magnitude of displacement at 15  $V_{pp}$  is similar to that of 10  $V_{pp}$  because the increased fDEP force cannot overcome the counter force from the wall.

Another interesting phenomenon was observed during the detection of immunoglobulin proteins in serum. Carboxylated nanoparticles were flowed against serum and the magnitude of displacement was monitored down the axial length of the channel when an AC electric field was applied. The trend of displacement was linear, this occurs because the fDEP force is consistent down the axial length of the channel. Conversely, when protein A is present in the system, the trend becomes non-linear. Product formation occurs at the interface, altering the electrical properties, specifically conductivity, which increases the fDEP force. Since the reaction is propagating down the axial length of the channel, the fDEP force increases down the axial length, leading to the non-linear trend.

Detecting hCG in serum exhibited a similar response, however, the magnitude of displacement was not as prominent. We believe this occurs because protein A binds to all immunoglobulin proteins, while having the highest affinity for IgG, therefore, protein a

coated beads bind to more free proteins during the length of the device. More product formation was shown to increase the magnitude of displacement. We also observed a difference in response when varying the receptor concentration (**Figure S10-2**). By increasing the receptor concentration, the response, magnitude of displacement, also increased, which is to be expected. Since we previously found that using a bead-based assay decreased the limit of detection by three orders of magnitude, we also looked at how the bead-based and in solution assays compared with one another (**Figure 10-3**). We found that with the bead-based assay the response increased and we were also able to distinguish concentrations of hCG in solution with higher specificity. This becomes crucial when determining the concentration during pregnancy, but also has broader implications. By simply switching the receptor on the bead, using this method one could theoretically detect any analyte-of-interest at the switch of a solution. Beads also allow the user to have higher specificity which becomes crucial in assays where it is not only important to detect the presence of a substance, but also the quantity.

Interestingly, we found that results were affected when detection was performed in series. When displacement measurements were performed for varying hCG concentrations we noticed increased error in the data. We found that performing detection without rinsing the microfluidic device between trials led to increased error. In **Figure S10-3** we show the comparison between devices that have been rinsed between trials and those that have not. We believe hCG is adsorbed into the PDMS and surface of the device and alters the hCG concentration between runs. Because of this, expected hCG concentrations are altered and the sensor response is affected leading to increased error.

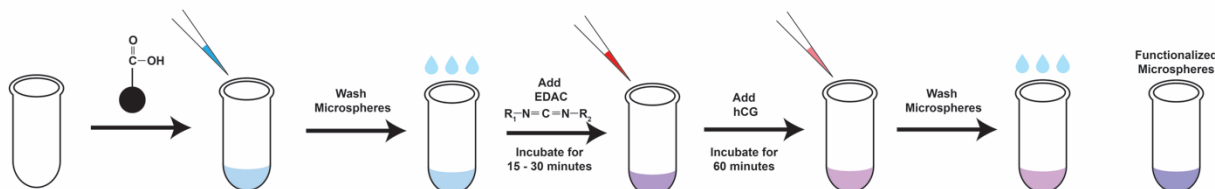
Finally, we produced a portable system by implementing a vacuum pump at the outlet of the device. Both the serum sample containing hCG and AHA containing anti-hCG microparticles were pipetted onto each inlet port in 100  $\mu\text{L}$  aliquots. The vacuum pump was regulated to pull the two fluids at a flow rate of 5  $\mu\text{L}/\text{min}$ . There was a difference between the negative control and serum sample containing hCG – the impedance decreased with the introduction of anti-hCG functionalized microparticles. The response however is different from those performed with the elveflow system ~ 35% decrease. The main reason for this is a new serum pool was obtained with a different conductivity, however, the AHA was not altered to yield the same conductivity difference. The interfacial conductivity in the portable system was lower than that in **Figure 10-5**, and because of this the magnitude of displacement without a reaction is lower.

## **10.5 Conclusion**

Sensing strategies have long since been confined to complex steps, laboratory settings and require technicians to perform the assays. Unfortunately, in many scenarios, quick, easy-to-use and portable sensors are required. In solution, liquid interfacial sensors offer several advantages to conventional sensors in that there is minimal surface fouling, small sample volumes and quick response times. However, until now, these methods required expensive transducers, primarily fluorescence microscopy. By implementing electric fields, we can determine minute electrical changes of the liquid interface when a biomolecular reaction occurs. Furthermore, conjugated beads allow for endless detection schemes by simply altering the receptor attached to the bead. Next steps will be creating a system in which one push-of-the-button actuates the system and performs the

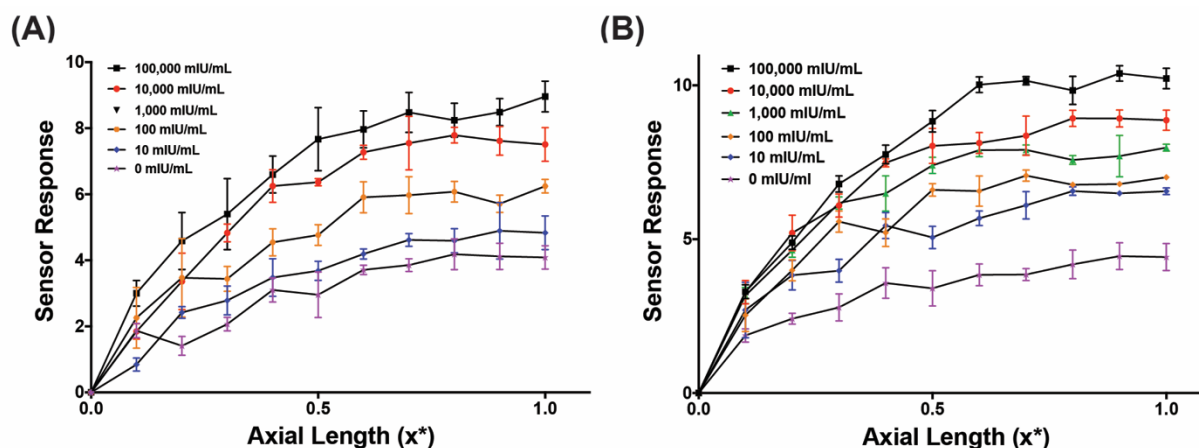
diagnostic test in one step. Finally, we will begin implementing other design alterations to perform multiplexing detection.

## 10.6 Supplemental Materials



**Supplementary Figure 10-1. Microparticle functionalization process**

Dry carboxylated microspheres were obtained from Bang's lab. They were suspended in ethanol and was with DI water. The microspheres were then incubated into a cross-linking solution. Anti-hCG was added to the microspheres and incubated for four hours. While a minimum of 60 minutes is suggested, for 1  $\mu\text{m}$  particles, optimal functionalization is achieved with a four-hour incubation. Finally, the functionalized microspheres were washed and the supernatant was kept to determine the concentration of anti-hCG attached to the microspheres.

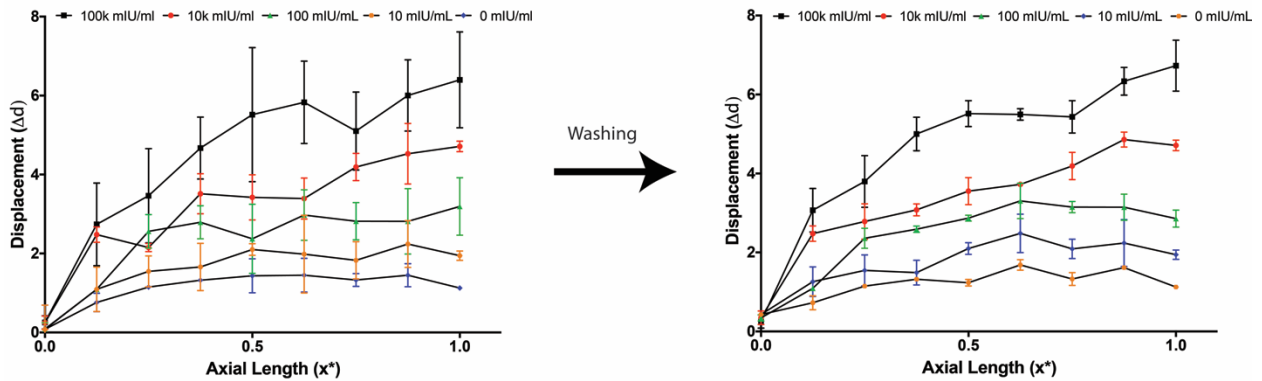


**Supplementary Figure 10-2. Comparing heterogeneous detection of hCG with different anti-hCG functionalization concentrations**

Heterogeneous detection of hCG in human serum at varying concentrations: 0, 10, 100, 1,000, 10,000 and 100,000 mIU/ml. **(A)** Microspheres functionalized with 200 ng of anti-hCG were run against serum samples containing hCG. The maximum response is  $\sim 8$  with clear discrepancies between sample concentration. However, it is difficult to distinguish 0 and 10 mIU/ml with certainty. **(B)** Microspheres functionalized with 500 ng of anti-hCG were run against serum samples containing hCG. The sensor response increased with increased anti-hCG concentration, with a maximum signal of  $\sim 10$ . Now



there is a clear difference between 0 and 10 mIU/ml; the minimum concentration to positively diagnosis pregnancy.



**Supplementary Figure 10-3. Sensor response is affected by washing between trials**

The magnitude of displacement for homogeneous detection of hCG in serum was performed over 5 different concentrations: 0, 10, 1,000, 10,000 and 100,000 mIU/ml. Measurements were performed on the same device without rinsing steps which led to substantial error. However, when the microfluidic device was washed with ethanol and DI water after every trial, the error drastically decreased yielding more accurate signals.

# 11 *Conclusions and future work*

---

## 11.1 *Conclusions*

Implementing electrokinetics with traditional microfluidic sensors created a truly non-optical, label-free biosensor. In this work, we built upon traditional liquid-interfacial sensors, specifically moving interfaces relying on diffusion, making the liquid-liquid interface the substrate upon which a biomolecular event occurs. Utilizing the electrical mismatch between the two co-flowing fluids, we polarized the interface and observed interfacial motion whereby the magnitude and direction was frequency dependent. Furthermore, a reaction at the electrical interface altered the electrical properties of the liquid interface, specifically conductivity, which was transduced by interfacial displacement – COF and low frequency displacement. In this new sensor, the liquid-liquid interface is not only the substrate but becomes the transduction element.

In **Chapter 4 and 5** we explored the physics behind liquid interfacial polarization. Traditional dielectrophoresis occurs when a force is exerted on a dielectric particle in a non-uniform electric field. The strength of the force, as well as the direction the force, exerted is dependent on the electrical properties – conductivity and permittivity – of the particle and medium. In this same manner, we created an electrical mismatch with two co-flowing liquids where one had a higher conductivity,  $\sigma_1 > \sigma_2$ , and the adjacent had a higher permittivity,  $\varepsilon_2 > \varepsilon_1$ . When the electrical interface was subjected to an AC electric field the interface displaced; at low applied frequencies the high conductivity stream displaced into the low conductive, and at high applied frequencies, the displacement

direction reversed and the high dielectric stream displaced into the low dielectric stream. There exists a frequency where both conductive and dielectric forces are equal and the interface does not displace known as the crossover frequency (COF). We termed this phenomenon ‘fluidic dielectrophoresis’ (fDEP) as polarization acts similarly to traditional DEP. We then developed an electrohydrodynamic model that could predictively map how polarization and interfacial displacement is affected by the electrical properties of the fluids, specifically conductivity and permittivity.

In **Chapter 6** we utilized fDEP to create a gradient generator through active, chaotic mixing. We fabricated a microfluidic device to generate a tri-liquid interface such that the solute-free stream would enter the gradient chamber when the mixer was off. The tri-liquid interface consisted of a solute stream with a high conductivity ‘sandwiching’ a solute-free stream with a lower conductivity. When an AC electric field was applied to the tri-liquid interface, chaotic mixing was observed. The two outer, high conductive streams, forcibly displaced into the low conductive stream. When the two outer streams met in the center of the device, it created a vortex. Microfluidic mixing was then used to create a fully mixed solution sent to a downstream gradient generator. A stable gradient was formed within seconds.

In **Chapter 7** we demonstrated that we could monitor a reaction at the liquid interface through fDEP. In previous chapters, we showed that interfacial polarization, specifically the COF and displacement, was dependent on the electrical properties of the fluids – conductivity and permittivity. We began by creating a reaction at the interface between biotin and avidin. We monitored the COF down the axial length of the channel and found it increased with increasing avidin concentration. The reaction between biotin

and avidin increased the COF because it also increased the interfacial conductivity of the system. We tested the sensitivity and selectivity within the system finding the theoretical LOD to be roughly 200 fM. We also detected avidin in the presence of a background of 5 mg/ml BSA and found the LOD to be roughly 600 fM.

We then explored the use of functionalized nanoparticles, in **Chapter 8**, to increase the number of binding sites at the interface, hypothesizing this would increase the sensitivity. We performed similar sensorgrams with biotin and streptavidin functionalized nanoparticles. Implementing nanoparticles in the system allowed us to detect the presence of biotin down to attomolar concentrations. The avidin – biotin reaction has one of the lowest reported dissociation constants making it extremely strong and almost irreversible. To test the viability of the sensor, we next detected the presence of human IgG using protein A functionalized nanoparticles. The sensor was capable of detecting between 12 – 1.25 mg/ml. Our sensor, up to now, still required optical methods to determine the presence of a reaction, as well as performed in clean samples.

In **Chapter 9**, we implemented a secondary electrode array downstream which monitored the bulk resistance of the fluid close to the surface of the device through impedance spectroscopy. The new sensor design consisted of two electrode arrays: displacement and sensing electrodes. An AC electric field was applied to the liquid interface displacing the interface, as shown in previous chapters. A constant excitation frequency was applied at the sensing electrodes and the impedance was monitored in real time. We first determined the operating excitation frequency by sweeping excitation frequencies at different interfacial positions. We then showed we could accurately

determine the interfacial position, non-optically, with impedance. Finally, we were able to determine the COF for two systems with different interfacial conductivities.

Finally, in **Chapter 10**, we combined our newly developed sensing platform with impedance spectroscopy to non-optically sense analytes-of-interest. In **Chapter 7 and 8** we found that a reaction at the liquid interface increases the interfacial conductivity, which can be transduced by monitoring the magnitude of displacement at low frequency AC fields. We monitored the magnitude of displacement in a system consisting of hCG in unadulterated human serum against a buffer containing anti-hCG. We implemented the sensing electrodes downstream and non-optically detected and characterized hCG at five different concentrations in serum. Finally, we developed a portable system, delivering samples with a vacuum pump and using a handheld impedance spectrometer to monitor the interfacial position non-optically.

## ***11.2 Suggestions for future work***

This thesis work illustrates a novel, label-free, non-optical sensor capable of sensitive and selective detection of target analytes. The ability to accurately detect analytes-of-interest quickly in a portable sensor at high sensitivities is of great need in developing countries but also urgent care and hospitals as well as at home use.

First, an imperative consideration before pursuing detection in clinical samples such as urine, saliva, whole blood and serum is to develop a theoretical model to predictively map product propagation. Our sensor utilizes co-flowing liquids and capitalizes on electrical mismatches between the fluids, as well as those created by a reaction at the interface. However, in this sensor, there are many factors that must be

considered and optimized to create a more robust sensor. Firstly, diffusion is a critical parameter to evaluate. Diffusion aids in this sensor as both the analyte-of-interest and receptor only react at the interface and diffusively travel to the interface where the reaction is then transduced. Having a model to understand how diffusion of molecules affects the sensor response will allow users to tune operating conditions including concentration of receptor as well as flow rate. Conversely, while diffusion assists in binding, ions are also diffusively migrating across the interface, smoothing and decreasing the electrical mismatch at the interface. Therefore, if flow rates are too slow, ions have more time to migrate, decreasing the interfacial conductivity, decreasing the sensor's response. Therefore, developing a model will help optimize all operating parameters: flow rate, buffer conductivity, receptor concentration, sensing electrode position.

Once a validated model has been created we can then move to testing clinical samples. There are many diseases and markers that make the use of this sensor advantageous over current state-of-the-art. Having a fast, sensitive sensor that can determine viral infections, differentiate between bacterial and viral infections, or common biomarkers tested in labs drawn in hospitals are critically needed. The next step is to determine the biomarker, as well as sample state, that needs a sensor with these characteristics. In respect to sample state, more non-invasive sensing for whole blood and serum are needed in at-home and hospital use. Another sample that can benefit from the sensor shown in this work is cerebral spinal fluid as extracting is painful and having a sensor that can operate on small volumes is needed.

Another crucial step that must be taken is engineering alterations that will allow the sensor to be capable of multiplexing. Currently, more channels and electrode arrays can

be added to run reactions in parallel. However, this tends to lead to an over complicated chip with too many moving parts. In order to have a commercially viable sensor, it must be capable of simple, easy-to-use multiplexing detection.

Finally, there are other platforms to pursue in terms of detecting. Specifically, paper sensors have gathered tremendous interest in the past decade. Paper is highly portable and extremely cheap. Electrokinetics has already been integrated into paper-based sensors. In the future, a paper-based fDEP sensor should be developed, optimized, and used for cheaper, portable, fast detection of analytes-of-interest.

Overall, this sensor offers another method for fast, sensitive, portable, and easy-to-use sensing; the sensor is capable of competing with the current state-of-the-art.

# References

---

1. Fogel, R. & Limson, J. Developing Biosensors in Developing Countries: South Africa as a Case Study. *Biosensors* **6**, 10.3390/bios6010005 (2016).
2. Lim, D. V., Simpson, J. M., Kearns, E. A. & Kramer, M. F. Current and developing technologies for monitoring agents of bioterrorism and biowarfare. *Clin.Microbiol.Rev.* **18**, 583–607 (2005).
3. Peruski, A. H., Johnson, L. H. & Peruski, L. F. Rapid and sensitive detection of biological warfare agents using time-resolved fluorescence assays. *Journal of Immunological Methods* **263**, 35–41 (2002).
4. Peruski, L. F. & Peruski, A. H. Rapid diagnostic assays in the genomic biology era: detection and identification of infectious disease and biological weapon agents. *BioTechniques* **35**, 840–846 (2003).
5. Bahadir, E. B. & Sezginurk, M. K. Applications of commercial biosensors in clinical, food, environmental, and biothreat/biowarfare analyses. *Anal. Biochem.* **478**, 107–120 (2015).
6. Weng, X., Gaur, G. & Neethirajan, S. Rapid Detection of Food Allergens by Microfluidics ELISA-Based Optical Sensor. *Biosensors* **6**, 24 (2016).
7. Kumvongpin, R. *et al.* Detection assay for HPV16 and HPV18 by loopmediated isothermal amplification with lateral flow dipstick tests. *Molecular medicine reports* **15**, 3203–3209 (2017).
8. Koczula, K. M. & Gallotta, A. Lateral flow assays. *Essays in biochemistry* **60**, 111–120 (2016).
9. Khalilpour, A. *et al.* Lateral flow test using *Echinococcus granulosus* native antigen B and comparison of IgG and IgG4 dipsticks for detection of human cystic echinococcosis. *The American Journal of Tropical Medicine and Hygiene* **91**, 994–999 (2014).
10. Yetisen, A. K., Akram, M. S. & Lowe, C. R. Paper-based microfluidic point-of-care diagnostic devices. *Lab Chip* **13**, 2210–2251 (2013).
11. Hu, J. *et al.* Advances in paper-based point-of-care diagnostics. *Biosens Bioelectron* **54**, 585–597 (2014).
12. Islam, K., Suhail, A. & Pan, G. A Label-Free and Ultrasensitive Immunosensor for Detection of Human Chorionic Gonadotrophin Based on Graphene FETs. *Biosensors* **7**, 10.3390/bios7030027 (2017).
13. Balakrishnan, S. R. *et al.* A Point-of-Care Immunosensor for Human Chorionic Gonadotropin in Clinical Urine Samples Using a Cuneated Polysilicon Nanogap Lab-on-Chip. *PLoS ONE* **10**, e0137891 (2015).
14. Fatin, M. F. *et al.* HIV-1 Tat biosensor: Current development and trends for early detection strategies. *Biosens Bioelectron* **78**, 358–366 (2016).
15. Nehra, A., Chen, W., Dimitrov, D. S., Puri, A. & Singh, K. P. Graphene Oxide-Polycarbonate Track-Etched Nanosieve Platform for Sensitive Detection of Human Immunodeficiency Virus Envelope Glycoprotein. *ACS Appl Mater Interfaces* **9**, 32621–32634 (2017).
16. Gong, Q., Wang, Y. & Yang, H. A sensitive impedimetric DNA biosensor for the determination of the HIV gene based on graphene-Nafion composite film. *Biosens Bioelectron* **89**, 565–569 (2017).
17. Soni, A. & Jha, S. K. Smartphone based non-invasive salivary glucose biosensor. *Analytica Chimica Acta* **996**, 54–63 (2017).
18. Agustini, D., Bergamini, M. F. & Marcolino-Junior, L. H. Tear glucose detection combining microfluidic thread based device, amperometric biosensor and microflow injection analysis. *Biosens Bioelectron* **98**, 161–167 (2017).
19. Lane, J. E., Shivers, J. P. & Zisser, H. Continuous glucose monitors: current status and future developments. *Current opinion in endocrinology, diabetes, and obesity* **20**, 106–111 (2013).
20. Horiguchi, Y. *et al.* Direct and label-free influenza virus detection based on multisite binding to sialic acid receptors. *Biosens Bioelectron* **92**, 234–240 (2017).
21. Ahmed, S. R., Kim, J., Suzuki, T., Lee, J. & Park, E. Y. Detection of influenza virus using peroxidase-mimic of gold nanoparticles. *Biotechnol. Bioeng.* **113**, 2298–2303 (2016).



22. Chang, Y. F. *et al.* Simple Strategy for Rapid and Sensitive Detection of Avian Influenza A H7N9 Virus Based on Intensity-Modulated SPR Biosensor and New Generated Antibody. *Anal. Chem.* (2018).
23. Nedelkov, D. & Nelson, R. W. Analysis of human urine protein biomarkers via biomolecular interaction analysis mass spectrometry. *American Journal of Kidney Diseases : The Official Journal of the National Kidney Foundation* **38**, 481–487 (2001).
24. Guo, T. *et al.* Highly sensitive detection of urinary protein variations using tilted fiber grating sensors with plasmonic nano-coatings. *Biosens Bioelectron* **78**, 221–228 (2016).
25. Kuo, Y. C., Lee, C. K. & Lin, C. T. Improving sensitivity of a miniaturized label-free electrochemical biosensor using zigzag electrodes. *Biosens Bioelectron* **103**, 130–137 (2018).
26. Bhatnagar, D., Kaur, I. & Kumar, A. Ultrasensitive cardiac troponin I antibody based nanohybrid sensor for rapid detection of human heart attack. *International journal of biological macromolecules* **95**, 505–510 (2017).
27. Diware, M. S. *et al.* Ultrasensitive, label-free detection of cardiac biomarkers with optical SIS sensor. *Biosens Bioelectron* **87**, 242–248 (2017).
28. Shanmugam, N. R., Muthukumar, S. & Prasad, S. A review on ZnO-based electrical biosensors for cardiac biomarker detection. *Future science OA* **3**, 0006. eCollection 2017 Nov (2017).
29. Koo, B. *et al.* An isothermal, label-free, and rapid one-step RNA amplification/detection assay for diagnosis of respiratory viral infections. *Biosens Bioelectron* **90**, 187–194 (2017).
30. Jung, I. Y. *et al.* A Highly Sensitive Molecular Detection Platform for Robust and Facile Diagnosis of Middle East Respiratory Syndrome (MERS) Corona Virus. *Advanced healthcare materials* **5**, 2168–2173 (2016).
31. Olaru, A., Bala, C., Jaffrezic-Renault, N. & Aboul-Enein, H. Y. Surface plasmon resonance (SPR) biosensors in pharmaceutical analysis. *Critical Reviews in Analytical Chemistry* **45**, 97–105 (2015).
32. Myszka, D. G. & Rich, R. L. Implementing surface plasmon resonance biosensors in drug discovery. *Pharmaceutical Science & Technology Today* **3**, 310–317 (2000).
33. Shi, L. *et al.* Development of SPR biosensor for simultaneous detection of multiplex respiratory viruses. *Bio-medical materials and engineering* **26 Suppl 1**, 2207 (2015).
34. Diao, W. *et al.* Highly sensitive surface plasmon resonance biosensor for the detection of HIV-related DNA based on dynamic and structural DNA nanodevices. *Biosens Bioelectron* **100**, 228–234 (2018).
35. Atencia, J. & Beebe, D. J. Controlled microfluidic interfaces. *Nature M1* - **437**, 648 (2004).
36. Novotny, J. & Foret, F. Fluid manipulation on the micro-scale: Basics of fluid behavior in microfluidics. *J. Sep. Sci.* **40**, 383–394 (2017).
37. Squires, T. M. & Quake, S. R. Microfluidics: Fluid physics at the nanoliter scale. *Reviews of modern physics M1* - **77**, 977 (2005).
38. Lee, C.-Y., Chang, C.-L., Wang, Y.-N. & Fu, L.-M. Microfluidic Mixing: A Review. *International Journal of Molecular Sciences* **12**, 3263–3287 (2011).
39. Martel, J. M. *et al.* Continuous Flow Microfluidic Bioparticle Concentrator. *Sci. Rep.* **5**, 3 (2015).
40. Yamada, M. & Seki, M. Microfluidic Particle Sorter Employing Flow Splitting and Recombining. *Anal. Chem.* **78**, 1357–1362 (2006).
41. Lu, Y. *et al.* Long-range electrothermal fluid motion in microfluidic systems. *International Journal of Heat and Mass Transfer* **98**, 341–349 (2016).
42. Williams, S. J. & Green, N. G. Electrothermal pumping with interdigitated electrodes and resistive heaters. *Electrophoresis* **36**, 1681–1689 (2015).
43. Yuan, Q. & Wu, J. Thermally biased AC electrokinetic pumping effect for lab-on-a-chip based delivery of biofluids. *Biomed Microdevices* **15**, 125–133 (2013).
44. Garcia-Sanchez, P., Ramos, A., Gonzalez, A., Green, N. G. & Morgan, H. Flow reversal in traveling-wave electrokinetics: an analysis of forces due to ionic concentration gradients. *Langmuir* **25**, 4988–4997 (2009).
45. Kim, D., Raj, A., Zhu, L., Masel, R. I. & Shannon, M. A. Non-equilibrium electrokinetic micro/nano fluidic mixer. *Lab Chip* **8**, 625–628 (2008).
46. Choi, E., Kwon, K., Lee, S. J., Kim, D. & Park, J. Non-equilibrium electrokinetic micromixer with 3D nanochannel networks. *Lab Chip* **15**, 1794–1798 (2015).

47. Cheng, I. F., Chiang, S. C., Chung, C. C., Yeh, T. M. & Chang, H. C. Ripple structure-generated hybrid electrokinetics for on-chip mixing and separating of functionalized beads. *Biomicrofluidics* **8**, 061102 (2014).
48. Sin, M. L., Shimabukuro, Y. & Wong, P. K. Hybrid electrokinetics for separation, mixing, and concentration of colloidal particles. *Nanotechnology* **20**, 4484/20/16/165701. Epub 2009 Apr 1 (2009).
49. Magaretti, P., Pagonabarraga, I. & Rubi, J. M. Entropic electrokinetics: recirculation, particle separation, and negative mobility. *Phys. Rev. Lett.* **113**, 128301 (2014).
50. Zhao, C. & Yang, C. Continuous-flow trapping and localized enrichment of micro- and nano-particles using induced-charge electrokinetics. *Soft Matter* (2018).
51. Paustian, J. S., Pascall, A. J., Wilson, N. M. & Squires, T. M. Induced charge electroosmosis micropumps using arrays of Janus micropillars. *Lab Chip* **14**, 3300–3312 (2014).
52. Minden, J. S., Dowd, S. R., Meyer, H. E. & Stuhler, K. Difference gel electrophoresis. *Electrophoresis* **30 Suppl 1**, 156 (2009).
53. Arlett, J. L., Myers, E. B. & Roukes, M. L. Comparative advantages of mechanical biosensors. *Nat Nanotechnol* **6**, 203–215 (2011).
54. Engvall, E. & Perlmann, P. Enzyme-linked immunosorbent assay (ELISA) quantitative assay of immunoglobulin G. *Immunochemistry* **8**, 871–874 (1971).
55. Englebienne, P., Hoonacker, A. V. & Verhas, M. Surface plasmon resonance: principles, methods and applications in biomedical sciences. *Journal of Spectroscopy M1 - 17*, 255–273 (2003).
56. Jones, R. B., Gordus, A., Krall, J. A. & MacBeath, G. A quantitative protein interaction network for the ErbB receptors using protein microarrays. *Nature M1 - 439*, 168 (2006).
57. Wegner, G. J., Lee, H. J., Marriott, G. & Corn, R. M. Fabrication of histidine-tagged fusion protein arrays for surface plasmon resonance imaging studies of protein– protein and protein–DNA interactions. *Anal. Chem.* **75**, 4740–4746 (2003).
58. Karlsson, R. & F It, A. Experimental design for kinetic analysis of protein-protein interactions with surface plasmon resonance biosensors. *Journal of Immunological Methods* **200**, 121–133 (1997).
59. Shumaker-Parry, J. S., Zareie, M. H., Aebersold, R. & Campbell, C. T. Microspotting streptavidin and double-stranded DNA arrays on gold for high-throughput studies of protein– DNA interactions by surface plasmon resonance microscopy. *Anal. Chem.* **76**, 918–929 (2004).
60. Brockman, J. M., Frutos, A. G. & Corn, R. M. A multistep chemical modification procedure to create DNA arrays on gold surfaces for the study of protein– DNA interactions with surface plasmon resonance imaging. *J. Am. Chem. Soc.* **121**, 8044–8051 (1999).
61. Fong, C.-C. *et al.* Study of substrate–enzyme interaction between immobilized pyridoxamine and recombinant porcine pyridoxal kinase using surface plasmon resonance biosensor. *Biochimica et Biophysica Acta (BBA)-Protein Structure and Molecular Enzymology M1 - 1596*, 95–107 (2002).
62. Beseničar, M., Maček, P., Lakey, J. H. & Anderluh, G. Surface plasmon resonance in protein– membrane interactions. *Chem.Phys.Lipids M1 - 141*, 169–178 (2006).
63. Karamanska, R. *et al.* Surface plasmon resonance imaging for real-time, label-free analysis of protein interactions with carbohydrate microarrays. *Glycoconj.J. M1 - 25*, 69–74 (2008).
64. Yau, Y. H. & Shochat, S. G. in *Biosensors and Biodetection* **1138**, 271–284 (Springer New York, 2014).
65. Luo, M. *et al.* Chemiluminescence biosensors for DNA detection using graphene oxide and a horseradish peroxidase-mimicking DNAzyme. *Chemical Communications M1 - 48*, 1126–1128 (2012).
66. Yu, J., Ge, L., Huang, J., Wang, S. & Ge, S. Microfluidic paper-based chemiluminescence biosensor for simultaneous determination of glucose and uric acid. *Lab on a Chip M1 - 11*, 1286–1291 (2011).
67. Zhang, J. *et al.* Electrogenerated chemiluminescence DNA biosensor based on hairpin DNA probe labeled with ruthenium complex. *Anal. Chem.* **80**, 2888–2894 (2008).
68. Ma, C., Wang, W., Mulchandani, A. & Shi, C. A simple colorimetric DNA detection by target-induced hybridization chain reaction for isothermal signal amplification. *Anal. Biochem.* **457**, 19–23 (2014).

69. Liu, J. & Lu, Y. Colorimetric biosensors based on DNAzyme-assembled gold nanoparticles. *J. Fluoresc. M1* - **14**, 343–354 (2004).
70. Li, X., Ballerini, D. R. & Shen, W. A perspective on paper-based microfluidics: current status and future trends. *Biomicrofluidics M1* - **6**, 011301 (2012).
71. Martinez, A. W., Phillips, S. T., Butte, M. J. & Whitesides, G. M. Patterned paper as a platform for inexpensive, low-volume, portable bioassays. *Angewandte Chemie International Edition M1* - **46**, 1318–1320 (2007).
72. Warren, A. D., Kwong, G. A., Wood, D. K., Lin, K. Y. & Bhatia, S. N. Point-of-care diagnostics for noncommunicable diseases using synthetic urinary biomarkers and paper microfluidics. *Proceedings of the National Academy of Sciences M1* - **111**, 3671–3676 (2014).
73. San Park, T., Li, W., McCracken, K. E. & Yoon, J.-Y. Smartphone quantifies Salmonella from paper microfluidics. *Lab on a Chip M1* - **13**, 4832–4840 (2013).
74. Hossain, S. Z., Luckham, R. E., McFadden, M. J. & Brennan, J. D. Reagentless bidirectional lateral flow bioactive paper sensors for detection of pesticides in beverage and food samples. *Anal. Chem.* **81**, 9055–9064 (2009).
75. San Park, T. & Yoon, J.-Y. Smartphone detection of Escherichia coli from field water samples on paper microfluidics. *IEEE Sensors Journal M1* - **15**, 1902–1907 (2015).
76. Martinez, A. W., Phillips, S. T., Whitesides, G. M. & Carrilho, E. Diagnostics for the developing world: microfluidic paper-based analytical devices. *Anal. Chem.* **82**, 3–10 (2010).
77. Carrilho, E., Martinez, A. W. & Whitesides, G. M. Understanding wax printing: a simple micropatterning process for paper-based microfluidics. *Anal. Chem.* **81**, 7091–7095 (2009).
78. Dungchai, W., Chailapakul, O. & Henry, C. S. A low-cost, simple, and rapid fabrication method for paper-based microfluidics using wax screen-printing. *Analyst M1* - **136**, 77–82 (2011).
79. Li, X., Tian, J., Nguyen, T. & Shen, W. Paper-based microfluidic devices by plasma treatment. *Anal. Chem.* **80**, 9131–9134 (2008).
80. Olkkonen, J., Lehtinen, K. & Erho, T. Flexographically printed fluidic structures in paper. *Anal. Chem.* **82**, 10246–10250 (2010).
81. Chitnis, G., Ding, Z., Chang, C.-L., Savran, C. A. & Ziaie, B. Laser-treated hydrophobic paper: an inexpensive microfluidic platform. *Lab on a Chip M1* - **11**, 1161–1165 (2011).
82. Karyakin, A. A., Gitelmacher, O. V. & Karyakina, E. E. Prussian Blue-Based First-Generation Biosensor. A Sensitive Amperometric Electrode for Glucose. *Anal. Chem.* **67**, 2419–2423 (2002).
83. Wang, J. Amperometric biosensors for clinical and therapeutic drug monitoring: a review. *J Pharm Biomed Anal* **19**, 47–53 (1999).
84. Zelada-Guillén, G. A., Sebastián-Avila, J. L., Blondeau, P., Riu, J. & Rius, F. X. Label-free detection of Staphylococcus aureus in skin using real-time potentiometric biosensors based on carbon nanotubes and aptamers. *Biosens Bioelectron* **31**, 226–232 (2012).
85. Lakard, B., Herlem, G., Lakard, S., Antoniou, A. & Fahys, B. Urea potentiometric biosensor based on modified electrodes with urease immobilized on polyethylenimine films. *Biosensors and Bioelectronics* **19**, 1641–1647 (2004).
86. Bertok, T., Gemeiner, P., Mikula, M., Gemeiner, P. & Tkac, J. Ultrasensitive impedimetric lectin based biosensor for glycoproteins containing sialic acid. *Microchimica Acta M1* - **180**, 151–159 (2013).
87. Xi, F., Gao, J., Wang, J. & Wang, Z. Discrimination and detection of bacteria with a label-free impedimetric biosensor based on self-assembled lectin monolayer. *J Electroanal Chem M1* - **656**, 252–257 (2011).
88. Baur, J. *et al.* Label-free femtomolar detection of target DNA by impedimetric DNA sensor based on poly (pyrrole-nitrilotriacetic acid) film. *Anal. Chem.* **82**, 1066–1072 (2009).
89. Wegener, J., Keese, C. R. & Giaever, I. Electric cell–substrate impedance sensing (ECIS) as a noninvasive means to monitor the kinetics of cell spreading to artificial surfaces. *Exp. Cell Res.* **259**, 158–166 (2000).
90. Szulcek, R., Bogaard, H. J. & van Nieuw Amerongen, G. P. Electric cell-substrate impedance sensing for the quantification of endothelial proliferation, barrier function, and motility. *Journal of visualized experiments: JoVE M1* - (2014).

91. Gamal, W. *et al.* Real-time quantitative monitoring of hiPSC-based model of macular degeneration on Electric Cell-substrate Impedance Sensing microelectrodes. *Biosensors and Bioelectronics M1* - **71**, 445–455 (2015).
92. Arkan, E., Saber, R., Karimi, Z. & Shamsipur, M. A novel antibody–antigen based impedimetric immunosensor for low level detection of HER2 in serum samples of breast cancer patients via modification of a gold nanoparticles decorated multiwall carbon nanotube-ionic liquid electrode. *Analytica Chimica Acta* **874**, 66–74 (2015).
93. Palomar, Q., Gondran, C., Holzinger, M., Marks, R. & Cosnier, S. Controlled carbon nanotube layers for impedimetric immunosensors: High performance label free detection and quantification of anti-cholera toxin antibody. *Biosensors and Bioelectronics M1* - **97**, 177–183 (2017).
94. Ramanathan, M. *et al.* Gold-coated carbon nanotube electrode arrays: Immunosensors for impedimetric detection of bone biomarkers. *Biosensors and Bioelectronics M1* - **77**, 580–588 (2016).
95. Deng, C. *et al.* Impedimetric aptasensor with femtomolar sensitivity based on the enlargement of surface-charged gold nanoparticles. *Anal. Chem.* **81**, 739–745 (2008).
96. Guan, J.-G., Miao, Y.-Q. & Zhang, Q.-J. Impedimetric biosensors. *Journal of bioscience and bioengineering M1* - **97**, 219–226 (2004).
97. Skl dal, P., Santos Riccardi, dos, C., Yamanaka, H. & da Costa, P. I. C. Piezoelectric biosensors for real-time monitoring of hybridization and detection of hepatitis C virus. *J. Virol. Methods M1* - **117**, 145–151 (2004).
98. Kumar, A. Biosensors based on piezoelectric crystal detectors: theory and application. *JOM-e M1* - **52**, 1–6 (2000).
99. Rodahl, M., Höök, F., Krozer, A., Brzezinski, P. & Kasemo, B. Quartz crystal microbalance setup for frequency and Q-factor measurements in gaseous and liquid environments. *Review of Scientific Instruments* **66**, 3924–3930 (1995).
100. Atay, S. *et al.* Quartz crystal microbalance based biosensors for detecting highly metastatic breast cancer cells via their transferrin receptors. *Analytical Methods M1* - **8**, 153–161 (2016).
101. Rocha-Santos, T. A. Sensors and biosensors based on magnetic nanoparticles. *TrAC Trends in Analytical Chemistry M1* - **62**, 28–36 (2014).
102. Ravalli, A. & Marrazza, G. Gold and magnetic nanoparticles-based electrochemical biosensors for cancer biomarker determination. *Journal of nanoscience and nanotechnology M1* - **15**, 3307–3319 (2015).
103. Ramanathan, K., Jönsson, B. R. & Danielsson, B. Sol–gel based thermal biosensor for glucose. *Analytica Chimica Acta* **427**, 1–10 (2001).
104. Ramanathan, K. & Danielsson, B. Principles and applications of thermal biosensors. *Biosensors and Bioelectronics M1* - **16**, 417–423 (2001).
105. Atencia, J. & Beebe, D. J. Controlled microfluidic interfaces. *Nature M1* - **437**, 648 (2004).
106. Hatch, A. *et al.* A rapid diffusion immunoassay in a T-sensor. *Nature Biotechnology* **19**, 461 (2001).
107. Maruyama, T. *et al.* Enzymatic degradation of p-chlorophenol in a two-phase flow microchannel system. *Lab on a Chip M1* - **3**, 308–312 (2003).
108. Surmeian, M. *et al.* Three-layer flow membrane system on a microchip for investigation of molecular transport. *Anal. Chem.* **74**, 2014–2020 (2002).
109. Gagnon, Z. R. Cellular dielectrophoresis: applications to the characterization, manipulation, separation and patterning of cells. *Electrophoresis M1* - **32**, 2466–2487 (2011).
110. Green, N. G., Ramos, A., Gonz lez, A., Morgan, H. & Castellanos, A. Fluid flow induced by nonuniform ac electric fields in electrolytes on microelectrodes. I. Experimental measurements. *Physical review E M1* - **61**, 4011 (2000).
111. Gonzalez, A., Ramos, A., Green, N. G., Castellanos, A. & Morgan, H. Fluid flow induced by nonuniform ac electric fields in electrolytes on microelectrodes. II. A linear double-layer analysis. *Phys. Rev. E* **61**, 4019–4028 (2000).
112. Morgan, H., Green, N. G., Ramos, A. & Garcia-S nchez, P. Control of two-phase flow in a microfluidic system using ac electric fields. *Appl. Phys. Lett.* **91**, 254107 (2007).
113. Gagnon, Z. R. & Chang, H.-C. Electrothermal ac electro-osmosis. *Appl. Phys. Lett.* **94**, 024101 (2009).

114. Gagnon, Z. R. & Chang, H.-C. Dielectrophoresis of ionized gas microbubbles: Dipole reversal due to diffusive double-layer polarization. *Appl. Phys. Lett.* **93**, 224101 (2008).
115. Gagnon, Z., Senapati, S. & Chang, H.-C. Optimized DNA hybridization detection on nanocolloidal particles by dielectrophoresis. *Electrophoresis M1* - **31**, 666–671 (2010).
116. Regtmeier, J., Eichhorn, R., Bogunovic, L., Ros, A. & Anselmetti, D. Dielectrophoretic trapping and polarizability of DNA: the role of spatial conformation. *Anal. Chem.* **82**, 7141–7149 (2010).
117. Giraud, G. *et al.* Dielectrophoretic manipulation of ribosomal RNA. *Biomicrofluidics M1* - **5**, 024116 (2011).
118. Markx, G. H., Talary, M. S. & Pethig, R. Separation of viable and non-viable yeast using dielectrophoresis. *J. Biotechnol. M1* - **32**, 29–37 (1994).
119. Thaokar, R. M. & Kumaran, V. Electrohydrodynamic instability of the interface between two fluids confined in a channel. *Phys. Fluids M1* - **17**, 084104 (2005).
120. Hardt, S. & Hahn, T. Microfluidics with aqueous two-phase systems. *Lab on a Chip M1* - **12**, 434–442 (2012).
121. Arnold, W. M. & Zimmermann, U. Dielectric properties of zwitterion solutions. *Biochemical Society Transactions M1* - (1993).
122. Whitesides, G. M., Ostuni, E., Takayama, S., Jiang, X. & Ingber, D. E. Soft lithography in biology and biochemistry. *Annu. Rev. Biomed. Eng.* **3**, 335–373 (2001).
123. Gagnon, Z., Mazur, J. & Chang, H.-C. Integrated AC electrokinetic cell separation in a closed-loop device. *Lab on a Chip M1* - **10**, 718–726 (2010).
124. Gagnon, Z., Gordon, J., Sengupta, S. & Chang, H.-C. Bovine red blood cell starvation age discrimination through a glutaraldehyde-amplified dielectrophoretic approach with buffer selection and membrane cross-linking. *Electrophoresis M1* - **29**, 2272–2279 (2008).
125. Brody, J. P. & Yager, P. Diffusion-based extraction in a microfabricated device. *Sensors and Actuators A: Physical M1* - **58**, 13–18 (1997).
126. Johnson, T. J., Ross, D. & Locascio, L. E. Rapid microfluidic mixing. *Anal. Chem.* **74**, 45–51 (2002).
127. Laser, D. J. & Santiago, J. G. A review of micropumps. *J. Micromech. Microeng.* **14**, R35 (2004).
128. Nguyen, N.-T., Huang, X. & Chuan, T. K. MEMS-micropumps: a review. *Journal of fluids Engineering M1* - **124**, 384–392 (2002).
129. Henares, T. G., Mizutani, F. & Hisamoto, H. Current development in microfluidic immunosensing chip. *Analytica Chimica Acta* **611**, 17–30 (2008).
130. Huang, W.-H., Ai, F., Wang, Z.-L. & Cheng, J.-K. Recent advances in single-cell analysis using capillary electrophoresis and microfluidic devices. *Journal of Chromatography B M1* - **866**, 104–122 (2008).
131. Teh, S.-Y., Lin, R., Hung, L.-H. & Lee, A. P. Droplet microfluidics. *Lab on a Chip M1* - **8**, 198–220 (2008).
132. Yin, H. & Marshall, D. Microfluidics for single cell analysis. *Curr. Opin. Biotechnol. M1* - **23**, 110–119 (2012).
133. Siegrist, J. *et al.* Validation of a centrifugal microfluidic sample lysis and homogenization platform for nucleic acid extraction with clinical samples. *Lab on a Chip M1* - **10**, 363–371 (2010).
134. Sasaki, N. Recent applications of AC electrokinetics in biomolecular analysis on microfluidic devices. *Analytical Sciences M1* - **28**, 3 (2012).
135. Fuhr, G., Schnelle, T. & Wagner, B. Travelling wave-driven microfabricated electrohydrodynamic pumps for liquids. *J. Micromech. Microeng.* **4**, 217 (1994).
136. Ahualli, S., Jiménez, M. L., Carrique, F. & Delgado, A. V. AC electrokinetics of concentrated suspensions of soft particles. *Langmuir M1* - **25**, 1986–1997 (2009).
137. Eagles, P. A., Qureshi, A. N. & Jayasinghe, S. N. Electrohydrodynamic jetting of mouse neuronal cells. *Biochem. J. M1* - **394**, 375–378 (2006).
138. Zeng, J. & Korsmeyer, T. Principles of droplet electrohydrodynamics for lab-on-a-chip. *Lab on a Chip M1* - **4**, 265–277 (2004).
139. Cheng, L.-J. & Chang, H.-C. Switchable pH actuators and 3D integrated salt bridges as new strategies for reconfigurable microfluidic free-flow electrophoretic separation. *Lab on a Chip M1* - **14**, 979–987 (2014).

140. Zhang, L. & Yin, X-F. Field amplified sample stacking coupled with chip-based capillary electrophoresis using negative pressure sample injection technique. *Journal of Chromatography A M1* - **1137**, 243–248 (2006).
141. Green, N. G., Ramos, A., Gonzalez, A., Castellanos, A. & Morgan, H. Electrothermally induced fluid flow on microelectrodes. *J. Electrostatics M1* - **53**, 71–87 (2001).
142. Oddy, M. H., Santiago, J. G. & Mikkelsen, J. C. Electrokinetic instability micromixing. *Anal. Chem.* **73**, 5822–5832 (2001).
143. Ramos, A., Morgan, H., Green, N. G. & Castellanos, A. Ac electrokinetics: a review of forces in microelectrode structures. *J. Phys. D M1* - **31**, 2338 (1998).
144. Zeng, S., Chen, C.-H., Mikkelsen, J. C., Jr & Santiago, J. G. Fabrication and characterization of electroosmotic micropumps. *Sensors and Actuators B: Chemical* **79**, 107–114 (2001).
145. Ajdari, A. Pumping liquids using asymmetric electrode arrays. *Physical review E M1* - **61**, R45 (2000).
146. Giddings, J. C., Yang, F. J. & Myers, M. N. Flow-field-flow fractionation: a versatile new separation method. *Science M1* - **193**, 1244–1245 (1976).
147. Giddings, J. C. Field-flow fractionation: analysis of macromolecular, colloidal, and particulate materials. *Science M1* - **260**, 1456–1465 (1993).
148. Williams, P. S., Levin, S., Lenczycki, T. & Giddings, J. C. Continuous SPLITT fractionation based on a diffusion mechanism. *Ind. Eng. Chem. Res.* **31**, 2172–2181 (1992).
149. Hatch, A. *et al.* A rapid diffusion immunoassay in a T-sensor. *Nature Biotechnology* **19**, 461 (2001).
150. Choban, E. R., Markoski, L. J., Wieckowski, A. & Kenis, P. J. Microfluidic fuel cell based on laminar flow. *J. Power Sources M1* - **128**, 54–60 (2004).
151. Kamholz, A. E. & Yager, P. Theoretical analysis of molecular diffusion in pressure-driven laminar flow in microfluidic channels. *Biophysical Journal* **80**, 155–160 (2001).
152. Bhagat, A. A. S., Kuntaegowdanahalli, S. S. & Papautsky, I. Enhanced particle filtration in straight microchannels using shear-modulated inertial migration. *Phys. Fluids M1* - **20**, 101702 (2008).
153. Desmond, M., Mavrogiannis, N. & Gagnon, Z. Maxwell-Wagner polarization and frequency-dependent injection at aqueous electrical interfaces. *Phys. Rev. Lett.* **109**, 187602 (2012).
154. Pohl, H. A. The motion and precipitation of suspensoids in divergent electric fields. *Journal of Applied Physics* **22**, 869–871 (1951).
155. Gascoyne, P. R. & Vykoukal, J. Particle separation by dielectrophoresis. *Electrophoresis M1* - **23**, 1973 (2002).
156. Hughes, M. P. Strategies for dielectrophoretic separation in laboratory-on-a-chip systems. *Electrophoresis M1* - **23**, 2569–2582 (2002).
157. Anwar, K., Han, T., Yu, S. & Kim, S. M. Integrated micro/nano-fluidic system for mixing and preconcentration of dissolved proteins. *Microchimica Acta M1* - **173**, 331–335 (2011).
158. Gambin, Y. *et al.* Visualizing a one-way protein encounter complex by ultrafast single-molecule mixing. *Nature methods M1* - **8**, 239 (2011).
159. Ko, Y.-J., Maeng, J.-H., Ahn, Y. & Hwang, S. Y. DNA ligation using a disposable microfluidic device combined with a micromixer and microchannel reactor. *Sensors and Actuators B: Chemical* **157**, 735–741 (2011).
160. Wang, X. *et al.* Fast DNA hybridization on a microfluidic mixing device based on pneumatic driving. *Talanta M1* - **84**, 565–571 (2011).
161. Yang, Y., Swennenhuis, J. F., Rho, H. S., Le Gac, S. V. & Terstappen, L. W. Parallel single cancer cell whole genome amplification using button-valve assisted mixing in nanoliter chambers. *PLoS One M1* - **9**, e107958 (2014).
162. Viktorov, V., Mahmud, M. R. & Visconte, C. Design and characterization of a new HC passive micromixer up to Reynolds number 100. *Chemical Engineering Research and Design* **108**, 152–163 (2016).
163. Tofteberg, T., Skolimowski, M., Andreassen, E. & Geschke, O. A novel passive micromixer: lamination in a planar channel system. *Microfluidics and Nanofluidics M1* - **8**, 209–215 (2010).
164. Buchegger, W., Wagner, C., Lendl, B., Kraft, M. & Vellekoop, M. J. A highly uniform lamination micromixer with wedge shaped inlet channels for time resolved infrared spectroscopy. *Microfluid Nanofluid* **10**, 889–897 (2010).

165. Jain, M. & Nandakumar, K. Novel index for micromixing characterization and comparative analysis. *Biomicrofluidics M1 - 4*, 031101 (2010).
166. Chen, Z. *et al.* Performance analysis of a folding flow micromixer. *Microfluidics and nanofluidics M1 - 6*, 763–774 (2009).
167. Kang, T. G., Singh, M. K., Anderson, P. D. & Meijer, H. E. A chaotic serpentine mixer efficient in the creeping flow regime: from design concept to optimization. *Microfluidics and nanofluidics M1 - 7*, 783 (2009).
168. Lee, C.-Y., Wang, W.-T., Liu, C.-C. & Fu, L.-M. Passive mixers in microfluidic systems: A review. *Chemical Engineering Journal* **288**, 146–160 (2016).
169. Matlock-Colangelo, L., Colangelo, N. W., Fenzl, C., Frey, M. W. & Baemner, A. J. Passive Mixing Capabilities of Micro-and Nanofibres When Used in Microfluidic Systems. *Sensors M1 - 16*, 1238 (2016).
170. Lynn, N. S., Jr. *et al.* Biosensing enhancement using passive mixing structures for microarray-based sensors. *Biosensors and Bioelectronics M1 - 54*, 506–514 (2014).
171. Jacobson, S. C., McKnight, T. E. & Ramsey, J. M. Microfluidic devices for electrokinetically driven parallel and serial mixing. *Anal. Chem.* **71**, 4455–4459 (1999).
172. Losey, M. W., Jackman, R. J., Firebaugh, S. L., Schmidt, M. A. & Jensen, K. F. Design and fabrication of microfluidic devices for multiphase mixing and reaction. *J. Microelectromech. Syst.* **11**, 709–717 (2002).
173. Biswas, S. K., Das, T. & Chakraborty, S. Nontrivial augmentations in mixing performance through integrated active and passive mixing in serpentine microchannels. *Journal of Applied Physics* **111**, 054904 (2012).
174. Ober, T. J., Foresti, D. & Lewis, J. A. Active mixing of complex fluids at the microscale. *Proceedings of the National Academy of Sciences M1 - 112*, 12293–12298 (2015).
175. Glasgow, I. & Aubry, N. Enhancement of microfluidic mixing using time pulsing. *Lab on a Chip M1 - 3*, 114–120 (2003).
176. Lu, L.-H., Ryu, K. S. & Liu, C. A magnetic microstirrer and array for microfluidic mixing. *J. Microelectromech. Syst.* **11**, 462–469 (2002).
177. Cao, Q., Han, X. & Li, L. An active microfluidic mixer utilizing a hybrid gradient magnetic field. *International Journal of Applied Electromagnetics and Mechanics* **47**, 583–592 (2015).
178. Scherr, T. F., Ryskoski, H. B., Doyle, A. B. & Haselton, F. R. A two-magnet strategy for improved mixing and capture from biofluids. *Biomicrofluidics M1 - 10*, 024118 (2016).
179. Bui, T., Morana, B., Scholtes, T., Chu Duc, T. & Sarro, P. M. A mixing surface acoustic wave device for liquid sensing applications: Design, simulation, and analysis. *Journal of Applied Physics* **120**, 074504 (2016).
180. Shilton, R., Tan, M. K., Yeo, L. Y. & Friend, J. R. Particle concentration and mixing in microdrops driven by focused surface acoustic waves. *Journal of Applied Physics* **104**, 014910 (2008).
181. Mavrogiannis, N., Desmond, M. & Gagnon, Z. R. Fluidic dielectrophoresis: The polarization and displacement of electrical liquid interfaces. *Electrophoresis M1 - 36*, 1386–1395 (2015).
182. Mavrogiannis, N., Ibo, M., Fu, X., Crivellari, F. & Gagnon, Z. Microfluidics made easy: A robust low-cost constant pressure flow controller for engineers and cell biologists. *Biomicrofluidics M1 - 10*, 034107 (2016).
183. Peruski, A. H. & Peruski, L. F. Immunological methods for detection and identification of infectious disease and biological warfare agents. *Clin. Diagn. Lab. Immunol.* **10**, 506–513 (2003).
184. Palchetti, I. & Mascini, M. Nucleic acid biosensors for environmental pollution monitoring. *Analyst M1 - 133*, 846–854 (2008).
185. Raz, S. R. & Haasnoot, W. Multiplex bioanalytical methods for food and environmental monitoring. *TrAC Trends in Analytical Chemistry M1 - 30*, 1526–1537 (2011).
186. Cooper, M. A. Optical biosensors in drug discovery. *Nature reviews Drug discovery M1 - 1*, 515 (2002).
187. Lee, H., Sun, E., Ham, D. & Weissleder, R. Chip–NMR biosensor for detection and molecular analysis of cells. *Nat. Med.* **14**, 869 (2008).
188. Roelse, M., de Ruijter, N. C., Vrouwe, E. X. & Jongsma, M. A. A generic microfluidic biosensor of G protein-coupled receptor activation—monitoring cytoplasmic [Ca<sup>2+</sup>] changes in human HEK293 cells. *Biosensors and Bioelectronics M1 - 47*, 436–444 (2013).

189. Voura, E. B., Jaiswal, J. K., Mattoussi, H. & Simon, S. M. Tracking metastatic tumor cell extravasation with quantum dot nanocrystals and fluorescence emission-scanning microscopy. *Nat. Med.* **10**, 993 (2004).
190. Wan, Y., Su, Y., Zhu, X., Liu, G. & Fan, C. Development of electrochemical immunosensors towards point of care diagnostics. *Biosens Bioelectron* **47**, 1–11 (2013).
191. Watkins, N. N. *et al.* Microfluidic CD4<sup>+</sup> and CD8<sup>+</sup> T lymphocyte counters for point-of-care HIV diagnostics using whole blood. *Science Translational Medicine* **5**, 214ra170 (2013).
192. Yoo, J.-C., La, G.-S., Kang, C. J. & Kim, Y.-S. Microfabricated polydimethylsiloxane microfluidic system including micropump and microvalve for integrated biosensor. *Current Applied Physics M1 - 8*, 692–695 (2008).
193. Lin, M. X. *et al.* Continuous labeling of circulating tumor cells with microbeads using a vortex micromixer for highly selective isolation. *Biosensors and Bioelectronics M1 - 40*, 63–67 (2013).
194. Ismagilov, R. F., Stroock, A. D., Kenis, P. J., Whitesides, G. & Stone, H. A. Experimental and theoretical scaling laws for transverse diffusive broadening in two-phase laminar flows in microchannels. *Appl. Phys. Lett.* **76**, 2376–2378 (2000).
195. Pollet, J. *et al.* Fiber optic SPR biosensing of DNA hybridization and DNA–protein interactions. *Biosensors and Bioelectronics M1 - 25*, 864–869 (2009).
196. Rodriguez, M. C., Kawde, A.-N. & Wang, J. Aptamer biosensor for label-free impedance spectroscopy detection of proteins based on recognition-induced switching of the surface charge. *Chemical Communications M1 - 4267–4269* (2005).
197. Coltro, W. K. T., de Santis Neves, R., de Jesus Motheo, A., Da Silva, J. A. F. & Carrilho, E. Microfluidic devices with integrated dual-capacitively coupled contactless conductivity detection to monitor binding events in real time. *Sensors and Actuators B: Chemical* **192**, 239–246 (2014).
198. Ariyaratne, A. & Zocchi, G. Plasmon resonance enhanced mechanical detection of ligand binding. *Appl. Phys. Lett.* **106**, 013702 (2015).
199. Cao, L. *et al.* Visual and high-throughput detection of cancer cells using a graphene oxide-based FRET aptasensing microfluidic chip. *Lab on a Chip M1 - 12*, 4864–4869 (2012).
200. Dong, C. & Ren, J. Coupling of fluorescence correlation spectroscopy with capillary and microchannel analytical systems and its applications. *Electrophoresis M1 - 35*, 2267–2278 (2014).
201. Yoo, J. H., Woo, D. H., Chang, M.-S. & Chun, M.-S. Microfluidic based biosensing for Escherichia coli detection by embedding antimicrobial peptide-labeled beads. *Sensors and Actuators B: Chemical* **191**, 211–218 (2014).
202. Giraud, G. *et al.* Fluorescence lifetime biosensing with DNA microarrays and a CMOS-SPAD imager. *Biomedical optics express M1 - 1*, 1302–1308 (2010).
203. Lee, Y.-K., Deval, J., Tabeling, P. & Ho, C.-M. in *Microreaction Technology* 185–191 (Springer M1 -, 2001).
204. Fu, X., Mavrogiannis, N., Doria, S. & Gagnon, Z. Microfluidic pumping, routing and metering by contactless metal-based electro-osmosis. *Lab on a Chip M1 - 15*, 3600–3608 (2015).
205. De, M. *et al.* Sensing of proteins in human serum using conjugates of nanoparticles and green fluorescent protein. *Nature chemistry M1 - 1*, 461–465 (2009).
206. Lee, H., Yoon, T. J. & Weissleder, R. Ultrasensitive Detection of Bacteria Using Core–Shell Nanoparticles and an NMR-Filter System. *Angewandte Chemie International Edition M1 - 48*, 5657–5660 (2009).
207. Miranda, O. R. *et al.* Colorimetric bacteria sensing using a supramolecular enzyme–nanoparticle biosensor. *J. Am. Chem. Soc.* **133**, 9650–9653 (2011).
208. Riboh, J. C., Haes, A. J., McFarland, A. D., Ranjit Yonzon, C. & Van Duyne, R. P. A Nanoscale Optical Biosensor: Real-Time Immunoassay in Physiological Buffer Enabled by Improved Nanoparticle Adhesion. *The Journal of Physical Chemistry B* **107**, 1772–1780 (2003).
209. Wang, L. *et al.* Direct fluorimetric determination of  $\gamma$ -globulin in human serum with organic nanoparticle biosensor. *Spectrochimica Acta Part A: Molecular and Biomolecular Spectroscopy M1 - 61*, 129–133 (2005).
210. Stern, E. *et al.* Label-free immunodetection with CMOS-compatible semiconducting nanowires. *Nature M1 - 445*, 519 (2007).
211. Liu, T., Zhao, J., Zhang, D. & Li, G. Novel method to detect DNA methylation using gold nanoparticles coupled with enzyme-linkage reactions. *Anal. Chem.* **82**, 229–233 (2009).



212. Su, M., Li, S. & Dravid, V. P. Microcantilever resonance-based DNA detection with nanoparticle probes. *Appl. Phys. Lett.* **82**, 3562–3564 (2003).
213. Cai, H., Wang, Y., He, P. & Fang, Y. Electrochemical detection of DNA hybridization based on silver-enhanced gold nanoparticle label. *Analytica Chimica Acta* **469**, 165–172 (2002).
214. Goluch, E. D. *et al.* A bio-barcode assay for on-chip attomolar-sensitivity protein detection. *Lab on a Chip M1 - 6*, 1293–1299 (2006).
215. Jia, J. *et al.* A method to construct a third-generation horseradish peroxidase biosensor: Self-assembling gold nanoparticles to three-dimensional sol-gel network. *Anal. Chem.* **74**, 2217–2223 (2002).
216. Bunimovich, Y. L. *et al.* Quantitative real-time measurements of DNA hybridization with alkylated nonoxidized silicon nanowires in electrolyte solution. *J. Am. Chem. Soc.* **128**, 16323–16331 (2006).
217. Nicu, L. *et al.* Resonating piezoelectric membranes for microelectromechanically based bioassay: detection of streptavidin-gold nanoparticles interaction with biotinylated DNA. *Sensors and Actuators B: Chemical* **110**, 125–136 (2005).
218. Bonanno, L. M. & DeLouise, L. A. Steric crowding effects on target detection in an affinity biosensor. *Langmuir M1 - 23*, 5817–5823 (2007).
219. Spisak, S., Tulassay, Z., Molnar, B. & Guttman, A. Protein microchips in biomedicine and biomarker discovery. *Electrophoresis M1 - 28*, 4261–4273 (2007).
220. Kim, J. H.-S., Marafie, A., Jia, X.-Y., Zoval, J. V. & Madou, M. J. Characterization of DNA hybridization kinetics in a microfluidic flow channel. *Sensors and Actuators B: Chemical* **113**, 281–289 (2006).
221. Cesaro-Tadic, S. *et al.* High-sensitivity miniaturized immunoassays for tumor necrosis factor  $\alpha$  using microfluidic systems. *Lab on a Chip M1 - 4*, 563–569 (2004).
222. Matthews, S. A. M. *et al.* Quantitative kinetic analysis in a microfluidic device using frequency-domain fluorescence lifetime imaging. *Anal. Chem.* **79**, 4101–4109 (2007).
223. Kamholz, A. E., Weigl, B. H., Finlayson, B. A. & Yager, P. Quantitative analysis of molecular interaction in a microfluidic channel: the T-sensor. *Anal. Chem.* **71**, 5340–5347 (1999).
224. Mavrogianis, N., Crivellari, F. & Gagnon, Z. R. Label-free biomolecular detection at electrically displaced liquid interfaces using interfacial electrokinetic transduction (IET). *Biosensors and Bioelectronics M1 - 77*, 790–798 (2016).
225. Weber, P. C., Ohlendorf, D. H., Wendoloski, J. J. & Salemme, F. R. Structural origins of high-affinity biotin binding to streptavidin. *Science M1 - 243*, 85–88 (1989).
226. Belongia, B. M. & Baygents, J. C. Measurements on the diffusion coefficient of colloidal particles by Taylor-Aris dispersion. *Journal of colloid and interface science* **195**, 19–31 (1997).
227. Akerström, B. & Björck, L. A physicochemical study of protein G, a molecule with unique immunoglobulin G-binding properties. *Journal of Biological Chemistry* **261**, 10240–10247 (1986).
228. Moen, K., Brun, J. G., Madland, T. M., Tynning, T. & Jonsson, R. Immunoglobulin G and A antibody responses to *Bacteroides forsythus* and *Prevotella intermedia* in sera and synovial fluids of arthritis patients. *Clin. Diagn. Lab. Immunol.* **10**, 1043–1050 (2003).
229. G nther, A. & Jensen, K. F. Multiphase microfluidics: from flow characteristics to chemical and materials synthesis. *Lab on a Chip M1 - 6*, 1487–1503 (2006).
230. Kim, K. *et al.* Interfacial liquid-state surface-enhanced Raman spectroscopy. *Nature communications M1 - 4*, 2182 (2013).
231. Chan, K. A., Gulati, S., Edel, J. B., de Mello, A. J. & Kazarian, S. G. Chemical imaging of microfluidic flows using ATR-FTIR spectroscopy. *Lab on a Chip M1 - 9*, 2909–2913 (2009).
232. Salverda, J. M. *et al.* Fluorescent cyclic voltammetry of immobilized azurin: direct observation of thermodynamic and kinetic heterogeneity. *Angewandte Chemie International Edition M1 - 49*, 5776–5779 (2010).
233. Wu, S. L. *et al.* EIS study of the surface film on the surface of carbon steel from supercritical carbon dioxide corrosion. *Applied Surface Science* **228**, 17–25 (2004).
234. Xiao, C. & Luong, J. H. On-line monitoring of cell growth and cytotoxicity using electric cell-substrate impedance sensing (ECIS). *Biotechnol. Prog.* **19**, 1000–1005 (2003).
235. Lee, J. A. *et al.* An electrochemical impedance biosensor with aptamer-modified pyrolyzed carbon electrode for label-free protein detection. *Sensors and Actuators B: Chemical* **129**, 372–379 (2008).

236. Cai, H., Lee, T. M.-H. & Hsing, I.-M. Label-free protein recognition using an aptamer-based impedance measurement assay. *Sensors and Actuators B: Chemical* **114**, 433–437 (2006).
237. Ensafi, A. A., Taei, M., Rahmani, H. R. & Khayamian, T. Sensitive DNA impedance biosensor for detection of cancer, chronic lymphocytic leukemia, based on gold nanoparticles/gold modified electrode. *Electrochimica Acta* **56**, 8176–8183 (2011).
238. Hu, Y. *et al.* Decorated graphene sheets for label-free DNA impedance biosensing. *Biomaterials M1* - **33**, 1097–1106 (2012).
239. Xu, Y., Jiang, Y., Cai, H., He, P.-G. & Fang, Y.-Z. Electrochemical impedance detection of DNA hybridization based on the formation of M-DNA on polypyrrole/carbon nanotube modified electrode. *Analytica Chimica Acta* **516**, 19–27 (2004).
240. Hu, Y. *et al.* Label-free electrochemical impedance sensing of DNA hybridization based on functionalized graphene sheets. *Chemical Communications M1* - **47**, 1743–1745 (2011).
241. Shih, S. C., Barbulovic-Nad, I., Yang, X., Fobel, R. & Wheeler, A. R. Digital microfluidics with impedance sensing for integrated cell culture and analysis. *Biosensors and Bioelectronics M1* - **42**, 314–320 (2013).
242. Reitingner, S., Wissenwasser, J. R., Kapferer, W., Heer, R. & Lepperdinger, G. N. Electric impedance sensing in cell-substrates for rapid and selective multipotential differentiation capacity monitoring of human mesenchymal stem cells. *Biosensors and Bioelectronics M1* - **34**, 63–69 (2012).
243. Nguyen, T. A., Yin, T.-I., Reyes, D. & Urban, G. A. Microfluidic chip with integrated electrical cell-impedance sensing for monitoring single cancer cell migration in three-dimensional matrixes. *Anal. Chem.* **85**, 11068–11076 (2013).
244. Hong, J.-L., Lan, K.-C. & Jang, L.-S. Electrical characteristics analysis of various cancer cells using a microfluidic device based on single-cell impedance measurement. *Sensors and Actuators B: Chemical* **173**, 927–934 (2012).
245. Michaelis, S., Wegener, J. & Robelek, R. Label-free monitoring of cell-based assays: Combining impedance analysis with SPR for multiparametric cell profiling. *Biosensors and Bioelectronics M1* - **49**, 63–70 (2013).
246. Johnson, T. J., Ross, D. & Locascio, L. E. Rapid microfluidic mixing. *Anal. Chem.* **74**, 45–51 (2002).
247. Kwon, J. W. & Kim, E. S. Multi-level microfluidic channel routing with protected convex corners. *Sensors and Actuators A: Physical M1* - **97**, 729–733 (2002).
248. Solomon, D. E. & Vanapalli, S. A. Multiplexed microfluidic viscometer for high-throughput complex fluid rheology. *Microfluidics and nanofluidics M1* - **16**, 677–690 (2014).
249. Hatch, A., Garcia, E. & Yager, P. Diffusion-based analysis of molecular interactions in microfluidic devices. *Proceedings of the IEEE* **92**, 126–139 (2004).
250. Mandal, S., Goddard, J. M. & Erickson, D. A multiplexed optofluidic biomolecular sensor for low mass detection. *Lab on a Chip M1* - **9**, 2924–2932 (2009).
251. Weng, X., Jiang, H. & Li, D. Microfluidic DNA hybridization assays. *Microfluidics and nanofluidics M1* - **11**, 367 (2011).
252. Song, H. & Ismagilov, R. F. Millisecond kinetics on a microfluidic chip using nanoliters of reagents. *J. Am. Chem. Soc.* **125**, 14613–14619 (2003).
253. Mavrogianis, N., Crivellari, F. & Gagnon, Z. R. Label-free biomolecular detection at electrically displaced liquid interfaces using interfacial electrokinetic transduction (IET). *Biosensors and Bioelectronics M1* - **77**, 790–798 (2016).
254. Crivellari, F., Mavrogianis, N. & Gagnon, Z. Nanoparticle-based biosensing using interfacial electrokinetic transduction. *Sensors and Actuators B: Chemical* **240**, 926–933 (2017).
255. Mavrogianis, N., Ibo, M., Fu, X., Crivellari, F. & Gagnon, Z. Microfluidics made easy: A robust low-cost constant pressure flow controller for engineers and cell biologists. *Biomicrofluidics M1* - **10**, 034107 (2016).

# Curriculum Vitae

---

**Nicholas Mavrogiannis**

nmavrog1@jhu.edu

18 E Madison Street Unit 4 Baltimore, MD 21202

908.803.0638

## Education

---

**Johns Hopkins University**, Baltimore, Maryland

**PhD Candidate:** *Chemical and Biomolecular Engineering*

January 2018

**Master of Science:** *Chemical and Biomolecular Engineering*

August 2014

GPA: 3.7/4.0

**Bachelor of Science:** *Chemical and Biomolecular Engineering*

May 2013

GPA: 3.3/4.0

## Professional Experience

---

**Zachary Gagnon Lab**, Johns Hopkins University

January 2012 – Present

- Developing a novel non-optical, label-free microfluidic biosensor with high sensitivity and selectivity
- Co-Authored 9 original papers in peer-reviewed journals
- Presented work at 5 different conferences; one as co-chair of a conference session
- 1 patent pending for novel microfluidic biosensing device coupled with electrokinetic phenomena

**GE Healthcare**, Piscataway, NJ

Summer 2011

*Bioprocess Chromatography Engineer*

- Developed Pressure-Flow curves and resin integrity tests for Capto SR ImpRes resin packed in Axichrom 100 Chromatography columns
- Data was used to determine optimal packing parameters for the media/column combination and was logged in a companywide library database for GEHC Customer Support personnel

*Bioprocess Chromatography Engineer*

Summer 2010

- Developed Van Deemter and Pressure-Flow curves for GEHC Sepharose IEX resin packed in BPG 100 and 200 Chromatography columns
- Data was used to determine optimal packing parameters for the media/column combination and was logged in a companywide library database for GEHC Customer Support personnel

## Honors and Awards

---

1. Johns Hopkins University Chemical and Biomolecular Engineering Graduate Student Excellence Award (2017)
2. AES Electrophoresis Society Travel Award (2014)
3. Johns Hopkins University Chemical and Biomolecular Engineering Excellence Member (2013)
4. Johns Hopkins University Chemical and Biomolecular Engineering Undergraduate Research Award (2013)

## Journal Publications (\* denotes equal contribution)

---

1. **Mavrogiannis, N.**, Lavi, E., Cole, J., Desmond, M., and Gagnon, Z., "Active Microfluidic Gradient Generator for Regulating Dictyostelium Discoideum Migration Using Fluidic Dielectrophoresis," **In preparation**
2. Lewis, D.\*, **Mavrogiannis, N.\***, Gagnon, Z., and Gerecht, S., "Microfluidic Platform for the Real Time Measurement and Observation of Endothelial Barrier Function Under Shear Stress" **Submitted**
3. **Mavrogiannis, N.**, Gagnon, Z., "Non-optical, label-free detection in human serum using interfacial electrokinetic transduction (IET)." **In preparation**
4. Fu, X., **Mavrogiannis, N.**, and Gagnon, Z., "Piezoresistive Conductive Microfluidic Membranes for Low-cost, On-chip pressure and flow sensing." **Submitted**
5. Crivellari, F., **Mavrogiannis, N.**, and Gagnon, Z., "Nanoparticle-based biosensing using interfacial electrokinetic transduction." *Sensors and Actuators B.* 240, 926 (2017)
6. **Mavrogiannis, N.**, Fu, X., Desmond, M., McLarnon, R., and Gagnon, Z., "Monitoring microfluidic interfacial flows using impedance spectroscopy." *Sensors and Actuators B.* 239, 218 (2017)
7. **Mavrogiannis, N.**, Desmond, M., Ling, K., and Gagnon, Z., "Microfluidic Mixing and Analog On-Chip Concentration Control Using Fluidic Dielectrophoresis." *Micromachines.* 7, 214 (2016). **Highlight Feature Paper**
8. Fu, X., **Mavrogiannis, N.**, Ibo, M., Crivellari, F., and Gagnon, Z., "Microfluidic free-flow zone electrophoresis and isotachopheresis using carbon black nano-composite PDMS sidewall membranes." *Electrophoresis*, 38, 327 (2016)
9. **Mavrogiannis, N.**, Ibo, M., Fu, X., Crivellari, F., and Gagnon, Z., "Microfluidics made easy: A robust low-cost constant pressure flow controller for engineers and cell biologists." *Biomicrofluidics.* 10, 034107 (2016)
10. **Mavrogiannis, N.**, Crivellari, F., and Gagnon, Z., "Label-Free Biomolecular Detection at Electrically Displaced Liquid Interfaces Using Interfacial Electrokinetic Transduction (IET)." *Biosensors and Bioelectronics.* 77, 790 (2016)
11. **Mavrogiannis, N.**, Desmond, M., and Gagnon, ZR., "Fluidic dielectrophoresis: The polarization and displacement of electrical liquid interfaces." *Electrophoresis.* 36, 1386 (2015).
12. Fu, X., **Mavrogiannis, N.**, Doria, S., and Gagnon, Z., "Microfluidic pumping, routing and metering by contactless metal-based electro-osmosis." *Lab Chip.* 15, 3600 (2015)

13. Desmond, M., **Mavrogiannis, N.**, and Gagnon, Z., “Maxwell-Wagner Polarization and Frequency-Dependent Injection at Aqueous Electrical Interfaces.” *Phys. Rev. Lett.* 109, 187602 (2012).

## Presentations

---

1. **Presenter**, “Non-optical biomolecular detection in human serum using interfacial electrokinetic transduction,” 2017 Annual Meeting of the AES Electrophoresis Society AICHE, Oct. 29 – Nov. 3, 2017, Minneapolis, MN
2. **Presenter**, “AC Electrohydrodynamics of Polarized Laminar Interfaces,” 2017 Annual Meeting of the AES Electrophoresis Society AICHE, Oct. 29 – Nov. 3, 2017, Minneapolis, MN
3. **Presenter**, “Non-optical biomolecular detection in human serum using interfacial electrokinetic transduction,” 2016 Annual Meeting of the AES Electrophoresis Society AICHE, November 13-18, 2016, San Francisco, California
4. **Co-Chair and Presenter**, “Chemical and Biomolecular Detection at a Polarizable Electrical Interface,” 17<sup>th</sup> International Conference on Microfluidics and Nanofluidics WASET, July 9-10, 2015, Prague, Czech Republic
5. **Presenter**, “Electrokinetic detection of biomolecular interactions at polarizable liquid interfaces,” 89<sup>th</sup> ACS Colloid & Surface Science Symposium, June 15-17, 2015, Pittsburgh, Pennsylvania
6. **Presenter**, “Electrokinetic Biosensing at Liquid Interfaces by Fluidic Dielectrophoresis,” 2014 Annual Meeting of the AES Electrophoresis Society AICHE, November 16-21, 2014, Atlanta, Georgia
7. **Poster**, “Gagnon Microfluidics Lab,” ChemBE PhD Recruitment Weekend 2014-2016, Johns Hopkins University, Baltimore Maryland
8. **Poster**, “Ca<sup>2+</sup> Detection Through Fluidic Dielectrophoresis at a Liquid-Liquid Interface,” Advances in Microfluidics and Nanofluidics 2013, May 24-26, 2013, University of Notre Dame, South Bend, Indiana

## Teaching Experience

---

### Teaching Assistant

Fall 2015 – Fall 2017

#### *Transport Phenomenon II – Undergraduate Course*

- Hold recitation hours to assist students with lecture notes, assignments and course related questions and concerns
- Substituted as lecturer for course as needed

## Leadership/Outreach

---

### Graduate Student Liaison Committee (GSLC)

Fall 2014 – Fall 2016

#### *Social Chair*

- Act as a representative of the Graduate ChemBE class, communicating comments and concerns to administration
- Organize symposiums, professional developing and social events for department

## Women in Science and Engineering (WISE)

Spring 2014 – 2015

### High School Mentor

- Mentor a high school student throughout a semester, teaching research methodology and techniques
- Generate specific research projects for the semester involving literature research and experiments
- Assist student in development of experiments and presentation of their research project to classmates, teachers and principal

## Outreach Program

Summer 2013

- Organized a youth outreach program immersing inner city middle school students in STEM
- Created several experiments teaching students about microfluidics, laminar flow and biological reactions

## Mentored Students (\* denotes active students)

---

### Undergraduate Student Mentor:

1. Edwin Lavi\*. B.S and M.S in Chemical and Biomolecular Engineering. Johns Hopkins University, Baltimore, MD. Mentored 2016-present
2. Luis Miguel Rodriguez\*. B.S in Chemical and Biomolecular Engineering. Johns Hopkins University, Baltimore, MD. Mentored 2016-present

### **Provost Undergraduate Research Award (PURA) recipient**

*ChemBE research award for undergraduate research (2017)*

3. Hieu Tran. B.S in Chemical and Biomolecular Engineering. Johns Hopkins University, Baltimore, MD. Mentored 2016-present
4. Kenny Ling\*. B.S in Chemical and Biomolecular Engineering. Johns Hopkins University, Baltimore, MD. Mentored 2015-present
5. Robert McLarnon. B.S in Chemical and Biomolecular Engineering. Johns Hopkins University, Baltimore, MD. Mentored 2014-2015
6. Arya Reddy. B.S in Chemical and Biomolecular Engineering. Johns Hopkins University, Baltimore, MD. Mentored 2013-2014
7. Steven Doria\*. B.S and M.S in Chemical and Biomolecular Engineering. Johns Hopkins University, Baltimore, MD. Mentored 2012-present

### High School Student Mentor:

8. Swadhin Nalubola. Student Summer Internship. Centennial High School. Howard County, MD. Mentored Summer 2017  
**Regeneron STS Scholar**
9. Paige Simmons. Women in Science and Engineering (WISE) Program. Garrison Forrest High School. Owings Mills, MD. Mentored 2014
10. Lindy Wittenberg. Women in Science and Engineering (WISE) Program. Garrison Forrest High School. Owings Mills, MD. Mentored 2013